A Coupled Eulerian-PFEM Model for the Simulation of overtopping in Rockfill Dams
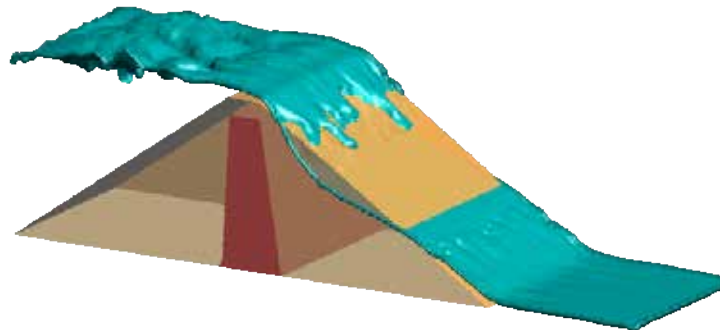
A. Larese De Tetto
E. Oñate
R. Rossi

A Coupled Eulerian-PFEM Model for the Simulation of overtopping in Rockfill Dams

A. Larese De Tetto
E. Oñate
R. Rossi

"La filosofia è scritta in questo grandissimo libro che continuamente ci sta aperto innanzi a gli occhi (io dico l'universo), ma non si può intendere se prima non s'impara a intender la lingua, e conoscer i caratteri, ne' quali è scritto. Egli è scritto in lingua matematica, e i caratteri son triangoli, cerchi, ed altre figure geometriche, senza i quali mezzi è impossibile a intenderne umanamente parola; senza questi è un aggirarsi vanamente per un oscuro laberinto."

Galileo Galilei, Il Saggiatore (1623)

Acknowledgments

I would like to thank all the people that are someway linked to this work and that contribute to its realization in different but equally important manners.

First of all I want to express my warmest gratitude to Prof. Eugenio Oñate who has given me the possibility of developing this work, encouraging me since the early beginning. His enthusiasm and optimism have been a strong motivating force during these years. I am deeply indebted to Dr. Riccardo Rossi whose endless patience made possible the realization of this monograph.

In 2010 Prof. Djeordje Perić gave me the opportunity to visit the College of Engineering of Swansea University for three months. I would like to thank him for the warm welcome and his nice tutoring during this period. This internship gave me the possibility to meet Prof. De Souza Neto, whose extreme kindness I will not forget, and Steffen Bauer, a good friend.

I am very grateful to all the professors of the RMEE department of the Universitat Politècnica de Catalunya because their doors have always been opened for answering any doubt and for any useful advice. A really special thank goes to one of them, who believed in me long before I even knew about believing in myself, thank you Prof. Miguel Cervera.

If CIMNE is a very pleasant place to work in, it is because of the people it is made of. Especially for all the members of office $C4$, maybe the noisiest but the nicest office of all CIMNE as well! Thank you Pooyan, Miguel Angel, Roberto, eRiccardo, Salva, Mónica, Pablo, Miquel and Ferran. They have been much more than simple office mates.

Thank you to all the others researchers that are, or have been, part of CIMNE. Among them I would like to mention Carlos and Adelina and also Miguel, Kike, Abel, Eduardo, Kazem, Jordi, Robert.

I am very grateful to all "the women" of CIMNE, in particular to MaJesus, Mercè and Lelia for their kindness and interest shown.

It has been a pleasure to be involved in these years in the XPRES and EDAMS projects which gave me the possibility of starting a good collaboration with the partners of UPM and CEDEX. I am very grateful to all of them and in particular to Prof. Miguel Angel Toledo, Rafa Moran and Fernando Salazar. Thank you for constantly helping me with all the physical aspects of dam engineering and for sharing nice moments during all the congresses of dams. In this context I would like to mention Prof. Iñaki Escuder who gave me the opportunity of becoming voting member of the Committee on Numerical Aspects of Dams of SpanCOLD and involved me in the organization of the last Benchmark Workshop on Numerical Analysis of Dams.

I am especially grateful to Dr. Janosch Stascheit and Prof. Umberto Perego for their useful advises during the revision of this document.

During these years I have met and known a huge number of people that left me unforgettable memories. Some of them became great friends and deserve a special mention for constantly supporting me and sharing bad and good moments. Thank you Elisa Maria, MaCarmen, Maria Laura, Esther and Mara.

When I was at the beginning of this experience, I could not even imagine that in spite of the distance, my "old" Italian friends would have always been so present in my life! Thank you for making me feel so loved.

Last but not least I would like to thank my family: my parents Elda and Ivo and my brother Paolo with Claudia for their endless love and my nephew Tobia who still does not know that this work will become his first and only storybook! Finally I would like to thank a special person who has tirelessly (and not always successfully) tried to teach me to give the right importance to things without falling apart after any failure: thank you Roberto.

Abstract

Rockfill dams are nowadays often preferred over concrete dams because of their economic advantages, their flexible design and thank to the great advance achieved in geosciences and geomechanics. Unfortunately their behavior in case of overtopping is still an open issue. In fact very little is known on this phenomenon that in most cases leads to the complete failure of the structure with catastrophic consequences in term of loss of lives and economic damage.

The principal aim of the present work is the development of a computational method to simulate the overtopping and the beginning of failure of the downstream shoulder of a rockfill dam. The whole phenomenon is treated in a continuous framework.

The fluid free surface problem outside and inside the rockfill slope is treated using a unique Eulerian fixed mesh formulation. A level set technique is employed to track the evolution of the free surface. The traditional Navier-Stokes equations are modified in order to automatically detect the presence of the porous media. The non-linear seepage is evaluated using a quadratic form of the resistance law for which the Ergun's coefficients have been chosen.

The structural response of the solid skeleton is evaluated using a continuum viscous model. A non-Newtonian modified Bingham law is proposed for the simulation of the behaviour of a granular non-cohesive material. This approach has the possibility of considering a pressure sensitive resistance criterion. This is obtained inserting a Mohr-Coulomb failure criterion in the Bingham relation. Due to the large deformation of the mesh during the failure process, a Lagrangian framework is preferred to a fixed mesh one: the Particle Finite Element Method (PFEM) is therefore used. Its specific features make it appropriate to treat the rockfill material and its large deformations and shape changes.

Finally a tool for mapping variables between non-matching meshes is developed to allow passing information between the fluid fixed and the dam moving meshes.

All the numerical results are compared with experiments on prototype rockfill dams.

Resumen

Hoy en día las presas de escollera resultan a menudo una elección preferible respeto a las tradicionales presas de hormigón por su menor impacto económico y, sobretodo, por su mayor flexibilidad de diseño gracias a los grandes avances alcanzados en geociencias y en geomecánica.

Sin embargo, desafortunadamente su comportamiento frente a un sobrevertido sigue siendo un aspecto desconocido y muy difícil de analizar. Cuando el nivel de agua supera la coronación, en la mayoría de los casos se produce la rotura completa de la presa con consecuencias catastróficas tanto en términos de perdida de vidas humanas como en términos económicos.

El principal objetivo de este trabajo es el desarrollo de un método computacional que pueda simular el sobrevertido y el principio de la rotura del espaldón aguas abajo de una presa de escollera. Todo el fenómeno se trata con modelos continuos.

El problema de flujo en superficie libre tanto fuera como dentro de la escollera se trata con una única formulación usando un método Euleriano de malla fija y una técnica de level set para trazar la evolución de la superficie libre. Se han modificado las clásicas ecuaciones de Navier-Stokes de manera que se detecte automaticamente la presencia de un medio poroso. La filtración no lineal se evalúa mediante una ley de resistencia cuadrática en la cual se han empleado los coeficientes de Ergun.

La respuesta estructural se evalúa usando un modelo continuo viscoso. Se propone una versión modificada de la ley de Bingham para fluidos no Newtonianos que permite simular el comportamiento granular no cohesivo de la escollera. La diferencia de este enfoque consiste en la posibilidad de considerar un criterio de resistencia que sea función de la presión. Esto se obtiene insertando un criterio de fallo de Mohr Coulomb en la relación de Bingham. Debido a las grandes deformaciones a las que se ve sometida

la malla durante el proceso de rotura se ha preferido usar un método Lagrangiano respecto a uno de malla fija: el Métodos de Elementos Finitos y Partículas (PFEM). Sus características lo hacen apropiado para simular la escollera y sus grandes deformaciones y cambios de forma.

Finalmente se ha desarrollado una herramienta para interpolar datos entre mallas no coincidentes para permitir la transferencia de informaciones entre el modelo fluido de malla fija y el modelo de la presa con malla en movimiento.

Todos los resultados numéricos se han comparado con experimentos hechos sobre presas prototipo.

Contents

List of Figures

List of Tables

List of Symbols

$\mathbf{u}$:   fluid Darcy velocity;

$\overline{\mathbf{u}}$:   fluid velocity;

$\mathbf{u}_s$:   structural velocity;

$\mathbf{u}_C$:   coupled velocity;

$\mathbf{u}_M$:   mesh velocity;

$\mathbf{u}_g$:   fluid Darcy velocity on the Gauss point;

$\overline{\mathbf{u}}_g$:   fluid velocity on the Gauss point;

p :   fluid pressure;

p_s :   solid total pressure;

p'_s :   solid effective pressure;

p_C :   coupled pressure;

$\mathbf{v}$:   vector of unknowns;

$\mathbf{x}$:   vector of fluid displacements;

$\mathbf{x}_s$:   vector of solid displacements;

$\boldsymbol{\sigma}$:   stress tensor;

$\boldsymbol{\tau}$:   deviatoric part of the stress tensor;

$\boldsymbol{\varepsilon}$:   rate of strain tensor;

τ_0 :   yield stress;

$\dot{\gamma}$:   equivalent strain rate;

ϕ :   internal friction angle;

n :   porosity;

$\mathbf{n}$:   external normal vector;

ρ	:	fluid density;
ρ_s	:	solid density;
μ	:	fluid dynamic viscosity;
μ_s	:	structure dynamic viscosity;
$\tilde{\mu}$	:	apparent solid dynamic viscosity;
ν	:	fluid kinematic viscosity;
m	:	regularization coefficient in the non-Newtonian exponential approximation;
$\mathbf{w}$	:	velocity weight function;
q	:	pressure weight function;
$\mathcal{V}$	:	velocity space;
$\mathcal{Q}$	:	pressure space;
$\mathcal{V}_h$	:	velocity finite element space;
$\mathcal{Q}_h$	:	pressure finite element space;
τ	:	intrinsic time (stabilization parameter)
Ω	:	control volume;
Ω_E	:	empty volume;
Γ	:	Boundary of Ω ($\partial\Omega$);
E_1, E_2	:	linear and non linear Darcy coefficient;
$\overline{E}_1, \overline{E}_2$	:	non-linear Darcy coefficient divided by density;
$\partial_N\Omega$	:	Neumann boundary;
$\partial_D\Omega$	:	Dirichlet boundary;
$\partial\Omega_m$	:	moving boundary;
$\mathbf{M}$	:	mass matrix in the element-based formulation
$\mathbf{K}$	:	viscous operator in the element-based formulation
$\mathbf{G}$	:	gradient operator in the element-based formulation
$\mathbf{D}$	:	divergence operator in the element-based formulation
$\overline{\mathbf{M}}$	:	stabilized mass matrix in the element-based formulation
$\overline{\mathbf{C}}$	:	stabilized damping matrix in the element-based formulation
$\overline{\mathbf{K}}$	:	stabilized stiffness in the element-based formulation
$\tilde{\mathbf{M}}$	:	mass matrix in the edge-based formulation
$\tilde{\mathbf{K}}$	:	viscous, convective and Darcy operator in the edge-based formulation
$\tilde{\mathbf{G}}$	:	gradient operator in the edge-based formulation
$\tilde{\boldsymbol{\nabla}}$	:	weak gradient operator in the edge-based formulation

$\tilde{\mathbf{D}}$:   divergence operator in the edge-based formulation

β, δ :   stability parameters of Bossak method

ϕ :   level set function

D_p :   diameter of the sieve at which the $p\%$ of the material pass;

g :   gravity;

$\mathbf{b}$:   body force;

$\mathbf{t}$:   tension;

Re :   Reynolds number;

k :   permeability or intrinsic permeability;

K :   permeability coefficient;

f_d :   Darcy-Weisbach friction coefficient;

r_H :   hydraulic radius;

e :   roughness;

θ :   shape coefficient;

i :   hydraulic gradient;

$\bar{i}$:   pressure drop;

h :   nodal dimension;

h_{el} :   element dimension;

$(\cdot)^n$:   (.) at time step n;

$(\cdot)^k$:   (.) at iteration k;

$(\cdot)_h$:   (.) in the finite element space;

Chapter 1

Introduction

The rehabilitation of existing dams and their safety analysis are nowadays open fields of research. In fact in many countries the design criteria of these structures have recently been reviewed with the intention of increasing safety level facing an exceptional flooding. This is justified considering that many dams and dikes exhibit now a higher potential to experience overtopping during exceptional flood events. Climate change induced by global warming is, for instance, one of the main causes that might lead to more devastating flooding than ever [128].

While in a concrete dam, an overflow does not easily affect the integrity of the structure, in an embankment dam in most cases it compromises the dam body [64]. If a dam or dike fails, loss of life and economic damage are direct consequences of such event. Early warning is therefore crucial for saving lives in flood-prone areas. That is the reason why an increasing interest is rising on the study of rockfill and earthfill dams, termed embankment dams, during extreme phenomena.

The analysis of the possible consequences of an accidental overspill is still impossible or very imprecise and the necessary economical measures for solving the problem are then inefficient. An appropriate computational method will help to reduce the economic impact of the investments in dam safety and in emergency plans for embankment dams.

The possibility of studying the behavior of water throughout and over the dam in case of sudden change of upstream conditions and of his effect on the rockfill is currently limited by the absence of a suitable numerical tool. It should simulate the sudden dynamic change in the seepage and flow condition and predict the subsequent onset and evolution of breaching in the rockfill slope. The current work aims to give a contribution

to this field, creating and validating a new computational method of general applicability for simulating, with a unique formulation, the flow throughout and over the dam while failure occurs together with the dam structural response.

1.1   Embankment dams

In recent years technology on embankments dams has developed sensibly due to the advances in soil mechanics knowledge and in all related sciences. This, combined with the evident economic advantage of construction, make often this kind of structure a more appealing choice than the traditional concrete dams [64]. The design of embankment dams is in fact very flexible and makes use of different shapes and materials, that can often be found *in situ*. The tallest dams in the world are embankment dams (i.e. Rogún dam (335m) or Nurek dam (300m)) and their number exceed that of the classical concrete dam structure [64].

Nevertheless the vulnerability of embankment dams to overtopping still remains their weakest point. In fact, according to the ICOLD bulletin [64], this is their principal or secondary cause of failure in 31% and 18% of cases respectively. In concrete dams, on the contrary, the effects of an overflow usually does not compromise the structure integrity and the causes of failure should be found in other reasons, often connected with problems in the foundations.

Several examples of dam failures as a consequence of overtopping can be found in the literature. Usually the causes of the overflow are an extreme meteorological event, often accompanied by malfunctioning of the spillway capacities.

By far the most catastrophic dam disaster ever happened was the failure of the Banqiao dam (see Figure 1.1). It was a 118 m high embankment dam built in the early 1950. It was designed to support the once-in-1000-years-flood. Nevertheless in 1975, due to the Typhon Nina the once-in-2000-years-flood was reached and Banqiao dam failed (followed by the failure of other 62 dams of the same basin). 62 000 people died because of the flood and around 145 000 because of famine and epidemics. This event is, for dam engineering, what Chernobyl and Bhopal have represented for the nuclear and chemical industry respectively [128].

Among others, the failure of the Tous dam in Valencia should be mentioned. In October 1982, a tsunami of 20 million of m^3 of water flowed through the *Comunidad Valenciana* (Figure 1.2). In that case the cause of the exceptional flooding was a particular mete-

Figure 1.1: Image of Banqiao dam. Image taken from [1].

Figure 1.2: Image of Tous dam after the overtopping of October 19th, 1982.

orological condition called "gota fria" which consists of a cold high-altitude depression surrounded by warm air with high moisture content that leads to extremely heavy rain fall in the hinterland of the Mediterranean coast of Spain.

These and many other similar historical events demonstrate that when the water exceeds the crest of the dam, the consequences can be catastrophic. An exceptional flooding compromises seriously the structure, leading, in almost all cases, to its failure. Nevertheless the breaching formation is a relatively slow process. It is never an explosive sudden failure. Chanson in [30] for example, reported that in the case of the Glashütte dam (Figure 1.3), the complete failure of the structure occurs 4 hours later the beginning of the overtopping. In the case of the Teton dam the reservoir was drained after approximately 12 hours.

Figure 1.3: Glashütte embankment dam (Germany). Image taken from [30].

When the water overpasses the crest of the dam a seepage process begins in the downstream slope that leads to its progressive saturation. The first breach usually appears at the toe of the dam, where the resistance is lower. According to Toledo [122, 123], two are the main mechanisms that compromise the rockfill:

- Mass sliding or loss of stability of a part of the downstream region due to the land slide. This is the predominant failure mechanism when the downstream slope is very steep. The saturation of the rockfill leads to a reduction of effective stresses that, together with seepage, induce the formation of a failure circle that abruptly crumbles. This phenomenon usually affects the whole width of the dam as can be observed in Figure 1.4(a).

- Superficial dragging of rockfill particles. When the downstream slope is flat ($1V$:

$3H$ for instance) this is the predominant failure mechanism. The water coming out from the toe of the dam drags away the superficial rocks. It leads to the formation of channels in the downstream slope (see for instance Figure 1.4(b)).

(a) Mass sliding failure.   (b) Superficial dragging failure.
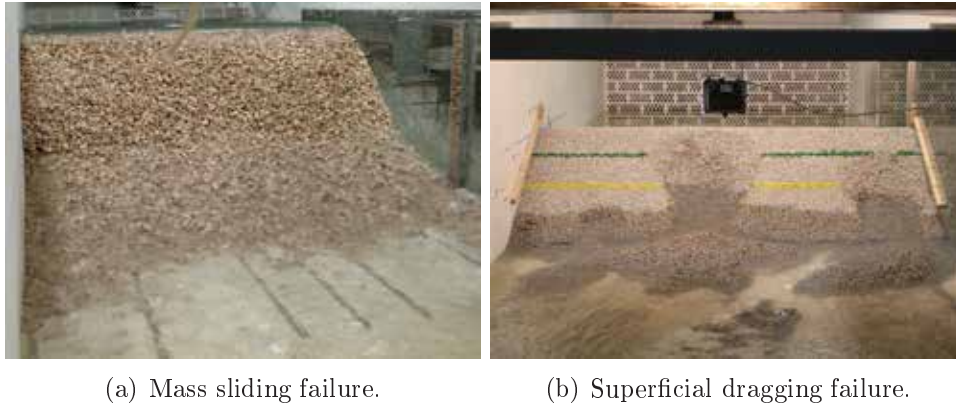
Figure 1.4: The images show two experiments carried out at the UPM laboratories. On the left an example of mass sliding failure (initial slope $1V : 1.5H$) whereas on the right the failure is mainly due to superficial dragging of particles (initial slope $1V : 3H$).

These two mechanisms usually act in a combined way depending on the failure process evolution [122].
The clay core represents an additional barrier before the complete failure of the structure when the protection given by the rockfill is no longer present (see Figure 1.5 for a typical cross section of a rockfill dam). Its failure can be the consequence of surface erosion or of mechanical fracture of the same under the pushing of the water retained upstream.
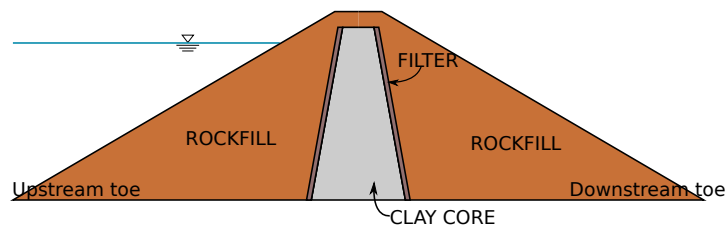
Figure 1.5: Schematic cross section of a rockfill dam.

1.2 The XPRES and E-DAMS projects

In the last years the Spanish Ministry of Science and Innovation has been funding the XPRES [127] and E-DAMS [53] projects, a joint work between the Polytechnic

University of Madrid (UPM), the Centre for Hydrographical Studies of CEDEX and the International Centre for Numerical Methods in Engineering (CIMNE).

The principal aim is the study of beginning and evolution of the breach caused by an overtopping on rockfill prototype dams both from a physical and numerical point of view.

UPM and CEDEX team have a wide experience on this topic and their effort has been addressed to reach a better characterization of the failure in function of a series of parameters. These are for examples, the downstream slope, the impervious system adopted, the material used for the experiments and so on.

Their extensive experimental campaign consists of more than 100 experiments. Further information can be found in Chapter 5 of the present work and for more details on the topic, the consultation of [21, 76] is recommended.

All the experiments have been performed in three flumes of different dimensions shown in Figure 1.6.

(a) Small channel. 0.4m width, 0.6m height, 12m long.

(b) Medium channel. 1.0m width, 1.1m height, 16m long.

(c) Large channel. 2.48m width, 1.4m height, 13.7m long.

Figure 1.6: UPM and CEDEX experimental channels used for XPRES and E-DAMS projects.

The experimental data in terms of bottom pressure distribution and evolution of the seepage line, have been largely used in this work to validate the numerical approach of the .. code during its development. Some examples of validation are presented in Chapter 5.

1.3   Objectives

This work faces the problem of the numerical simulation of the overtopping and beginning of failure in a prototype rockfill dam.

This leads to the development of two different numerical tools:

1. A fluid code to simulate a free surface flow in a variable porosity medium in order to accurately predict the hydrodynamic forces acting on the rockfill slope;

2. A coupled fluid-structure analysis code to simulate the beginning of failure in case of overtopping.

The idea is to solve both problems (seepage and unset and evolution of failure), using a continuous approach and to integrate an Eulerian fluid model with a Lagrangian structural one. This is done in order to minimize the computational effort for the fluid calculation and to have a Lagrangian tool which can naturally following the large deformation of the rockfill slope.

Three are the main developments to be done in this work in order to achieve its objectives:

- A *free surface fluid model* able to take into account the presence of a porous media. It should work with any variable incoming discharge condition.

- A *structural model* to simulate the behaviour of a rockfill slope in presence (or not) of variable hydrodynamic forces.

- A *coupling tool* to integrate the previously mentioned models and to simulate the whole transitory phenomenon of failure of a rockfill slope due to exceptional flooding.

The assumption of a Newtonian incompressible viscous fluid is taken for the flow of water. The solution system is a modified form of the traditional Navier-Stokes equations. The effect of porosity is implicitly taken into account using the Darcy velocity as a variable of the problem and adding the corresponding extra term in the momentum equations. This term takes into account the seepage forces.

For the study of the fluid behavior in a variable porosity medium an Eulerian approach with a fixed mesh is chosen. A level set technique is used for the tracking of the evolution of the free surface.

A Non-Newtonian constitutive law is used to simulate the behaviour of a rockfill slope. A Bingham plastic with a variable yield threshold is proposed to accurately identify the beginning of failure of the slope material, according to a Mohr Coulomb failure criteria. The Particle Finite Element Method (PFEM) is the technique used for the structural analysis. Its Lagrangian approach is a key feature to accurately follow the large distortion of the slope in case of failure.

The presence of water should be taken into account in terms of variable hydrodynamic forces. The problem is always fully drained since the pores can be considered interconnected according to experimental results.

The coupling of the two models is done in an explicit staggered way by projecting information between the Eulerian and the Lagrangian models. For that purpose a tool to project information between non-matching meshes is developed.

The objectives of this work can be considered fulfilled when the experiments on the prototype rockfill dams carried on by UPM and CEDEX can be reproduced.

All the algorithms presented in this work have been implemented in Kratos [47, 48], a framework for developing finite element codes for multiphysics problems.

1.4 Layout of the document

The layout of the document is the following:

Chapter 2. The physical problem of seepage in rockfill is described and the non linear form of the resistance law governing the phenomena is chosen. A brief overview of the state of the art is presented. The governing equations are derived and the numerical formulation is presented in detail. Two different Eulerian approaches are described, a traditional element-based approach and an edge-based one. In both cases the level set technique is used to track the evolution of the free surface.

Chapter 3. The behaviour of the rockfill material is treated as a non-Newtonian granular fluid. After an overview of traditional non-Newtonian materials, a regularized Bingham model is presented. This classical approach is modified to take into account the variability of the yield stress in a granular non cohesive material. A Lagrangian kinematical description is adopted and PFEM is used for the structural analysis.

Chapter 4. The governing equations of the monolithic coupled problem are presented

and the balance equation of the fluid and structure models are derived The coupling is performed in a fully staggered way using a tool to manage the transfer of informations between the two models. This is done using an algorithm that allows the data mapping between non matching meshes, described at the end of the chapter.

Chapter 5. The code is validated by reproducing experiments carried out by UPM and CEDEX using either $2D$ and $3D$ models. Different prototype dam models are considered in the examples.

Chapter 6. The summary of the achievements is described and the main points of the future research work are outlined.

Appendix A. The main features of Kratos Multiphysics are briefly presented.

Chapter 2

The fluid problem

In this chapter the numerical algorithm developed for the simulation of the free surface flow in presence of a variable porosity medium is described.

First, a brief overview of the traditional studies of flux in porous media is performed in order to chose a suitable resistance law for the problem of interest. The balance equations are obtained and two solution strategies are adopted for their numerical treatment. An *element-based* formulation and an *edge-based* approach are studied and implemented. The choice of a fixed mesh method leads to the need of tracking the evolution of the free surface. The level set technique adopted for this purpose is described in the last part of the chapter. The chapter finishes with a series of examples that aim to check the correct behavior of the presented algorithms.

2.1   Introduction

The classical approaches of fluid flow in porous media are not applicable for the analysis of the water motion within the rockfill of a dam. Traditionally water is considered in slow motion or as a stationary load [130]. On the contrary in the case of an overtopping, the possibility to follow the rapid transition of the water level in the downstream slope is a key point for the identification of the beginning of the failure mechanism.

On the other hand, the typical problem of evaluating the saturation level of the pores loses its importance in the case studied, due to the large dimension of the granular material. Under these circumstances, in fact, the pores can be considered always interconnected and the problem fully drained [122].

According to traditional studies of flow in porous media [117, 122], at a *micro* level the flux between the rocks is assimilated to flow in pipes. This analogy is used for the derivation of the resistance law used for the calculation of the hydraulic gradient[1] due to seepage. The well known Darcy law is not applicable to the analyzed problem. In the following sections it is explained how to obtain a suitable resistance law to be used in the balance equations.

It should be pointed out that a key point for the complete simulation of the hydro-dynamic effect of an overtopping is the capability of the code for simulating at once, not only the seepage, but also the fluid flow upstream, downstream and over the dam. For that purpose the balance equations are derived considering the flow inside a generic porous material. The key point is represented by the fact that they automatically reduce to the classical Navier-Stokes equations when porosity is equal to one; that is when no porous medium is present. The resistance law is inserted in the balance equation as well. Its contribution goes to zero out of the granular material. A similar approach has been used by Nithiarasu and coworkers [88–90] to study the natural and forced convective flux in a cavity filled by a variable porosity medium.

The easy definition of a control domain and of spatial variables (like for instance the porosity, defining the presence of a granular material), induces to choose an Eulerian fixed mesh approach. Moreover this kinematical framework is also more efficient allowing an easier parallelization of the code.

This choice leads to the need of choosing a level set technique for tracking the evolution of the free surface.

Two different solution strategies are presented in the chapter, an element based and an edge based approach. After a comparative analysis of both methodologies, the latter is chosen for being implemented in $3D$ and being coupled with the structural code.

2.1.1   Flow in rockfill material

The flux in porous media is traditionally studied using the empirical relation that Darcy obtained in 1856. Studying the flow of water through a sand-filled column he discovered that the pressure drop ($\bar{i}$) and the velocity of water inside a porous material (u) are

---

[1]The hydraulic gradient is the measure of the variation of the hydraulic head for unit length [58].

linearly related. This observation leads to the formulation of the well known Darcy law,

$$\bar{i} = \frac{\mu}{k} u. \tag{2.1}$$

where μ is the water dynamic viscosity and k is the permeability of the porous media [12].

Relation 2.1 was derived studying the unidirectional flux in sand at low Reynolds numbers. On the contrary,in the case of flux through rockfill material, the local fluid velocities were observed not to be linearly related to the pressure drop. In fact it was experimentally proved that over certain average dimension of the particles, equation 2.1 is not anymore valid.

Many authors have deeply studied this aspect with essentially two objectives:

- Discover the range of validity of Darcy's law (equation 2.1).

- Define an alternative resistance law[2] in case equation 2.1 is not anymore valid.

Remark 1. Velocity u in equation 2.1 is by definition the *Darcy velocity*, i.e. the fluid velocity averaged over the total control volume Ω (often called *macroscopic velocity* or *unit discharge* being the discharge per unit volume), whereas the *fluid velocity* $\overline{u}$ is averaged over the empty part of Ω (called Ω_E). Their relation is stated by the Dupuit-Forchheimer equation [87]:

$$u = n\overline{u} \tag{2.2}$$

where n is the porosity that, by definition [3] is

$$n := \frac{\Omega_E}{\Omega}. \tag{2.3}$$

See Figure 2.1 for a graphical explanation.

---

[2]Equation 2.1 and all the alternative non linear formulations that are presented in the next sections are commonly called *resistance laws* because they measure the resistance made by the porous matrix to the fluid flow.

[3] Equation 2.3 is by definition the *volumetric porosity* n^v whereas in Figure 2.1 a cross section of the control volume is considered and a *sectional porosity* $n^a := A_E/A$ should be defined like the ratio between the area of pores and the total cross section area. Consequently, a *lineal porosity* can be also defined as the ratio between the length of pores over the total length ($n^l := l_E/l$). Fortunately Bears in [12] demonstrated that in a porous medium this distinction is unnecessary being

$$n^v = n^a = n^l.$$
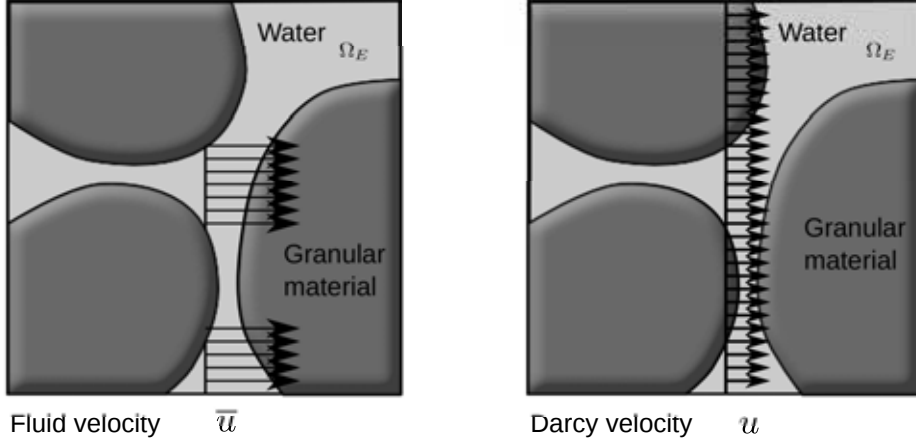
Figure 2.1: Graphical description of fluid velocity $\overline{u}$ (averaged over the empty volume Ω_E) and Darcy velocity u (averaged over the total control volume Ω).

Remark 2. Permeability k introduced in 2.1, also called *intrinsic permeability*, is measured in squared meters (m^2) and is defined as

$$k := \frac{n^3 D_p^2}{5(1-n)^2 \theta} \tag{2.4}$$

where D_p is an equivalent diameter of the porous material[4], whereas θ is a shape coefficient of the particles. It is important to stress that the Darcy's law can also be found in the form

$$i = \frac{1}{K}u.$$

where K is the *permeability coefficient*, often called simply *permeability* as well, which represents the hydraulic conductivity and has the dimension of a velocity (m/s). In this case i is not any more the pressure drop $\overline{i}$ (measured in Pa/m), but it represents the head loss per unit length, that is the hydraulic gradient and it is dimensionless.

2.1.2 Analogy between flow in porous media and pipes flow

It is generally accepted to consider the flow in the pores of rock particles essentially similar to flow in a pipe network but with a more complicated configuration [117, 122]. All the empirical formulae to evaluate the pressure drop due to friction in pipes have been used and adapted to get similar empirical relationships in the case of porous material

---

[4]D_p is the diameter of the sieve at which the $p\%$ of the material passed.

[50, 79, 125].

Some brief recall of flow in pipes

The Darcy-Weisbach formula is traditionally used for the evaluation of the hydraulic gradient i in pipes (only in a second time it was adapted to be used in open channel flows). It states

$$i = \frac{f_d}{4\,r_H}\frac{u^2}{2g};$$ (2.5)

where f_d if the Darcy-Weisbach friction coefficient, r_H is the hydraulic radius[5] (in pipes of diameter D is $r_H = D/4$), g is the gravity acceleration and u is the velocity.

In general f_d is function of the Reynolds number[6] (Re) and of the roughness of the pipe (e). It is demonstrated [58] that:

- In laminar regime f_d is a function of Re only,

$$f_d = \frac{64}{Re}.$$

- In turbulent regime f_d is constant

$$f_d = const.$$

- In the transition regime

$$f_d = f_d(Re, e).$$

Above explanations imply that the hydraulic gradient, using equation 2.5, can be calculated as follow

- For laminar regime

$$i = \frac{64\mu}{2gD_p^2\rho}\,u.$$ (2.6)

- For turbulent regime

$$i = \frac{const}{2g\,D_p}\,u^2.$$ (2.7)

---

[5] The hydraulic radius is defined as the ratio between the fluid area and the wet perimeter.

[6] The Reynolds number is the dimensionless coefficient that, being the ratio between inertia and viscous forces, quantifies the relative importance of each one for a given flow [58]. It is defined as $\frac{\rho u\,l}{\mu}$ where ρ is the fluid density and l is a characteristic length (in pipes it coincide with the diameter).

Therefore in case of laminar regime, the relation between the hydraulic gradient and velocity is linear (like it is in Darcy's law), whereas in turbulent regime it becomes quadratic. Hence, as a preliminary conclusion, the possibility to classify whether the regime of the flux is turbulent or laminar seems to be very important to define the range of validity of Darcy's law. Even though, as explained in the next sections, this is not the only aspect to be taken into account.

Definition of the range of validity of Darcy's law

Many different approaches are present in literature on the application of the Darcy-Weisbach relation to flow in porous media to define the range of application of Darcy's law. The deep analysis of each of them is not relevant for the aim of this work and the consultation of [79, 122] is recommended for a more comprehensive understanding of the topic. Nevertheless some important aspects that led to the definition of different resistance law are reported here to fully introduce the problem.

The main issue is related to the definition of the Reynolds number Re in a porous material. In fact the following aspects have to be taken into account:

- Whether to take the velocity of equation 2.5 equal to the Darcy velocity (u) or to the fluid velocity ($\overline{u}$). This choice leads to a different definition of the Reynolds number

$$Re(u) = \frac{u\,l}{\nu} = \frac{n\overline{u}\,l}{\nu} = n\,Re(\overline{u});\qquad(2.8)$$

(equation 2.2 has been used).

- How to define the characteristic length l in equation 2.8. Some authors prefer to chose an *equivalent diameter* D_p (often the choice is D_{10} or D_{50}). In fact it is easier to measure the granular dimension than the dimension of the pores. Others define $l \approx r_H$ arriving to express l as a function of the permeability k.

- Finally it is important to remember that equation 2.5 is one of the most popular, but not the only possible choice for the calculation of the hydraulic gradient [50].

Different choices lead to different values of Re. Nevertheless all authors agree that the beginning of appearance of turbulence is for values of Re in the range $60 - 150$ (not 2000 like in pipes).

Many authors think that the range of validity of Darcy's law coincides with the laminar regime, considering that turbulence appears at lower Re for higher D_p. Nevertheless according to [122], the experimental results put in evidence that:

- The transition between the linear and the non linear relation between i and u is gradual (differently from the transition from laminar to turbulent regime in pipes);

- The starting point of non-linear behavior appears for $Re \in [1 - 10]$ whereas turbulent phenomena appear for $Re \in [60 - 150]$.

Following [122], Scheideger justifies the first aspect with the co-presence of a laminar regime in the thinner "porous channels" and a turbulent one in the thicker ones. On the other hand, non-linearity is often attributed to the presence of inertial forces that are usually small but can be important for low Re in comparison with the viscous one. Considering that inertia forces are proportional to the square of velocity, a quadratic relation between velocity and pressure drop is justified.

In Figure 2.2 some classification of the range of validity of Darcy law are shown. For more details on how they are obtained the consultation of [79, 122, 125] is recommended.
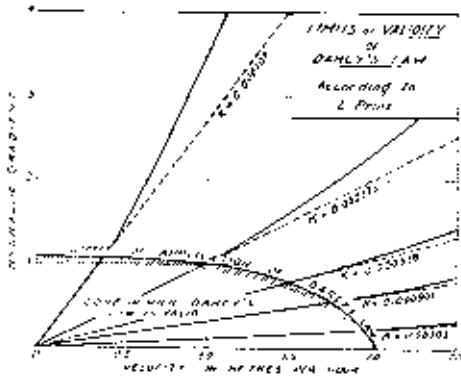
(a) E. Prinz diagram (taken from [77]).   (b) J. Bear diagram (taken from [12]).
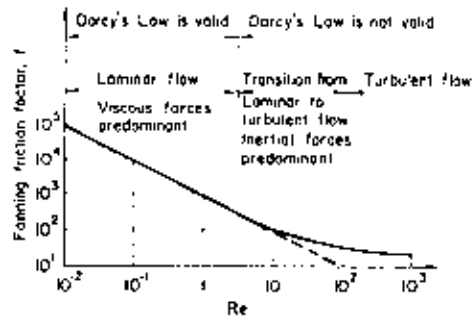
Figure 2.2: Range of validity of Darcy law in its linear form.

2.1.3 Resistance laws

Forchheimer was one of the first authors in proposing in 1901 a quadratic resistance law like

$$\mathbf{i} = \alpha\mathbf{u} + \beta\mathbf{u}^2; \tag{2.9}$$

where constants α and β depend only on the characteristics of rockfill material. Alternatively Prony in 1804 and Jeager in 1956 proposed an exponential law like

$$\mathbf{i} = \gamma\mathbf{u}^\eta; \tag{2.10}$$

where γ and η depend on the flow condition, the characteristics of the porous medium and the fluid.

Both the quadratic and the power relationships are based on experimental results although some theoretical basis have been provided for their justification [79]. Nowadays both equations 2.9 and 2.10 are accepted and widely used. In recent years almost all efforts have been addressed in determining the α and β or γ and η constants.

In fact in some of the formulae the coefficients depend on physical parameters of the rockfill material only, such as the size of the particles, porosity and the particle shape (following [122] this is the case of Ergun (1952), Wilkins(1956), McCorquodale (1978), Stephenson(1979), Martins (1990) and Gent (1991)). In other cases, the coefficients depend on the experimental value of the hydraulic conductivity. Since building prototypes for estimating these parameters can be very expensive, it is often easier and cheaper to choose one of the first group of formulae.

A comprehensive overview of the different models can be found in [79, 122, 125].

Selection of the seepage model: Ergun's correlation

In the previous paragraphs an overview of the state of the art of seepage models has been presented. In order to choose the suitable non-linear resistance law to be used in this work, some additional remarks should be done.

- The objective of the model is to develop a tool to simulate the free surface flow through the rockfill and outside of the same, so an essential requirement for the resistance law is that it should automatically go to zero when $n = 1$.

- The quadratic form of the resistance laws is easier to implement than the exponential one;

Collecting the previous considerations, a quadratic form of the non-linear resistance law is adopted and the Ergun's definition of the constant coefficients is chosen [57].

Therefore, the pressure drop is

$$\bar{\mathbf{i}} = E_1 \mathbf{u} + E_2 \mathbf{u}^2; \tag{2.11}$$

Following Ergun theory and calling D_p the average diameter of the granular material ($D_p \equiv D_{50}$), E_1 and E_2 coefficients are defined like

$$E_1 = 150 \cdot \frac{(1-n)^2}{n^3} \cdot \frac{\mu}{D_p^2}; \tag{2.12}$$

and

$$E_2 = 1.75 \cdot \frac{(1-n)}{n^3} \cdot \frac{\rho}{D_p}; \tag{2.13}$$

Defining the permeability shape coefficient $\theta = 30$ of equation 2.4, the permeability k can be calculated as a function of n and D_p

$$k = \frac{n^3 D_p^2}{150(1-n)^2}. \tag{2.14}$$

The final form of the resistance law chosen in this work is then:

$$\boxed{\bar{\mathbf{i}} = \frac{\mu}{k}\mathbf{u} + \frac{1.75}{\sqrt{150}}\frac{\rho}{\sqrt{k}n^{3/2}}\mathbf{u}^2.} \tag{2.15}$$

It is interesting to observe that the linear part of equation 2.15 is equivalent to the Darcy's law

2.2 Continuous form

Once the resistance law has been chosen, the balance of linear momentum and the continuity equation for an incompressible fluid can be derived. The principal objective of the present approach is to define a unique set of balance equations governing both the free surface flow and the seepage problem. In other words the governing equations have to be able to reproduce the free surface flow in a variable porosity medium (considering the open air as a porous medium with porosity $n = 1$).

An approach similar to the one presented in the following sections, can be found in chapter 5 of the 5th edition of [132]. This methodology is largely used for the treatment of heat transfer in a fluid saturated porous media [8, 88, 89, 124].

2.2.1   Variables of the problem

The unknowns of the problem are:

- $\mathbf{u}$, fluid Darcy velocity (see equation 2.2 for its definition).

- p, fluid pressure;

Other parameters are:

- ρ is the fluid density. In the present work water is treated as an incompressible fluid with constant density over the whole fluid domain, regardless of the presence of a porous medium.

- μ is the fluid dynamic viscosity.

- n is the porosity (see equation 2.3 for its definition). In the most general case it is a function of space and time:

$$n = n(\mathbf{x}, t); \tag{2.16}$$

In the present work, according to experimental analysis, the variation of porosity in time, within the fluid solver, can be neglected, considering only its variation in space. Nevertheless it should be remarked that porosity does change in time according to the structural deformation of the porous material, which will be explained in chapter 3 and has been considered in the coupled problem described in chapter 5.

Therefore, as a fluid variable, n is only function of the spatial coordinates

$$n = n(\mathbf{x}); \tag{2.17}$$

The fluid is considered here as a continuum and the presence of a porous matrix is implicitly taken into account via the porosity n as will be explained in sec 2.2.3.

2.2.2   Constitutive law.   Water as a Newtonian incompressible fluid

The water is treated as a Newtonian incompressible fluid. In general a fluid at rest does not present shear stresses and the Cauchy stress tensor takes the form $\boldsymbol{\sigma} = -p\mathbf{I}$. The

tangential stresses are non zero in a fluid in motion and the stress tensor becomes

$$\boldsymbol{\sigma} := -p\mathbf{I} + \boldsymbol{\tau} \tag{2.18}$$

where $\boldsymbol{\tau}$ is the deviatoric part. The latter is linearly related to the strain rate tensor through viscosity which is assumed to be constant.

Therefore the stress tensor for a Newtonian fluid is

$$\boldsymbol{\sigma} := -p\mathbf{I} + 2\mu\nabla^s\overline{\mathbf{u}}; \tag{2.19}$$

where μ is the dynamic viscosity and

$$(\nabla^s\overline{\mathbf{u}})_{kl} := \frac{1}{2}\left(\frac{\partial\overline{u}_k}{\partial x_l} + \frac{\partial\overline{u}_l}{\partial x_k}\right); \tag{2.20}$$

is the symmetric part of the velocity gradient [51, 132]. It should be observed that equation 2.19 does not take into account the possible presence of a porous medium. A more general form of the same will be derived in the next sections in order to have a relation that holds both for the case of free fluid and of flow in rockfill material.

2.2.3 Modified form of the Navier-Stokes equations

In order to take into account the flow in a variable porosity medium, some modifications should be introduced in the traditional form of the Navier-Stokes equations. The modified system of solution equations is derived here imposing continuity and conservation of linear momentum within a fixed control volume.

In the following sections a balance on a finite volume is first carried out and brought later to the infinitesimal form.

Remark 3. It is important to stress that it is always used a continuous approach to treat the fluid in the whole domain regardless of it is inside or not the porous media.

Continuity equation

Let us consider a $2D$ square finite control volume $dxdy$ as the one plotted in Figure 2.3, and let's define $\overline{dx}\overline{dy} = n\,dxdy$ as the empty part of it, that is the portion of this volume that can be occupied by the fluid (see the definition of porosity at equation 2.3).
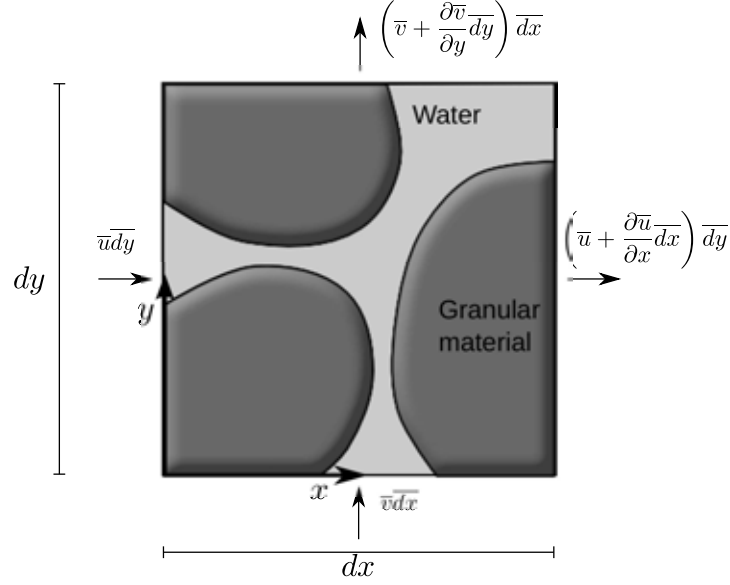
Figure 2.3: Balance of conservation of mass in a discrete volume $dx\,dy$. $d\overline{x}d\overline{y} = n\,dx\,dy$ is the empty volume where the fluid can circulate.

Imposing the continuity of the fluid field velocity $\overline{\mathbf{u}} = [\overline{u}, \overline{v}]$ over the fluid control domain $d\overline{x}d\overline{y}$, yields

$$\rho\left(\overline{u} + \frac{\partial\overline{u}}{\partial x}d\overline{x}\right)d\overline{y} - \rho\overline{u}d\overline{y} + \rho\left(\overline{v} + \frac{\partial\overline{v}}{\partial y}d\overline{y}\right)d\overline{x} - \rho\overline{v}d\overline{x} + \frac{d\rho}{dt}d\overline{x}d\overline{y} = 0; \qquad (2.21)$$

Considering that the fluid is incompressible, equation 2.21 can be rewritten as

$$\begin{aligned}
\frac{\partial\overline{u}}{\partial x}d\overline{x}d\overline{y} + \frac{\partial\overline{v}}{\partial y}d\overline{x}d\overline{y} &= \\
\frac{\partial u}{\partial x}dxdy + \frac{\partial v}{\partial y}dxdy &= 0.
\end{aligned} \qquad (2.22)$$

where the definition of the Darcy velocity $\mathbf{u} = [u, v]$ (equation 2.2) has been used. Therefore the continuity equation is

$$\frac{\partial u}{\partial x} + \frac{\partial v}{\partial y} = 0; \qquad (2.23)$$

that can be rewritten as

$$\boxed{\nabla \cdot \mathbf{u} = 0;} \qquad (2.24)$$

Momentum equation

The balance of linear momentum in the $i - th$ direction is

$$\rho \frac{d\overline{u}_i}{dt} d\overline{x}d\overline{y} - \frac{\partial \sigma_{ij}}{\partial x_j} d\overline{x}d\overline{y} - \rho f_i^{ext} d\overline{x}d\overline{y} = 0; \tag{2.25}$$

where f^{ext} are the volumetric forces and the sum over j spatial index is supposed. Observing Figure 2.4 and remembering that the constitutive equation 2.19 is

$$\begin{bmatrix} \sigma_x & \tau_{xy} \\ \tau_{xy} & \sigma_y \end{bmatrix} = - \begin{bmatrix} p & 0 \\ 0 & p \end{bmatrix} + 2\mu \begin{bmatrix} \partial \overline{u}/\partial x & 1/2 \left(\partial \overline{u}/\partial y + \partial \overline{v}/\partial x \right) \\ 1/2 \left(\partial \overline{u}/\partial y + \partial \overline{v}/\partial x \right) & \partial \overline{v}/\partial y \end{bmatrix} \tag{2.26}$$
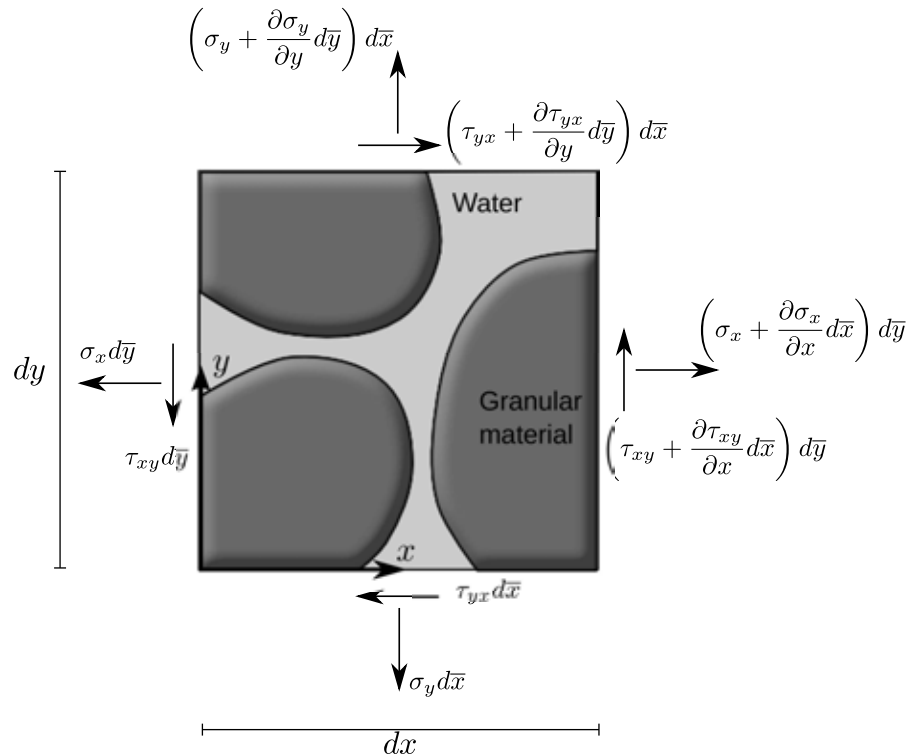
Figure 2.4: Balance of conservation of linear momentum in a discrete volume $dx\,dy$. $d\overline{x}d\overline{y} = n\,dx\,dy$ is the empty volume where the fluid can circulate.

the balance equation in x-direction becomes

$$\rho\frac{\partial\overline{u}}{\partial t}d\overline{x}d\overline{y} + \rho\overline{u}\frac{\partial\overline{u}}{\partial x}d\overline{x}d\overline{y} + +\rho\overline{v}\frac{\partial\overline{u}}{\partial y}d\overline{x}d\overline{y}$$
$$-\frac{\partial\sigma_x}{\partial x}d\overline{x}d\overline{y} + \frac{\partial\tau_{xy}}{\partial y}d\overline{x}d\overline{y} - \rho b_x d\overline{x}d\overline{y} + \hat{D}_x d\overline{x}d\overline{y} \quad = 0; \tag{2.27}$$

where the $\hat{D}_x$ represents the x component of the hydraulic gradient due to seepage, e.g. the resistance law discussed in Section 2.1.3 (i.e. equation 2.15). Its matricial form will be detailed at the end of this section. In equation 2.27 the definition of material time derivative has been implicitly taken into account $\left(\rho\frac{d\overline{u}_i}{dt} = \rho\frac{\partial\overline{u}}{\partial t} + \rho\overline{u}\frac{\partial\overline{u}}{\partial x} + +\rho\overline{v}\frac{\partial\overline{u}}{\partial y}\right)$.
Substituting $d\overline{x}d\overline{y} = n\,dxdy$ into equation 2.27 and inserting the definition of Darcy velocity gives

$$\rho\frac{\partial u}{\partial t} + \rho\overline{u}\frac{\partial u}{\partial x} + \rho\overline{v}\frac{\partial u}{\partial y} + n\frac{\partial p}{\partial x}$$
$$-2\mu\frac{\partial^2 u}{\partial x^2} - \mu\left(\frac{\partial^2 u}{\partial x\partial y} + \frac{\partial^2 v}{\partial x^2}\right)n - \rho b_x n + n\hat{D}_x = 0; \tag{2.28}$$

This expression holds for any infinitesimal domain $dxdy$.

Finally, calling $D_y = n\hat{D}_y$, and using the same procedure in the other spatial dimension leads to analogous results. In summary the equation of balance of linear momentum is written as

$$\boxed{\rho\partial_t\mathbf{u} + \rho\overline{\mathbf{u}}\cdot\nabla\mathbf{u} + n\nabla p - 2\nabla\cdot\mu\nabla^s\mathbf{u} - \rho\mathbf{b}n + \mathbf{D} = \mathbf{0};} \tag{2.29}$$

where $\partial_t\mathbf{u} = \dfrac{\partial\mathbf{u}}{\partial t}$. In equation 2.29 $\mathbf{D}$ is the matricial form of the resistance law 2.15 or, what is the same, the Darcy term. It represents the dissipative effects due to the interaction between the solid and the fluid part. Details of this term can be found in Section 2.1.3. The matricial form of the non-linear Darcy's law 2.15 is

$$\mathbf{D} = \frac{n\mu}{k}\mathbf{u} + \frac{1.75}{\sqrt{150}}\frac{\rho n}{\sqrt{k}}\frac{|\mathbf{u}|}{n^{3/2}}\mathbf{u}. \tag{2.30}$$

Remark 4. Let us define the Ergun coefficients $\overline{E}_1$ and $\overline{E}_2$ per unit density as

$$\overline{E}_1 = 150\cdot\frac{(1-n)^2}{n^2}\cdot\frac{\mu}{D_p^2\rho}; \tag{2.31}$$

and

$$\overline{E}_2 = 1.75 \cdot \frac{(1-n)}{n^2} \cdot \frac{1}{D_p}. \tag{2.32}$$

These expressions will be useful in the next chapter especially during the explanation of the stabilization techniques.

Remark 5. A more general form of the constitutive equation of water can be now formulated as

$$\boldsymbol{\sigma} := -np\mathbf{I} + 2\mu\nabla^s\mathbf{u}. \tag{2.33}$$

This equation automatically reduces to equation 2.19 if the porosity is equal to one (i.e. the free surface flow problem is considered).

2.3   Weak form

Equation 2.24 and 2.29 represent the modified form of the Navier-Stokes problem. They take into account the presence of a porous medium and reduce to the classical Navier Stokes equations when the porosity is $n = 1$ (free fluid flow). The equations to be solved are therefore

$$\rho\partial_t\mathbf{u} + \rho\overline{\mathbf{u}} \cdot \nabla\mathbf{u} + n\nabla p - 2\nabla \cdot \mu\nabla^s\mathbf{u}$$
$$-\rho\mathbf{b}n + E_1\mathbf{u} + E_2|\mathbf{u}|\mathbf{u} = \mathbf{0} \text{ in } \Omega, \ t \in (0, T); \tag{2.34}$$
$$\nabla \cdot \mathbf{u} = 0 \text{ in } \Omega, \ t \in (0, T).$$

where $\Omega \subset \mathbb{R}^d$ (where d is the space dimension) is the fluid domain in a time interval $(0, T)$.
The boundary and initial condition of the previous problem are:

$$\begin{aligned}
\mathbf{u}(\mathbf{x}, 0) &= \mathbf{u}_0(\mathbf{x}) & \text{in} & \quad \Omega; \\
\mathbf{u}(\mathbf{x}, t) &= \mathbf{g}(\mathbf{x}, t) & \text{on} & \quad \partial\Omega_D, \quad t \in (0, T); \\
\mathbf{n} \cdot \boldsymbol{\sigma}(\mathbf{x}, t) &= \mathbf{t}(\mathbf{x}, t) & \text{on} & \quad \partial\Omega_N, \quad t \in (0, T);
\end{aligned} \tag{2.35}$$

where $\boldsymbol{\sigma}$ is defined by equation 2.33 and Ω_D and Ω_N are the Dirichlet and Neumann boundary respectively.

Remark 6. Note that $\mathbf{n}$ indicates the outer unit normal vector whereas n is defined in equation 2.3 and indicates the porosity.

The weak form of equations 2.34 is derived next using a Galerkin formulation. A mixed finite element method is obtained, that is the approximation of both the velocity components and the pressure (and their respective weighted functions) need to be introduced. The weak form of equation 2.34 is

$$
\begin{aligned}
&\int_\Omega \mathbf{w}\rho\partial_t\mathbf{u}d\Omega + \int_\Omega \mathbf{w}\rho\overline{\mathbf{u}}\cdot\nabla\mathbf{u}d\Omega + \int_\Omega \mathbf{w}n\nabla p d\Omega \\
&- \int_\Omega \mathbf{w}\nabla\cdot 2\mu\nabla^s\mathbf{u}d\Omega + \int_\Omega \mathbf{w}(E_1\mathbf{u}+E_2|\mathbf{u}|\mathbf{u})d\Omega - \int_\Omega \mathbf{w}\rho n\mathbf{b}d\Omega = \mathbf{0} \quad \forall\mathbf{w}\in\mathcal{V}; (2.36) \\
&\hspace{8cm} \int_\Omega q\nabla\cdot\mathbf{u} = 0 \quad \forall q\in\mathcal{Q};
\end{aligned}
$$

where, for a fixed $t\in(0,T)$, $\mathbf{u}$ is assumed to belong to the velocity space $\mathcal{V}\in[\mathbf{H}^1(\Omega)]^d$ of vector functions whose components and their first derivatives are square-integrable, and p belongs to the pressure space $\mathcal{Q}\in\mathbf{L}_2$ of square-integrable functions. $\mathbf{w}$ and q are velocity and pressure weighting functions belonging to the velocity and the pressure spaces respectively. Integrating by parts the pressure and convective terms, calling $\Gamma=\partial\Omega$ gives

$$
\begin{aligned}
\int_\Omega \mathbf{w}n\nabla p d\Omega &= -\int_\Omega np\nabla\cdot\mathbf{w}d\Omega + \int_{\partial\Omega}\mathbf{w}\cdot np\mathbf{n}d\Gamma; \\
\int_\Omega \mathbf{w}\nabla\cdot 2\mu\nabla^s\mathbf{u}d\Omega &= -2\int_\Omega \nabla\mathbf{w}:\mu\nabla^s\mathbf{u}d\Omega + \int_{\partial\Omega}\mathbf{w}\cdot(2\mu\mathbf{n}\cdot\nabla^s\mathbf{u})d\Gamma;
\end{aligned} \quad (2.37)
$$

where $\mathbf{n}$ is the outer normal vector (see remark 6). Substituting relations 2.37 into equations 2.36 and considering the Neumann boundary condition, the system to be solved becomes

$$
\begin{aligned}
&\int_\Omega \mathbf{w}\rho\partial_t\mathbf{u}d\Omega + \int_\Omega \mathbf{w}\rho\overline{\mathbf{u}}\cdot\nabla\mathbf{u}d\Omega - \int_\Omega np\nabla\cdot\mathbf{w}d\Omega \\
&\quad + 2\int_\Omega \nabla\mathbf{w}:\mu\nabla^s\mathbf{u}d\Omega + \int_\Omega \mathbf{w}(E_1\mathbf{u}+E_2|\mathbf{u}|\mathbf{u})d\Omega \\
&\hspace{2cm} - \int_\Omega \mathbf{w}\rho n\mathbf{b}d\Omega - \int_{\partial\Omega_N}\mathbf{w}\cdot\mathbf{t}d\Gamma = \mathbf{0} \quad \forall\mathbf{w}\in\mathcal{V}; \\
&\hspace{6cm} \int_\Omega q\nabla\cdot\mathbf{u}d\Omega = 0 \quad \forall q\in\mathcal{Q};
\end{aligned} \quad (2.38)
$$

Let $\mathcal{V}_h$ be a finite element space to approximate $\mathcal{V}$, and $\mathcal{Q}_h$ a finite element approxima-

tion to $\mathcal{Q}$. The problem is now finding $\mathbf{u}_h \in \mathcal{V}_h$ and $p_h \in \mathcal{Q}_h$ such that

$$
\begin{aligned}
\int_\Omega \mathbf{w}_h \rho \partial_t \mathbf{u}_h d\Omega + \int_\Omega \mathbf{w}_h \rho \overline{\mathbf{u}}_h \cdot \nabla \mathbf{u}_h d\Omega - \int_\Omega n \, p_h \nabla \cdot \mathbf{w}_h d\Omega & \\
+2 \int_\Omega \nabla \mathbf{w}_h : \mu \nabla^s \mathbf{u}_h d\Omega + \int_\Omega \mathbf{w}_h (E_1 \mathbf{u}_h + E_2 |\mathbf{u}_h| \mathbf{u}_h) d\Omega & \\
- \int_\Omega \mathbf{w}_h \rho n \mathbf{b} d\Omega - \int_{\partial \Omega_N} \mathbf{w}_h \cdot \mathbf{t}_h d\Gamma & = \mathbf{0} \quad \forall \mathbf{w}_h \in \mathcal{V}_h; \\
\int_\Omega q_h \nabla \cdot \mathbf{u}_h d\Omega & = 0 \quad \forall q_h \in \mathcal{Q}_h;
\end{aligned}
$$

$$(2.39)$$

In the next sections the two different solution strategies developed in the present work are described:

- An element-based solver;

- An edge-based solver;

The traditional finite element (i.e. element-based) approach implies a loop over the elements in order to recalculate all the elemental contributions at each iteration of each time step. In the calculation of the elemental contributions a gather/scatter procedure, from nodal to elemental to nodal information is needed in order to build the global solution system together with an assembling solution procedure. Löhner [81], demonstrated that these indirect addressing operations are very time consuming and can be reduced using an edge-based data structure. Nevertheless, the simplicity and the accuracy of an element-based formulation makes it a very attracting choice. Advantages and drawbacks of both technologies are detailed in the following pages.

2.4   Element-based approach: monolithic solver

A traditional element based approach is presented here. Equations 2.39 are solved using a monolithic scheme. Namely velocity and pressure are calculated at the same time.
The nodal degrees of freedom (velocity $\mathbf{u}$ and pressure p) form the vector of unknowns of the solution system. The Navier-Stokes equations are stabilized with an ASGS technique presented in Section 2.4.1 and a particular form of the generalized α time integration schemes is used: the Bossak method, as explained in Section 2.4.3. The linearization is achieved with a quasi Newton method using a residual based approach and a predictor multi-corrector scheme.

Remark 7. All the material variables (density ρ, dynamic viscosity μ, porosity n and average diameter D_{50}) that appear in the solution equations have to be understood as elemental variables although, for reason of simplicity, the upper index el will be omitted. A short remark should be made on the evaluation of elemental porosity of boundary elements. Porous nodes are characterized by $n < 1$ whereas non-porous ones have $n = 1$. In the present work a dominant porosity approach is used: if the element has one node which is non-porous, then the elemental porosity is $n = 1$. This can be done because porosity is assigned on geometric entities that are then meshed inserting nodes on the boundary of the objects (figure 2.5 shows a graphical example). This will lead to an error in case of variable geometry of the porous material. For instance, this is the case of the coupled problem treated in Chapter 4 where this error is accepted.

(a) Geometrical Entities	(b) Nodal porosity	(c) Elemental porosity
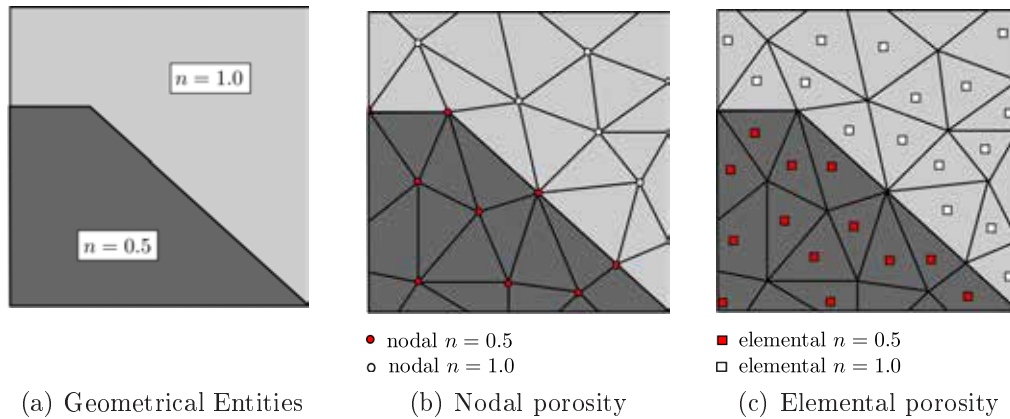
Figure 2.5: Definition of elemental porosity with a dominant porosity criteria.

2.4.1 Stabilized formulation

The instabilities connected with the convection term in a convection-dominated problem and the violation of the *inf-sup condition* are the two well known causes of instability of the numerical solution of the Navier-Stokes equations. The first problem is induced by the Galerkin approximation itself, whose truncation error appears in the form of a negative diffusion operator. This lack of diffusion leads to serious oscillations when convection dominates. This is measured by the mesh Péclet number (Pe) that is an non-dimensional coefficient expressing the ratio between convective and diffusive transport. Considering $\overline{\mathbf{u}}$ the convective velocity and h the dimension of the mesh, the solution

presents a lack of diffusion if

$$Pe := \frac{\overline{\mathbf{u}}h}{2\mu} \geq 1;$$

i.e. when convection dominates over diffusion [51].

The second reason of instability is connected with the choice of the finite element space for pressure and velocity.

In order to better understand the origin of this kind of instability it is convenient to recall the classical stationary Stokes problem

$$\begin{aligned} -\nu\Delta\mathbf{u} + \nabla p &= \mathbf{b}; \\ \nabla \cdot \mathbf{u} &= 0; \end{aligned} \tag{2.40}$$

that, in matrix form, becomes

$$\begin{bmatrix} \mathbf{K} & \mathbf{G} \\ \mathbf{D} & \mathbf{0} \end{bmatrix} \begin{bmatrix} \mathbf{u} \\ \mathbf{p} \end{bmatrix} = \begin{bmatrix} \mathbf{F} \\ \mathbf{0} \end{bmatrix} \tag{2.41}$$

where $\mathbf{K} = -\nu\mathbf{L} \leftarrow -\nu\Delta$ is the viscous operator (being $\mathbf{L}$ the Laplacian), $\mathbf{G}$ is the discrete gradient operator, $\mathbf{D}$ is the divergence operator $(\mathbf{D} = \mathbf{G}^T)$, $\mathbf{u}$ is the vector of nodal velocities, $\mathbf{p}$ is the vector of nodal pressures and $\mathbf{F}$ is the external force vector. The zero matrix on the lower diagonal position of the system matrix, derived from the imposition of the incompressibility constrain, leads to some restrictions in the numerical solvability of the problem. It can be shown that the solution of system 2.41 exists and it is unique (i.e. the global matrix 2.41 is non-singular) if the kernel[7] of matrix $\mathbf{G}$ is zero. In fact from the first equation it is possible to get $\mathbf{u} = \mathbf{K}^{-1}(\mathbf{F} - \mathbf{Gp})$ that substituted in the second equation leads to

$$(\mathbf{D}\mathbf{K}^{-1}\mathbf{G})\mathbf{p} = (\mathbf{D}\mathbf{K}^{-1}\mathbf{F});$$

where $\mathbf{D}\mathbf{K}^{-1}\mathbf{G}$ is symmetric, being $\mathbf{K}$ symmetric, but it is positive definite only if $ker\ \mathbf{G} = 0$. In the latter case the pressure matrix is non singular and the value of $\mathbf{p}$ can be calculated and substituted in order to evaluate $\mathbf{u}$ [51].

Ladyzhenskaya - Babuška - Brezzi demonstrated that both the continuous and the discrete space of velocity and pressure (see Section 2.3 for their definition) cannot be arbitrarily chosen but they have to satisfy the so called *inf-sup* (or LBB from the initials

---

[7] The kernel of a matrix $\mathbf{A}$ is defined as $ker\mathbf{A} := \{\mathbf{q} \,|\, \mathbf{q} \in \mathbb{R}^d \ and \ \mathbf{A}\,\mathbf{q} = \mathbf{0}\}$.

of the authors) condition. It states that a stable finite element solution $\mathbf{u}_h, p_h$ to the Stokes problem exists if it is ensured that

$$\forall p_h \in Q_h \quad \exists \quad \mathbf{u}_h \in V_h \qquad \text{such that} \qquad \beta ||p_h|| \, ||\mathbf{u}_h||_{H^1} \leq b(p_h, \mathbf{u}_h); \qquad (2.42)$$

or equivalently

$$\inf_{p_h \in Q_h} \sup_{\mathbf{u}_h \in V_h} \frac{b(p_h, \mathbf{u}_h)}{||p_h|| \, ||\mathbf{u}_h||_{H^1}} \geq \beta; \qquad (2.43)$$

where $b(,)$ is the bilinear form $b(\mathbf{p}_h, \mathbf{u}_h) = -\int_\Omega \mathbf{p}_h \nabla \cdot \mathbf{u}_h d\Omega$ and $|| \, ||$ is the L_2 norm whereas $|| \, ||_{H^1}$ is the H^1 norm [9, 16].

There are several pairs of pressure velocity interpolations that allow the satisfaction of 2.43 like for instance the $Q1/P0$ element (continuous bilinear velocity, discontinuous constant pressure), or the $Q2/P1$ multiquadratic velocity, piecewise linear pressure or, among the continuous pressure interpolations, the so called *mini-element* ($P1 + /P1$) for example, with a linear velocity enriched with an internal bubble and linear pressure. More details can be found in [10, 42, 51, 106].

Unfortunately the simplest element, the $P1/P1$ (piecewise linear velocity and pressure), which is used in the present work for practical reasons, does not satisfy the *inf-sup* condition and a stabilization technique is necessary to fixed both sort of instability.

A wide range of stabilization techniques can be found in literature. One of the first ideas to overcome numerical oscillations on convection dominated problems, was to introduce diffusion on the direction of the stream lines. This led to the classical and extensively used *streamline-upwind/Petrov-Galerkin* (SUPG) method by Brooks and Hughes [17]. A generalization of SUPG for Stokes flows was proposed by Tezduyar [120, 121]: the *pressure-stabilizing/Petrov-Galerkin* (PSPG). In this case the stabilization term varies with the Reynolds number. In the zero Reynolds number limit, the PSPG stabilization term reduces to the SUPG one. Another, more general, stabilization approach was proposed by Hughes [63] (the *Galerkin least-squares* or GLS). He found out a way to use an equal order interpolation for velocity and pressure for the Stokes problem for incompressible fluids just adding the pressure gradient in the stabilizing terms in a SUPG-like strategy. The GLS method for time dependent problems uses both space and time finite elements discretization leading to a space-time finite element formulation of the problem.

So far all the stabilization techniques presented require the addition of some artificial diffusion term. As an alternative Oñate derived the stabilization terms using a *Finite*

calculus (FIC) approach based on imposing the balance equations over a finite domain [92, 93, 97, 101]. This approach allows to reinterpret the stabilization terms as an intrinsic and natural contribution to the original differential equations, instead of a correction term introduced at discrete level. With this natural stabilization approach many of the already existing stabilization techniques can be reinterpreted in a more physical manner.

A popular family of stabilization methods is derived by the so called *subgrid scale* (SGS) approach, introduced by Hughes in [62]. His novel idea is to split the unknowns ($\mathbf{u}$) into a part that can be represented by the finite element mesh ($\mathbf{u}_h$) and another part that accounts for the unresolvable scale ($\tilde{\mathbf{u}}$), that is for the variation of the unknown that cannot be captured by the finite element mesh. This corresponds to a splitting of the space $\mathcal{V}$ into the space of the finite elements ($\mathcal{V}_h$) and the subgrid space ($\tilde{\mathcal{V}}$) as

$$\mathcal{V} = \mathcal{V}_h \oplus \tilde{\mathcal{V}}; \tag{2.44}$$

Among the different SGS methods, two are the chosen techniques used in this work:

- The *Algebraic Sub-Grid Scale* stabilization (ASGS) that has been implemented in the element based formulation;

- The *Orthogonal Subgrid Scale* (OSS) technique that has been employed to stabilize the edge-based equations (see Section 2.5.1).

The main difference between these two techniques is that in ASGS the whole residual is used to approximate the sub-scales whereas in OSS only its orthogonal projection is used.

Typically, stabilized methods add to the left hand side of the discrete residual of the problem (i.e. the discretized weak form), a term of the form

$$\tilde{\mathbf{r}}(\mathbf{u}_h, \mathbf{w}_h) = \sum_{el} \int_{\Omega^{el}} \mathcal{P}^{el}(\mathbf{w}_h)^T \tau^{el} \mathcal{R}^{el}(\mathbf{u}_h) d\Omega; \tag{2.45}$$

where the so called *intrinsic time*, τ^{el} is an algorithmic parameter with dimension of time, $\mathcal{P}^{el}(\mathbf{w}_h)$ is a certain operator applied to the test function (it will be defined later on) and $\mathcal{R}^{el}(\mathbf{u}_h)$ is the residual of the differential equation to be solved. The upper index el in equation 2.45 indicates that the contribution is element-wise and will be omitted later on for the sake of simplicity.

Let us introduce the stabilized form of equation 2.39 using an ASGS technique. Referring to equation 2.45 Table 2.1 can be obtained. $\alpha \in [0,1]$ is an input parameter to control the influence of dynamic contribution, h is the *element length*[8]. The upper-indexes m and c refer to the momentum and the continuity equation respectively

Momentum equation	
$\mathcal{P}^m(\mathbf{w}_h)$	$\overline{\mathbf{u}}_h \cdot \nabla \mathbf{w}_h + \nabla q_h$
τ_1	$\left(\dfrac{\alpha}{\Delta t} + \dfrac{4\nu}{h^2} + \dfrac{2\|\overline{\mathbf{u}}_h\|}{h} + \overline{E}_1 + \overline{E}_2\|\mathbf{u}_h\| \right)^{-1}$
$\mathcal{R}^m(\mathbf{u}_h)$	$\partial_t \mathbf{u}_h + \overline{\mathbf{u}}_h \cdot \nabla \mathbf{u}_h - \nu \Delta \mathbf{u}_h + n\nabla p_h + \overline{E}_1 \mathbf{u}_h + \overline{E}_2 \|\mathbf{u}_h\| \mathbf{u}_h - n\mathbf{b}$
Continuity equation	
$\mathcal{P}^c(\mathbf{w}_h)$	$\nabla \cdot \mathbf{w}_h$
τ_2	$\dfrac{\mu}{\rho} + \dfrac{h\|\overline{\mathbf{u}}_h\|}{2}$
$\mathcal{R}^c(\mathbf{u}_h)$	$\nabla \cdot \mathbf{u}_h$

Table 2.1: Stabilizing elemental terms in the ASGS method.

Therefore the stabilized problem becomes:

$$
\begin{aligned}
\int_\Omega \mathbf{w}_h \rho \partial_t \mathbf{u}_h d\Omega + \int_\Omega \mathbf{w}_h \rho \overline{\mathbf{u}}_h \cdot \nabla \mathbf{u}_h d\Omega - \int_\Omega n\, p_h \nabla \cdot \mathbf{w}_h d\Omega & \\
+2 \int_\Omega \nabla \mathbf{w}_h : \mu \nabla \mathbf{u}_h d\Omega + \int_\Omega \mathbf{w}_h (E_1 \mathbf{u}_h + E_2 \|\mathbf{u}_h\|\mathbf{u}_h) d\Omega & \\
- \int_\Omega \mathbf{w}_h \rho n \mathbf{b} d\Omega - \int_{\partial\Omega_N} \mathbf{w}_h \mathbf{t}_h d\Gamma + \sum_{el} \int_{\Omega^{el}} \tau_1 \mathcal{P}^m \cdot \mathcal{R}^m d\Omega &= \mathbf{0} \quad \forall \mathbf{w}_h \in \mathcal{V}_h; \\
\int_\Omega q_h \nabla \cdot \mathbf{u}_h d\Omega + \sum_{el} \int_{\Omega^{el}} \tau_2 \mathcal{P}^c \cdot \mathcal{R}^c d\Omega &= 0 \quad \forall q_h \in \mathcal{Q}_h;
\end{aligned}
\tag{2.46}
$$

---

[8]The *element length* is defined as the edge of a regular triangle in $2D$ (or of a regular tetrahedron in $3D$), inscribed in the circumference (sphere in $3D$) that circumscribes the element itself.

2.4.2   Discretization procedure

Calling $\mathbf{u}$ and $\mathbf{p}$ the vector of nodal velocities and pressures respectively, system 2.46 in its matricial form is expressed as

$$
\begin{bmatrix} \mathbf{M} & \mathbf{0} \\ \mathbf{0} & \mathbf{0} \end{bmatrix} \cdot \begin{bmatrix} \dot{\mathbf{u}} \\ \dot{\mathbf{p}} \end{bmatrix} + \begin{bmatrix} \mathbf{K} & \mathbf{G} \\ \mathbf{D} & \mathbf{0} \end{bmatrix} \cdot \begin{bmatrix} \mathbf{u} \\ \mathbf{p} \end{bmatrix} = \begin{bmatrix} \mathbf{F} \\ \mathbf{0} \end{bmatrix} \tag{2.47}
$$

where the correspondence between the block matrices of 2.47 and the continuum form of the solution equation 2.39 can be seen in Table 2.2. Every block matrix is obtained, as usual, from the assembling of elemental contributions. Each node has as many degrees of freedom as the space dimension (n_{sd}) plus 1. That is the upper left elemental block matrix ($\mathbf{K}$) has dimensions $n_{sd} \times n_{sd}$ and $\mathbf{G}$ is a $n_{sd} \times 1$ matrix (consequently $\mathbf{D}$ is a $1 \times n_{sd}$). Therefore the global stiffness matrix is a square matrix of $n_{pts} \cdot (n_{sd}+1) \times n_{pts} \cdot (n_{sd}+1)$ (where n_{pts} is the number of nodes). The nonlinear terms are treated using the Picard method and they are evaluated at the element Gauss points at the previous iterations.

The matrix form of the stabilized system of equation 2.46 can be written as:

$$
\begin{bmatrix} \mathbf{M} + \mathbf{S}_{wu}^{M} & \mathbf{0} \\ \mathbf{0} & \mathbf{0} \end{bmatrix} \cdot \begin{bmatrix} \dot{\mathbf{u}} \\ \dot{\mathbf{p}} \end{bmatrix} + \begin{bmatrix} \mathbf{K} + \mathbf{S}_{wu} + \mathbf{S}^{c} & \mathbf{G} + \mathbf{S}_{wp} \\ \mathbf{D} + \mathbf{S}_{qu} & \mathbf{S}_{pq} \end{bmatrix} \cdot \begin{bmatrix} \mathbf{u} \\ \mathbf{p} \end{bmatrix} = \begin{bmatrix} \mathbf{F} + \mathbf{S}_{w}^{f} \\ \mathbf{S}_{q}^{f} \end{bmatrix} \tag{2.48}
$$

where all the stabilization matrices are inserted. Their detailed meaning can be found in Table 2.3 where $\mathbf{S}_{wv} = \mathbf{S}_{wv}^{C} + \mathbf{S}_{wv}^{\mu} + \mathbf{S}_{wv}^{D}$ and $\mathbf{S}_{qu} = \mathbf{S}_{qu}^{C} + \mathbf{S}_{qu}^{\mu} + \mathbf{S}_{qu}^{D}$.

Equation 2.48 can be written in compact form as

$$
\overline{\mathbf{M}}\dot{\mathbf{v}} + \mathbf{f}_{int}(\mathbf{v}(t), t) = \mathbf{f}_{ext}(t); \tag{2.49}
$$

where $\mathbf{v}^{T} = [\mathbf{u}, \mathbf{p}]$ and $\dot{\mathbf{v}}^{T} = [\dot{\mathbf{u}}, \dot{\mathbf{p}}]$ are the vector of unknowns and their time derivatives respectively.

Matricial term		Continuum term
$\mathbf{M}\dot{\mathbf{u}}$		$\sum_{el} \int_{\Omega_{el}} \mathbf{w}_h \rho \partial_t \mathbf{u}_h d\Omega$
	$\mathbf{K}^C\mathbf{u}$	$\sum_{el} \int_{\Omega_{el}} \mathbf{w}_h \rho \overline{\mathbf{u}}_h \cdot \nabla \mathbf{u}_h d\Omega$
$\mathbf{Ku}$	$\mathbf{K}^\mu\mathbf{u}$	$-2\sum_{el} \int_{\Omega_{el}} \mathbf{w}_h \nabla \mathbf{w}_h : \mu \nabla \mathbf{u}_h d\Omega$
	$\mathbf{K}^D\mathbf{u}$	$\sum_{el} \int_{\Omega_{el}} \mathbf{w}_h (E_1 \mathbf{u}_h + E_2 |\mathbf{u}_h| \mathbf{u}_h) d\Omega$
$\mathbf{Gp}$		$-\sum_{el} \int_{\Omega_{el}} n\, p_h \nabla \cdot \mathbf{w}_h d\Omega$
$\mathbf{Du}$		$\sum_{el} \int_{\Omega_{el}} q_h \nabla \cdot \mathbf{u}_h d\Omega$
$\mathbf{F}$		$\sum_{el} \int_{\Omega_{el}} \mathbf{w}_h \rho n \mathbf{b} d\Omega$

Table 2.2: Matrices and vectors of system 2.48 without stabilization terms.

	Momentum equation	
Matricial term		**Continuum term**
$\mathbf{S}_{wu}^{M}\dot{\mathbf{u}}$		$\displaystyle\sum_{el}\int_{\Omega_{el}}\tau_1\overline{\mathbf{u}}_h\cdot\nabla\mathbf{w}_h\partial_t\mathbf{u}_h d\Omega$
	$\mathbf{S}_{wu}^{C}\mathbf{u}$	$\displaystyle\sum_{el}\int_{\Omega_{el}}\tau_1\overline{\mathbf{u}}_h\cdot\nabla\mathbf{w}_h\overline{\mathbf{u}}_h\cdot\nabla\mathbf{u}_h d\Omega$
$\mathbf{S}_{wu}\mathbf{u}$	$\mathbf{S}_{wu}^{\mu}\mathbf{u}$	$\displaystyle-\sum_{el}\int_{\Omega_{el}}\tau_1\overline{\mathbf{u}}_h\cdot\nabla\mathbf{w}_h\nu\Delta\mathbf{u}_h d\Omega$
	$\mathbf{S}_{wu}^{D}\mathbf{u}$	$\displaystyle\sum_{el}\int_{\Omega_{el}}\tau_1\overline{\mathbf{u}}_h\cdot\nabla\mathbf{w}_h(\overline{E}_1\mathbf{u}_h+\overline{E}_2|\mathbf{u}_h|\mathbf{u}_h)d\Omega$
$\mathbf{S}_{wp}\mathbf{p}$		$\displaystyle\sum_{el}\int_{\Omega_{el}}\tau_1\overline{\mathbf{u}}_h\cdot\nabla\mathbf{w}_h n\nabla p_h d\Omega$
$\mathbf{S}_{w}^{f}$		$\displaystyle-\sum_{el}\int_{\Omega_{el}}\tau_1\overline{\mathbf{u}}_h\cdot\nabla\mathbf{w}_h n\mathbf{b}d\Omega$
	$\mathbf{S}_{qu}^{C}\mathbf{u}$	$\displaystyle\sum_{el}\int_{\Omega_{el}}\tau_1\nabla q_h\overline{\mathbf{u}}_h\cdot\nabla\mathbf{u}_h d\Omega$
$\mathbf{S}_{qu}\mathbf{u}$	$\mathbf{S}_{qu}^{\mu}\mathbf{u}$	$\displaystyle-\sum_{el}\int_{\Omega_{el}}\tau_1\nabla q_h\nu\Delta\mathbf{u}_h d\Omega$
	$\mathbf{S}_{qu}^{D}\mathbf{u}$	$\displaystyle\sum_{el}\int_{\Omega_{el}}\tau_1\nabla q_h(\overline{E}_1\mathbf{u}_h+\overline{E}_2|\mathbf{u}_h|\mathbf{u}_h)d\Omega$
$\mathbf{S}_{pq}\mathbf{p}$		$\displaystyle\sum_{el}\int_{\Omega_{el}}\tau_1\nabla q_h n\nabla p_h d\Omega$
$\mathbf{S}_{q}^{f}$		$\displaystyle-\sum_{el}\int_{\Omega_{el}}\tau_1\nabla q_h n\mathbf{b}d\Omega$
	Continuity equation	
$\mathbf{S}^{c}\mathbf{u}$		$\displaystyle\sum_{el}\int_{\Omega_{el}}\tau_2\nabla\cdot\mathbf{w}_h\nabla\cdot\mathbf{u}_h d\Omega$

Table 2.3: Stabilization matrices and vectors of system 2.48.

2.4.3   Bossak time integration scheme

The Navier-Stokes equations are solved in time using a Bossak scheme. First of all, let us recall the Newmark scheme from which it takes its origin. This is one of the most popular time integration procedures in structural dynamics and it is used with success in the linear regime. Its use in non-linear problems is possible, however in presence of large geometric non-linearities it is known to lead to unstable results unless the time step is severely reduced. This drawback derives form the fact that, in the stability of linear problems, the balance of energy equation implies an upper bound to the solutions. On the contrary, in a non linear regime this is not automatically verified when a linearization is performed. A stable algorithm can diverge in problems in which energy can grow up unlimitedly. It is therefore necessary to introduce some parameters in the time scheme able to lead to energy dissipation in high frequency modes [61, 118].

The momentum equation in structural problems is written in the general form as

$$\overline{\mathbf{M}}\ddot{\mathbf{x}} + \overline{\mathbf{C}}\dot{\mathbf{x}} + \overline{\mathbf{K}}\mathbf{x} = \overline{\mathbf{f}}_{ext}; \tag{2.50}$$

where $\mathbf{x}$ is the vector of displacements and $\overline{\mathbf{M}}$, $\overline{\mathbf{C}}$, $\overline{\mathbf{K}}$ are the stabilized mass, damping and stiffness matrices respectively. The overbar is used to distinguish the stabilized operators from those presented in equation 2.47.

Let's call $\mathbf{v}^T = [\mathbf{u},\ \mathbf{p}]$ and $\dot{\mathbf{v}}^T = [\dot{\mathbf{u}},\ \dot{\mathbf{p}}]$ the vector of unknowns and their time derivatives respectively. Equation 2.50, rewritten in terms of $\mathbf{v}$ and its derivative, represents the compact form of equations 2.48. It is

$$\overline{\mathbf{M}}\dot{\mathbf{v}} + \mathbf{f}_{int}(\mathbf{v}(t), t) = \mathbf{f}_{ext}(t); \tag{2.51}$$

where $\overline{\mathbf{M}}$ is the mass matrix. $\mathbf{f}_{int}$ takes into account of all the terms that depends on velocity and pressure (the internal forces) and $\mathbf{f}_{ext}$ is the vector of external forces, including all the contributions independent from the unknowns. Let's remark that equation 2.51 is an alternative way of writing equation 2.48.

Following the Newmark formulation $\mathbf{v}$ and $\mathbf{x}$ can be obtained at time step $n+1$ as

$$\mathbf{v}^{n+1} = \mathbf{v}^n + (1-\delta)\Delta t\,\dot{\mathbf{v}}^n + \delta\Delta t\dot{\mathbf{v}}^{n+1}; \tag{2.52a}$$

$$\mathbf{x}^{n+1} = \mathbf{x}^n + \Delta t\,\mathbf{v}^n + \left(\frac{1}{2} - \beta\right)\Delta t^2\dot{\mathbf{v}}^n + \beta\Delta t^2\dot{\mathbf{v}}^{n+1}; \tag{2.52b}$$

where Δt is the time step and δ and β are the two parameters that control the stability and accuracy of the scheme [116, 118]. The Newmark family of methods has its origin from the different choices of δ and β.

In implicit schemes, for instance, stability is ensured by

$$2\beta \geq \delta \geq \frac{1}{2};$$

that leads to an unconditionally stable method. Alternatively, using

$$\delta \geq \frac{1}{2} \qquad \beta \leq \frac{\delta}{2};$$

leads to a conditionally stable method. The stability condition in this case gives an upper bound to the natural frequency times the time step.

Calling $\hat{\mathbf{v}}^{n+1}$ and $\hat{\mathbf{x}}^{n+1}$ the prediction of the unknowns and displacements in terms of the known variables at time step n, equations 2.52 can be rewritten as

$$\mathbf{v}^{n+1} = \hat{\mathbf{v}}^{n+1} + \delta\Delta t\, \dot{\mathbf{v}}^{n+1}; \tag{2.53a}$$

$$\mathbf{x}^{n+1} = \hat{\mathbf{x}}^{n+1} + \beta\Delta t^2\, \dot{\mathbf{v}}^{n+1}. \tag{2.53b}$$

Equation 2.53a can be alternative written as

$$\dot{\mathbf{v}}^{n+1} = \frac{1}{\delta\Delta t} \left(\mathbf{v}^{n+1} - \hat{\mathbf{v}}^{n+1}\right). \tag{2.54}$$

Finally inserting equation 2.54 in equation 2.51 it gives

$$\frac{1}{\delta\Delta t}\overline{\mathbf{M}} \left(\mathbf{v}^{n+1} - \hat{\mathbf{v}}^{n+1}\right) + \mathbf{f}_{int}^{n+1} = \mathbf{f}_{ext}^{n+1}; \tag{2.55}$$

whose residual can be defined as

$$\mathbf{r}(\mathbf{v}^{n+1}) = -\frac{\overline{\mathbf{M}}}{\delta\Delta t} \left(\mathbf{v}^{n+1} - \hat{\mathbf{v}}^{n+1}\right) - \mathbf{f}_{int}^{n+1} + \mathbf{f}_{ext}^{n+1}. \tag{2.56}$$

The definition of the residual of the solution system (equation 2.56) discloses the residual based approach that is used in the predictor corrector solution strategy to solve the linearized system. This will be clarified in the next pages.

The α-method   Hilber Hughes and Taylor in 1977 presented the $\alpha - method$ able to introduce numerical dissipation at high frequency modes without degrading the order of accuracy of the solution [60]. The unknowns and their derivatives are calculated through a weighted average of their values at time step n and $n+1$. For instance in the case of a velocity formulation, the vector of unknowns is defined as

$$\mathbf{v}^{n+1+\alpha_H} = (1 + \alpha_H)\mathbf{v}^{n+1} - \alpha_H\mathbf{v}^n; \tag{2.57}$$

that reduces to the Newmark method if $\alpha_H = 0$.
 In equation 2.57 the choice

$$\alpha_H \in \left[-\frac{1}{3}, 0\right], \qquad \delta = \frac{1 - 2\alpha_H}{2}, \qquad \beta = \frac{(1 - \alpha_H)^2}{4}; \tag{2.58}$$

retains the second order accuracy and the unconditional stability. Maximum dissipation is obtained for $\alpha_H = -1/3$. In this scope the residual is slightly different form equation 2.56, taking the following form:

$$\begin{aligned}
\mathbf{r}(\mathbf{v}^{n+1+\alpha_H}) \;\; = \;\; &-\overline{\mathbf{M}}\left[\frac{1 + \alpha_H}{\delta\Delta t}\left(\mathbf{v}^{n+1} - \hat{\mathbf{v}}^{n+1}\right) - \alpha_H\dot{\mathbf{v}}^n\right] \\
&-\mathbf{f}_{int}^{n+1+\alpha_H} + \mathbf{f}_{ext}^{n+1+\alpha_H}.
\end{aligned} \tag{2.59}$$

Bossak scheme   The Bossak scheme follows a similar approach, but the modification affects exclusively the term related to the inertia forces. In fact

$$\dot{\mathbf{v}}^{n+1-\alpha_B} = (1 - \alpha_B)\dot{\mathbf{v}}^{n+1} + \alpha_B\dot{\mathbf{v}}^n; \tag{2.60}$$

and the residual form of the equilibrium equation is expressed as

$$\mathbf{r}(\mathbf{v}^{n+1-\alpha_B}) = -\overline{\mathbf{M}}\left[\frac{1 - \alpha_B}{\delta\Delta t}\left(\mathbf{v}^{n+1} - \hat{\mathbf{v}}^{n+1}\right) + \alpha_B\dot{\mathbf{v}}^n\right] - \mathbf{f}_{int}^{n+1} + \mathbf{f}_{ext}^{n+1}; \tag{2.61}$$

Introducing the prediction of velocity stated by equations 2.52a and 2.53a and grouping the unknowns at time $n+1$ the final expression of the residual linearized in time used in this work is

$$
\begin{aligned}
\mathbf{r}(\mathbf{v}^{n+1-\alpha_B}) \;=\; & -\overline{\mathbf{M}}\left(\frac{1-\alpha_B}{\delta\Delta t}\mathbf{v}^{n+1}\right) - \mathbf{f}_{int}^{n+1} + \mathbf{f}_{ext}^{n+1} \\
& -\overline{\mathbf{M}}\left[\frac{1-\alpha_B}{\delta\Delta t}\mathbf{v}^n + \left(\alpha_B - \frac{(1-\alpha_B)(1-\delta)}{\delta}\right)\dot{\mathbf{v}}^n\right];
\end{aligned}
\tag{2.62}
$$

Also in this case the unconditional stability and 2nd order accuracy are achieved with the following values of the parameters

$$
\alpha_B \in \left[-\frac{1}{3}, 0\right], \qquad \delta = \frac{1-2\alpha_B}{2}, \qquad \beta = \frac{(1-\alpha_B)^2}{4}; \tag{2.63}
$$

The $\alpha-method$ was proven to be more accurate than Bossak scheme when the numerical dissipation is maximal [61, 126]. However the latter presents some implementation advantages for non-linear problems as explained in [6]. These are the reasons for the choice of the Bossak scheme in this work.

Predictor multi corrector residual based strategy

The solution of the non linear problem is achieved using a residual based approach. A quasi Newton method allows the linearization of the non linear terms. Using a Taylor expansion of equation 2.62 at iteration k, the residual at iteration $k+1$ is obtained and is imposed to be zero, i.e.

$$
\mathbf{r}(\mathbf{v}^{n+1,k+1}) = \mathbf{r}(\mathbf{v}^{n+1,k}) + \frac{\partial \mathbf{r}(\mathbf{v}^{n+1,k})}{\partial \mathbf{v}^{n+1}}\Delta\mathbf{v}^k + \mathcal{O}(\Delta\mathbf{v}^k)^2 = 0; \tag{2.64}
$$

where $\Delta\mathbf{v}^k = \mathbf{v}^{n+1,k+1} - \mathbf{v}^{n+1,k}$ and

$$
\frac{\partial \mathbf{r}(\mathbf{v}^{n+1,k})}{\partial \mathbf{v}^{n+1}} = -\frac{\overline{M}}{\delta\Delta t} - \frac{\partial \mathbf{f}_{int}^{n+1,k}}{\partial \mathbf{v}^{n+1}}; \tag{2.65}
$$

The final solution system is

$$
\underbrace{-\frac{\partial \mathbf{r}(\mathbf{v}^{n+1,k})}{\partial \mathbf{v}^{n+1}}\Delta\mathbf{v}^k}_{LHS} = \underbrace{\mathbf{r}(\mathbf{v}^{n+1,k})}_{RHS}; \tag{2.66}
$$

where *LHS* stands for *left hand side* and it is the matrix of the derivative of the residual at the current iteration with respect to the unknowns. Whereas *RHS* stands for *right hand side*, it is the vector of the residual of momentum and continuity equations at the previous iteration.

The basic steps of the Newton-Raphson solution procedure are:

1. **Prediction** $\mathbf{v^{n+1,k+1} = v^{n+1,k}}$;

2. **Solve** the system in its residual based form (equation 2.66);

3. **Update** $\mathbf{v^{n+1,k+1} = v^{n+1,k}} + \Delta\mathbf{v}^k$;

4. Check **convergence**;

5. Go back to step 2 till convergence is achieved.

2.5   Edge-based approach: fractional step solver

Concerning the element-based approach presented in the previous sections, two set of variables are necessary in the evaluation of the right hand side (RHS): the nodal variables like velocities and pressure and the elemental contributions like elemental volumes, shape functions and shape function derivatives.

The main steps of the evaluation of the residual in an element-based formulation are:

1. Gather nodal information into the element;

2. Operate on element-data to evaluate the elemental residual;

3. Scatter the elemental information to point-data in order to obtain the global RHS;

The cost of addressing operations in steps 1 and 3 can be drastically reduced using an edge-based approach. With this different data structure some redundant operations are avoided. Löhner and co-workers demonstrated that the FLOPs (floating point operations) overhead ratio between element-based and edge-based formulation is approximately 2.5 [115]. All the matrix operators (mass, Laplacian, strong and weak gradient and divergence) can be calculated only once at the beginning of the run in the

case of a fixed mesh approach, like the one considered in the present work, because the connectivities between nodes do not change along the calculation [115] .

The idea is to express all the integral operators of the classical Galerkin discretization in terms of the neighboring contributions accessing each node only once and taking advance of the *Compressed Sparse Row* (*CSR*) matrix storing format[9].

Since symmetry is not exploited in the present implementation, the parallelization of an edge-base code is straight forward. Two nested loops are performed, the main loop (which is the one to parallelize) is made over the mesh node i, and the inner one is made over node j surrounding node i (the edges connected to node i). The contributions of the edge ij are computed only when the node i is accessed (edge ji for simplicity is considered different from edge ij). On the contrary in an element-based approach edge ij is accessed more than once being part of at least two different elements (see Figure 2.6). This implies that the contribution ij of every matrix comes from more than one element, thereby introducing some difficulties in parallelizing the elemental loop.
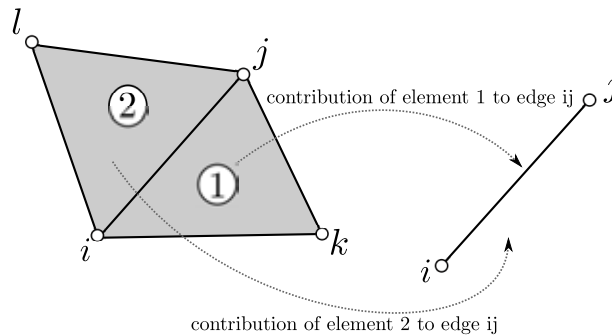
Figure 2.6: Build up contribution in an edge-based data structure for the elemental contribution.

---

[9]In *CSR* format, suitable for sparse matrices, only the non zero entries of the matrix are stored. Considering for example matrix $\mathbf{A}$ below. It can be stored in a *CSR* format through vectors $\mathbf{a}_{ij}$, $\mathbf{j}$ and $\mathbf{i}$ that are the vector of the non zero entries of $\mathbf{A}$, the vector of the column indexes of every non zero entry of $\mathbf{A}$ and the position of the first non zero entry of each row of $\mathbf{A}$ in $\mathbf{a}_{ij}$ respectively, i.e.

$$\mathbf{A} = \begin{bmatrix} 5 & 7 & 0 & 1 \\ 0 & 0 & 0 & 3 \\ 0 & 1 & 0 & 4 \\ 0 & 0 & 9 & 0 \end{bmatrix} \quad \begin{aligned} \mathbf{a}_{ij}^T &= \{5 \quad 7 \quad 1| \quad 3| \quad 1 \quad 4| \quad 9\} \\ \mathbf{j}^T &= \{0 \quad 1 \quad 3| \quad 3| \quad 1 \quad 3| \quad 2\} \\ \mathbf{i}^T &= \{0| \quad 3| \quad 4| \quad 6| \quad 6\} \end{aligned}$$

2.5.1   Stabilized formulation

As already mentioned in Section 2.4.1 in the edge-based approach, as well as in the element-based one, SGS methods are employed to stabilize equations 2.39. In the present work the *Orthogonal sub-grid scale* OSS method introduced by Codina [34, 38] is used. In this case the space for the sub-grid scale is taken orthogonal to the finite element one. Following strictly the operations outlined in [39, 41, 115], the problem already presented in equation 2.39, with the insertion of the convection and incompressibility stabilization terms, is: find $(\mathbf{u}_h, p_h, \boldsymbol{\pi}_h, \boldsymbol{\xi}_h)$ in $\mathcal{V}_h \times \mathcal{Q}_h \times \mathcal{V}_h \times \mathcal{V}_h$ such that

$$
\begin{aligned}
&\int_\Omega \mathbf{w}_h \partial_t \mathbf{u}_h d\Omega + \int_\Omega \mathbf{w}_h \overline{\mathbf{u}}_h \cdot \nabla \mathbf{u}_h d\Omega \\
&- \int_\Omega n p_h (\nabla \cdot \mathbf{w}_h) d\Omega + 2 \int_\Omega \nabla \mathbf{w}_h : \nu \nabla \mathbf{u}_h d\Omega \\
&\quad + \int_\Omega \mathbf{w}_h (\overline{E}_1 \mathbf{u}_h + \overline{E}_2 |\mathbf{u}_h| \mathbf{u}_h) d\Omega - \int_\Omega \mathbf{w}_h n \mathbf{b} d\Omega \qquad\qquad (2.67) \\
&\quad - \int_\Omega \tau (\overline{\mathbf{u}}_h \cdot \nabla \mathbf{w}_h) \mathcal{P}_h^\perp (\overline{\mathbf{u}}_h \cdot \nabla \mathbf{u}_h + \overline{E}_2 |\mathbf{u}_h| \mathbf{u}_h) d\Omega \;=\; \mathbf{0} \quad \forall \mathbf{w}_h \in \mathcal{V}_h; \\
&\qquad \int_\Omega q_h \nabla \cdot \mathbf{u}_h d\Omega + \int_\Omega \tau \nabla q_h \mathcal{P}_h^\perp (n \nabla p_h) d\Omega \;=\; 0 \quad \forall q_h \in \mathcal{Q}_h;
\end{aligned}
$$

where $\mathcal{P}_h^\perp$ is the space of *orthogonal projections* $\mathcal{P}_h^\perp = \mathcal{I} - \mathcal{P}_h$ and $\mathcal{P}_h$ is the $L_2 -$ *projection* onto $\mathcal{V}_h$. That is

$$\mathcal{P}_h^\perp (\overline{\mathbf{u}}_h \cdot \nabla \mathbf{u}_h + \overline{E}_2 |\mathbf{u}_h| \mathbf{u}_h) = \overline{\mathbf{u}}_h \cdot \nabla \mathbf{u}_h + \overline{E}_2 |\mathbf{u}_h| \mathbf{u}_h - \boldsymbol{\pi}_h; \qquad (2.68a)$$

$$\mathcal{P}_h^\perp (\nabla p_h) = n \nabla p_h - \boldsymbol{\xi}_h; \qquad (2.68b)$$

with $\boldsymbol{\pi}_h$ and $\boldsymbol{\xi}_h$ defined as

$$\int_\Omega \mathbf{w}_h \boldsymbol{\pi}_h d\Omega = \int_\Omega \mathbf{w}_h (\overline{\mathbf{u}}_h \cdot \nabla \mathbf{u}_h + \overline{E}_2 |\mathbf{u}_h| \mathbf{u}_h) d\Omega; \qquad \forall \mathbf{w}_h \in \mathcal{V}_h \qquad (2.69a)$$

$$\int_\Omega \mathbf{w}_h \boldsymbol{\xi}_h d\Omega = \int_\Omega \mathbf{w}_h n \nabla p_h d\Omega; \qquad \forall \mathbf{w}_h \in \mathcal{V}_h \qquad (2.69b)$$

The additional unknowns $\boldsymbol{\xi}$ and $\boldsymbol{\pi}$ can be easily expressed in function of velocity and pressure through this equations.

Remark 8. A *split-OSS* is implemented. The correct form of applying OSS to the momentum equation would be to consider a stabilization term like equation 2.45 where

the $\mathcal{P}^m(\mathbf{w}_h)$ and τ correspond to those presented in Table 2.1 for ASGS. The difference is represented by the choice of the $\mathcal{R}^m(\mathbf{u}_h)$ term. Instead of taking the whole residuum of the momentum equation, only its orthogonal projection (the projection onto $\mathcal{P}_h{}^\perp$) is taken into account. Two considerations should be made:

- The inertia term, the body force term and the linear part of the Darcy term belong to the finite element space $\mathcal{V}_h$ (i.e. their projection onto $\mathcal{P}_h{}^\perp$ is zero);

- The viscous term disappears using linear elements (i.e. the Laplacian of a linear function is zero);

Therefore $\mathcal{R}^m(\mathbf{u}_h)$ takes the form

$$\mathcal{R}^m(\mathbf{u}_h) = \mathcal{P}_h{}^\perp(\overline{\mathbf{u}}_h \cdot \nabla \mathbf{u}_h + \overline{E}_2|\mathbf{u}_h|\mathbf{u}_h + \nabla p_h); \qquad (2.70)$$

and the stabilization term should be

$$\int_\Omega \tau(\overline{\mathbf{u}}_h \cdot \nabla \mathbf{w}_h + \nabla q_h)\mathcal{R}^m(\mathbf{u}_h)d\Omega; \qquad (2.71)$$

which is different from

$$\int_\Omega \tau(\overline{\mathbf{u}}_h \cdot \nabla \mathbf{w}_h)\mathcal{P}_h{}^\perp(\overline{\mathbf{u}}_h \cdot \nabla \mathbf{u}_h + \overline{E}_2|\mathbf{u}_h|\mathbf{u}_h)d\Omega + \int_\Omega \tau\nabla q_h \mathcal{P}_h{}^\perp(\nabla p_h)d\Omega; \qquad (2.72)$$

In practice this second form has been seen to be very effective [115] and it is the one implemented in this work.

An error analysis leads to the definition of τ_i in function of the parameters of the differential equation (like advective velocity $\mathbf{u}$ or kinematic viscosity ν) [51]. Following the analysis of Codina [35, 37], and considering the additional presence of the Darcy term, τ is defined as

$$\tau_i = \left(\frac{\alpha}{\Delta t} + \frac{4\nu_i}{h_i^2} + \frac{2|\overline{\mathbf{u}}_i|}{h_i} + (\overline{E}_1 + \overline{E}_2|\mathbf{u_i}|)\right)^{-1} \qquad (2.73)$$

where h_i is the mesh size taken equal to the minimum edge length (l_{ij}) of the edges ij surrounding node i. α is a parameter that controls the importance of the dynamic term in the stabilization ($\alpha \in [0, 1]$). In the case of pressure stabilization the optimal α value is 1, whereas for the convective term, α it is taken equal to 0.01 therefore decreasing the importance to a 1%. Finally $\overline{E}_1$ and $\overline{E}_2$ are the Ergun's coefficients defined in 2.31 and 2.32 respectively.

2.5.2   Discretization procedure

System 2.67 can be rewritten in a semi discrete form as

$$\tilde{\mathbf{M}}\partial_t\mathbf{u} + \tilde{\mathbf{K}}^C\left(\mathbf{u}\right)\mathbf{u} - \tilde{\mathbf{G}}\mathbf{p} + \tilde{\mathbf{K}}^\mu\mathbf{u} + \tilde{\mathbf{K}}^D\left(\mathbf{u}\right)\mathbf{u} + \mathbf{S}^u\mathbf{u} - \mathbf{S}^\pi\boldsymbol{\pi} - \tilde{\mathbf{F}} = \mathbf{0}; \qquad (2.74\text{a})$$

$$\tilde{\mathbf{D}}\mathbf{u} + \mathbf{S}^p\mathbf{p} - \mathbf{S}^\xi\boldsymbol{\xi} = \mathbf{0}; \qquad (2.74\text{b})$$

$$\tilde{\mathbf{M}}\boldsymbol{\pi} - \tilde{\mathbf{K}}^C(\mathbf{u})\mathbf{u} = \mathbf{0}; \qquad (2.74\text{c})$$

$$\tilde{\mathbf{M}}\boldsymbol{\xi} - \tilde{\boldsymbol{\nabla}}\mathbf{p} = \mathbf{0}; \qquad (2.74\text{d})$$

where $\mathbf{u}$ is the vector of nodal velocities and $\mathbf{p}$ the vector of nodal pressures. The operators take the form presented in Table 2.4 and the stabilization operators $\mathbf{S}^i$ are defined as shown in Table 2.5.

In order to simplify the problem, equations 2.74c and 2.74d can be substituted in equations 2.74a and 2.74b respectively, giving

$$\tilde{\mathbf{M}}\partial_t\mathbf{u} + \tilde{\mathbf{K}}^C\left(\mathbf{u}\right)\mathbf{u} - \tilde{\mathbf{G}}\mathbf{p} + \tilde{\mathbf{K}}^\mu\mathbf{u}$$
$$+\tilde{\mathbf{K}}^D\left(\mathbf{u}\right)\mathbf{u} + \mathbf{S}^u\mathbf{u} - \mathbf{S}^\pi\tilde{\mathbf{M}}^{-1}\tilde{\mathbf{K}}^C(\mathbf{u})\mathbf{u} - \tilde{\mathbf{F}} = \mathbf{0}; \qquad (2.75\text{a})$$

$$\tilde{\mathbf{D}}\mathbf{u} + \mathbf{S}^p\mathbf{p} - \mathbf{S}^\xi\tilde{\mathbf{M}}^{-1}\tilde{\boldsymbol{\nabla}}\mathbf{p} = 0; \qquad (2.75\text{b})$$

The residual of the momentum equations without the dynamic term is defined as

$$\tilde{\mathbf{r}}\left(\mathbf{u},\mathbf{p}\right) \quad := \quad \tilde{\mathbf{K}}^C\left(\mathbf{u}\right)\mathbf{u} - \tilde{\mathbf{G}}\mathbf{p} + \tilde{\mathbf{K}}^\mu\mathbf{u}$$
$$+\tilde{\mathbf{K}}^D\left(\mathbf{u}\right)\mathbf{u} + \mathbf{S}^u\mathbf{u} - \mathbf{S}^\pi\tilde{\mathbf{M}}^{-1}\tilde{\mathbf{K}}^C(\mathbf{u})\mathbf{u} - \tilde{\mathbf{F}}; \qquad (2.76)$$

Remark 9. The *tilde* super-index over the matrix operators emphasizes the difference between the same operators in the element-based formulation presented in Table 2.2.

Matricial term		Continuum term
$\tilde{\mathbf{M}}_{ij}$		$\displaystyle\sum_j \int_\Omega N_i N_j d\Omega;$
	$\tilde{\mathbf{K}}^C_{ij}(\mathbf{u})$	$\displaystyle\int_\Omega N_i\left(\overline{\mathbf{u}}_g \cdot \nabla N_j\right) d\Omega;$
$\tilde{\mathbf{K}}_{ij}$	$\tilde{\mathbf{K}}^\mu_{ij}$	$\displaystyle\int_\Omega \nu_i \nabla N_i \cdot \nabla N_j d\Omega;$
	$\tilde{\mathbf{K}}^D_{ij}(\mathbf{u})$	$\displaystyle\sum_j \int_\Omega N_i \mathbf{u}_g N_j d\Omega$
$\tilde{\mathbf{G}}_{ij}$		$\displaystyle\int_\Omega n_i \nabla N_i N_j d\Omega;$
$\tilde{\boldsymbol{\nabla}}_{ij}$		$\displaystyle\int_\Omega n_i N_i \nabla N_j d\Omega;$
$\tilde{\mathbf{D}}_{ij}$		$\displaystyle\int_\Omega N_i \nabla N_j^T d\Omega;$
$\tilde{\mathbf{F}}_i$		$\displaystyle\int_\Omega n_i N_i d\Omega$

Table 2.4: Matrices and vectors of the semi discrete form of equations 2.75.

Matricial term	Continuum term
$\mathbf{S}^u_{ij}$	$\displaystyle\int_\Omega \tau_i(\overline{\mathbf{u}}_g \cdot \nabla N_i)(\overline{\mathbf{u}}_g \cdot \nabla N_j + E_2|\mathbf{u_g}|N_j)d\Omega$
$\mathbf{S}^\pi_{ij}$	$\displaystyle\int_\Omega \tau_i N_i(\overline{\mathbf{u}}_g \cdot \nabla N_j + E_2|\mathbf{u_g}|N_j)d\Omega$
$\mathbf{S}^p_{ij}$	$\displaystyle\int_\Omega \tau_i \nabla N_i \cdot \nabla N_j d\Omega$
$\mathbf{S}^\xi_{ij}$	$\displaystyle\int_\Omega \tau_i N_i \nabla N_j d\Omega$

Table 2.5: Stabilization matrices and vectors of system 2.75.

2.5.3 Fractional step solver using an explicit 4th order Runge Kutta time scheme

The modified form of the Navier-Stokes equations are solved using a fractional step algorithm. Pressure-splitting approaches of the fractional-step type are very convenient due to their high computational efficiency for flows at high Re, and have enjoyed widespread popularity since the original works of Chorin [33] and Temam [119]. The fundamental idea is to solve the momentum equation keeping fixed the pressure and later correcting the pressure so as to guarantee the satisfaction of the divergence constraint. A modern algebraic presentation of the method can be found in [36]. The fractional step approach is traditionally presented in an implicit context, typically using a first or second order Backward Differentiation Formula (BDF1 or BDF2 algorithm respectively) for the time integration of the momentum equation. In dealing with free-surface problems unfortunately, the shape of the fluid domain, and consequently the boundary conditions on the free surface, are subjected to frequent and radical changes. This implies that, to allow a satisfactory representation of the solution, an accurate tracking should be performed. In practice, it is typically observed that, even fully implicit schemes are practically limited to time steps for which the free surface approximately moves of one element length per time step. Such heuristic constraint is equivalent in essence, to a restriction on the practical CFL (Courant Friedrichs Lewy)[10] number to values in the order of unity. This observation effectively implies that explicit schemes will be competitive provided that $CFL \approx 1$ can be used and meshes of sufficiently good quality can be generated. This motivates the use of an explicit form of the fractional step scheme (see for example [109]) based on the use of a $4th$ order Runge Kutta (RK4) in dealing with the momentum equation.

Before proceeding in the description of the method, it should be observed that the algebraic splitting proposed by Codina in [36] leads naturally to the definition of a *discrete Laplacian* $\mathbf{DM^{-1}G}$ which in principle does not introduce any additional error in the imposition of the divergence freeness condition with respect to the original monolithic scheme. However, in practice the use of the *discrete Laplacian* implies a large

---

[10]The CFL, for hyperbolic system of partial differential equations (PDEs), is defined by

$$CFL = \frac{\lambda_{max} \cdot dt}{h};$$

(2.77)

where λ_{max} is the maximum eigenvalue of the system, dt the time step and h the size of the element [81, 109].

computational burden as the matrix is rather densely populated. In order to overcome such problem the *discrete Laplacian* is typically substituted by a *continuum Laplacian* which has a much smaller stencil than the discrete one (around six times smaller in $3D$). This fact has important consequences both on the efficiency and on the stability of the numerical scheme (see e.g. [36]) but in particular it has an important impact on the mass conservation properties of the method [66]. One practical issue is that while the use of a *discrete Laplacian* matrix guarantees an invertible matrix, this is not the case when the continuum form is chosen implying that pressure needs to be fixed on the Neumann boundary, that is, pressure is to be imposed *strongly*, at least for the solution of the pressure step. This implies that when FS is to be used the pressure is known beforehand on the Neumann boundary.

Given such situation, it is convenient, to avoid integrating by parts the pressure gradient term, using the equivalent formula

$$\int_\Omega \mathbf{w} \cdot \nabla p d\Omega = - \int_\Omega p \nabla \cdot \mathbf{w} d\Omega + \int_{\partial\Omega} \mathbf{w} \cdot p\mathbf{n} d\Gamma \tag{2.78}$$

This implies that the pressure space should be in $[\mathcal{H}^1(\Omega)]^d$ which is an additional requirement to the smoothness of the function. Such modified form has the important advantage that no boundary integrals need to be computed (second integral of the right and side of equation 2.78) for the pressure which leads to an easier application of the pressure boundary condition on the free surface as it will be explained in Section 2.6.4.

This consideration leads to the following expression for the residual at node i (note the use of $\tilde{\boldsymbol{\nabla}}$ instead of $\tilde{\mathbf{G}}$).

$$\begin{aligned} \tilde{\mathbf{r}}\left(\mathbf{u},\mathbf{p}\right) \;\; := \;\; & \tilde{\mathbf{K}}^C\left(\mathbf{u}\right)\mathbf{u} + \tilde{\boldsymbol{\nabla}}\mathbf{p} + \tilde{\mathbf{K}}^\mu\mathbf{u} \\ & + \tilde{\mathbf{K}}^D\left(\mathbf{u}\right)\mathbf{u} + \mathbf{S}^u\mathbf{u} - \mathbf{S}^\pi\tilde{\mathbf{M}}^{-1}\tilde{\mathbf{K}}^C(\mathbf{u})\mathbf{u} - \tilde{\mathbf{F}}; \end{aligned} \tag{2.79}$$

Remark 10. Using Eq. 2.78 implies a pointwise application of the normal force on the Neumann boundary instead of its weak imposition. This is an acceptable approximation for low viscosity flows for which the term $\int_\Omega \mathbf{n} \cdot \mu\Delta\mathbf{u} d\Omega$ is negligible.

On the basis of such definition the time integration can now be performed.

Runge Kutta time integration scheme

The lower computational cost of an explicit time integration technique (that does not require solving of a system of equations), is not the only advantage of this approach. Its implementation is highly parallelizable, which is the main reason why it has been chosen in this work. Moreover considering the m-Runge Kutta schemes, it is known that the order of the time integration can be arbitrarily chosen, although they give $m - th$ order of accuracy up to $m = 4$ [51]. Whenever for $m > 4$ the order is lower than m. That is the reason of the popularity of the 4-steps scheme (RK4).

It is demonstrated that the RK4 is the optimal compromise between the number of intermediate steps and the permissible time step size in spite of its conditional stability. For more details the consultation of [51] is recommended.

RK4 makes use of the solution at t^n to evaluate the solution at time t^{n+1} by calculating the residual of the equations at a certain number of intermediate steps.

This means that for a general Cauchy problem

$$\frac{\partial y}{\partial t} = f(y(t), t); \tag{2.80}$$

a one step explicit approach leads to a time scheme with the following general format

$$\frac{y^{n+1} - y^n}{\Delta t} = f(y^n, t^n); \tag{2.81}$$

whereas for the 4th order Runge Kutta method

$$\frac{y^{n+1} - y^n}{\Delta t} = \frac{1}{6}(r_1 + 2\,r_2 + 2\,r_3 + r_4); \tag{2.82}$$

where r_i with $i = 1, 2, 3, 4$ are the residuals of the stationary form of 2.80 evaluated at

$$
\begin{aligned}
r_1 &= f\left(t^n, y^n\right); \\
r_2 &= f\left(t^n + \frac{\Delta t}{2}, y^n + \frac{\Delta t}{2} \cdot r_1\right); \\
r_3 &= f\left(t^n + \frac{\Delta t}{2}, y^n + +\frac{\Delta t}{2} \cdot r_2\right); \\
r_4 &= f\left(t^n + \Delta t, y^n + \Delta t \cdot r_3\right).
\end{aligned}
\tag{2.83}
$$

In order to fully explain every stage of the integration scheme applied to the momentum equation let us use the definition of the stabilized residual obtained in equation 2.79. The semi-discrete form of the momentum equations in terms of the residuals at the intermediate stages is then

$$
\begin{aligned}
\tilde{\mathbf{M}}\frac{\mathbf{u}^{n+1} - \mathbf{u}^n}{\Delta t} &= \frac{1}{6}\left[\tilde{\mathbf{r}}_1 + 2\,\tilde{\mathbf{r}}_2 + 2\,\tilde{\mathbf{r}}_3 + \tilde{\mathbf{r}}_4\right]; \\
&= \frac{1}{6}\left[\tilde{\mathbf{r}}(\mathbf{u}^n,\mathbf{p}^n) + 2\,\tilde{\mathbf{r}}(\mathbf{u}^{\theta1},\mathbf{p}^{\theta1}) + 2\,\tilde{\mathbf{r}}(\mathbf{u}^{\theta2},\mathbf{p}^{\theta2}) + \tilde{\mathbf{r}}(\mathbf{u}^{\theta3},\mathbf{p}^{\theta3})\right];
\end{aligned}
\tag{2.84}
$$

where $\tilde{\mathbf{r}}(\mathbf{u}^{\theta_i},\mathbf{p}^{\theta_i})$ are the residuals of the momentum equations defined by equation 2.79 evaluated at θ_i intermediate stages.

To correctly evaluate the residual at each intermediate time step, the solution of the continuity equation would have been required. This would have considerably reduced the efficiency requiring a huge computational effort. In order to overcome this issue, according to [111], a linear variation of pressure is assumed in the time step. It should be remarked that this assumption leads the velocity field to be divergence free only at the end of the step.

Redefining equation 2.79 as

$$
\tilde{\mathbf{r}}(\mathbf{u},\mathbf{p}) = \tilde{\mathbf{r}}^u(\mathbf{u}) + \tilde{\mathbf{r}}^{\mathbf{p}}(\mathbf{p});
\tag{2.85}
$$

being $\tilde{\mathbf{r}}^u(\mathbf{u})$ the part of the residual related to velocity and $\tilde{\mathbf{r}}^{\mathbf{p}}(\mathbf{p})$ the part related to the pressure gradients. The residuals become

$$
\begin{aligned}
\tilde{\mathbf{r}}_1 &:= \tilde{\mathbf{r}}(\mathbf{u}^n,\mathbf{p}^n) &&= \tilde{\mathbf{r}}^u(\mathbf{u}^n) + \tilde{\boldsymbol{\nabla}}\mathbf{p}^n; \\
\tilde{\mathbf{r}}_2 &:= \tilde{\mathbf{r}}(\mathbf{u}^{\theta1},\mathbf{p}^{\theta1}) &&= \tilde{\mathbf{r}}^u(\mathbf{u}^{\theta1}) + \frac{1}{2}\left(\tilde{\boldsymbol{\nabla}}\mathbf{p}^n + \tilde{\boldsymbol{\nabla}}\mathbf{p}^{n+1}\right); \\
\tilde{\mathbf{r}}_3 &:= \tilde{\mathbf{r}}(\mathbf{u}^{\theta2},\mathbf{p}^{\theta2}) &&= \tilde{\mathbf{r}}^u(\mathbf{u}^{\theta2}) + \frac{1}{2}\left(\tilde{\boldsymbol{\nabla}}\mathbf{p}^n + \tilde{\boldsymbol{\nabla}}\mathbf{p}^{n+1}\right); \\
\tilde{\mathbf{r}}_4 &:= \tilde{\mathbf{r}}(\mathbf{u}^{\theta3},\mathbf{p}^{\theta3}) &&= \tilde{\mathbf{r}}^u(\mathbf{u}^{\theta3}) + \tilde{\boldsymbol{\nabla}}\mathbf{p}^{n+1};
\end{aligned}
\tag{2.86}
$$

And the global momentum equation 2.84 can be symbolically rewritten as

$$\tilde{\mathbf{M}}\frac{\mathbf{u}^{n+1} - \mathbf{u}^n}{\Delta t} = \frac{1}{6}\left[\tilde{\mathbf{r}}^u(\mathbf{u}^n) + 2\,\tilde{\mathbf{r}}^u(\mathbf{u}^{\theta 1}) + 2\,\tilde{\mathbf{r}}^u(\mathbf{u}^{\theta 2}) + \tilde{\mathbf{r}}^u(\mathbf{u}^{\theta 3})\right]$$

$$+\frac{1}{2}\left[\tilde{\boldsymbol{\nabla}}\mathbf{p}^n + \tilde{\boldsymbol{\nabla}}\mathbf{p}^{n+1}\right] \tag{2.87}$$

Final system using a fractional step approach and a RK4

In order to decouple the solution for the velocity and pressure, the traditional pressure splitting procedure is performed and the fractional step velocity $\tilde{\mathbf{u}}$ is inserted. This gives

$$\tilde{\mathbf{M}}\frac{\tilde{\mathbf{u}} - \mathbf{u}^n}{\Delta t} = \frac{1}{6}\left[\tilde{\mathbf{r}}^u(\mathbf{u}^n) + 2\,\tilde{\mathbf{r}}^u(\tilde{\mathbf{u}}^{\theta 1}) + 2\,\tilde{\mathbf{r}}^u(\tilde{\mathbf{u}}^{\theta 2}) + \tilde{\mathbf{r}}^u(\tilde{\mathbf{u}}^{\theta 3})\right] + \frac{1}{2}\tilde{\boldsymbol{\nabla}}\mathbf{p}^n; \tag{2.88a}$$

$$\tilde{\mathbf{M}}\frac{\mathbf{u}^{n+1} - \tilde{\mathbf{u}}}{\Delta t} + \frac{1}{2}\tilde{\boldsymbol{\nabla}}(\mathbf{p}^{n+1} - \mathbf{p}^n) = \mathbf{0}; \tag{2.88b}$$

$$\tilde{\mathbf{D}}\mathbf{u}^{n+1} + \mathbf{S}^p\mathbf{p}^{n+1} - \mathbf{S}^\xi\tilde{\mathbf{M}}^{-1}\tilde{\mathbf{G}}\mathbf{p}^{n+1} = 0; \tag{2.88c}$$

where it has to be remarked that equation 2.88a only depends on the pressure at the previous time step and on the intermediate fractional step velocities, leading to a slightly different RK4 steps as explained later on.

From equation 2.88b

$$\mathbf{u}^{n+1} = \tilde{\mathbf{u}} - \frac{\Delta t}{2}\tilde{\mathbf{M}}^{-1}\tilde{\boldsymbol{\nabla}}(\mathbf{p}^{n+1} - \mathbf{p}^n); \tag{2.89}$$

that substituted in equation 2.88c gives

$$\tilde{\mathbf{D}}\tilde{\mathbf{u}} - \frac{\Delta t}{2}\tilde{\mathbf{D}}\tilde{\mathbf{M}}^{-1}\tilde{\boldsymbol{\nabla}}(\mathbf{p}^{n+1} - \mathbf{p}^n) + \mathbf{S}^p\mathbf{p}^{n+1} - \mathbf{S}^\xi\tilde{\mathbf{M}}^{-1}\tilde{\mathbf{G}}\mathbf{p}^{n+1} = 0. \tag{2.90}$$

Finally substituting the discrete Laplacian $(\tilde{\mathbf{D}}\tilde{\mathbf{M}}^{-1}\tilde{\boldsymbol{\nabla}})$ by the continuous one $(\mathbf{L})$, the final system to be solved is [109]:

$$\tilde{\mathbf{M}}\frac{\tilde{\mathbf{u}} - \mathbf{u}^n}{\Delta t} = \frac{1}{6}\left[\tilde{\mathbf{r}}^u(\tilde{\mathbf{u}}^n) + 2\,\tilde{\mathbf{r}}^u(\tilde{\mathbf{u}}^{\theta 1}) + 2\,\tilde{\mathbf{r}}^u(\tilde{\mathbf{u}}^{\theta 2}) + \tilde{\mathbf{r}}^u(\tilde{\mathbf{u}}^{\theta 3})\right] + \frac{1}{2}\tilde{\boldsymbol{\nabla}}\mathbf{p}^n; \tag{2.91a}$$

$$\frac{\Delta t}{2}\mathbf{L}\left(\mathbf{p}^{n+1} - \mathbf{p}^n\right) = \tilde{\mathbf{D}}\tilde{\mathbf{u}} + \mathbf{S}^p\mathbf{p}^{n+1} - \mathbf{S}^\xi\tilde{\mathbf{M}}^{-1}\tilde{\mathbf{G}}\mathbf{p}^{n+1}; \tag{2.91b}$$

$$\mathbf{u}^{n+1} = \tilde{\mathbf{u}} - \frac{\Delta t}{2}\tilde{\mathbf{M}}^{-1}\tilde{\boldsymbol{\nabla}}\left(\mathbf{p}^{n+1} - \mathbf{p}^n\right); \tag{2.91c}$$

where the residuals of equation 2.91a are evaluated according to the following steps

$$\tilde{\mathbf{r}}^u(\mathbf{u}^n); \tag{2.92a}$$

$$\tilde{\mathbf{u}}^{\theta 1} = \mathbf{u}^n + \tilde{\mathbf{M}}^{-1}\frac{\Delta t}{2}\left[\tilde{\mathbf{r}}^u(\mathbf{u}^n) + \tilde{\boldsymbol{\nabla}}\mathbf{p}^n\right]; \tag{2.92b}$$

$$\tilde{\mathbf{r}}^u(\tilde{\mathbf{u}}^{\theta 1}); \tag{2.92c}$$

$$\tilde{\mathbf{u}}^{\theta 2} = \mathbf{u}^n + \tilde{\mathbf{M}}^{-1}\frac{\Delta t}{2}\left[\tilde{\mathbf{r}}^u(\tilde{\mathbf{u}}^{\theta 1}) + \frac{1}{2}\tilde{\boldsymbol{\nabla}}\mathbf{p}^n\right]; \tag{2.92d}$$

$$\tilde{\mathbf{r}}^u(\tilde{\mathbf{u}}^{\theta 2}) \tag{2.92e}$$

$$\tilde{\mathbf{u}}^{\theta 3} = \mathbf{u}^n + \tilde{\mathbf{M}}^{-1}\Delta t\left[\tilde{\mathbf{r}}^u(\tilde{\mathbf{u}}^{\theta 2}) + \frac{1}{2}\tilde{\boldsymbol{\nabla}}\mathbf{p}^n\right]; \tag{2.92f}$$

$$\tilde{\mathbf{r}}^u(\tilde{\mathbf{u}}^{\theta 3}); \tag{2.92g}$$

2.5.4 The edge-based operators

Having made the choice of using an explicit scheme for the time integration of the momentum equation, a suitable data structure for the fast calculation of the residuals should be devised. The idea to be exploited is that many of the integrals involved in the computation of the residual can be written in terms of constant operators which can be directly applied to the nodal values. Different techniques were developed over the years to reach such goal. In writing this work the nodal-based approach described in [34] is blended with the edge-based proposed in [81, 115].

The starting point is the systematic usage of the partition-of-unity property of the FE shape functions, which provides the relations

$$\sum_i N_i = 1 \implies N_i = 1 - \sum_{j\neq i} N_j; \tag{2.93}$$

and, as a consequence,

$$\sum_i \nabla N_i = 0 \implies \nabla N_i = -\sum_{j\neq i} \nabla N_j. \tag{2.94}$$

The edge-based approach is obtained by applying systematically such relations for the computation of the discrete operators of interest.

In the following the different terms involved in the calculation of the residual are considered one by one, by expressing the contributions to the entry corresponding to a given

node i. The j index indicates one of the neighbor nodes of i which share an edge with it.

Gradient term. The gradient term (not integrated by parts) which appears in the momentum equation, reads

$$
\begin{aligned}
\sum_j \int_\Omega N_i \nabla N_j p_j d\Omega &= \sum_{j \neq i} \int_\Omega N_i \nabla N_j p_j d\Omega + \int_\Omega N_i \nabla N_i p_i d\Omega \\
&= \sum_{j \neq i} \int_\Omega N_i \nabla N_j p_j d\Omega - \int_\Omega N_i \left(\sum_{j \neq i} \nabla N_j \right) p_i d\Omega \\
&= \sum_{j \neq i} \int_\Omega N_i \nabla N_j \left(p_j - p_i \right) d\Omega \\
&= \sum_{j \neq i} \tilde{\boldsymbol{\nabla}}_{ij} \left(p_j - p_i \right).
\end{aligned}
\tag{2.95}
$$

Applying equation 2.94 it can be demonstrated that the pressure gradient term can be computed by using the $\tilde{\boldsymbol{\nabla}}_{ij}$ for any edge ij. Note that the term ii is never needed with the approach proposed.

Divergence term. The derivation of the divergence term is basically identical to the previous one, with the only difference that a scalar product is involved. Following exactly the same steps as before it can be readily shown that

$$
\sum_j \tilde{\mathbf{D}}_{ij} \cdot \mathbf{u}_j = \sum_{j \neq i} \tilde{\mathbf{D}}_{ij} \cdot \left(\mathbf{u}_j - \mathbf{u}_i \right) d\Omega.
\tag{2.96}
$$

Convection term. The non-linear convection term has to be approximated to fit within the framework of the present edge based formulation. Several possibilities exist to obtain a suitable form to be used in the calculations. One could start by considering

the conservative form of the convection operator $\nabla \cdot (\mathbf{u} \otimes \mathbf{u})$.

$$\sum_j \int_\Omega N_i \nabla N_j \cdot (\mathbf{u}_j \otimes \mathbf{u}_j) \, d\Omega =$$

$$= \sum_{j \neq i} \int_\Omega N_i \nabla N_j \cdot \mathbf{u}_j \mathbf{u}_j d\Omega - \int_\Omega N_i \left(\sum_{j \neq i} \nabla N_j \right) \cdot \mathbf{u}_i \mathbf{u}_i d\Omega; \tag{2.97}$$

which tells us that the convective term can be estimated as

$$\sum_{j \neq i} \left(\tilde{\boldsymbol{\nabla}}_{ij} \cdot \mathbf{u}_j \right) \mathbf{u}_j - \sum_{j \neq i} \left(\tilde{\boldsymbol{\nabla}}_{ij} \cdot \mathbf{u}_i \right) \mathbf{u}_i. \tag{2.98}$$

Alternatively, one can start with the non-conservative form of the same equation and use a nodal integration rule as proposed in [34]. This approach estimates the convective term contribution as

$$\sum_{j \neq i} \left(\tilde{\boldsymbol{\nabla}}_{ij} \cdot \mathbf{u}_i \right) (\mathbf{u}_j - \mathbf{u}_i) . \tag{2.99}$$

The first approach is "globally conservative" by construction in the sense that the sum over all of the nodes in the mesh is guaranteed to give zero. This property is only approximately verified by the second technique, since the integration rule is not exact. In practice, both approaches work effectively. Nevertheless the second approximation appears to be slightly more robust and was the one chosen in that work.

"Weak" gradient term. The migration from a classical finite element to an edge-based implementation requires describing the gradient of a scalar function integrated by parts. Since in the current formulation the pressure gradient term is not integrated by parts, this is not strictly needed for the implementation of the present method. In any case, following [86]

$$\begin{aligned} \sum_j \int_\Omega n_i \nabla N_i N_j p_j &= \sum_{j \neq i} \int_\Omega n_i \nabla N_i N_j p_j d\Omega + \int_\Omega n_i \nabla N_i N_i p_i d\Omega \\ &= \sum_{j \neq i} \int_\Omega n_i \nabla N_i N_j p_j d\Omega - \int_\Omega \left(\sum_{j \neq i} n_i \nabla N_j \right) N_i p_i d\Omega \\ &= \tilde{\mathbf{G}}_{ij} p_j - \tilde{\boldsymbol{\nabla}}_{ij} p_i. \end{aligned} \tag{2.100}$$

Viscous term. The viscous term in the Navier-Stokes equations requires estimating the scalar Laplacian operator L_{ij}. Although the possibility exists of storing directly on each edge an entry of the type $L_{ij} := \int_\Omega \nabla N_i \cdot \nabla N_j d\Omega$, in the present work it is preferred to store *a matrix term* of the type

$$\mathbf{L}_{ij}^d = \int_\Omega \nabla N_i \otimes \nabla N_j d\Omega; \tag{2.101}$$

on each edge of the mesh. The scalar gradient can then be obtained as needed by the trace operator as

$$L_{ij} = Tr\left(\mathbf{L}_{ij}^d\right); \tag{2.102}$$

which allows writing the viscous term as

$$\sum_{i \neq j} Tr\left(\mathbf{L}_{ij}^d\right) \mu \left(\mathbf{u}_j - \mathbf{u}_i\right) \tag{2.103}$$

"Special terms". The terms described until now include all of the terms that are needed for the implementation of the Navier-Stokes equations. Nevertheless, it is appropriate to remark that storing the matrix Laplacian $\mathbf{L}_{ij}^d$ instead of its scalar counterpart, is justified for the implementation of the stabilization operators. A detailed description of the use of $\mathbf{L}_{ij}^d$ in this context can be found in [83]. The need for storing such operator can be also understood by considering a SUPG-like stabilization operator. On a given node i, the stabilization operator has the form

$$\sum_{i \neq j} \nabla \cdot (\mathbf{u}_i \otimes \mathbf{u}_i) \nabla \left(\mathbf{u}_j - \mathbf{u}_i\right). \tag{2.104}$$

By using the matrix laplacian operator, this can be approximated as

$$\sum_{i \neq j} \left(\mathbf{u}_i \cdot \mathbf{L}_{ij}^d \cdot \mathbf{u}_i\right) \nabla \cdot \left(\mathbf{u}_j - \mathbf{u}_i\right); \tag{2.105}$$

which requires considering $\mathbf{L}_{ij}^d$ in the computation. Similarly, the matrix form is also useful in the computation of the sub-scale residuals and for the definition of a cross-wind dissipation term which is useful for controlling unwanted numerical oscillations.

Remark 11. The common features of all of the terms described is that they can be evaluated for each node i independently of all of the others. This implies that the

calculation of the residuals can be performed in parallel for each node of the mesh.

Remark 12. All the other magnitudes that have not been specifically treated here are taken as nodal, such as, for instance, the intrinsic time τ.

2.5.5   Improving mass conservation

Independently on the time accuracy of the numerical scheme used for the first step, the overall scheme can not be more than second order accurate due to the pressure splitting procedure. Furthermore, the use of the continuum Laplacian operator, mandatory in the context of a semi-explicit scheme, implies some volume loss particularly concentrated in the vicinity of the free surface (Neumann boundary). The origin of such loss can be traced back to two distinct phenomena:

1. As observed in [66], the pressure is fixed on the Neumann boundary as this is needed to make the Laplacian resolvable. This implies that it loses the capacity to adapt locally so to attempt guaranteeing the local mass conservation.

2. The divergence constraint ($\mathbf{Du} = 0$) is generally evaluated at time step $n + 1$ implying that it depends exclusively on the velocity at $n + 1$. Any error in the fulfillment of this constraint at the preceding step ($\mathbf{Du}^n = 0$) is simply discarded and never recovered.

The algorithm devised for the solution of the free surface problem attempts to minimize the first issue. The idea, as shown in Section 2.6.4, is that the pressure will be fixed on the nodes outside the free surface, thus letting some freedom to the nodes in its proximity.

On the other hand, the fulfillment of the divergence free condition at the present time step $(n+1)$ and at the previous one (n) are combined in order to overcome the drawback stated in point 2. The idea is the following: if no error was made in the past, it can be stated that $\mathbf{Du}^n = 0$. However this assumption is not verified in practice and volume is either created or destructed at a rate of $\mathbf{Du}^n$. While usually this information is simply discarded, in the present work the divergence free condition ($\mathbf{Du}^{n+1} = 0$) is modified in order to sum up the volume variation lost (or gained) at the previous time ($\mathbf{Du}^n$).

In mathematical terms the proposal is simply to modify the divergence constraint as

$$\mathbf{Du}^{n+1} + \mathbf{Du}^n = 0 \tag{2.106}$$

As shown in some of the examples, this simple modification improves the volume conservation of the overall scheme.

2.6   Free surface tracking. The Level Set method

The proposed technique is based on the use of a fixed-grid approach. Hence at each time step the fluid domain should be defined, implying:

1. The definition of a tracking method that allows:

   - moving the fluid free surface;

   - defining the position of the fluid boundary at each time step;

2. The application of the boundary conditions at the fluid boundary that do not necessarily coincide with mesh edges;

A level set technique is employed to face the first issue. The **level set method** was conceived as a methodology to following moving interfaces. The moving boundaries are composed of the zero-valued iso-surface of a given smooth function (at least Lipschitz continuous[11] [11]) $\varphi(\mathbf{x}, t)$.

Let us call $\Omega^0 \subset \mathbb{R}^d$ (where d is the space dimension) the global control domain of analysis. The fluid domain defined in the previous section at time t is $\Omega(t) \subset \Omega^0$. The boundary of $\Omega(t)$ is defined by part of $\partial\Omega^0$ and by a moving boundary defined as

$$\partial\Omega_m(t) := \{\mathbf{x} \mid \varphi(\mathbf{x}, t) = 0\} \tag{2.107}$$

From now on $\Omega(t) = \Omega$, and $\Omega_m(t) = \Omega_m$ and the explicit indication of time will be omitted for simplicity. Following the same criteria, the fluid domain at a given time step t^n is $\Omega(t^n) = \Omega^n$.

---

[11]In mathematics Lipschitz continuity is a stronger requirement than simple continuity conditioning the speed of change of the function. Let $\mathbf{f} : \mathbb{R}^m \to \mathbb{R}^m$. Given an open set $B \subseteq \mathbb{R}^m$, $\mathbf{f}$ is *Lipschitz-continuous on the open subset B* if there exists a constant $\Lambda \in \mathbb{R}_0^+$ such that

$$||\mathbf{f}(\mathbf{x}) - \mathbf{f}(\mathbf{y})|| \leq \Lambda ||\mathbf{x} - \mathbf{y}|| \qquad \forall \mathbf{x}, \mathbf{y} \in B.$$

The level set function is defined as

$$\begin{aligned}
\varphi(\mathbf{x}, t) &> 0 \quad \text{if} \quad x \notin \Omega; \\
\varphi(\mathbf{x}, t) &= 0 \quad \text{if} \quad x \equiv \partial \Omega_m; \\
\varphi(\mathbf{x}, t) &< 0 \quad \text{if} \quad x \in \Omega;
\end{aligned} \tag{2.108}$$
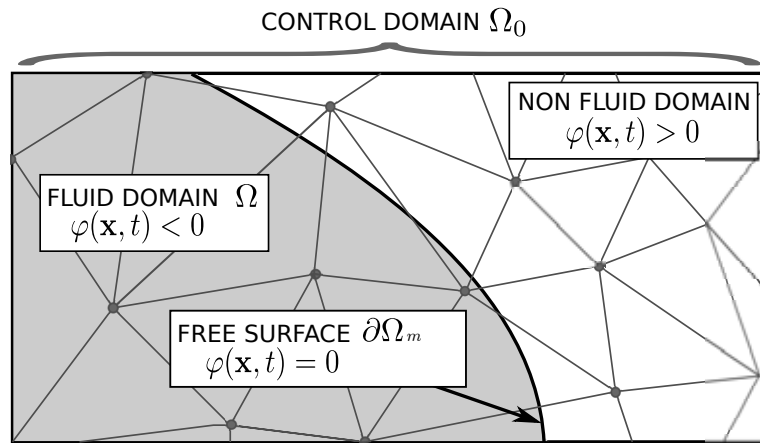
Figure 2.7: Graphic representation of the level set function φ.

see Figure 2.7 for a graphic representation of the level set function.

In the present work the level set function is taken to be a signed distance function. The Euclidian distance function is by definition

$$d(\mathbf{x}) = min|\mathbf{x} - \mathbf{x}_i| \qquad \forall \mathbf{x}_i \in \partial \Omega_m \tag{2.109}$$

The level set function, for a given time instant t, is defined as

$$\begin{aligned}
\varphi(\mathbf{x}) &= d(\mathbf{x}) & \text{if} \quad x \notin \Omega, t \in (0, T); \\
\varphi(\mathbf{x}) &= d(\mathbf{x}) = 0 & \text{if} \quad x \in \partial \Omega_m, t \in (0, T); \\
\varphi(\mathbf{x}) &= -d(\mathbf{x}) & \text{if} \quad x \in \Omega, t \in (0, T);
\end{aligned} \tag{2.110}$$

As exhaustively detailed in [103] this function inherits of all the properties of implicit surfaces (being signed distance functions a subset of the latter). Moreover, its monotonicity across the interface allows its differentiation.

The fundamental idea of using the level set approach can now be understood considering the mass conservation equation for a variable-density fluid:

$$\frac{d\rho}{dt} + \mathbf{u} \cdot \nabla\rho + \rho\nabla \cdot \mathbf{u} = 0 \tag{2.111}$$

The case of interest is that $\rho \neq 0$ inside the fluid domain and $\rho = 0$ outside the free surface, where a regularization function should be considered to be applied to ρ to make it differentiable in space.

Let us split equation 2.111 in the following two equations

$$\frac{d\rho}{dt} + \mathbf{u} \cdot \nabla\rho = 0 \tag{2.112}$$

and

$$\rho\nabla \cdot \mathbf{u} = 0 \rightarrow \nabla \cdot \mathbf{u} = 0 \tag{2.113}$$

It is easy to understand that if such two equations are verified equation 2.111 will also be verified. This requirement is in fact stricter the the original one. Now, equation 2.112 represents the transport of the density with the mean flow velocity. Since the density can be rather badly behaved as it approximates a jump, it is convenient to replace it by the transport of a smooth scalar φ (in the present work φ is the distance function) which can be used to recover the density distribution at any moment. The problem is thus transferred to the solution of the transport problem

$$
\begin{aligned}
\partial_t\varphi + \overline{\mathbf{u}} \cdot \nabla\varphi &= 0 && \text{in} \quad \Omega^0, \quad t \in (0, T), \\
\varphi &= \overline{\varphi} && \text{on} \quad \partial\Omega_{in}, \quad t \in (0, T), \\
\varphi(\mathbf{x}, 0) &= \varphi_0(\mathbf{x}) && \text{in} \quad \Omega^0,
\end{aligned}
\tag{2.114}
$$

where $\partial\Omega_{in} := \{\mathbf{x} \in \partial\Omega^0 \mid \mathbf{u}\cdot\mathbf{n} < 0\}$ is the inflow part of $\partial\Omega_m$. When the fluid enters the porous matrix an acceleration of the advancing front can be observed because of a restriction of the empty area. This is taken into account by considering the advective velocity equal to the actual fluid velocity defined in equation 2.2.

Two different solution approaches are used for the edge-based and the element-based algorithm for the solution of the convective system 2.114. In the edge-based technique a 4th order Runge Kutta scheme 2.114 is implemented and an OSS stabilization technique is used, similarly to what has already been explained in Section 2.5.1. Conversely a

Crank-Nicolson time integration scheme is employed in the element-based approach stabilized with the ASGS method.

2.6.1 Coupling the level set equation and the Navier-Stokes solver

In order to completely define the approach used in this work, the description of the coupling between the Navier-Stokes solver and the newly added level set equations is needed. Conceptually, the velocity obtained from the solution of the Navier-Stokes equation has to be used in convecting φ, while the zero level set function provides the position of the free-surface and is consequently needed to prescribe the pressure condition on the Neumann boundary. Many different approaches have been proposed over the years to perform such coupling; some based on sub-integration techniques on the cut elements [42] and others based on some form of regularization for the density function in the vicinity of the free surface. The proposal in this work rises from the observation that, once a continuous pressure distribution is assumed, only the gradient of the existing pressure appears in the momentum equation (as already observed before,the pressure term is not integrated by parts). This implies that the momentum equation can be solved approximately without knowing exactly the position of the free surface, provided that an estimate of the pressure gradient is given in any active (or potentially active) area of the fluid domain. On the other hand, the imposition of the zero traction condition on the Neumann boundary could be applied in the pressure correction step through the imposition of adapt boundary conditions at the level of the pressure Laplacian system. To complete the algorithm some other ingredients are needed:

- An *extrapolation function* to define the values of the velocity on a band containing the free surface of the fluid and to allow the imposition of the incompressibility condition on the free surface;

- A tool for calculating the *nodal distances* in the whole domain Ω_0;

- A method to impose the boundary conditions on the free surface.

2.6.2 The extrapolation procedure

In order to allow the convection of the free surface $\partial\Omega_m$ in regions of Ω_0 out of Ω^n , an extrapolation of the velocity field in the part of the domain close to the free surface but

external to Ω^n is needed and it should be extended sufficiently far to cover all of the region upon which the fluid domain is likely to extend during time step $n + 1$.

On the other hand, the pressure gradient and the pressure nodal values are needed in order to impose the incompressibility condition in the edge-based procedure (for more details see Section 2.6.4). In the present work an explicit extrapolation is performed.

An auxiliary data structure is defined. It contains the layers of nodes close to the free surface. As an examples, let us refer to Figure 2.8 that represents the domain at the end of t^n. The gray area is the fluid part and the black circles represent the calculated nodes.

The layers are defined using the following criteria:

- **LAYER 0** (L^0) is the first layer of nodes of the fluid domain internal the free surface $(L^0 \in \Omega^n)$.

- **LAYER i** (L^k) $(k = 1, 2, ..., nl^{12})$ is the layer of non-fluid nodes neighboring with L^{k-1} $(L^k \notin \Omega^n)$
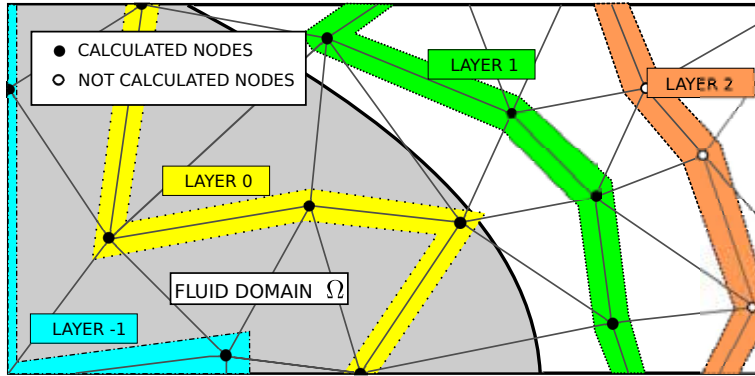
Figure 2.8: Extrapolation layers and calculated nodes in the time interval $t^n - t^{n+1}$.

The fluid velocity and pressure fields on the layers L^k with $k \leq 1$ are known from the previous time step t^n (the black nodes in Figure 2.8). In the present work however, such values are not used in performing the extrapolation of pressure, velocity and gradient of pressure, but rather velocity is taken starting from layer L^0 and pressure and pressure gradient from L^{-1}. The rationale of this choice is that the pressure and pressure gradients in the immediate vicinity of the free surface may show a certain level of spurious oscillations, since pressure is imposed strongly on layer L^1 and the effect of a non-smooth

---

[12]nl denotes the number of extrapolation layers set up by the user.

pressure boundary condition may be still felt on layer L^0. The extrapolation of pressure (and pressure gradient) is thus started from the inner layer (L^{-1}), which guarantees a much smoother behavior of the extrapolation area.

In symbols, we define the pressure gradient on each node i of a given layer k, as the arithmetic average (avg) of all of its neighbors j which belong to the layer of lower order, i.e.

$$\nabla p_i^k := avg\left(\nabla p_j^{k-1}\right) \forall k = 0...nl \ \ i \in L^k \ \ j \in L^{k-1} \tag{2.115}$$

Given such pressure gradients, pressure is then evaluated on node i so as to maintain the extrapolated pressure gradient, that is

$$p_i^k := avg\left(p_j^{k-1} + \mathbf{h}_{ij} \cdot \nabla p_j^{k-1}\right) \forall k = 0...nl \ \ i \in L^k \ \ j \in L^{k-1} \tag{2.116}$$

where $\mathbf{h}_{ij} := \mathbf{x}_j - \mathbf{x}_i$ is the vector from i to j.

The extrapolation of the velocity is performed in a very similar way, with the only difference that the extrapolation starts from layer L^0, not from L^{-1} (see Figure 2.8 for a graphical representation).

$$u_i^k := avg\left(u_j^{k-1}\right) \forall k = 1...nl \ \ i \in L^k \ \ j \in L^{k-1} \tag{2.117}$$

The extrapolation procedure described above provides a prediction of the velocity and pressure fields that is likely to be found outside of the pressure domain. Such extrapolation is performed before convecting the distance function, and should be extended sufficiently far to cover all of the area upon which the fluid domain is likely to extend during the following time step. It should be remarked that the data structure that contains the different layers should be updated every time the distance function is convected.

It is interesting also to observe that the choice of using the *strong* form of the pressure gradients in the momentum equations appears at this point to be beneficial. The idea is that since the pressure gradient was not integrated by parts, no boundary integral of the pressure is needed on the free surface (in the solution of the momentum equation) and the only thing needed on any fluid element (including the elements cut by the free surface) is the correct computation of the pressure gradient, which is automatically available once the pressure is extrapolated as described.

Remark 13. The data structure that contains the different layers should be updated every time the distance function is convected.

Remark 14. The extrapolation of pressure and pressure gradient is necessary only in the edge-based formulation in order to approximately prescribe the zero pressure condition on the free surface, as it will be explained in Section 2.6.4. For the element-based formulation a virtual sub-splitting is proposed and no pressure gradients are needed.

2.6.3   The distance function

Once the convection operation has been performed the level set function is no longer the Euclidean distance function presented in 2.110. To recover its original nature a tool to re-evaluate the nodal distance from the new calculated free surface, has been developed. Due to the dynamic nature of the analyzed problem, a redefinition of the fluid domain $\Omega := \{\mathbf{x} \in \Omega_0 \quad | \quad \varphi(\mathbf{x}) \leq 0\}$ is necessary at each time step. In the present section the methodology for the calculation of the distance field is described. The $3D$ case is taken into account although the $2D$ case has also been implemented. For the calculation of the distance field of the domain Ω_0, numerical methods have to be employed because the use of analytical solution is not trivial. The method proposed by Elias, Martins and Coutinho (see [56] for more details) is taken as a reference. It takes its origin from the Fast Marching Method (FMM), a technique, first developed by Sethian (see [114]), for the computation of the arrival time of a front. In the FMM the Eikonal equation (equation 2.118) is given as a boundary condition

$$\|\nabla T\| \cdot F = 1; \tag{2.118}$$

where T is the time arrival of the front and F is the speed of the front. That means that $T(p)$ is the time arrival of the front to point p. Taking $F = 1$, $T(p)$ is nothing but the distance missed by the front to arrive at the point p. That means that function T coincides with the signed distance function φ adopted in the present work.

$$\|\nabla T\| = \|\nabla \varphi\|; $$

The key idea of Elias and coworkers, that makes the difference from the FMM, was the use of a finite element interpolation for the calculation of the level set function $\varphi(\mathbf{x}, t)$. For each element its gradient is then discretized as follows

$$\|\nabla \varphi^e\| = \|\mathbf{B^T d}\|; \tag{2.119}$$

where $\mathbf{d}^T = (d_1, d_2, d_3, d_4)$ is the vector of the nodal distances of a tetrahedral element, and $\mathbf{B}$

$$
\mathbf{B} = \frac{1}{6\Omega^{el}} \begin{bmatrix} N_{1,x} & N_{1,y} & N_{1,z} \\ N_{2,x} & N_{2,y} & N_{2,z} \\ N_{3,x} & N_{3,y} & N_{3,z} \\ N_{4,x} & N_{4,y} & N_{4,z} \end{bmatrix}
$$

is the matrix of the derivatives of the shape functions in the three cartesian directions. Then

$$
\begin{bmatrix} \varphi_{,x} \\ \varphi_{,y} \\ \varphi_{,z} \end{bmatrix} = \begin{bmatrix} N_{1,x}d_1 + N_{2,x}d_2 + N_{3,x}d_3 + N_{4,x}d_4; \\ N_{1,y}d_1 + N_{2,y}d_2 + N_{3,y}d_3 + N_{4,y}d_4; \\ N_{1,z}d_1 + N_{2,z}d_2 + N_{3,z}d_3 + N_{4,z}d_4; \end{bmatrix} \tag{2.120}
$$

Therefore, equation 2.118, with $F \equiv 1$ can be written as

$$
(\varphi_{,x}^e)^2 + (\varphi_{,y}^e)^2 + (\varphi_{,z}^e)^2 = 1; \tag{2.121}
$$

That means that if the distance of three over four nodes of a $3D$ element is known (suppose known d_1, d_2, d_3) the value of d_4 can be easily calculated. Considering the following simplification:

$$
\begin{aligned}
d_x &= N_{1,x}d_1 + N_{2,x}d_2 + N_{3,x}d_3; \\
d_y &= N_{1,y}d_1 + N_{2,y}d_2 + N_{3,y}d_3; \\
d_z &= N_{1,z}d_1 + N_{2,z}d_2 + N_{3,z}d_3;
\end{aligned} \tag{2.122}
$$

and substituting equation 2.122 into equation 2.121 it results

$$
(d_x + N_{4,x}d_4)^2 + (d_y + N_{4,y}d_4)^2 + (d_z + N_{4,z}d_4)^2 = 1. \tag{2.123}
$$

Equation 2.123 is a second order equation where the only unknown is d_4. The maximum value between the two possible solutions of equation 2.123 will be the solution of the problem. In the case of an imaginary solution, it is possible to define the distance function arriving from another element. If this is not possible, the node will be skipped and the solution will be interpolated at the end of the loop [56].

Using a fixed mesh approach the free surface will not necessarily coincide with a layer of nodes but it will cut the elements. This means that the distance values of at least

one layer of nodes have to be known in order to define the initial conditions for starting
the above described procedure. The problem is solved by evaluating in a different way
the distances of the nodes of those elements crossed by the interface.
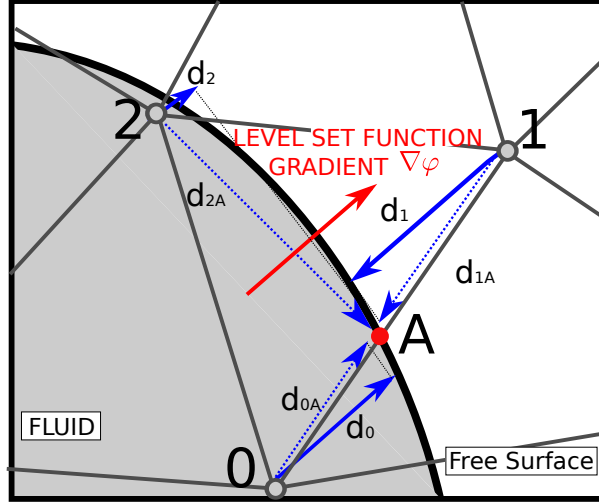
Figure 2.9: Calculation of nodal distances d_i on the nodes i of one element cut by the
free surface.

Once all these elements are identified, for each of them the steps are the following:

1. Calculate the coordinates of point A of Figure 2.9. It is one of the points of
   intersection between the convected free surface and the element edges;

2. Calculate the distance of any node to point A (d_{iA} with $i = 0, ..., n_{pts}$).

$$\mathbf{d}_{iA} = \mathbf{x}_i - \mathbf{x}_A; \tag{2.124}$$

   In Figure 2.9 they are represented by the blue dotted arrows;

3. Evaluate $\nabla\varphi$. It is the gradient of the level set function inside the element;

4. Calculate the components of the distances $\mathbf{d}_{iA}$ in the direction of $\nabla\varphi$

$$\mathbf{d}_i = \mathbf{d}_{iA} \cdot \frac{\nabla\varphi}{||\nabla\varphi||}; \tag{2.125}$$

where d_i are the distance values of the nodes from the new free surface (blue arrows in
Figure 2.9).

Once these initial conditions are defined, a loop over all the elements is performed, in order to identify those elements whose nodal distances are all known but one. Equation 2.123 can then be used.

2.6.4 Prescribing the boundary condition on the free surface $\partial \Omega_m$

Finally the last important issue is the imposition of the zero pressure boundary conditions on the evolving free surface $\partial \Omega_m$ at each time step. In boundary fitting meshes, the imposition of boundary conditions is straightforward, since the whole boundary of the domain coincides with some edges or faces of the mesh. This is not possible if a fixed grid approach is used, as there are no element edges which define the free surface of the domain. This requires devising some alternative strategies to prescribe boundary conditions. Reading [40] is recommended to have an overview of many different fixed grid approaches and respective technique to assign boundary conditions. In the present work two different methods are implemented in the element and the edge-based approaches.

In the first case a virtual splitting of the elements is performed at each time step in order to consider in the calculation only the fluid portion of the element divided by the free surface. In the edge-base case an approximate technique using the extrapolated pressure gradients is presented.

Element-based approach

In the element-base approach a virtual splitting of the elements cut by the free surface is performed without modifying the global degrees of freedom of the problem. This is done in order to evaluate the integrals only on the portion of the element covered by fluid.

When an element is crossed by the free surface, it is split in 4 virtual sub elements. If an edge is crossed by the free surface, a linear interpolation of the distance values of the nodes is performed in order to identify the point of intersection between the free surface and the edge itself, if not, the virtual point is set in the middle of the edge.

In Figure 2.10(b) an example of splitting is shown. The position of node 3 and 4 is calculated with a linear interpolation of the distance value of the nodes $0 - 2$ and $2 - 1$ respectively. Node 5 is finally placed in the middle of the edge $0 - 1$. Four virtual sub elements are identified and their geometric and material characteristics are calculated,

e.g. their Gauss points (called auxiliary Gauss points), their area, density, viscosity and so on.

(a) Free surface elements

(b) Virtual division in sub elements
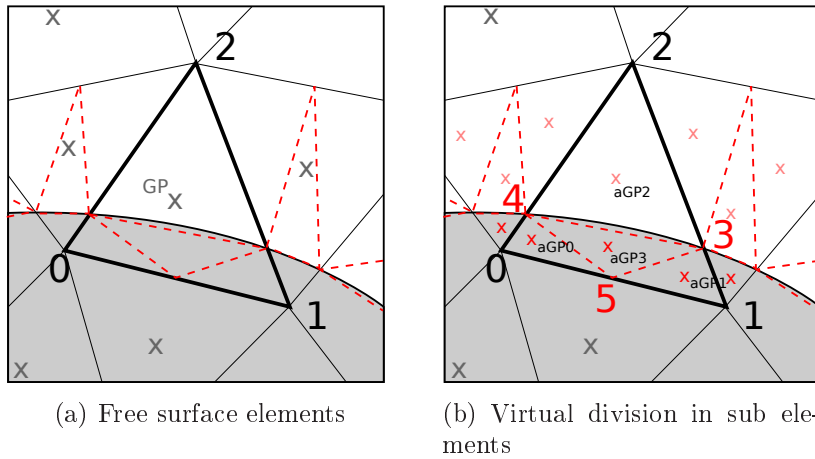
Figure 2.10: Splitting procedure for the elements cut by the free surface.

A numerical integration on the four *auxiliary Gauss points* ($aGPi$ in Figure 2.10(b)) is performed but only the contribution of the fluid part (i.e. sub-elements $0 - 5 - 4$, $4 - 5 - 3$ and $5 - 1 - 3$) is assembled in the global system. Just as an example, looking at element $0 - 1 - 2$ of Figure 2.10(b), any X degree of freedom of node 0 will be given as the sum of the values of X evaluated on $aGP0$, $aGP1$,$aGP3$ multiplied for the area of the respective sub-elements. On the contrary sub-element $2 - 4 - 3$ is not taken into account as it is not a fluid element.

Edge-based approach

Despite its advantages, the pressure extrapolation described in Section 2.6.2 does not impose in any way the traction-free condition on the free surface. This is done in the second step of the fractional step procedure, by fixing the value of the pressure at the time step $n + 1$ so that the pressure field is zero on the free surface.

Since the free surface cuts the element at an arbitrary position, as already explained in the previous sections, no nodes are available for directly fixing the pressure In the case of the edge-based procedure, an additional difficulty is that element splitting of the cut elements, as described in the previous section, and the subsequent integration only on the fluid portion, is impossible within an edge-based formulation unless one wants to recompute the edges and lose efficiency.

The chosen approach is to consider correct the predicted pressure gradient in the vicinity

of the free surface. Therefore pressure at nodes laying in L^1 is fixed so to guarantee that its value is zero on the free surface, provided that the pressure gradient is kept fixed. Note that in doing so layer L^1 should be recomputed since it does not necessarily coincide with the one used in the extrapolation step.

The idea is to evaluate the gradient of pressure of node i ($\in L^1$) in the direction of the distance (which is the gradient of the level set function) and calculate the pressure at nodes i considering a zero pressure on the free surface whose distance from node i is known and then interpolating linearly.
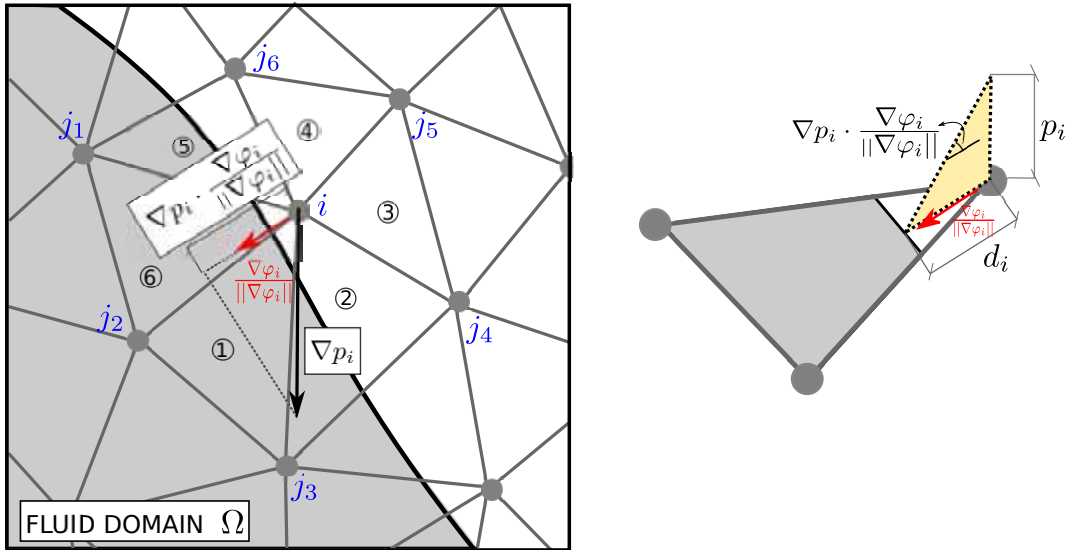
Figure 2.11: Graphical explanation of the evaluation of pressure on the first layer of non fluid nodes in order to respect the incompressibility condition.

Defining as i-patch the cluster of elements whose node i belongs to (elements $1 - 6$ of Figure 2.11), pressure on node i is evaluated as the value of the level set function on node i times the gradient of pressure in the direction of the gradient of the level set function itself, i.e.

$$p_i^1 = \nabla p_i^n \cdot \frac{\nabla \varphi_i^{n+1}}{||\nabla \varphi_i^{n+1}||} \varphi_i^{n+1}; \tag{2.126}$$

where $\nabla \varphi_i^{n+1}$ and $||\nabla \varphi_i^{n+1}||$ are the gradients of the level-set function at node i and its L_2 norm respectively and φ_i^n is the level-set function itself. $\nabla \varphi_i^{n+1}$ is calculated considering the contribution of the gradient of the level-set function on each edge concurring on node i. For instance edges ij_p (with $p = 1, 2, .., 6$) of Figure 2.11.

Remark 15. It is important to observe that Eqn.2.126 is the only point at which the level set function is actually required to be a distance. Since its value is only needed on L^1, it is convenient to recompute it as accurately as possible at every time step. This can be done geometrically for the elements crossed by the zero of the level set function with a minor computational cost.

Remark 16. The correct calculation of the residual of the momentum equations would have required integrating only on the fluid area of the cut elements. This is impossible within an edge-based formulation, unless one wants to recompute the edges and lose efficiency. In this work it is accepted to integrate on the whole element area considering that both the body force and the pressure gradient are extrapolated on the outside of the fluid. This is acceptable for most situations and is exact for the hydrostatic case where the gradient of pressure and the body force exactly cancel each other (see Section 2.8.1 for an empirical verification).

2.7   The algorithm

The steps of the global algorithm are finally summarized in the box below.

Element-based algorithm

1. Given the level set function φ^n, **extrapolate** velocity, pressure and pressure gradient so to obtain $\mathbf{u}_{ext}^n$, p_{ext}^n and ∇p_{ext}^n defined as the velocity, pressure and pressure gradient over the extrapolated domain.

2. **Convect** the level set function φ defining the new free surface at t^{n+1} using $\mathbf{u}^n$ and $\mathbf{u}_{ext}^n$. Note that the extrapolated values are only required within a limited number of layers which are the ones on which the convection will be actually performed.

3. **Re-calculate** (if needed) the **distances** in the whole domain starting from the zero of the level set function at t^{n+1} obtained at step 2.

4. Check **split elements** and assemble only the fluid sub-elements contributions;

5. **Solve** the monolithic system;

6. Move to next time step.

Edge-based algorithm

1. Given the level set function φ^n, **extrapolate** velocity, pressure and pressure gradient so to obtain $\mathbf{u}^n_{ext}$, p^n_{ext} and ∇p^n_{ext} defined as the velocity, pressure and pressure gradient over the extrapolated domain.

2. **Convect** the level set function φ defining the new free surface at t^{n+1} using $\mathbf{u}^n$ and $\mathbf{u}^n_{ext}$. Note that the extrapolated values are only required within a limited number of layers which are the ones on which the convection will be actually performed.

3. **Re-compute** (if needed) the **distance** in the whole domain starting from the zero of the level set function at t^{n+1} obtained at step 2.

4. **Solve the momentum** equations 2.91a. Note that the solution is performed on the domain at the predicted free surface position (φ^{n+1}).

5. Set the approximate **pressure boundary conditions** on $\partial\Omega^{n+1}$ so to guarantee that the pressure is (approximately) zero at the position indicated by the zero of the level set function. In order to do that, the geometric distance is evaluated on L^1.

6. **Solve for the pressure** (equation 2.91b).

7. **Solve for the correction** (equation 2.91c).

8. Move to next time step.

2.8   Numerical examples

In the following sub-sections a series of benchmark tests are presented. First two very simple examples are presented to compare the element-based and the edge-based free surface algorithms for a variable porosity medium.

Their performance is analyzed both in the static case (Section 2.8.1) and in the dynamic one (Section 2.8.2). In both cases the analytical solution is known and is compared with the numerical one obtained.

The mass conservation capability is then analyzed both in a $2D$ and in a $3D$ example. No porous media is considered because its presence has been verified to help mass conservation thanks to the introduction of an additional dissipative effect.

All the $3D$ examples are only performed with the edge-based algorithm being the only one implemented in $3D$.

In the last part of the section the edge-based technique for free surface flows (without porous medium) is tested in a series of examples and its results are compared with results obtained with a Lagrangian approach using the Particle Finite Element Method (PFEM).

2.8.1   Still water example

The still water example allows to verify the correct calculation of pressure in a variable porosity medium.

The domain of analysis is a square of $10m$ edge. The right hand side of the domain is porous ($n = 0.5$) whereas the left hand side is not ($n = 1$), as shown in Figure 2.12. The level of water is set at $y = 5m$ and slip boundary conditions are imposed on the bottom and on the side edges. Gravity is $10m/s^2$. Pressure is expected to vary linearly from $0Pa$ at the free surface till $50000Pa$ at the bottom independently from which vertical section is chosen.

The element-based algorithm reproduces perfectly the expected distribution. The distribution of the iso-lines of pressure can be seen in Figure 2.13(a). No oscillations are formed in the element-based example, confirming the exact imposition of the pressure boundary condition on the free surface via the element splitting technique described in Section 2.6.4.

For the edge-based algorithm, although the free surface does not move, a small oscillation on the pressure is observed. This is caused by the approximated imposition of
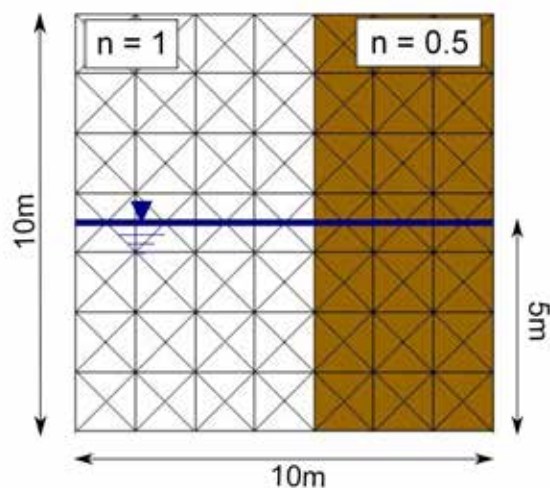
Figure 2.12: Geometry, structured mesh and conditions of the still water model.
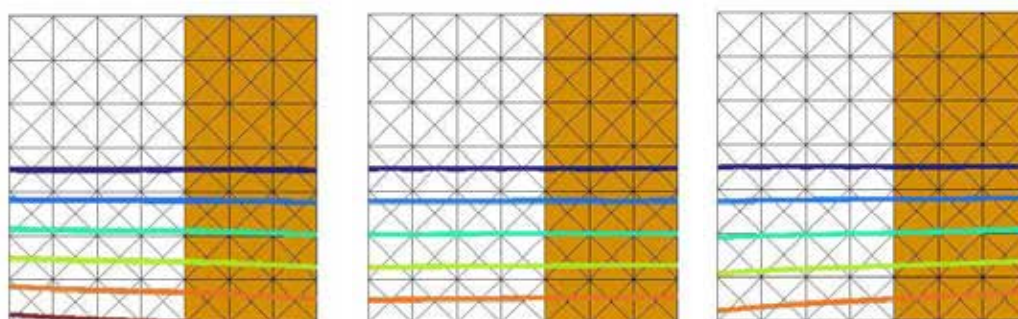
(a) Edge-based
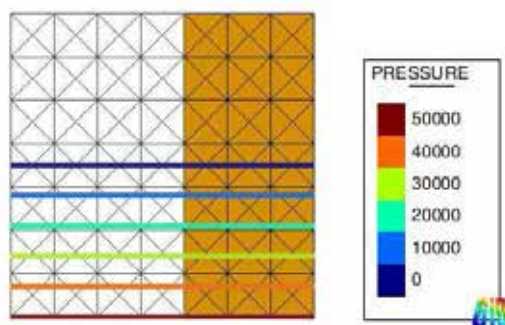
(b) Element-based

Figure 2.13: Pressure distribution.

the zero pressure condition on the free surface (see Section 2.6.4). The oscillation of the bottom pressure is shown in Figure 2.13(a).
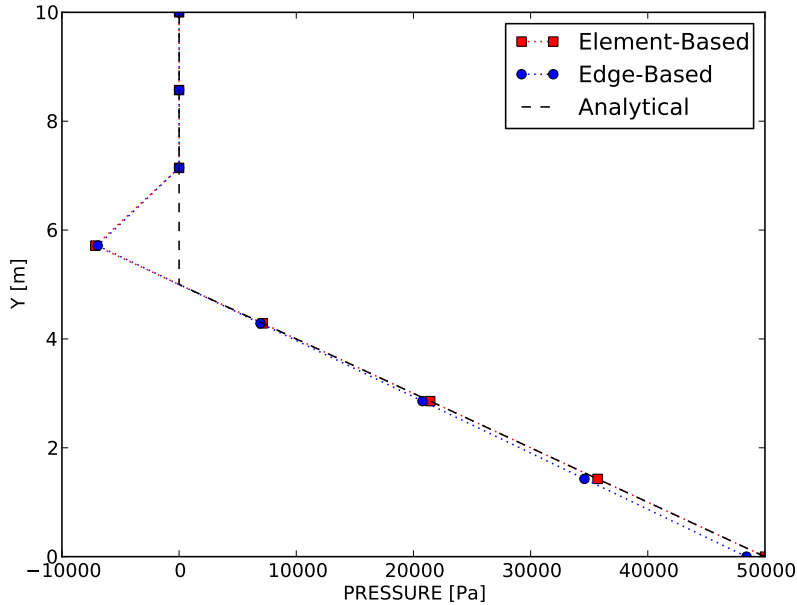
Figure 2.14: Pressure distribution in a vertical section. Comparison between the two algorithms.

Figure 2.14 finally shows the pressure distribution along a vertical section for both algorithms and it is compared to the analytical solution. The negative pressure of the first node above the free surface is the consequence of the imposition on the cut elements of the zero pressure condition on the free surface 2.6.4.

2.8.2   Water flowing through two materials

The second example aims to analyze the behavior of the free surfaces algorithms when a variable porosity medium is present in dynamic conditions. The domain of analysis is a square of edge $10m$. Only the upper part is porous with porosity $n = 0.5$ while the lower part corresponds to a pure air material ($n = 1$). A vertical entrance of water is set from the bottom edge. Slip boundary conditions are imposed to the vertical walls
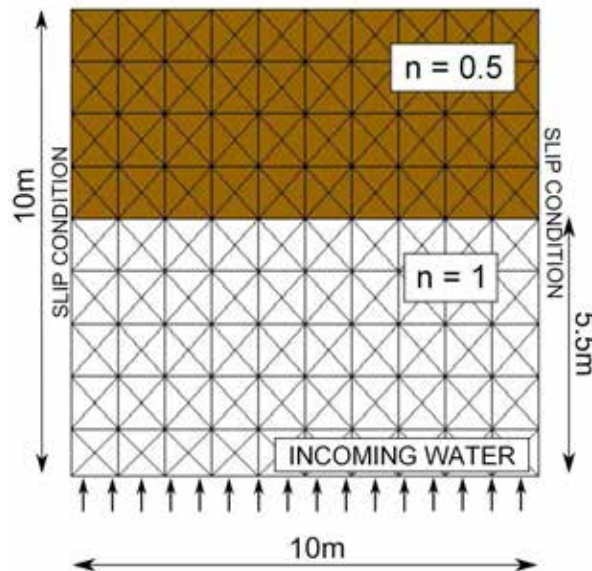
Figure 2.15: Geometry, structured mesh and conditions of the two material model with bottom incoming water.

and $0Pa$ pressure condition is set, in the case of the edge-based algorithm, to the upper side. The mesh is structured as shown in Figure 2.15.

In the sequences presented in Figure 2.16 the free surface line is perturbed when entering the porous media. Nevertheless it recovers the horizontal plane shape as soon as the discontinuity has passed.

Figures 2.17 and 2.18 show the distribution of pressure in the vertical central section of the two models, when the water level is $2.5m$ and $9.9m$ respectively. A comparison with the analytical results is presented. There is a very good accordance of pressure values in the case that no porous media is still present, as can be seen in Figure 2.17. The element-based algorithm perfectly calculate the pressure distribution also when water has entered the porous media. On the contrary the error of the edge-based algorithm is not negligible (Figure 2.18).

(a) Edge-based. (b) Element-based.
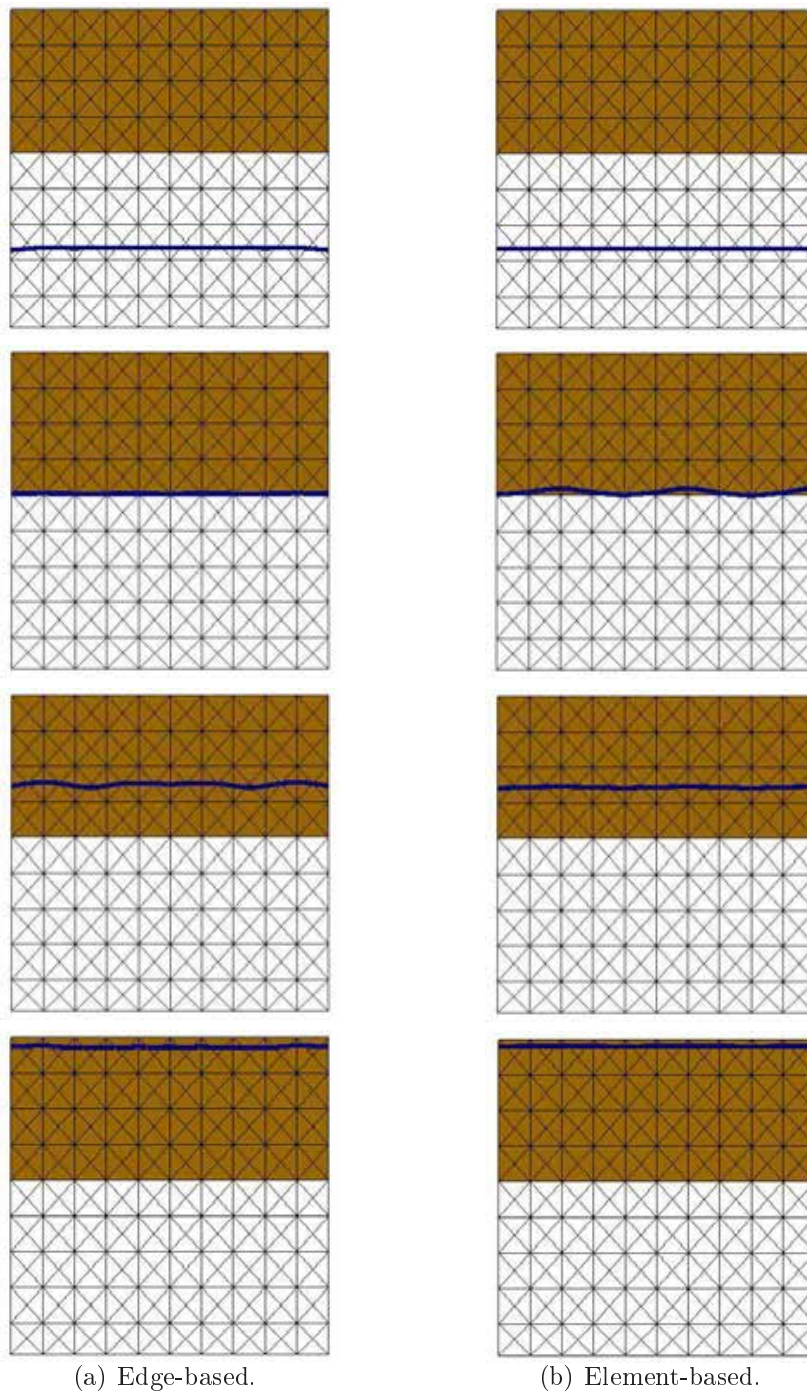
Figure 2.16: Evolution of free surface for both algorithms.
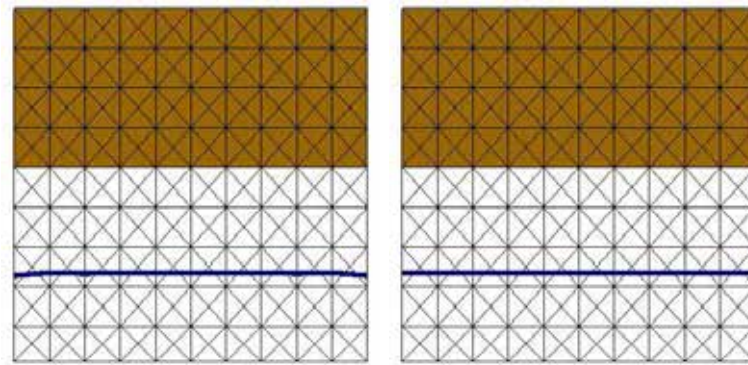
(a) Edge-based   (b) Element-Based
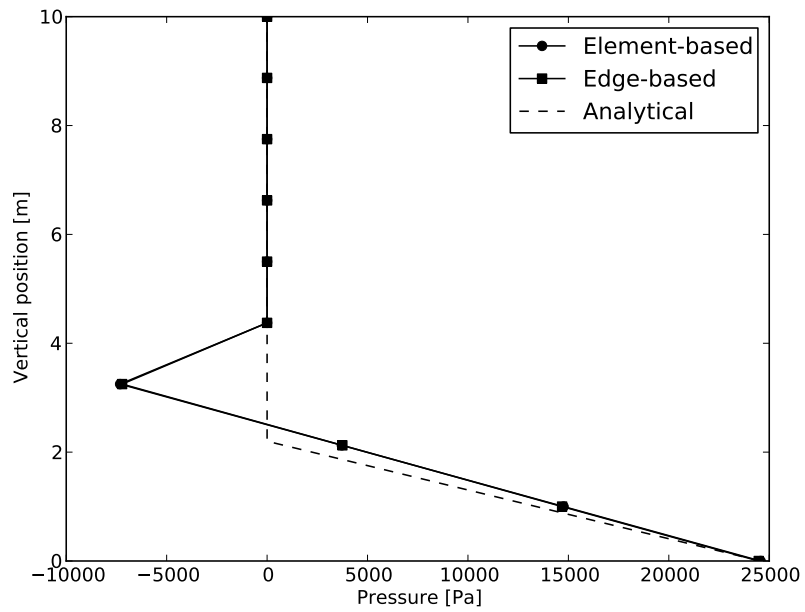
(c) Pressure distribution in a vertical section

Figure 2.17: Pressure distribution when water level reaches $2.5m$ from the bottom.
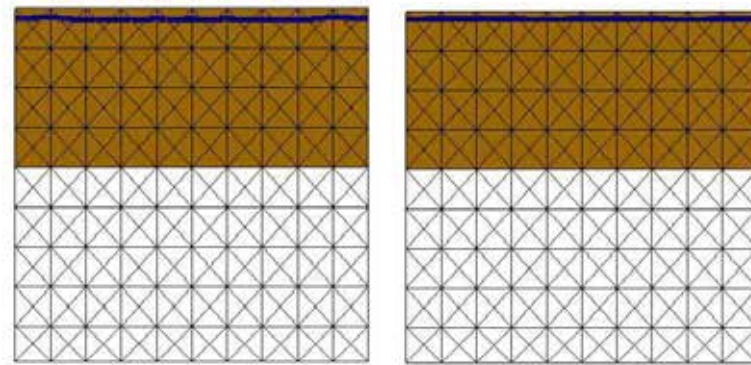
(a) Edge-based   (b) Element-Based
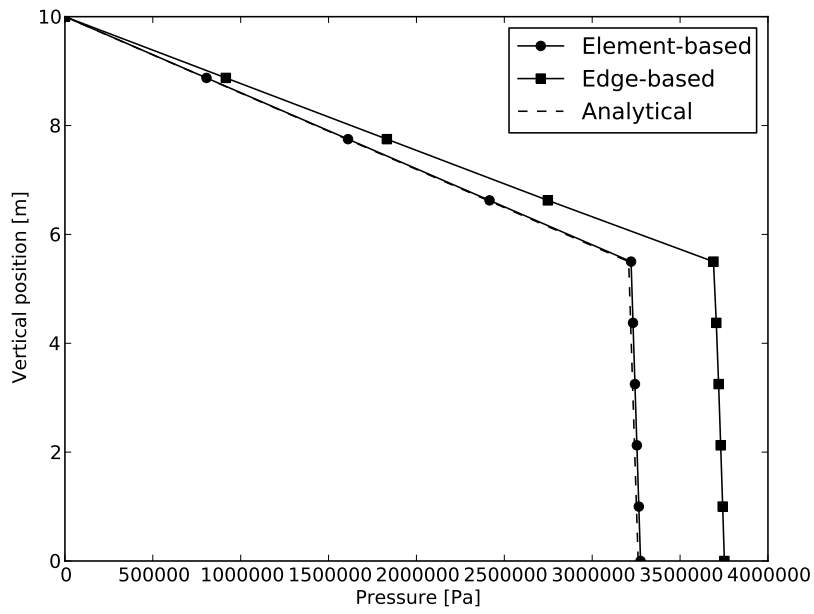
(c) Pressure distribution in a vertical section

Figure 2.18: Pressure distribution when water level reaches the top.

2.8.3   Mass conservation

$2D$ vertical column Edge-based and element-based method

A second example has been performed in order to check the mass conservation capability in both algorithms. No porous media has been considered ($n = 1$) because its dissipative effect has been shown to help the mass to be conserved. The worst case is then analyzed. A rectangular domain of $5m$ width and $10m$ height is set. A discharge of $1m^3/s$ is entering the domain from the bottom edge. The inlet vertical velocity is then $0.2m/s$. Slip boundary conditions are imposed on the vertical edges and zero pressure is imposed on the upper edge (only for the edge-based formulation).

Two different meshes are considered as shown in Fig.2.19.

(a) Mesh 0.2cm   (b) Mesh 0.5cm
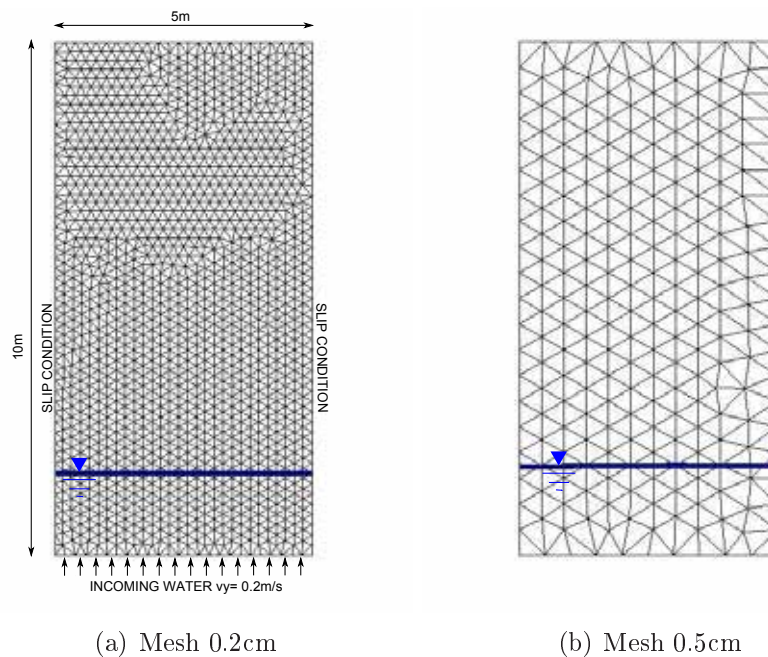
Figure 2.19: Geometry, mesh and conditions of the mass conservation model.

A good conservation of mass is seen in both algorithms. Figures 2.20 and 2.21 show the evolution of the free surface at $10 - 20 - 30 - 40 - 50\, sec$ respectively.

$3D$ Vertical column edge-based method

In the present example a vertical rectangular column with an inlet in the bottom side and an outlet on the top face is simulated. Geometry and conditions of the present

(a) Mesh 0.2cm
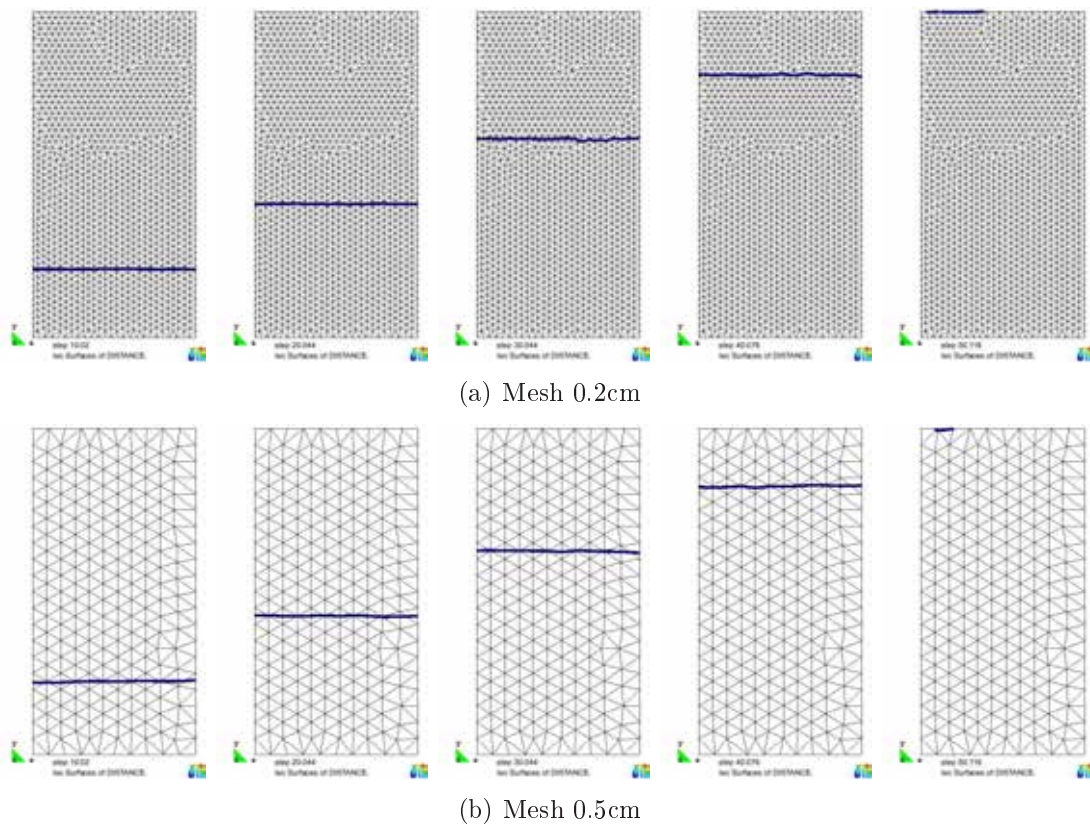
(b) Mesh 0.5cm

Figure 2.20: $2D$ Vertical column. Element-based algorithm. Evolution of free surface at $10 - 20 - 30 - 40 - 50 \, sec$.
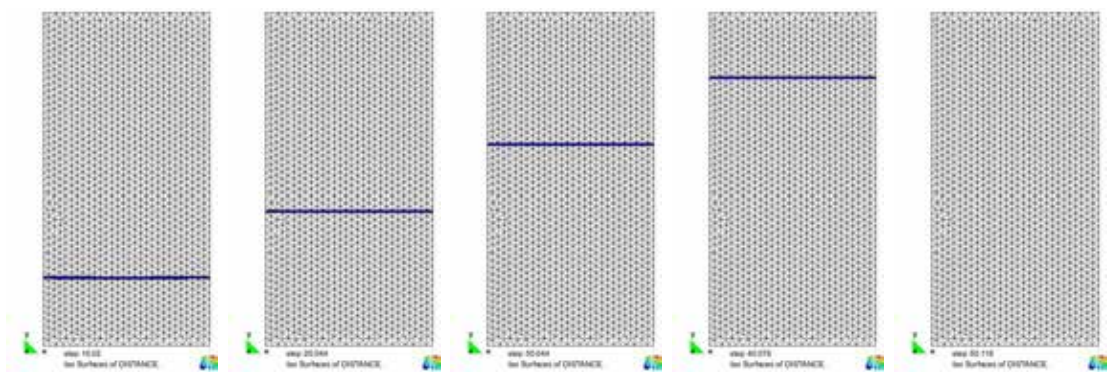
(a) Mesh 0.2*cm*
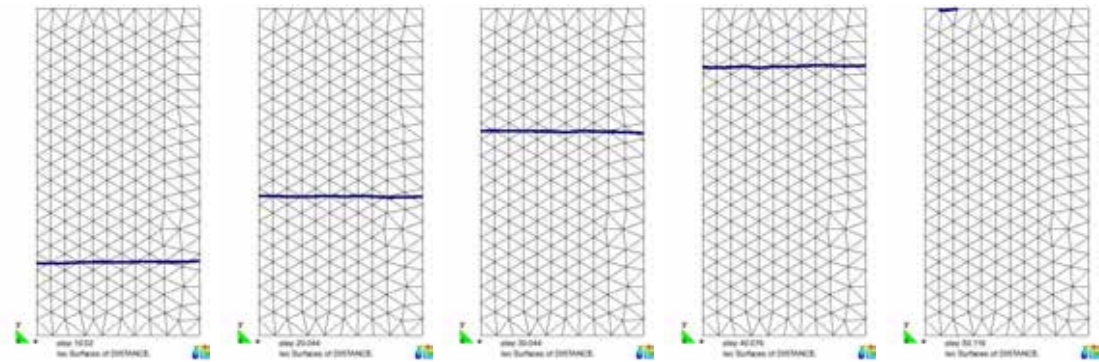
(b) Mesh 0.5*cm*

Figure 2.21: 2*D* Vertical column. Edge-based algorithm. Evolution of free surface at 10-20-30-40-50 sec.

example are taken from [43] (although in that case the interaction between two fluids with different specific weight was taken into account). Nevertheless the problem presents the same difficulties of maintenance of a flat free surface both in the transitory and in the stationary regime.

The problem has been studied using two meshes: a structured one and an unstructured one (Figure 2.22).

	STRUCTURED	UNSTRUCTURED	
	Medium	Medium	Coarse
n. nodes.	2981	1210	723
n. elem	13800	6117	3720
elem length [m]	-	1	1.2
elem per side	$5 \times 5 \times 20$	-	-

Table 2.6: $3D$ vertical column. Number of nodes, number of elements, elemental length (unstructured meshes) and number of elements per edge (structured mesh) of the meshes considered in the analysis.

Figures 2.23 and 2.24 show the evolution of the free surface (identified with the zero of the level set function ($\varphi = 0$) during the filling process. Considering that the free surface at time $t = 0$ is located at $h = 1m$ from the bottom and the velocity inlet is $v = 1m/s$ a very good agreement with expected level of the free surface can be noticed at each time step (Figures 2.23 and 2.24). In both cases the expected level of water at $2s$, $6s$, $10s$, $14s$ and $18s$ is respected and it is $3m$, $7m$, $11m$, $15m$ and $19m$ respectively. No oscillations are observed neither for the unstructured nor the structured mesh.

If a lateral entrance of water is considered and the value of inlet velocity is decreased to $v_{in} = 0.1m/s$ (see Figure 2.25 for the details on the geometry and the boundary conditions considered), the improvement of volume conservation explained in Section 2.5.5 plays a relevant role. Two meshes are considered for the calculation: a coarse and a fine one whose characteristics are summarized in Table 2.7 and shown in Figure 2.27.

Figure 2.26(a) shows the beneficial effect of the volume correction. The expected level of water is compared with the one calculated for the fine mesh model with and without volume conservation improvements. On the other hand, it is important to observe that

(a) Structured mesh. Free surface.

(b) Unstructured mesh. Free surface.
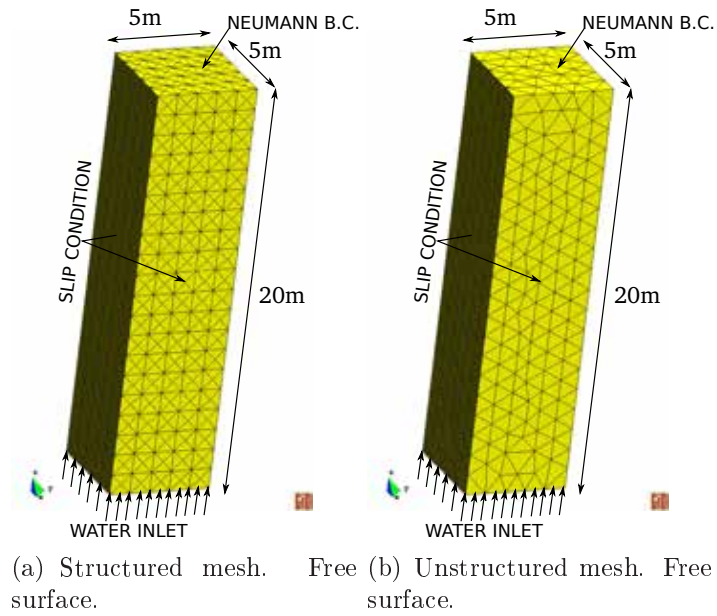
Figure 2.22: $3D$ vertical column. Geometry and mesh taken into account.

(a) t = 2s   (b) t = 6s   (c) t = 10s   (d) t = 14s   (e) t = 18s
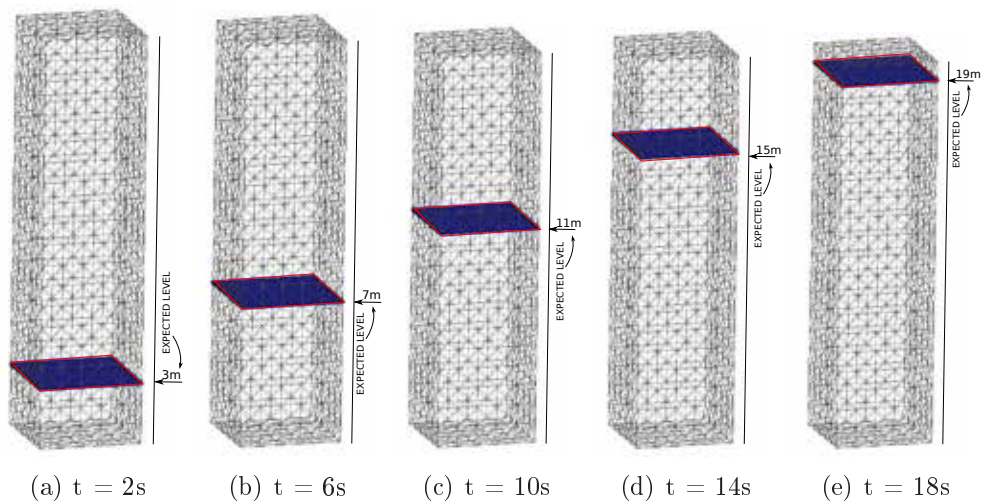
Figure 2.23: $3D$ vertical column. Structured medium mesh. Evolution of free surface for $1m/s$ bottom incoming velocity. On the right of each snapshot the expected level is indicated.

(a) t = 2s   (b) t = 6s   (c) t = 10s   (d) t = 14s   (e) t = 18s
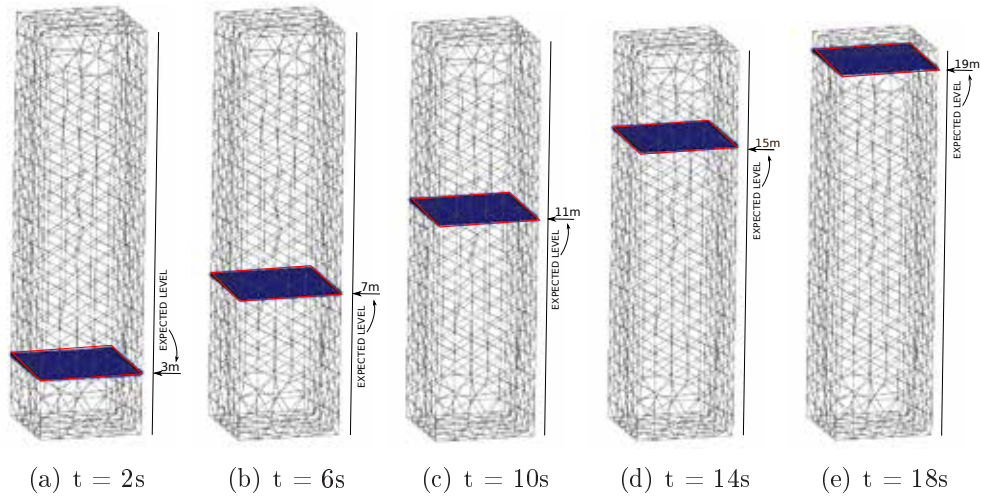
Figure 2.24: $3D$ vertical column. Unstructured medium mesh. Evolution of free surface for $1m/s$ bottom incoming velocity. On the right of each snapshot the expected level is indicated.

with the volume correction, no relevant changes are observed when a coarser mesh is employed (observe graph 2.26(b)).

(a) Fine mesh   (b) Coarse mesh
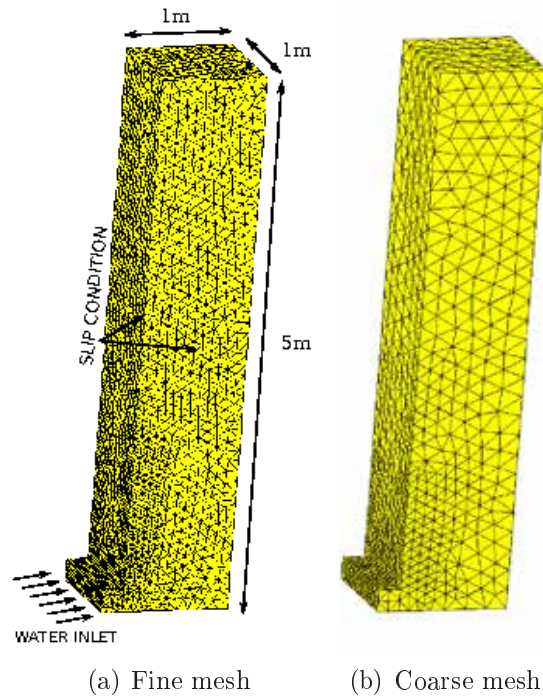
Figure 2.25: Mesh and geometry of the vertical channel with lateral entrance of water

Another important aspect is that the use of the volume correction leads to a flat free surface reducing the oscillations. This can be observed by comparing Figures 2.27(a) and 2.27(b) where the volume correction is used in both the fine and coarse mesh with Figures 2.27(c) where not.

	Fine	Coarse
n. nodes.	12 100	3 050
n. elem	61 600	14 400

Table 2.7: Vertical column with lateral entrance example. Number of nodes and number of elements for the meshes considered in the analysis.
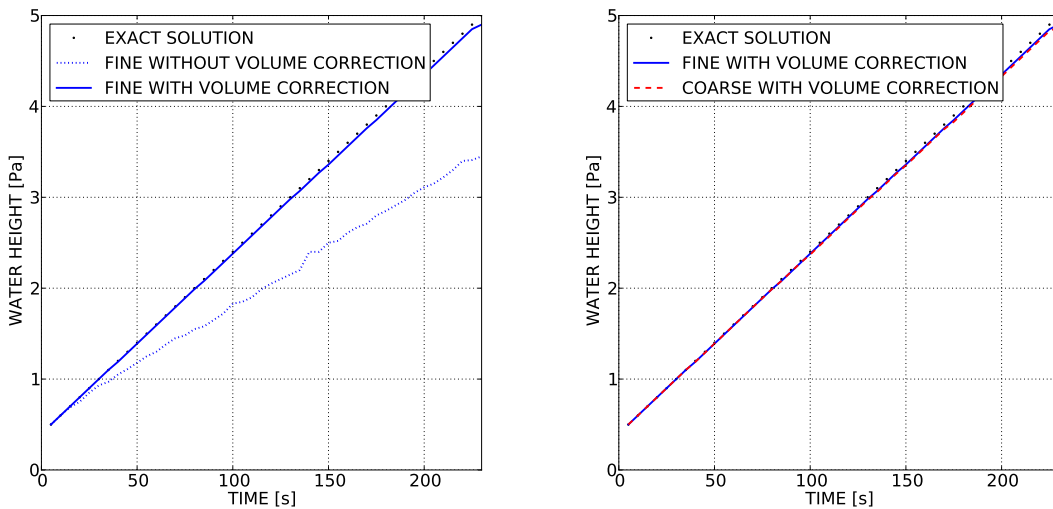
(a) With or without volume correction. Fine mesh.

(b) With volume correction. Coarse and fine mesh.

Figure 2.26: Vertical column with lateral entrance example. Level of water in terms of time.
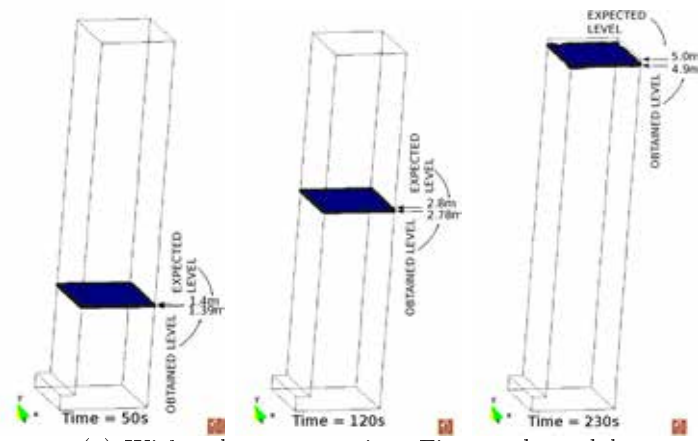
(a) With volume correction. Fine mesh model
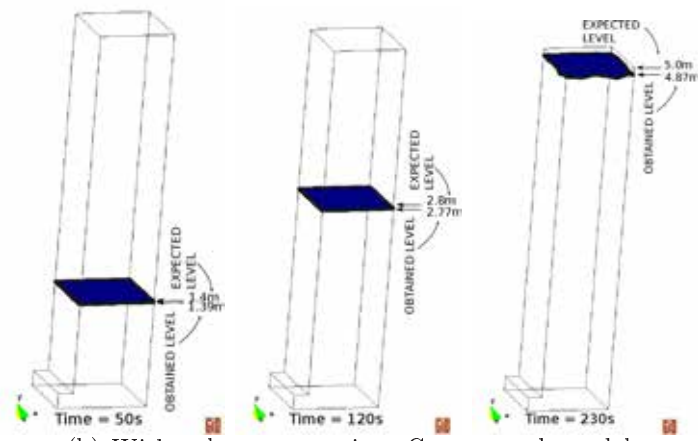
(b) With volume correction. Coarse mesh model
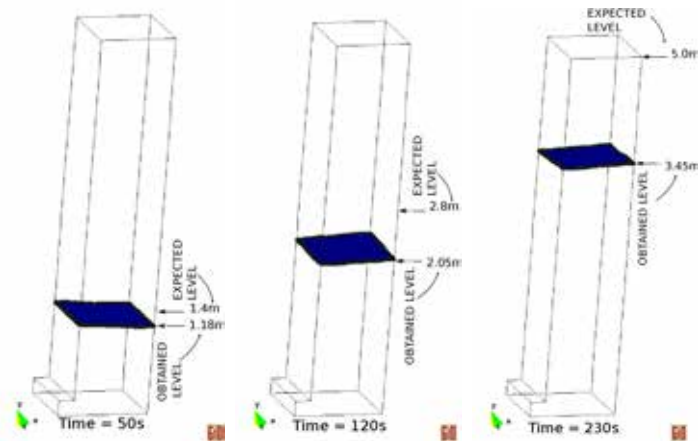
(c) Without volume correction. Fine mesh model

Figure 2.27: Vertical column with lateral entrance example. Evolution of the free surface at $50s$, $120s$, and $230s$.

2.8.4 Comparison of the level set algorithm with PFEM

In this section the performance of the edge-based level set approach are compared with the capability of the particle finite element method (PFEM). PFEM is a well established numerical method whose own nature makes it very appropriate to simulate free surface flows and breaking waves. The consultation of [67, 75, 93, 96, 100] is recommended for an overview of its principal features. More details on the method are presented in Chapter 3 of the present work. The comparison of the presented level-set approach with PFEM can be very challenging and can represent a good validation of the developed free surface tool.

2.8.5 Flip bucket

The present example reproduces an experiment carried out by Hager and coworkers whose results can be found in [70]. The performance of the present level set technique is compared with the results obtained using PFEM [67, 98, 100] and published in [75]. The geometry data, initial and boundary condition can be found in [75]. The case with Froude number 5 is considered. The control domain and the mesh used can be seen in Fig.2.28 and 2.29 respectively.
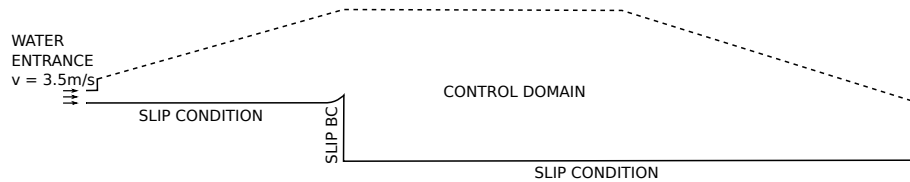
Figure 2.28: Geometry and boundary condition of the flip bucket example.
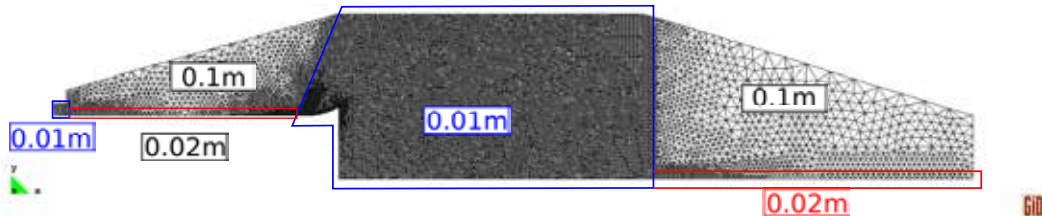
Figure 2.29: Mesh of the flip bucket example.

An entrance of water is imposed in the left side. After a transitory phase shown in Figure 2.30 the stationary regime is achieved and pressure is registered on the bucket
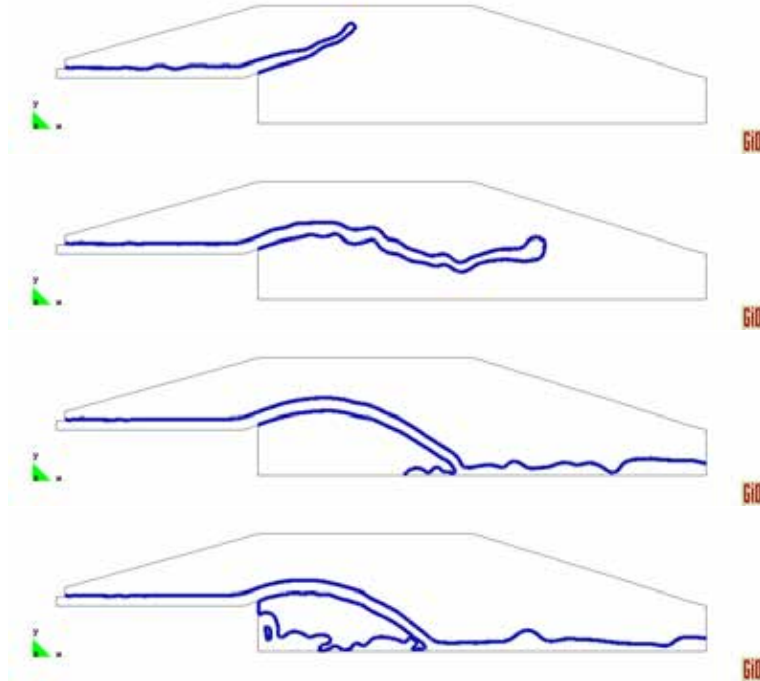
Figure 2.30: Sequence of the transitory phase of the jet.

as shown in Figure 2.31(a). The jet shape is also compared in Figure 2.31(b) where the darker line is the level set whereas the lighter represents the PFEM results.

A good agreement with experimental pressure along the bucket can be seen in Figure 2.31(a). The black points are the experimental results found in [70], whereas the continuous line and the dotted line are the level set and the PFEM solutions respectively.

2.8.6   3D dambreak

The present example is a $3D$ dam break example already studied by the authors in [75] using PFEM.

Data are taken from the experiments performed at the Maritime Research Institute Netherlands (MARIN) for breaking dam flows [72]. Several numerical results of this case study are available in literature for VOF techniques. This is the case of [72] employing Cartesian grids, or [54] using an edge-based approach. Finally other level set simulations can also be found. Among others, in [7, 71], an application of isogeometric analysis is presented.

The water column is left free to fall over a step where pressure sensors are set following
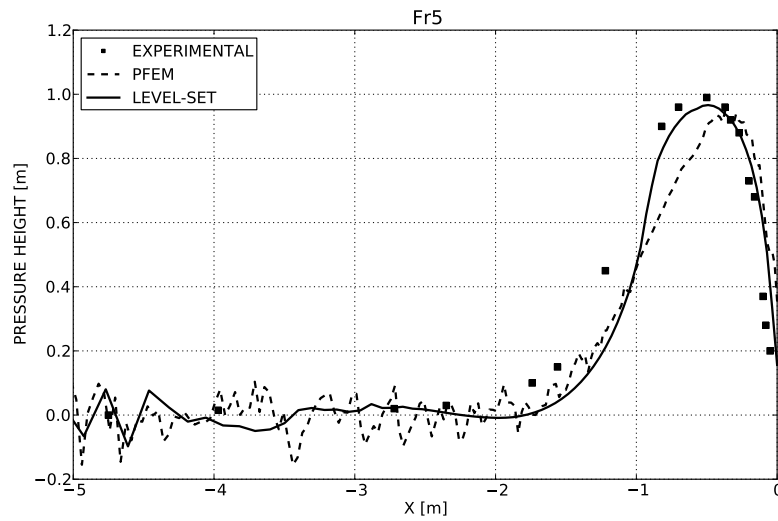
(a) Pressure distribution on the bucket. Experimental and numerical comparison.
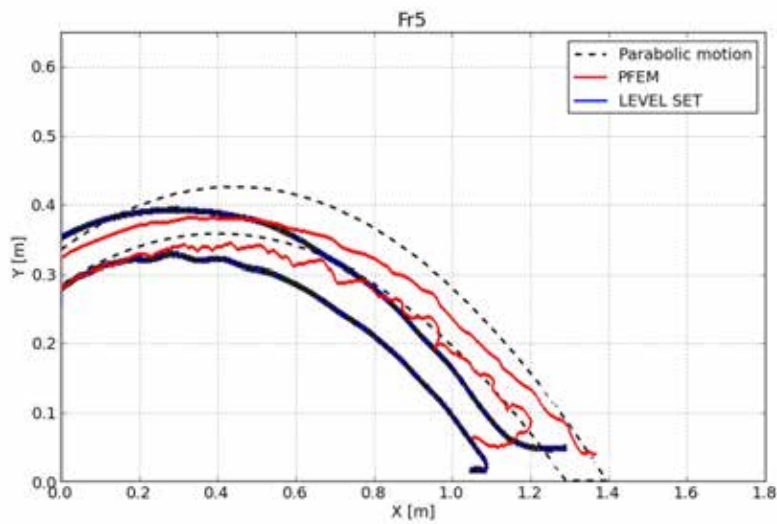
(b) Jet trajectory. Relative comparison.

Figure 2.31: Level set and PFEM comparisons in the pressure head calculation and the jet development

the scheme of Figure 2.32. The details of geometry can be found in [54].
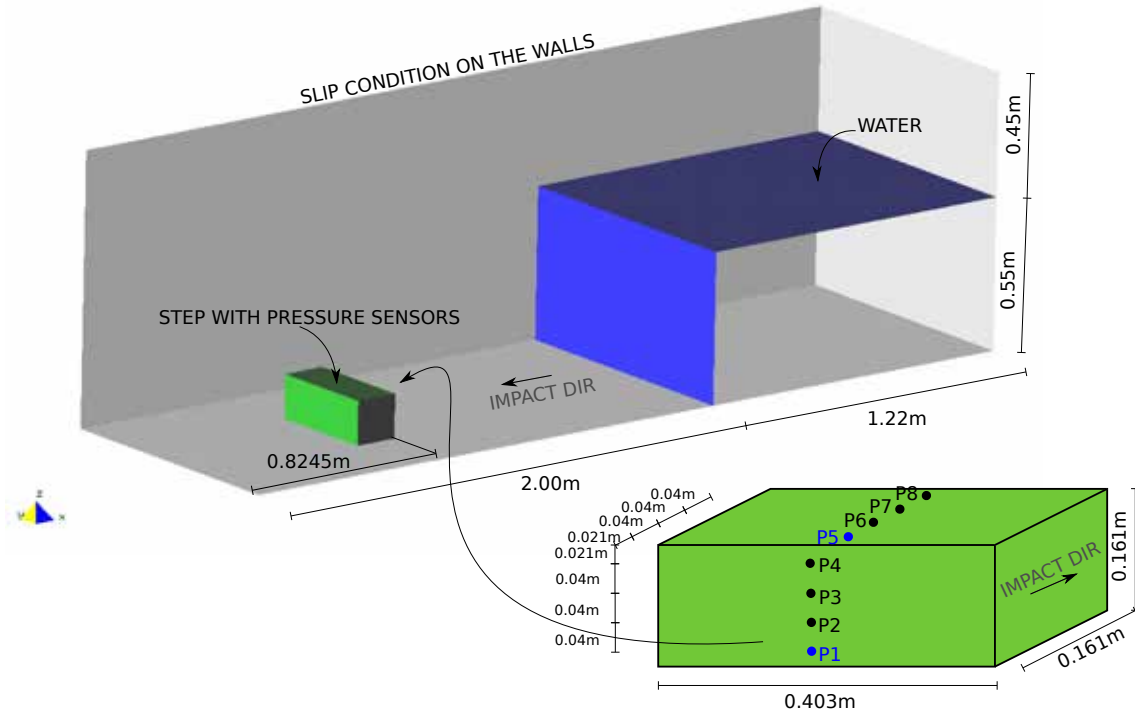
Figure 2.32: Geometry and boundary condition of the 3D dam break example. On the lower left corner a zoom on the pressure sensors distribution on the step

Two meshes are considered in the present work, their characteristics are detailed in Table 2.8 and they are shown in Figure 2.33.

	Mesh A	Mesh B
n. nodes.	51 627	392 130
n. elem	296 157	2 310 984

Table 2.8: Dam break example. Number of nodes and number of elements of the two meshes considered in the analysis.

A sequence of the falling of the water column can be seen in Figure 2.34 where the free surface evolution is plotted for the two meshes considered.

(a) Mesh A.   (b) Mesh B.
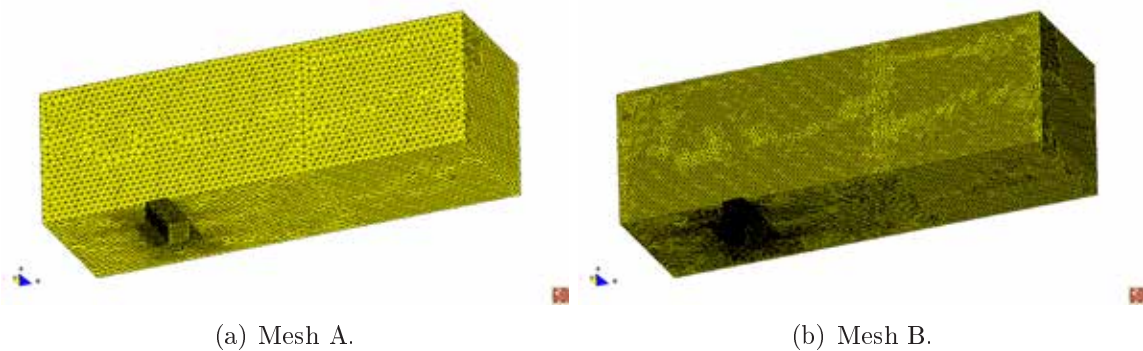
Figure 2.33: The two meshes considered. On the left Mesh A of 296 157 and Mesh B of 2 310 984 tetrahedra.

(a) Mesh A.   (b) Mesh B.
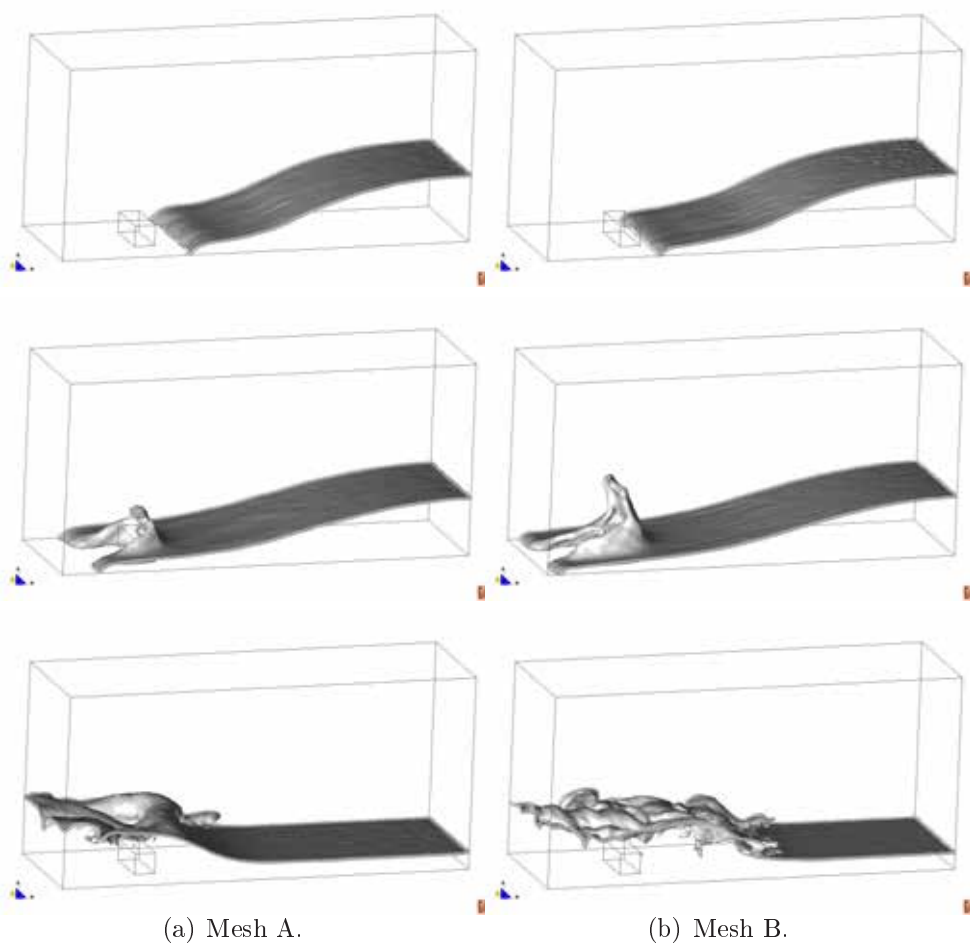
Figure 2.34: Evolution of the dam break at $0.4s$, $0.6s$ and $2.0s$. Comparison between the results obtained with meshes A and B.

The pressure evolution in time obtained with the two meshes is compared in Figures 2.35-2.42 with experimental results and PFEM results taken form [75].
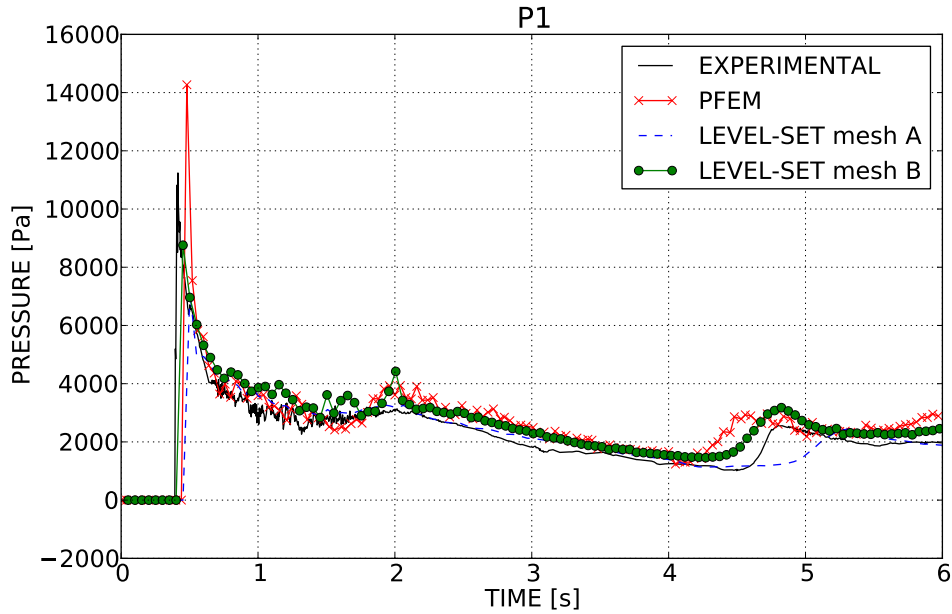
Figure 2.35: Pressure evolution on $P1$ on the vertical face of the step indicated in Figure 2.32. Comparison of level set, PFEM and experimental results.

A better behavior of the Eulerian approach with respect to PFEM can be observed especially with mesh B. Mesh refinement improves the accuracy of the solution and the capability of catching the second pressure waves with a correct timing, whereas a clear delay can be noticed for the coarse mesh (mesh A).

PFEM uses an unconditional stable scheme which leaves more freedom in the choice of the time increment than in the semi-explicit scheme of the Eulerian method. Nevertheless PFEM needs a frequent re-meshing procedure for which no parallelization is available yet. This aspect considerably slows down the time performance of PFEM in comparison with a parallel fixed mesh approach.
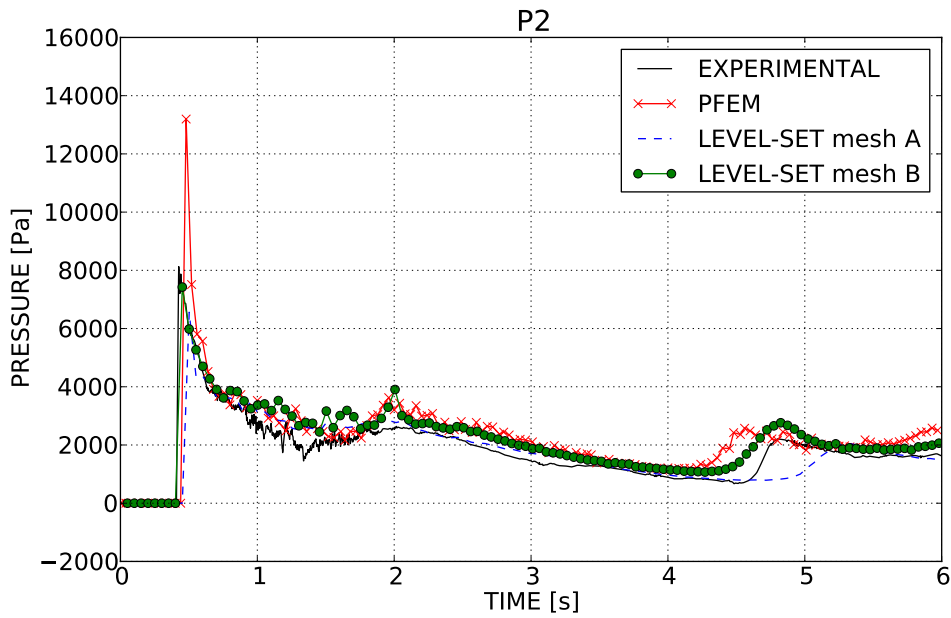
Figure 2.36: Pressure evolution on $P2$ on the vertical face of the step indicated in Fig. 2.32. Comparison of level set, PFEM and experimental results.
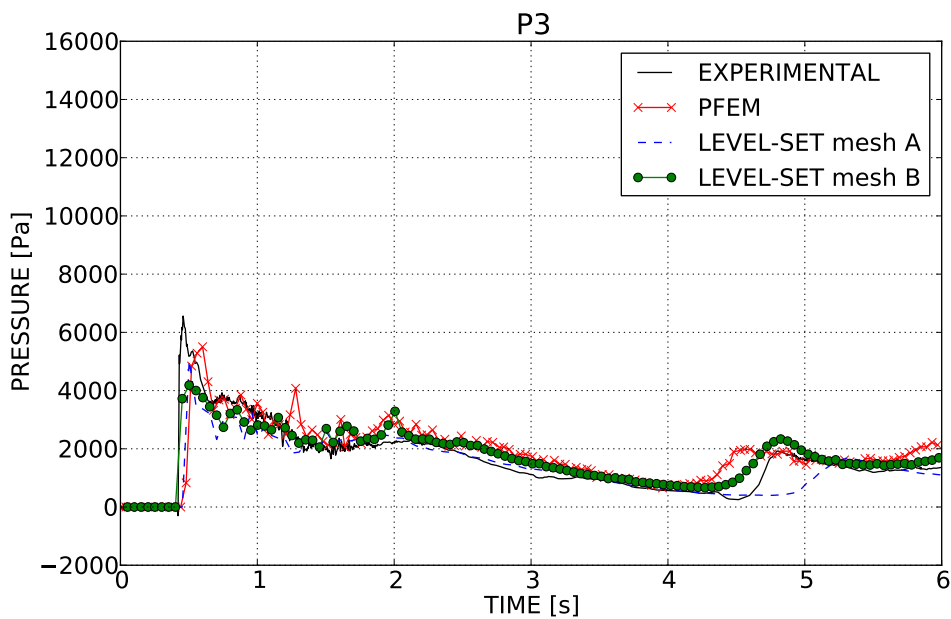
Figure 2.37: Pressure evolution on $P3$ on the vertical face of the step indicated in Fig. 2.32. Comparison of level set, PFEM and experimental results.
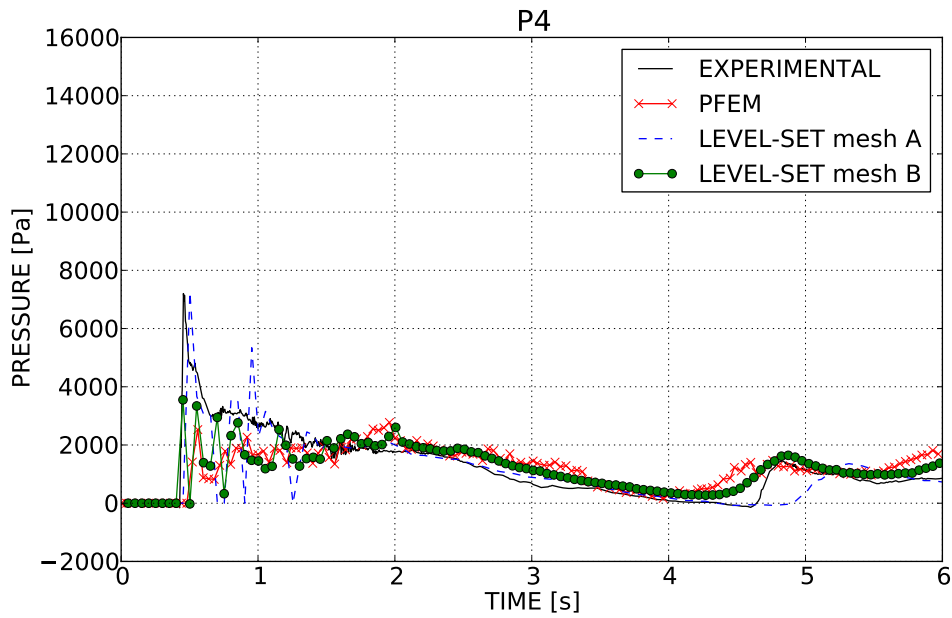
Figure 2.38: Pressure evolution on $P4$ on the vertical face of the step indicated in Fig. 2.32. Comparison of level set, PFEM and experimental results.
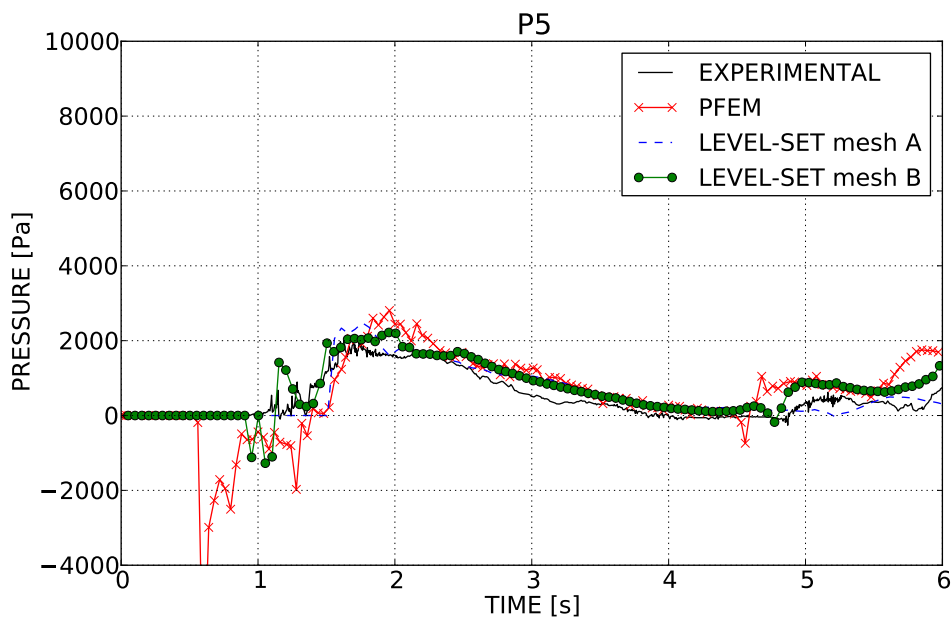
Figure 2.39: Pressure evolution on $P5$ on the top face of the step indicated in Fig. 2.32. Comparison of level set, PFEM and experimental results.
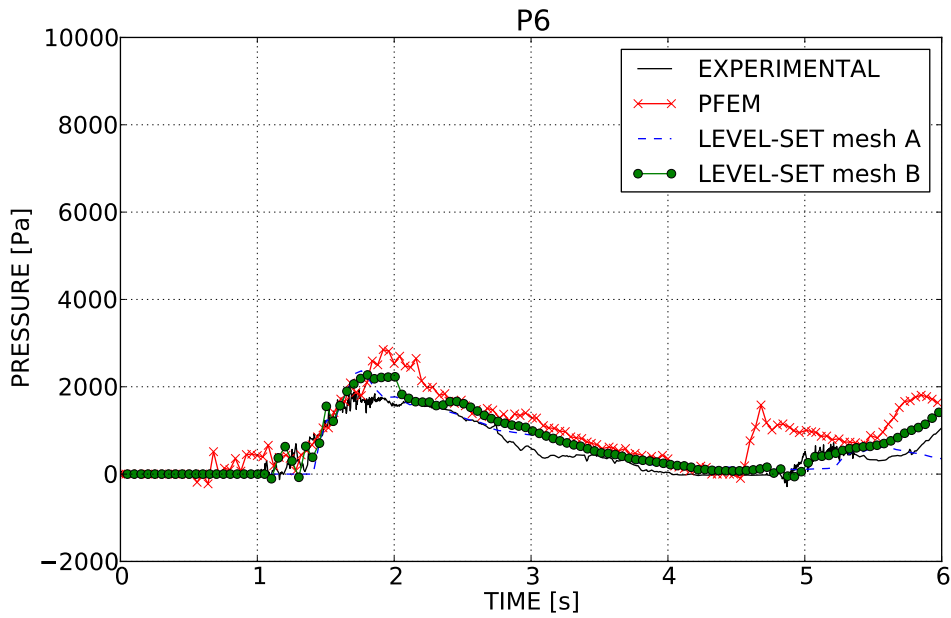
Figure 2.40: Pressure evolution on $P6$ on the top face of the step indicated in Fig. 2.32. Comparison of level set, PFEM and experimental results.
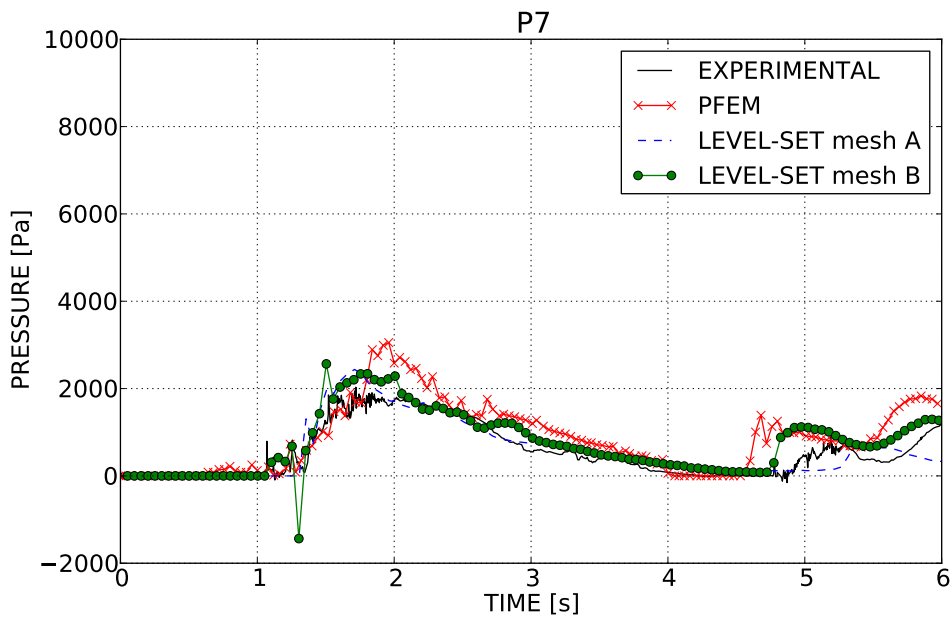
Figure 2.41: Pressure evolution on $P7$ on the top face of the step indicated in Fig. 2.32. Comparison of level set, PFEM and experimental results.
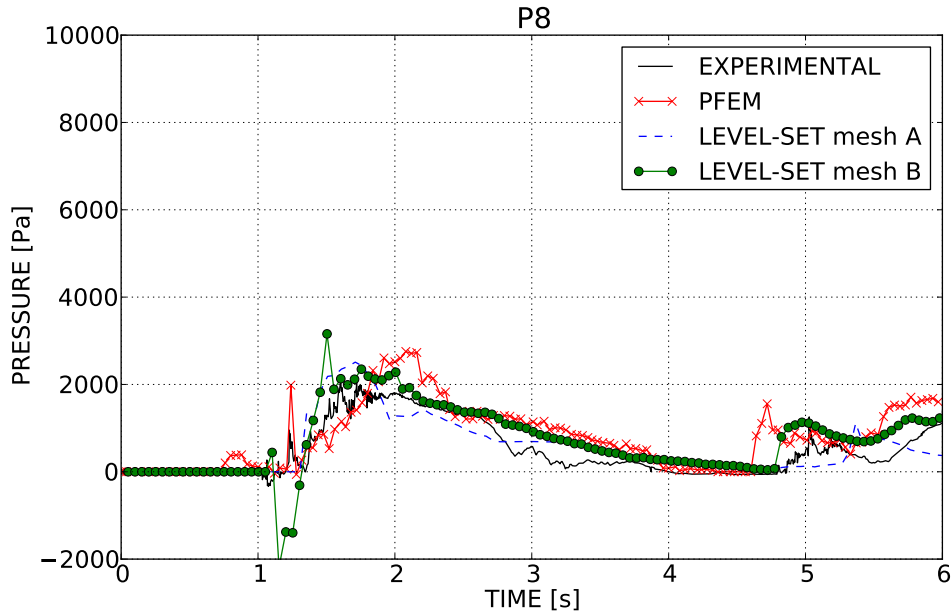
Figure 2.42: Pressure evolution on $P8$ on the top face of the step indicated in Fig. 2.32. Comparison of level set, PFEM and experimental results.

2.9   Conclusions

In this chapter the approach to numerically treat the problem of flow in a variable porosity medium has been presented. After the choice of the resistance law to be used in the algorithm, the two solution methods developed have been presented in detail:

- Element-based algorithm. It uses a monolithic approach to solve the weak form of the balance equations that are stabilized using an ASGS technique. A fully implicit method is used and a Bossak time integration technique is chosen.

- Edge-based algorithm. In this case a fractional step approach is used to solve the balance equations that are stabilized using an OSS stabilization technique. A semi-explicit method, i.e. a $4th$ order Runge Kutta scheme is implemented.

In both cases only simplicial meshes (3-noded triangles or 4-noded tethraedra) are taken into account.

The dynamic free surface tracking is done using a level set technique described in the second part of the chapter. An explicit extrapolation is performed in order to define the values of velocity on a band containing the free surface of the fluid. The level

set function (equation 2.110) is updated solving the problem 2.114. Points with zero distance function identify the new free surface. The calculation of the distance function is performed as detailed in Section 2.6.3.

Both algorithms have shown a good performance in the simulation of free surface simple problems in presence of a variable porosity medium. Mass conservation is acceptably respected thanks to the improvement presented in Section 2.5.5. Nevertheless the element-based approach still needs some effort in order to be used for the simulation of large problems. It is still limited to $2D$ problems and no parallel structures have been implemented yet. These aspects make the element-based algorithm to lose competitiveness compared with the edge-based one.

The performances of the edge-based semi explicit algorithm for the simulation of the free surface problems have been also compared with PFEM. The results show that the Eulerian algorithm better represents the pressure peaks both in the dam-break and in the flip-bucket examples. The parallel structure helps to have very good time performances despite of the small time step imposed by the conditional stable method.

On the basis of above considerations, the edge-based approach has been chosen for the study of real experiments on prototype embankments dams in Chapter 5 where a more extensive and complete validation of the algorithm can be found.

Chapter 3

The structural problem

In this chapter an algorithm to simulate the behavior of the granular non-cohesive material used in rockfill dams is proposed. Taking into account the high deformation the structure might be subjected to and the intrinsic incoherence of the rocks, the constitutive law of a non-Newtonian high viscosity material is chosen. After an overview of the traditional non-Newtonian relationships, a regularized Bingham model is selected and implemented as a starting point. This approach presents severe limitations in the simulation of granular behavior having a constant yield threshold. To overcome this issue a variable yield model using a Mohr Coulomb failure criteria is proposed in the second part of the chapter.

The weak form of the problem is then obtained and the numerical technique adopted is presented. The Lagrangian Particle Finite Element Method (PFEM) is chosen for its wide flexibility. In fact the structural domain is expected to undergo severe deformations as the failure progresses and therefore a Lagrangian approach is a natural choice.

In the last part of the chapter the validation of the Bingham model is performed through some benchmarks and the effectiveness of the proposed variable yield model is tested in some examples.

3.1 Introduction

In the present work, the simulation of the structural response of a slope made of granular material has been faced using a continuous approach despite the intrinsic incoherent nature of the rockfill. This is an acceptable choice under the assumption that the

rockfill size is small with respect to the overall size of the structure.

Nevertheless it should be mentioned that in recent years, the great advance in computer performance and in parallel computing has allowed the simulation of the mechanical behaviour of every single particle of a granular slope. The family of the so called discrete (or distinct) element methods (DEM) has been reaching a widespread popularity in the computational mechanics community. Their basic idea is that every particle is a discrete element interacting with the others considering its mechanical and material properties. This can be a valid alternative to the model presented in this chapter and it is actually being implemented by other researchers at CIMNE.

The adoption of a continuous approach leads to an additional requirement: the choice of a suitable constitutive law. Many plastic or rigid-plastic constitutive models are commonly used in geomechanics to describe the structural response of an incoherent non-cohesive material. It is usually accepted that a rockfill slope has the capability to support a certain amount of shear stress with almost no elastic strains before starting large deformations. When the yield stress is reached the material starts to flow until arriving to a stable configuration. It should be noted that the behaviour of the yielded material is more similar to the flowing of a fluid than to the process of deformation of a solid. On the other hand, in literature there exists a wide category of fluids which exhibits a rigid behaviour till reaching a yield threshold. They are part of the family of the so called non-Newtonian fluids.

These aspects, together with the natural way of managing large deformations in fluids, lead us to concentrate on variable viscosity models for the calculation of the structural part instead than on any other plastic or damage model. Consequently, a non-Newtonian constitutive law has been adopted for the rockfill body. This implies that the rockfill stiffness is controlled by very high values of the viscosity. Only when the yield threshold is exceeded, the viscosity dramatically decreases and the material starts flowing. When the material stops its motion, the viscosity recovers its initial values for which the stress level does not exceed the yield limit.

The model developed in this work has its origin in the traditional Bingham plastics using the regularization proposed by Papanastasiou to overcome numerical problems induced by the bilinear stress-strain curve [104]. Nevertheless in order to include a Mohr-Coulomb failure criteria (without cohesion), the possibility of considering a variable yield level is introduced.

The two constitutive models with constant and variable yield, are presented at the

beginning of the present chapter after a brief overview on non-Newtonian models.

The equations governing the structural problem are studied in their weak form arriving to the algebraic solution system which is solved with a fully implicit approach. A stabilized, equal-order, mixed velocity-pressure element technology is chosen so to guarantee a locking free behavior. In fact Cervera and coworkers have demonstrated that the use of a mixed approach is the appropriate framework for dealing with localization problems in incompressible and quasi-incompressible problems. They have successfully applied this approach in solid mechanics in plastic and damage models using linear/linear elements, providing a suitable stabilization technique [25–29, 32].

Since the structural domain is expected to undergo severe deformations as the failure progresses, the kinematic model has to adapt dynamically to such deformations. The Particle Finite Element Method (PFEM) provides the necessary flexibility with a powerful remeshing mechanism [75, 100]. Its features are described in the second part of this chapter.

In the last part of the chapter some examples are inserted to validate the Bingham model and to appreciate its differences with respect to the proposed variable viscosity approach. Finally some dambreaks of granular slopes with different frictional angles are simulated to verify that the model correctly reproduces the expected mechanical properties.

3.2 Structural constitutive law. An overview of non-Newtonian models

In Chapter 2 the constitutive model of a Newtonian fluid was used to describe the stress-strain behavior of water. The stress tensor can be decomposed in its hydrostatic and deviatoric parts as follow

$$\boldsymbol{\sigma} = -p\mathbf{I} + \boldsymbol{\tau} = -p\mathbf{I} + 2\,\mu\boldsymbol{\varepsilon}(\mathbf{u}), \tag{3.1}$$

where

$$\boldsymbol{\varepsilon}(\mathbf{u}) := \nabla^s \mathbf{u} = \frac{1}{2}\Big(\nabla\mathbf{u} + (\nabla\mathbf{u})^T\Big), \tag{3.2}$$

The deviatoric part of the stress tensor $\boldsymbol{\tau}$, is therefore linearly related to the rate of strain $\boldsymbol{\varepsilon}(\mathbf{u})$ through the constant viscosity μ.

Fluids for which the relations between $\boldsymbol{\tau}$ and $\boldsymbol{\varepsilon}(\mathbf{u})$ is not constant, are called non-Newtonians. In this case viscosity cannot be considered as a property of the material as it is strictly dependent on the deformation process. This classification is very general and includes a wide range of different constitutive relations. In order to briefly classify the different non-Newtonian fluids, let's consider the $1d$ problem and let's define an *apparent viscosity* $\tilde{\mu}$ like the ratio between the shear stress τ and the shear rate $\dot{\gamma}$

$$\tilde{\mu} := \tilde{\mu}(\dot{\gamma}) = \frac{\tau}{\dot{\gamma}}. \tag{3.3}$$

According to Chhabra [31] a possible classification of the non-Newtonian fluids is the following:

- Fluids with **time independent** behavior: those for which the current shear stress is function only of the shear rate $\tau = \tau(\dot{\gamma})$. In function of the evolution of their apparent viscosity, they can be divided in:

    1. **Shear-thinning** or *pseudo-plastic* fluids. Their apparent viscosity gradually decreases when increasing the shear rate. This is the case of polymeric systems like melts and solutions.

    2. **Shear-thickening** or *dilatant* fluids. Their apparent viscosity increases when the shear rates increases. This behavior is observed in concentrated suspensions, for instance.

    3. **Visco-plastic** fluids (with or without shear thinning behavior). They are characterized by the existence of a threshold stress, the yield stress, which must be exceeded for the fluid to deform. For lower values of stress the visco-plastic fluids are completely rigid or can show some sort of elasticity. Once the yield stress is reached and exceeded, they can exhibit a Newtonian-like behavior with a constant apparent viscosity (*Bingham plastics fluids*) or not, showing a shear thinning behavior (*yield-pseudoplastic fluids*).

- Fluids with **time dependent** behavior: their apparent viscosity is not only a function of shear stress and shear rate but also of the duration of the application of the shear stress and of its kinematic history. They can be classified into:

    1. **Thixotropic**. Under a constant shear their apparent viscosity decreases with time. A typical thixotropic material is the cement paste.

2. **Rheopectic**. Under constant shearing their apparent viscosity increases with time. For instance printers inks belong to this group.

A schematic overview of the relation between shear stress and rate of strain for different non-Newtonian models can be observed in Figure 3.1.
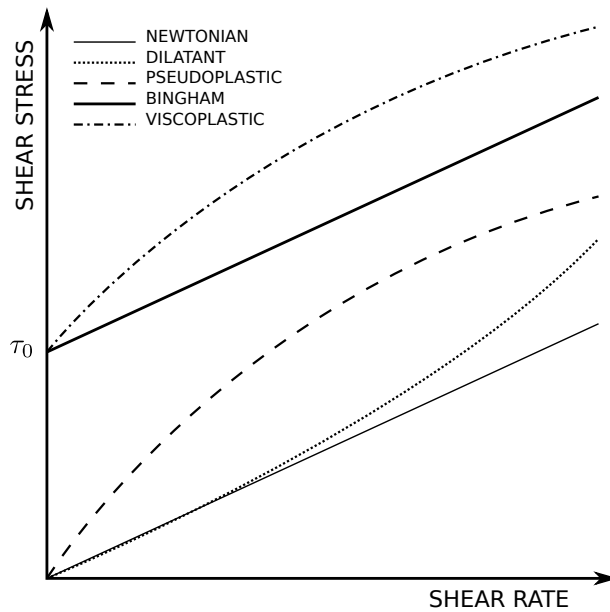
Figure 3.1: Qualitative flow curves for the different categories of non-Newtonian fluids.

A deep analysis of non-Newtonian fluids behavior falls outside the scope of this work. For a comprehensive review of the topic see [24, 31, 44].

3.2.1   Constant yield: the Bingham model

It was in 1919 when Eugene C. Bingham, while studying a possible constitutive model for paints, discovered that their deformation was almost absent till reaching a threshold: the yield stress. After exceeding this stress limit they followed a Newtonian behavior. According to Papanastasiou [104] a wide range of materials have been identified to have a yield threshold. Bird [15] was the first to give, in his book, a lists of several Bingham plastics, most of these products came from food or chemical industry. Among them we can list for instance slurries, pastes, nails, or food substances like margarine, ketchup, mayonnaise and others.

The $1D$ constitutive relation for a Bingham plastic can be defined as follows. Being τ_0

the yield stress

$$\begin{aligned}
\dot{\gamma} &= 0 && \text{if} \quad \tau < \tau_0 \\
\dot{\gamma} &= \frac{1}{\mu_s}(\tau - \tau_0) && \text{if} \quad \tau \geq \tau_0
\end{aligned} \tag{3.4}$$

where $\dot{\gamma}$ is the rate of strain, μ is the dynamic viscosity and τ the shear stress.

Figure 3.2 shows the difference between a Newtonian and a Non Newtonian fluid.
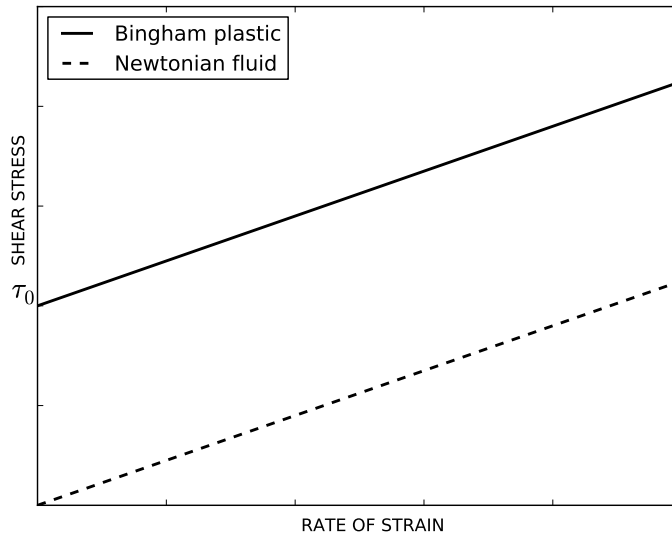
Figure 3.2: Comparison between a Newtonian fluid and a Bingham fluid behavior with a yield stress τ_0.

Equation 3.4 can be rewritten as

$$\tau = \left(\mu_s + \frac{\tau_0}{\dot{\gamma}}\right)\dot{\gamma} \qquad \text{if} \quad \tau \geq \tau_0. \tag{3.5}$$

Special care should be taken in equation 3.5 when the level of stress is lower than the yield stress. In this case, according to equation 3.3, the apparent viscosity approaches infinity, i.e. $\tilde{\mu} \to \infty$ as $\dot{\gamma} \to 0$. This behavior might induce numerical difficulties, some smooth laws are usually preferred. Nevertheless some authors [80] tried to simulate what is called bi-viscosity model but their predictions leads to inconsistencies. Consequently, in the present work the regularized model proposed by Papanastasiou [104] is chosen as a starting point for the development.

Following the ideas presented in [104], equation 3.4 is regularized as follow

$$\tau = \left[\mu_s + \frac{\tau_0}{\dot{\gamma}} \left(1 - e^{-m\dot{\gamma}} \right) \right] \dot{\gamma}, \tag{3.6}$$

where m is a regularization parameter that controls the approximation to the bilinear model as shown in Figure 3.3. The apparent viscosity is defined as

$$\tilde{\mu}(\dot{\gamma}) = \mu_s + \frac{\tau_0}{\dot{\gamma}} \left(1 - e^{-m\dot{\gamma}} \right), \tag{3.7}$$

Referring to equation 3.7, the problems connected with the singular point of the bilinear model are here avoided. In fact, in the un-yielded zone the shear strain rate $\tilde{\mu} = \mu + \tau_0 \, m$ as $\dot{\gamma} \to 0$.
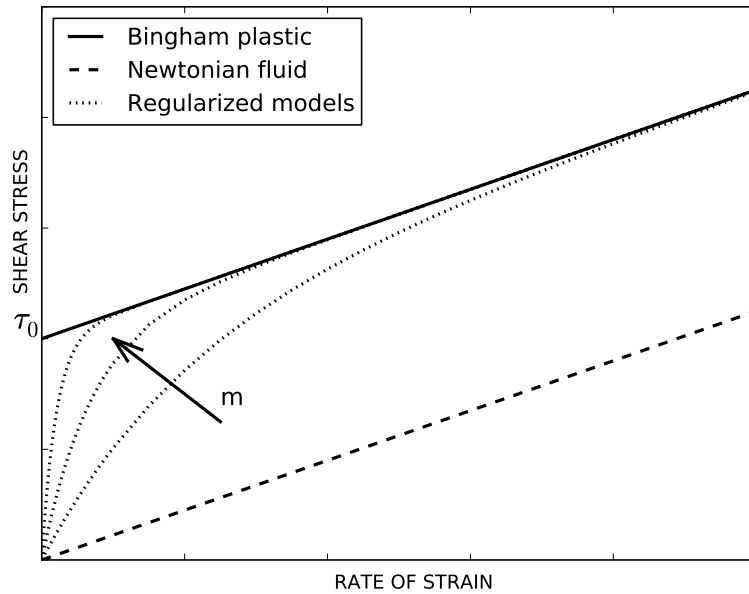
Figure 3.3: Newtonian and Bingham fluid compared with the regularized model for increasing values of the m parameter.

In order to introduce the constitutive model for $3D$ problems, the following *equivalent strain rate* $\dot{\gamma}$ and *yield stress* τ_0 are defined as the second invariants of the rate of strain tensor ($\boldsymbol{\varepsilon}$) and of the deviatoric part of the stress tensor ($\boldsymbol{\tau}$), respectively.

$$\dot{\gamma} = \left(\frac{1}{2} \boldsymbol{\varepsilon} : \boldsymbol{\varepsilon} \right)^{\frac{1}{2}} \tag{3.8}$$

$$\tau_0 = \left(\frac{1}{2}\boldsymbol{\tau} : \boldsymbol{\tau}\right)^{\frac{1}{2}} \tag{3.9}$$

Equation 3.6 becomes for $3D$ problems as

$$\boldsymbol{\tau} = 2\left[\mu_s + \frac{\tau_0}{\dot{\gamma}}\left(1 - e^{-m\dot{\gamma}}\right)\right]\boldsymbol{\varepsilon}(\mathbf{u}), \tag{3.10}$$

where

$$\tilde{\mu}(\dot{\gamma}) = \mu_s + \frac{\tau_0}{\dot{\gamma}}\left(1 - e^{-m\dot{\gamma}}\right), \tag{3.11}$$

3.2.2 Variable yield visco-rigid model

The Bingham model presented in the previous section was conceived for materials with a fixed yield stress. For granular materials, the definition of the yield stress depends on:

- The characteristics of the rockfill (its internal friction angle).

- The presence of water inside the grains. It acts decreasing the effective stress leading to a significant loss of resistance.

The model proposed in the present work has its origin in a classical Bingham constitutive relation but the yield stress τ_0 is pressure sensitive and it is defined using a Mohr-Coulomb failure criteria without cohesion.

$$\tau_0 = p'_s \, tg(\phi), \tag{3.12}$$

where p'_s is the effective pressure and ϕ is the internal friction angle. Equation 3.6 in $3D$ becomes

$$\boldsymbol{\tau} = 2\left[\mu_s + \frac{p'_s \, tg(\phi)}{\dot{\gamma}}\left(1 - e^{-m\dot{\gamma}}\right)\right]\boldsymbol{\varepsilon}(\mathbf{u}), \tag{3.13}$$

and the resulting apparent viscosity is therefore

$$\tilde{\mu}(\dot{\gamma}) = \mu_s + \frac{p'_s \, tg(\phi)}{\dot{\gamma}}\left(1 - e^{-m\dot{\gamma}}\right), \tag{3.14}$$

The idea of a pressure dependent yield stress has already been exploited for instance in [107], where a frictional fluid rehological model is used for the simulation of land slides.

Remark 17. In this chapter the presence of water and the coupling between structure and fluid behavior has not been taken into account yet. It is treated in Chapter 4. Nevertheless the failure criteria has already been expressed in function of the effective pressure in order to derives its more general form. For the structural model, in absence of water, the Mohr Coulomb failure criteria can be equivalently written as

$$\tau_0 = p_s \, tg(\phi). \tag{3.15}$$

3.3 Continuous form

In this section the strong form of the equations used to solve the structural problem are obtained. Their derivations starts from considering the balance equations of the monolithic coupled problem together with the balance equations of the fluid part, already treated in Section 2.2.3.

The non-Newtonian variables and parameters are characterized by the s sub-index, being the model used for the calculation of the structural response.

3.3.1 Variables of the problem

The unknowns of the structural problem are

- $\mathbf{u}_s$ velocity of the structure.

- p_s total pressure of the structure;

- p'_s effective pressure of the structure defined as $p'_s = p_s - p$ (being p the water pressure defined in Chapter 2);

Other parameters are:

- ρ_s is the solid dry density of the porous material. Calling $\overline{\rho}_s$ the density of the single grain, its relation with ρ_s is

$$\rho_s = (1 - n)\overline{\rho_s} \tag{3.16}$$

where n is the porosity defined in equation 2.3. In the present work the structural material is treated as an incompressible fluid with constant density.

- $\tilde{\mu}$ is the dynamic apparent viscosity. Its definition has been already presented in the previous sections.

- μ_s is the dynamic viscosity of the yielded material (when Newtonian behavior is recovered).

3.3.2   Balance equations

The balance equations governing the structural model are represented by the Navier-Stokes equations for a non-Newtonian fluid.

The presented model has been developed both in Lagrangian and Eulerian framework. Hence the convective velocity $\mathbf{a}_s$ of the balance equation is defined in its more general form as

$$\mathbf{a}_s := \mathbf{u}_s - \mathbf{u}_s^M; \tag{3.17}$$

being $\mathbf{u}_s^M$ the mesh velocity. According to 3.17, $\mathbf{a}_s = \mathbf{0}$ for a Lagrangian framework (where $\mathbf{u}_s^M = \mathbf{u}_s$) and $\mathbf{a}_s = \mathbf{u}_s$ in an Eulerian one, where $\mathbf{u}_s^M = \mathbf{0}$ (as in the previous chapter).

Calling $\Omega_s \subset \mathbb{R}^d$ (where d is the space dimension) the structural domain in a time interval $(0, T)$, the modified Navier-Stokes equations are

$$
\begin{aligned}
\rho_s \partial_t \mathbf{u}_s + \rho_s \mathbf{a}_s \cdot \nabla^s \mathbf{u}_s + \nabla p'_s - 2\nabla \cdot \tilde{\mu} \nabla \mathbf{u}_s - \rho_s \mathbf{b} &= \mathbf{0} \text{ in } \Omega_s, \ t \in (0, T), \\
\nabla \cdot \mathbf{u}_s &= 0 \text{ in } \Omega_s, \ t \in (0, T),
\end{aligned}
\tag{3.18}
$$

The problem is fully defined with the following boundary and initial condition:

$$
\begin{aligned}
\mathbf{u}_s(\mathbf{x}, 0) &= \mathbf{u}_{s\,0}(\mathbf{x}) & \text{in} & \quad \Omega_s, \\
\mathbf{u}_s(\mathbf{x}, t) &= \mathbf{g}_s(\mathbf{x}, t) & \text{on} & \quad \partial\Omega_{s\,D}, \quad t \in (0, T), \\
\mathbf{n} \cdot \boldsymbol{\sigma}_s(\mathbf{x}, t) &= \mathbf{t}_s(\mathbf{x}, t) & \text{on} & \quad \partial\Omega_{s\,N}, \quad t \in (0, T),
\end{aligned}
\tag{3.19}
$$

The apparent viscosity $\tilde{\mu}$ can be either the one of the Bingham model (equation 3.11), or that of the variable yield one (equation 3.14).

3.4   Weak form

The weak form of equations 3.18 is obtained following strictly the same steps than it was done in Chapter 2 for the fluid problem. No relevant differences are present.
Using the Galerkin formulation the weak form of the general problem becomes

$$
\begin{aligned}
\int_\Omega \mathbf{w}\rho_s\partial_t\mathbf{u}_s d\Omega + \int_\Omega \mathbf{w}\rho_s\mathbf{a}_s\cdot\nabla\mathbf{u}_s d\Omega & \\
+\int_\Omega \mathbf{w}\nabla p'_s d\Omega - \int_\Omega \mathbf{w}\nabla\cdot 2\tilde{\mu}\nabla^s\mathbf{u}_s d\Omega - \int_\Omega \mathbf{w}\rho_s\mathbf{b}d\Omega &= \mathbf{0} \quad \forall\mathbf{w}\in\mathcal{V}, \qquad (3.20) \\
\int_\Omega q\nabla\cdot\mathbf{u}_s &= 0 \quad \forall q\in\mathcal{Q},
\end{aligned}
$$

where , for a fixed $t\in(0,T)$, $\mathbf{u}_s$ is assumed to belong to the velocity space $\mathcal{V}\in[\mathbf{H}^1(\Omega)]^d$ of vector functions whose components and their 1st derivatives are square-integrable, and p'_s belongs to the pressure space $\mathcal{Q}\in\mathbf{L}_2$ of square-integrable functions. $\mathbf{w}$ and q are velocity and pressure weight functions belonging to velocity and pressure space respectively.
Performing the integration by part of the pressure and the viscous terms as explained in Section 2.3 (see equations 2.37), gives

$$
\begin{aligned}
\int_\Omega \mathbf{w}\rho_s\partial_t\mathbf{u}_s d\Omega + \int_\Omega \mathbf{w}\rho_s\mathbf{a}_s\cdot\nabla\mathbf{u}_s d\Omega - \int_\Omega p'_s\nabla\cdot\mathbf{w}d\Omega & \\
+2\int_\Omega \nabla\mathbf{w}:\tilde{\mu}\nabla^s\mathbf{u}_s d\Omega - \int_\Omega \mathbf{w}\rho_s\mathbf{b}d\Omega - \int_{\partial\Omega_N} \mathbf{w}\cdot\mathbf{h}d\Gamma &= \mathbf{0} \quad \forall\mathbf{w}\in\mathcal{V}, \qquad (3.21) \\
\int_\Omega q\nabla\cdot\mathbf{u}_s d\Omega &= 0 \quad \forall q\in\mathcal{Q},
\end{aligned}
$$

Let $\mathcal{V}_h$ be a finite element space to approximate $\mathcal{V}$, and $\mathcal{Q}_h$ a finite element approximation to $\mathcal{Q}$. The problem is now finding $\mathbf{u}_{sh}\in\mathcal{V}_h$ and $p_{sh}\in\mathcal{Q}_h$ such that

$$
\begin{aligned}
\int_\Omega \mathbf{w}_h\rho_s\partial_t\mathbf{u}_{sh}d\Omega \int_\Omega \mathbf{w}_h\rho_s\mathbf{u}_{sh}\cdot\nabla\mathbf{u}_{sh}d\Omega - \int_\Omega p'_{sh}\nabla\cdot\mathbf{w}_h d\Omega & \\
+2\int_\Omega \nabla\mathbf{w}_h:\tilde{\mu}\nabla^s\mathbf{u}_{sh}d\Omega - \int_\Omega \mathbf{w}_h\rho_s\mathbf{b}d\Omega - \int_{\partial\Omega_N} \mathbf{w}_h\cdot\mathbf{t}_{sh}d\Gamma &= \mathbf{0} \quad \forall\mathbf{w}_h\in\mathcal{V}_h, \;(3.22) \\
\int_\Omega q_h\nabla\cdot\mathbf{u}_{sh}d\Omega &= 0 \quad \forall q_h\in\mathcal{Q}_h.
\end{aligned}
$$

3.5   The structural approach: monolithic solver

The procedure used for obtaining the algebraic stabilized system of equation is analogous to what has already been explained in Section 2.4 of Chapter 2. In the following sections the stabilization technique, the time integration scheme and the solution strategy are briefly described.

Since many aspects of the structural solver coincide to the element-based one, only the differences are pointed out to lighten the reader from useless repetitions.

In order to obtain the final solution system, the weak form represented by equations 3.22 have to be stabilized and linearized in time. Finally as well as for the fluid solvers, a quasi-Newton residual based strategy is adopted to solve the non linear problem.

3.5.1   Stabilized formulation

The choice of adopting equal order linear elements for velocity and pressure, despite of the simplicity, entails the necessity of using a stabilization technique. An ASGS stabilization technique is employed for that purpose. The derivation of the stabilization scheme is analogous to what has been presented in Section 2.4.1. Therefore, in what follows, only the final stabilized form and the stabilization terms is reported.

The stabilized form of the balance equations becomes

$$
\begin{aligned}
\int_\Omega \mathbf{w}_h \rho_s \partial_t \mathbf{u}_{s\,h} d\Omega \int_\Omega \mathbf{w}_h \rho_s \mathbf{a}_{s\,h} \cdot \nabla \mathbf{u}_{s\,h} d\Omega & \\
- \int_\Omega p'_{s\,h} \nabla \cdot \mathbf{w}_h d\Omega + 2 \int_\Omega \nabla^s \mathbf{w}_h : \tilde{\mu} \nabla \mathbf{u}_{s\,h} d\Omega & \\
- \int_\Omega \mathbf{w}_h \rho_s \mathbf{b}_s d\Omega - \int_{\partial\Omega_N} \mathbf{w}_h \mathbf{t}_{s\,h} d\Gamma + \sum_{el} \int_{\Omega^{el}} \tau_{s\,1} \mathcal{P}_s^m \cdot \mathcal{R}_s^m d\Omega &= \mathbf{0} \quad \forall \mathbf{w}_h \in \mathcal{V}_h, \\
\int_\Omega q_h \nabla \cdot \mathbf{u}_{s\,h} d\Omega + \sum_{el} \int_{\Omega^{el}} \tau_{s\,2} \mathcal{P}_s^c \cdot \mathcal{R}_s^c d\Omega &= 0 \quad \forall q_h \in \mathcal{Q}_h,
\end{aligned}
\tag{3.23}
$$

where $\mathcal{P}_s^m$, $\mathcal{R}_s^m$, $\mathcal{P}_s^c$ and $\mathcal{R}_s^c$ are defined in Table 3.1.

In a Lagrangian framework the convective term is not present. Therefore only pressure stabilization is required.

Momentum equation	
$\mathcal{P}_s^m(\mathbf{w}_h)$	$\mathbf{a}_{s\,h} \cdot \nabla \mathbf{w}_h + \nabla q_h$
$\tau_{s\,1}$	$\left(\dfrac{\alpha}{\Delta t} + \dfrac{4\tilde{\mu}}{h^2\,\rho_s} + \dfrac{2|\mathbf{a}_{s\,h}|}{h} \right)^{-1}$
$\mathcal{R}_s^m(\mathbf{u}_{s\,h})$	$\partial_t \mathbf{u}_{s\,h} + \mathbf{a}_{s\,h} \cdot \nabla \mathbf{u}_{s\,h} - \nabla \cdot \dfrac{\tilde{\mu}}{\rho_s} \nabla^s \mathbf{u}_{s\,h} + \nabla p'_{s\,h} - \mathbf{b}_s$
Continuity equation	
$\mathcal{P}_s^c(\mathbf{w}_h)$	$\nabla \cdot \mathbf{w}_h$
$\tau_{s\,2}$	$\dfrac{\tilde{\mu}}{\rho_s} + \dfrac{h|\mathbf{a}_{s\,h}|}{2}$
$\mathcal{R}_s^c(\mathbf{u}_{s\,h})$	$\nabla \cdot \mathbf{u}_{s\,h}$

Table 3.1: Stabilizing elemental terms in ASGS for the non-Newtonian element.

3.5.2 Discretization procedure

According to what was explained in Section 2.4.2 of Chapter 2, the matrix form of the stabilized system of equations 3.23 can be written as:

$$
\begin{bmatrix} \mathbf{M} + \mathbf{S}_{wu}^M & \mathbf{0} \\ \mathbf{0} & \mathbf{0} \end{bmatrix} \cdot \begin{bmatrix} \dot{\mathbf{u}}_s \\ \dot{\mathbf{p}}_s \end{bmatrix} + \begin{bmatrix} \mathbf{K} + \mathbf{S}_{wu} + \mathbf{S}^c & \mathbf{G} + \mathbf{S}_{wp} \\ \mathbf{D} + \mathbf{S}_{qu} & \mathbf{S}_{pq} \end{bmatrix} \cdot \begin{bmatrix} \mathbf{u}_s \\ \mathbf{p}_s \end{bmatrix} = \begin{bmatrix} \mathbf{F}_s + \mathbf{S}_w^f \\ \mathbf{S}_q^f \end{bmatrix}
\tag{3.24}
$$

where the operators are explicitly written in Table 3.2 and the stabilization operators can be found in Table 3.3.

3.5.3 Bossak time integration scheme

As in the fluid element-based solver, a Bossak time integration scheme is used to advance in time the momentum equations. For more details about the method see Section 2.4.3. Equations 3.24 can be written in compact form as

$$
\overline{\mathbf{M}}\dot{\mathbf{v}}_s + \mathbf{f}_{s\,int}(\mathbf{v}_s(t), t) = \mathbf{f}_{s\,ext}(t).
\tag{3.25}
$$

Matricial term		Continuum term
$\mathbf{M}\dot{\mathbf{u}}_s$		$\displaystyle\sum_{el}\int_{\Omega_{el}}\mathbf{w}_h\rho_s\partial_t\mathbf{u}_{s\,h}d\Omega$
	$\mathbf{K}^C\mathbf{u}_s$	$\displaystyle\sum_{el}\int_{\Omega_{el}}\mathbf{w}_h\rho_s\mathbf{a}_{s\,h}\cdot\nabla\mathbf{u}_{s\,h}d\Omega$
$\mathbf{K}\mathbf{u}_s$		
	$\mathbf{K}^{\tilde{\mu}}\mathbf{u}_s$	$\displaystyle+2\sum_{el}\int_{\Omega_{el}}\mathbf{w}_h\nabla\mathbf{w}_h:\tilde{\mu}\nabla\mathbf{u}_{s\,h}d\Omega$
$\mathbf{G}\mathbf{p}_s$		$\displaystyle-\sum_{el}\int_{\Omega_{el}}p_{s\,h}\nabla\cdot\mathbf{w}_hd\Omega$
$\mathbf{D}\mathbf{u}_s$		$\displaystyle\sum_{el}\int_{\Omega_{el}}q_h\nabla\cdot\mathbf{u}_{s\,h}d\Omega$
$\mathbf{F}_s$		$\displaystyle\sum_{el}\int_{\Omega_{el}}\mathbf{w}_h\rho_s\mathbf{b}_sd\Omega$
$\mathbf{h}_s$		$\mathbf{0}$

Table 3.2: Matrices and vectors of system 3.24 without stabilization terms.

Momentum equation	
Matricial term	Continuum term
$\mathbf{S}_{wu}^{M}\dot{\mathbf{u}}_{s}$	$\sum_{el}\int_{\Omega_{el}}\tau_{s1}\mathbf{a}_{s\,h}\cdot\nabla\mathbf{w}_{h}\partial_{t}\mathbf{u}_{s\,h}d\Omega$

$\mathbf{S}_{wu}\mathbf{u}_{s}$

$\mathbf{S}_{wu}^{C}\mathbf{u}_{s}$	$\sum_{el}\int_{\Omega_{el}}\tau_{s1}\mathbf{a}_{s\,h}\cdot\nabla\mathbf{w}_{h}\mathbf{a}_{s\,h}\cdot\nabla\mathbf{u}_{s\,h}d\Omega$
$\mathbf{S}_{wu}^{\tilde{\mu}}\mathbf{u}_{s}$	$-\sum_{el}\int_{\Omega_{el}}\tau_{s1}\mathbf{a}_{s\,h}\cdot\nabla\mathbf{w}_{h}\nabla\cdot\dfrac{\tilde{\mu}}{\rho_{s}}\nabla^{s}\mathbf{u}_{s\,h}d\Omega$
$\mathbf{S}_{wp}\mathbf{p}_{s}$	$\sum_{el}\int_{\Omega_{el}}\tau_{s1}\mathbf{a}_{s\,h}\cdot\nabla\mathbf{w}_{h}\nabla p_{s\,h}d\Omega$
$\mathbf{S}_{w}^{f}$	$-\sum_{el}\int_{\Omega_{el}}\tau_{s1}\mathbf{a}_{s}\,h\cdot\nabla\mathbf{w}_{h}\mathbf{b}_{s\,h}d\Omega$

$\mathbf{S}_{qu}\mathbf{u}_{s}$

$\mathbf{S}_{qu}^{C}\mathbf{u}_{s}$	$\sum_{el}\int_{\Omega_{el}}\tau_{s1}\nabla q_{h}\mathbf{a}_{s\,h}\cdot\nabla\mathbf{u}_{s\,h}d\Omega$
$\mathbf{S}_{qu}^{\tilde{\mu}}\mathbf{u}_{s}$	$-\sum_{el}\int_{\Omega_{el}}\tau_{1}\nabla q_{h}\nabla\cdot\dfrac{\tilde{\mu}}{\rho_{s}}\nabla^{s}\mathbf{u}_{s\,h}d\Omega$
$\mathbf{S}_{qp}\mathbf{p}_{s}$	$\sum_{el}\int_{\Omega_{el}}\tau_{s1}\nabla q_{h}\nabla p_{s\,h}d\Omega$
$\mathbf{S}_{q}^{f}$	$-\sum_{el}\int_{\Omega_{el}}\tau_{s1}\nabla q_{h}\mathbf{b}_{s\,h}d\Omega$

Continuity equation	
$\mathbf{S}^{c}\mathbf{u}_{s}$	$\sum_{el}\int_{\Omega_{el}}\tau_{s2}\nabla\cdot\mathbf{w}_{h}\nabla\cdot\mathbf{u}_{s\,h}d\Omega$

Table 3.3: Stabilization matrices and vectors of system 3.24.

The resulting residual of the momentum equations linearized in time is

$$
\begin{aligned}
\mathbf{r}_s(\mathbf{v}_s^{n+1-\alpha_B}) \;\; = \;\; & -\overline{\mathbf{M}}\left(\frac{1-\alpha_B}{\gamma\Delta t}\mathbf{v}_s^{n+1}\right) - \mathbf{f}_{int\,s}^{n+1} \\
& +\mathbf{f}_{ext\,s}^{n+1} - \overline{\mathbf{M}}\left[\frac{1-\alpha_B}{\gamma\Delta t}\mathbf{v}_s^n + \frac{(1-\alpha_B)^2}{\gamma}\dot{\mathbf{v}}_{\mathbf{s}}^n - \alpha_B\dot{\mathbf{v}}_{\mathbf{s}}^n\right],
\end{aligned}
\tag{3.26}
$$

where $\mathbf{v}_s^T = [\mathbf{u}_s,\ \mathbf{p}_s']$ and $\dot{\mathbf{v}}_s^T = [\dot{\mathbf{u}}_s,\ \dot{\mathbf{p}}_{\mathbf{s}}']$ are the vectors of unknowns.

Predictor multi corrector residual based strategy

The predictor multi corrector strategy adopted has been already explained in Section 2.4.3. The linearization of the non-linear terms is performed using a quasi Newton method.

The viscous terms as well as the convective ones are the non linear part of the balance equations. When calculating the LHS of equation 2.66, they are linearized as follows

$$
\mathbf{a}_s^{n+1,\,k}\nabla\mathbf{u}_s^{n+1,\,k+1},
$$

and

$$
\left[\mu + \frac{{p_s'}^{n+1,\,k}\,tg(\phi)}{\dot{\gamma}^{n+1,\,k}}\left(1 - e^{m\,\dot{\gamma}^{n+1,\,k}}\right)\right]\nabla^s\mathbf{u}_s^{n+1,\,k+1}.
$$

3.6 Kinematic framework of the non-Newtonian structural element

The structural model is implemented in order to allow both an Eulerian and a Lagrangian kinematic description of motion.

The Eulerian formulation described in the previous sections has been developed in order to validate the Bingham model with some benchmarks found in literature (see for example Sections 3.8.1, 3.8.2 and 3.8.3).

It important to recall that the final purpose of this work is to couple this model with the fluid code and simulate the deforming process of a semi-saturated rockfill slope when failing. Therefore, since the structural domain is expected to undergo severe deformations as the failure progresses, the kinematic model has to adapt dynamically

to such deformations leading to the preferable choice of a Lagrangian approach. Among many possible Lagrangian methods, the Particle Finite Element Method (PFEM) has been chosen and implemented for its flexibility and reliability [75, 100].

3.7 The particle finite element method (PFEM)

The PFEM is a numerical method that uses a Finite Element mesh to discretize the physical domain and to integrate the differential governing equations (see [67, 75]). In PFEM the domain is modeled using an Updated Lagrangian Formulation. That is all the variables are assumed to be known in the current configuration at time t and they are brought in the next (or updated) configuration at time $t + dt$. The finite element method (FEM) is used to solve the continuum equations in a mesh built up from the underlying nodes (the particles). This is useful to model the separation of solid particles from the bed surface and to follow their subsequent motion as individual particles with a known density, an initial acceleration and a velocity subject to gravity forces [97, 100]. It is important to underline that in PFEM each particle is treated as a material point characterized by the density of the solid domain to which it belongs to. The global mass is obtained by integrating density at the different material points over the domain. The quality of the numerical solution depends on the discretization chosen as in the standard FEM. Adaptive mesh refinement techniques can be used to improve the solution in zones where large gradients of the fluid or the structure variables occur.

Since its first development especially focused on the simulation of free surface flows and breaking waves [67, 75], PFEM has been successfully used in a wide range of fields. Just to mention some of them, it is used in FSI and coupled problems [68, 95, 98, 99, 110], multi-fluid problems [65, 84], contact problems [22, 23], geotechnical simulations [23, 94] and fire engineering [19]. Moreover PFEM has also been successfully used in the implementation of Bingham plastics model for the simulation of landslides [46] and cement slump tests [45].

The basic ingredients of PFEM can be summarized in:

- An **Updated Lagrangian** kinematical description of motion;

- A fast **remeshing** algorithm;

- A boundary recognition method(**alpha-shape**);

- **FEM** for the solution of the governing equations;

3.7.1   Updated Lagrangian kinematical description of motion

The PFEM was conceived as a Lagrangian method to treat CFD problems including free surface flows and breaking waves [67, 100]. This approach is in contrast with the classical Eulerian way to treat CFD problems.

Lagrangian algorithms are traditionally used in structural mechanics where each node of the computational mesh follows the associated material particle evolution. This is a good way to trace easily the interface between fluid and structure and to consider materials with history-dependent constitutive relations. Its weakness is the inability to follow large distortions of the domain without the necessity of a continuum remeshing. This implies a difficult parallelization of the code as well.

Eulerian algorithms, on the other hand, are largely used in fluid dynamics because of the ease way to follow large movements. In this case the computational mesh is fixed and the continuum moves with respect to the grid. Being a fixed mesh approach, an interface tracking technique should be employed in Eulerian methods to follow the evolution of the free surface (see Section 2.6 for more information on the topic).

A third popular technique is a generalization of the two kinematical description of motion above described. It is known as the *Arbitrary Lagrangian- Eulerian* (ALE) description. In this case, the mesh is arbitrarily moved with a velocity $\mathbf{u}_M$ and the domain of the mesh is called the *reference domain* [51].

For $\mathbf{u}_M^T \equiv (0,0,0)$ an Eulerian configuration is recovered and the reference domain corresponds to the spatial one. Alternatively, if the mesh velocity coincides with the particle velocity ($\mathbf{u}_M \equiv \mathbf{u}$), then the convective term disappears and the Lagrangian formulation is recovered. In this case the reference domain coincides with the material one. The absence of the convective term in a Lagrangian framework, leads also to the elimination of the problems connected with convection dominating processes (see Section 2.4.1 of Chapter 2), simplifying the stabilization procedure.

According to [51], three possible Lagrangian formulations are possible

- The *total Lagrangian* , where variables are described in the initial configuration Ω_0, at time t_0;

- The *updated Lagrangian* , where variables are described in the current configuration Ω^n, at time t^n;

- The *end of step Lagrangian* , where variables are described in the configuration Ω^{n+1} at time t^{n+1}.

The *total Lagrangian* formulation is not the best choice for a problem with large domain deformations. Therefore, PFEM uses an *updated Lagrangian* description of motion.

3.7.2 Remeshing algorithm

The need of an efficient remeshing algorithm together with the the difficulty of parallelizing this procedure are the biggest drawback of a Lagrangian approach.

The mesh moves in accordance to the material points and large deformations occur. The code developed in this work uses external libraries to remesh the domain. They are the *TetGen* and *Triangle* for the 2D and the 3D cases respectively (for more information see [5]).

The mesh generation scheme is based on the Voronoi diagrams[1] and the Delaunay tessellation[2].

3.7.3 Boundary recognition method: alpha - shape method

Once the continuum domain is partitioned using the TetGen library, a criteria is needed to define the free surfaces and the boundaries on the material domain. In the case of PFEM, *alpha shape* [20] is the adopted technology.

Each node i of the domain has its own dimension h_i determined as the average distance of node i from its neighbors. In the same way, an elemental dimension h_{el} can be defined for each element as the average of the h_i of its nodes. Finally depending on the precision wanted, an α custom parameter greater but close to one (the alpha shape parameter) is defined.

If the radius of the sphere that circumscribes the element (r) is bigger than $\alpha \cdot h_{el}$, then the element is eliminated (see Figure 3.4). That is

---

[1] The *Voronoi diagram* of a set N is a partition of $\mathbb{R}^3$ into region V_i (closed and convex or unbounded), where each region V_i is associated with a node p_i, such that any point in V_i is closer to p_i than to any other node p_j. The Voronoi diagram is unique.

[2] A *Delaunay tessellation* within the set N is a partition of the convex hull Ω of all the nodes into region Ω_i such that $\Omega = \Omega_i$ where each Ω_i is the tetrahedron defined by 4 nodes of the same Voronoi sphere. A *Voronoi sphere* within the set N is any sphere, defined by 4 or more nodes, that contains no other node inside. Such sphere are otherwise known as empty circumspheres. The Delaunay triangulation and Voronoi diagram in $\mathbb{R}^2$ are dual to each other in the graph theoretical sense.

$$r \leq \alpha \cdot h_{el};   \qquad (3.27)$$

has to be respected to keep the element in the domain.

Different values of the alpha shape parameter can lead to different accuracy on the mesh boundaries as shown in Figure 3.4(c) and 3.4(d) where different values of the alpha parameter are used.

(a) Cloud of nodes.

(b) Mesh of the convex hull obtained with the *Triangle* library.

(c) Domain after applying alpha shape. $\alpha = \alpha_1$.

(d) Domain after applying alpha shape. $\alpha_2 > \alpha_1$.
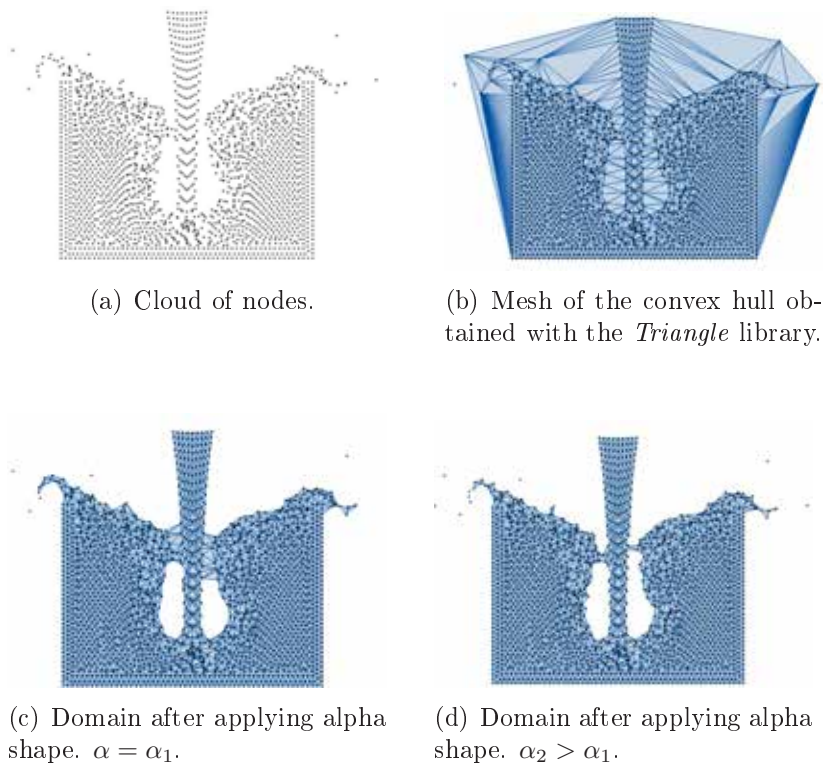
Figure 3.4: Possible boundaries of a cloud of nodes using alpha shapes method. Image taken from [20].

3.7.4   FEM

A finite element mesh and the connectivities of the nodes are provided by the previous described steps for the actual time step t^{n+1}. The studied FEM is then used to write the weak form of the governing equations.

3.7.5   PFEM algorithm

Considering known the solution at time step n, the basic steps of PFEM algorithm are summarized in the box that follows.

PFEM algorithm

1. Imposition of mesh velocity at time step n $\mathbf{u_{s\,M}} = \mathbf{u^n}$;

2. **Laplacian smoothing** [a] (free surface kept fixed);

3. **Remesh** (see Section 3.7.2);

4. **Solve** the monolithic system;

5. Back to step 1.

---

[a]The *Laplacian smoothing* is a geometrical technique that allows a more homogeneous redistribution of the nodes inside the analysis domain without changing the connectivities between nodes

---

3.8   Numerical Examples

3.8.1   The Couette flow

The Couette flow refers to the laminar flow of a viscous fluid between two parallel infinite plates separated by a given distance, one of which is moving relative to the other. The flow is driven by virtue of viscous drag force acting on the fluid and the applied pressure gradient parallel to the plates.

The model

The length of the computational domain is $6m$ and its height is $1m$ as shown in Figure 3.5. The Neumann boundary conditions are applied on the vertical edges in terms of external pressure. Dirichlet conditions are then applied on the horizontal edges (the plates). The lower plate is considered fixed, whereas the upper moves with a constant horizontal velocity. The horizontal velocity diagram in the central vertical section is analyzed.
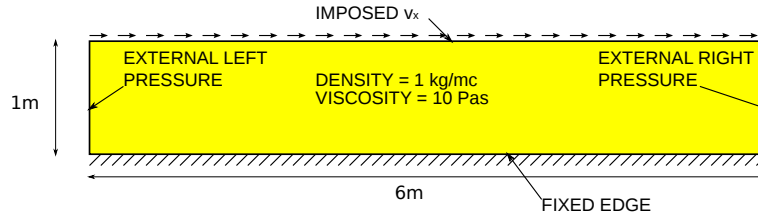
Figure 3.5: Geometrical data and boundary conditions.
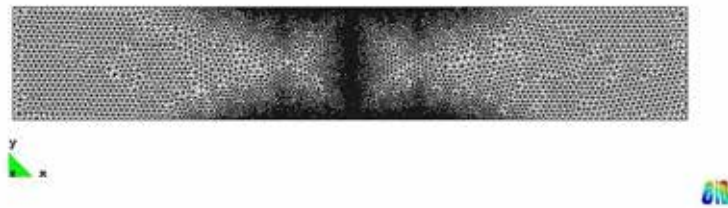
Figure 3.6: Linear triangular mesh used in the calculation.

The mesh used in every model is shown in Figure 3.6. It has 14736 linear triangular elements. Their dimension varies from $0.05m$ at the sides to $0.01m$ in the central vertical section.

The numerical results

In all the numerical examples the value of m and τ_0 are kept constant as well as the properties of the material. They are summarized in Table 3.4.

Density	ρ_s	$1 kg/m^3$
Fluidified viscosity	μ	$10 Pa\,s$
Smoothing coefficient	m	$300s$
Yield stress	τ_0	$10 Pa$

Table 3.4: Couette example. Material properties.

Figure 3.7 shows the used regularized approximation in comparison with the bilinear form.

The difference between the effects of a positive pressure gradient (adverse to the velocity field) and a negative one (favorable to the velocity field) are shown in Figure 3.9. In both
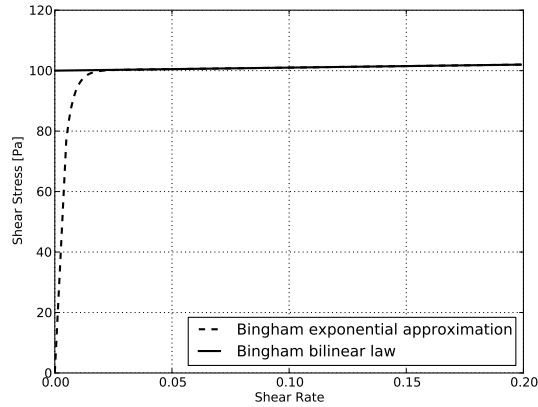
Figure 3.7: Exponential approximation with m=300 and $\tau_0 = 100 Pa$.

cases an increasing gradient of pressure is taken into account. The velocity of the upper plate is $u_x = 0.5 m/s$. The gradient of velocity is higher close to the plate. Consequently the value of tangential stress is also higher in these zones that are the regions where the yield stress is achieved. The central straight zone is the *unyielded* region where $\dot{\gamma} = 0$ and $\tilde{\mu} = \mu + \tau_0 \cdot m$. The viscosity behavior in the central vertical section is shown in Figure 3.8
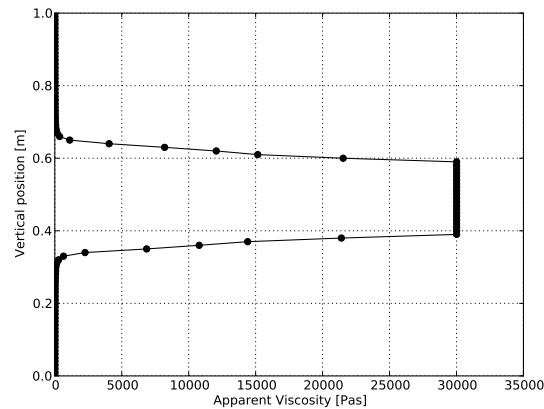
Figure 3.8: Variation f viscosity in the central vertical section.

Increasing the gradient of pressure the rigid *plateau* is narrowing and the yielded zone is increasing.

Finally, the upper velocity is set to $u_x = 0.01 m/s$ to reproduce the results of [105] and to have a direct comparison with the analytical results as shown in Figure 3.10.

(a) Negative Pressure Gradient   (b) Positive Pressure Gradient
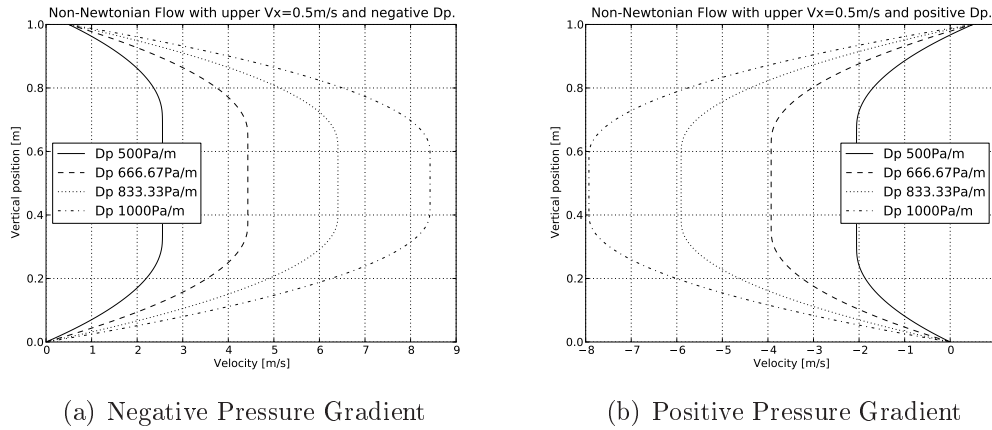
Figure 3.9: Velocity diagrams for different values of the gradient of pressure. Upper horizontal velocity 0.5m/s.

Different values of negative gradients of pressure are considered as shown in Figure 3.10. Right edge external pressure is kept constant and equal to $0Pa$ in all the cases, whereas the left hand side pressure is $1500Pa$, $1600Pa$, $1700Pa$, $1800Pa$, $1900Pa$ and $2000Pa$ respectively. The agreement is good and the yield point is reproduced correctly for all the pressure gradients.
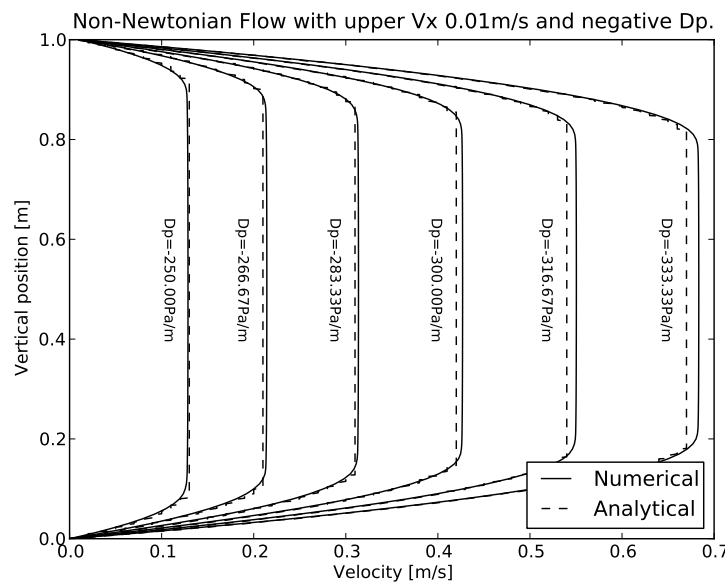
Figure 3.10: Velocity diagrams for different values of a negative gradient of pressure. Upper horizontal velocity 0.01m/s.

3.8.2 Cavity flow

(a) Homogeneous mesh.   (b) Locally refined mesh.
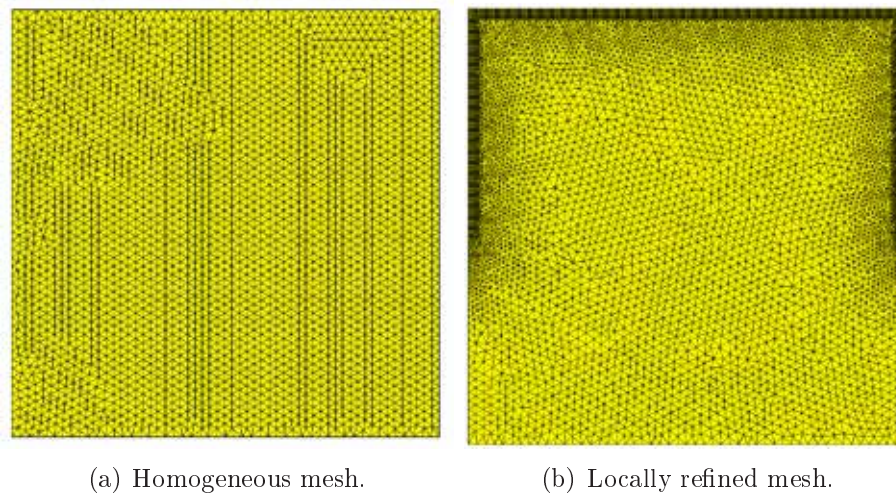
Figure 3.11: Cavity example. Meshes used in the calculation.

In the present section the Bingham model is tested in the classical cavity flow example. This benchmark applied to non-Newtonian fluids, and particularly Bingham plastics, has been widely studied in recent years and many examples can be found in the literature (see for instance [55, 59, 85, 129]).

A square unit domain with edge H is defined and the characteristic speed (that is, the velocity of the lid) is taken equal to $1m/s$.

The dynamic viscosity is $\mu_s = 1Pa\,s$ and density is $\rho_s = 1kg/m^3$.

Let us define the a dimensional Bingham number (Bn) as

$$Bn = \frac{\tau_0 H}{\mu_s u_s}, \tag{3.28}$$

where H and u_s are the edge length and the horizontal velocity of the upper lid respectively and τ_0 the yield stress.

In order to make a comparison to the work of Mitsoulis and Zisis [85], the model is tested for different values of Bn. In other words, the effect of the increasing yield stress is analyzed (being in the specific case $Bn = \tau_0$).

(a) Homogeneous mesh.   (b) Locally refined mesh.
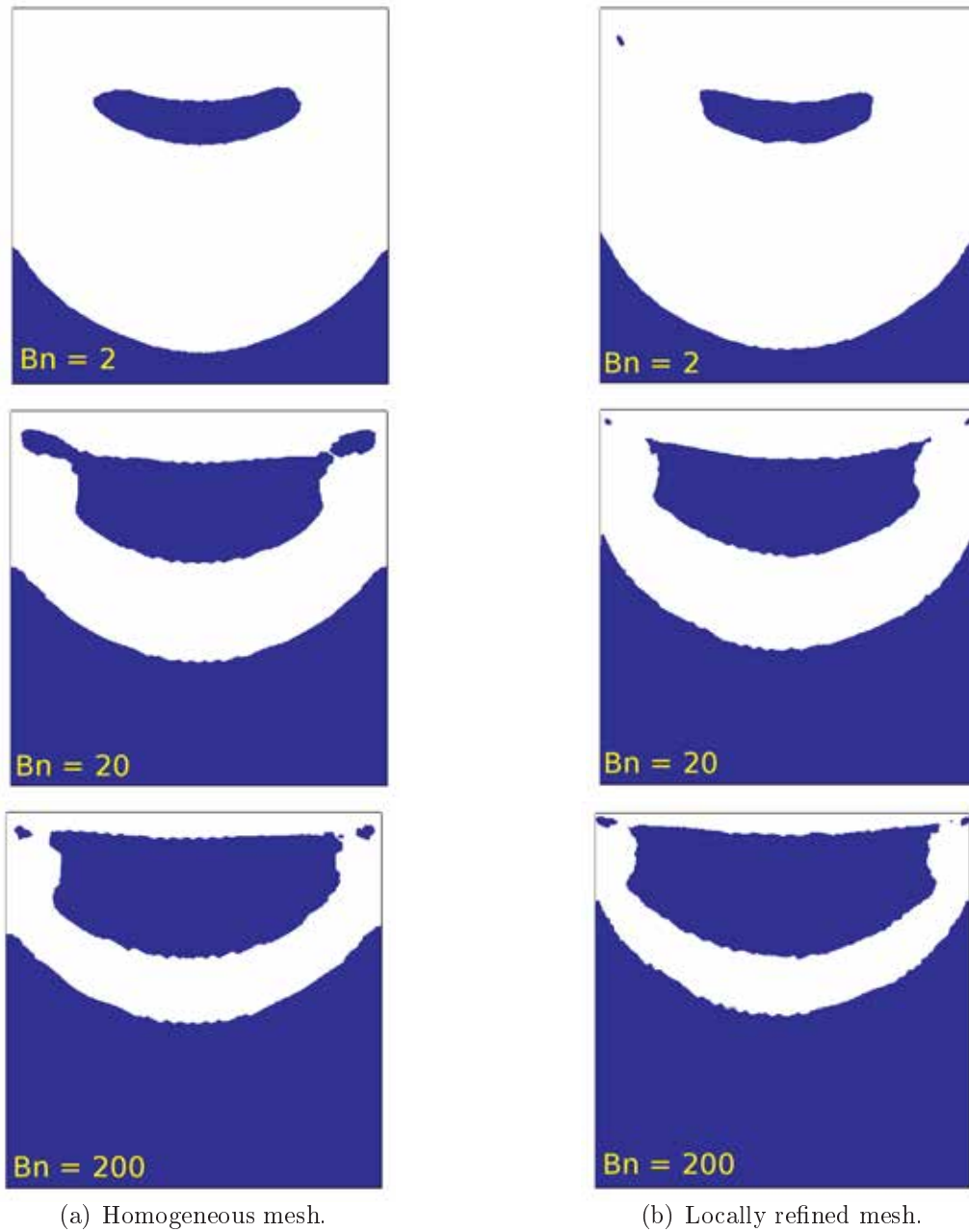
Figure 3.12: Cavity. White color shows the yielded regions. Comparison between the case with homogeneous mesh (Figure 3.11(a)) and the refined one (Figure 3.11(b)).

(a) Homogeneous mesh.　　　　　　　　(b) Locally refined mesh.
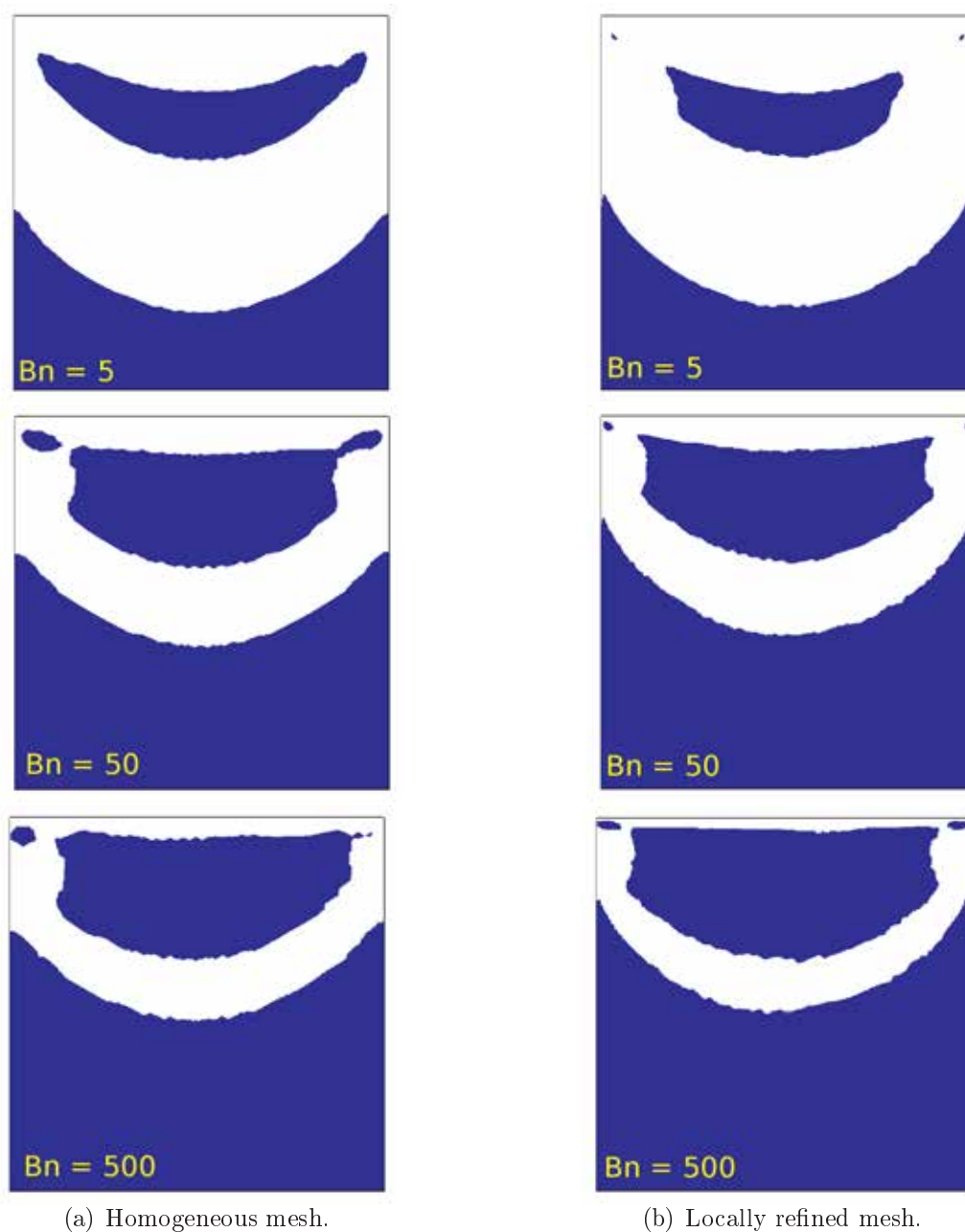
Figure 3.13: Cavity. White color shows the yielded regions. Comparison between the case with homogeneous mesh (figure 3.11(a)) and the refined one (figure 3.11(b)).

(a) Results taken from [85].

(b) Present model. Locally refined mesh.
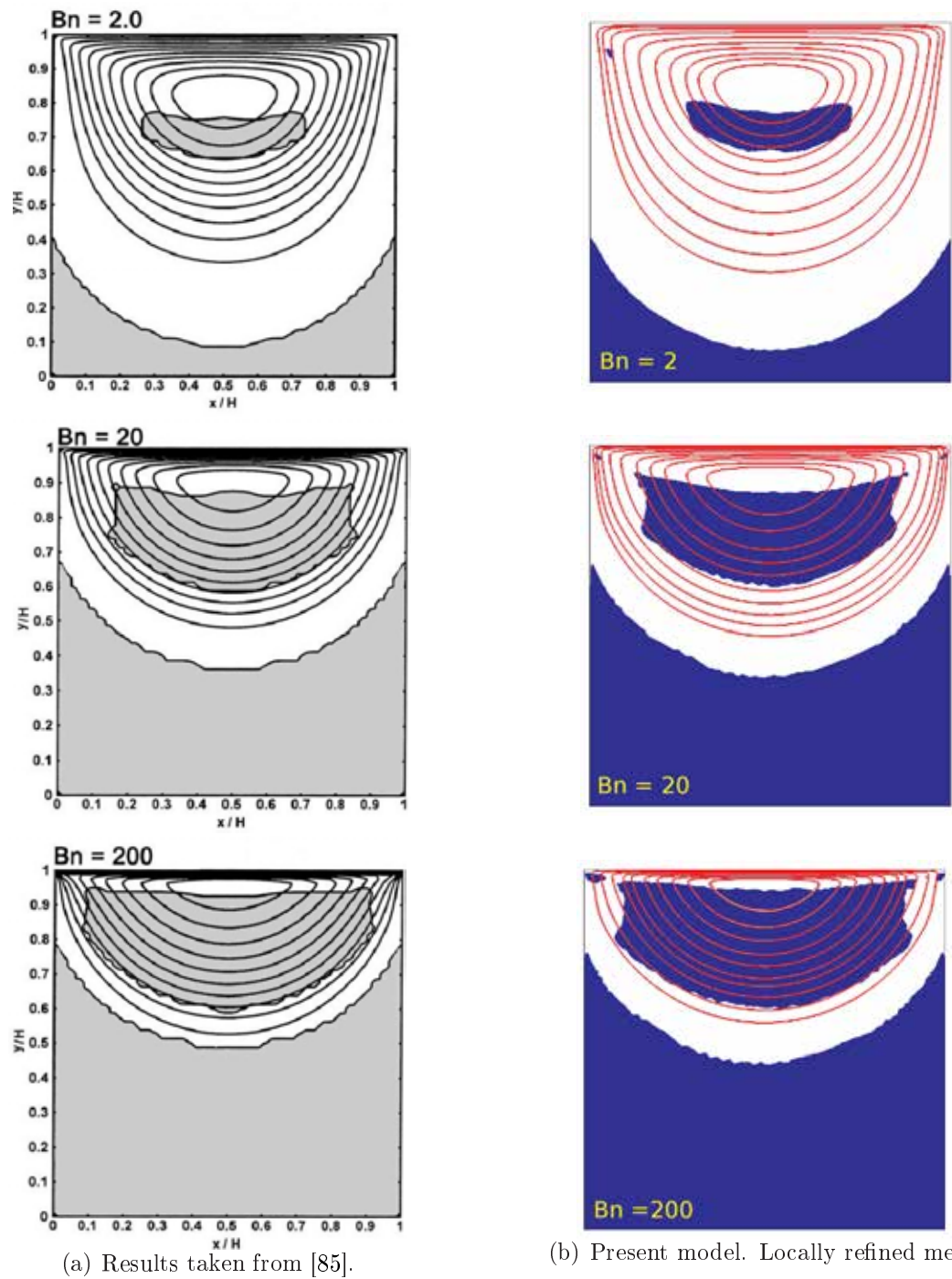
Figure 3.14: Cavity example. Streamlines and progressive evolution of the yielded area (white color) for increasing values of the Bingham number Bn ($Bn = 2, 20$ and 200 respectively).
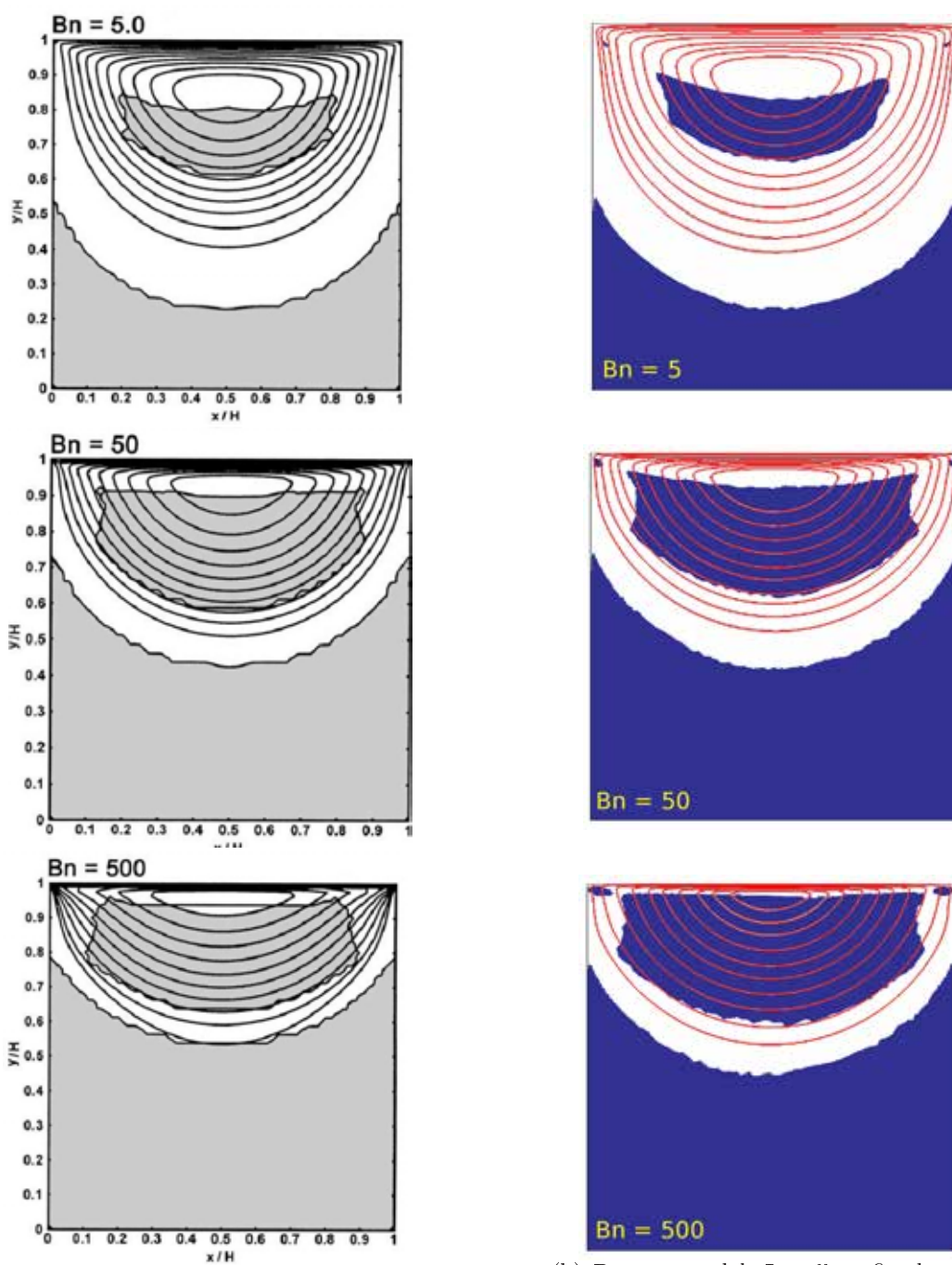
(a) Results taken from [85].

(b) Present model. Locally refined mesh.

Figure 3.15: Cavity example. Streamlines and progressive evolution of the yielded area (white color) for increasing values of the Bingham number Bn ($Bn = 5, 50$ and 500 respectively).

The choice of the mesh is crucial and can influence relevantly the correct definition of the yielded region. The adoption, for example of an homogeneous mesh with average dimension $h = 0.02m$, like the one shown in Figure 3.11(a) can be in some cases insufficient for the correct capturing of the rigid parts of the domain. This is shown in Figures 3.12 and 3.13 where the comparison of the yielded regions for increasing values of the Bn is shown for the homogeneous mesh of Figure 3.11(a) (left column) and the mesh shown in Figure 3.11(b) where a local refinement of $h_{ref} = 0.005m$ is performed on the lid and in the upper part of the vertical edges of the cavity (right column). The use of the mesh with local refinement leads to more precise results, according to [55, 85, 129]. In fact the direct comparison of the yielded regions and the streamlines results of the present model is in good agreement with the one in [85], as shown in Figures 3.14 and 3.15.

3.8.3 Extrusion process
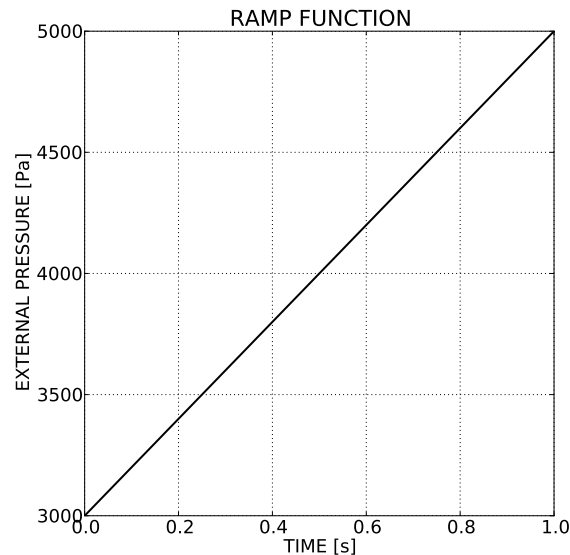
Figure 3.16: Extrusion example. Ramp function of external pressure BC applied on left vertical side.

The present example simulates an extrusion process of a Bingham plastic. Data and geometry are taken from [105]. A material with the characteristics detailed in Table 3.5 is pushed into a square die with a restriction of two-thirds of the cross sectional area.

Due to the symmetry of the problem, only half of the domain is calculated as shown in Figure 3.17. An increasing value of the external pressure (p_{ext}) is imposed on the left side with a pressure increment of $2Pa/step$ (the ramp function for applying the external boundary pressure is detailed in Figure 3.16). On the right side the external pressure is set to zero and kept constant. The walls are assumed to be frictionless.
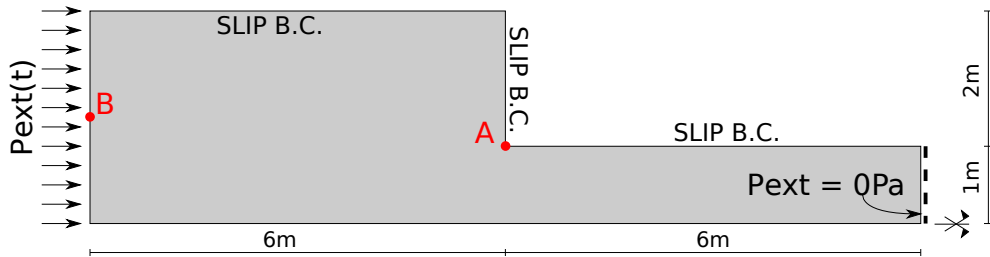
Figure 3.17: Extrusion example. Geometry and boundary conditions.
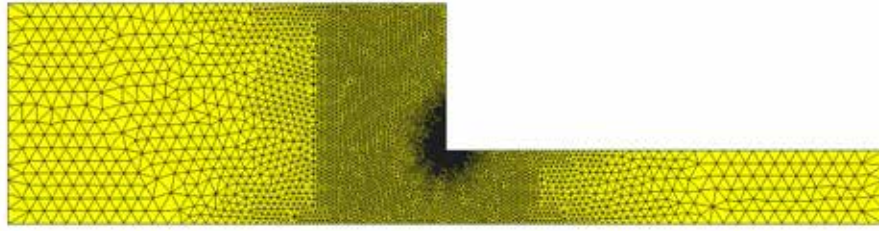
Figure 3.18: Extrusion example. Mesh used in the calculation. Average dimension $h = 0.2m$ with a local refinement $0.05m$ near point B of Figure 3.17 and in the restriction area and an additional refinement $0.005m$ close to point A of Figure 3.17. The total number of triangular elements and nodes are $11\,600$ and $5\,800$, respectively.

The mesh used in the calculation is shown in Figure 3.18. It is refined in the area of appearance of the slip lines to accurately catch their evolution.

As explained in [105], in the hypothesis of perfect plasticity, the value of maximum ram pressure (p_{ext}^{max}) is analytically calculated in [82]. It is given by the following relation

$$p_{ext}^{max} = \frac{4}{3} \left[1 + \frac{\pi}{2} \right] \tau_0 = 3426.7 Pa. \tag{3.29}$$

This is the analytical yield pressure, which corresponds numerically to the time interval between the onset of the slip line an its full development. In the present model this is represented by the interval in which the external pressure is between $3418Pa$ (beginning of the formation of the slip line) and $3472Pa$ (the slip line is fully formed). The analytical

value is therefore contained between these two extremes. In the Figures 3.19 and 3.20 the evolution of the slip lines is plotted and compared with the results shown in [105]. According to this paper, a contour fill of the equivalent strain rate $\dot{\gamma}$ is plotted in the range $0.08s^{-1} - 0.72s^{-1}$ and white and the dark area indicate values of $\dot{\gamma}$ lower than $0.08s^{-1}$ (rigid material), and larger than $0.72s^{-1}$ respectively (these two limits are chosen for homogeneity with [105]).

Density	ρ_s	$100kg/m^3$
Fluidified viscosity	μ	$10^{-6}Pa\,s$
Smoothing coefficient	m	$1000s$
Yield stress	τ_0	$1000Pa$

Table 3.5: Extrusion example. Material properties.

On the other hand, the yield pressure can be identified plotting the pressure-velocity graph in point B as shown in Figure 3.21. It can be observed that the material is almost rigid till reaching an external pressure value of $3418Pa$. After that, conserving the same external pressure increment per step, the velocity increases considerably indicating that the material starts to flow. Similar results are found in [105].

3.8.4 Bingham vs variable viscosity model. Pushed slope

The difference between the Bingham and the proposed variable yield model can be observed in this example.

A square domain in $2D$ and a cubic one in $3D$ are pushed towards a wall.

The geometry of the models and the mesh used in both cases is shown in Figure 3.22. The wall on the left side moves with constant velocity $u_0 = 0.1m/s$-

For the Bingham model the yield stress is $\tau_0 = 1000Pa$, whereas in the variable yield model the internal friction angle is $\phi = 30$.

In the sequences of the pushing process shown in Figure 3.23 and 3.24 the different behavior of the two models is evident.

For Bingham plastics, those points that do not exceed the constant yield threshold behave like a rigid body, whereas in the present model the yield stress of the exterior

Figure 3.19: Extrusion example. Evolution of the slip lines shown with a contour fill of the equivalent strain rate $\dot{\gamma}$. Comparison between the present model (left column) and the results presented in [105] (right column).

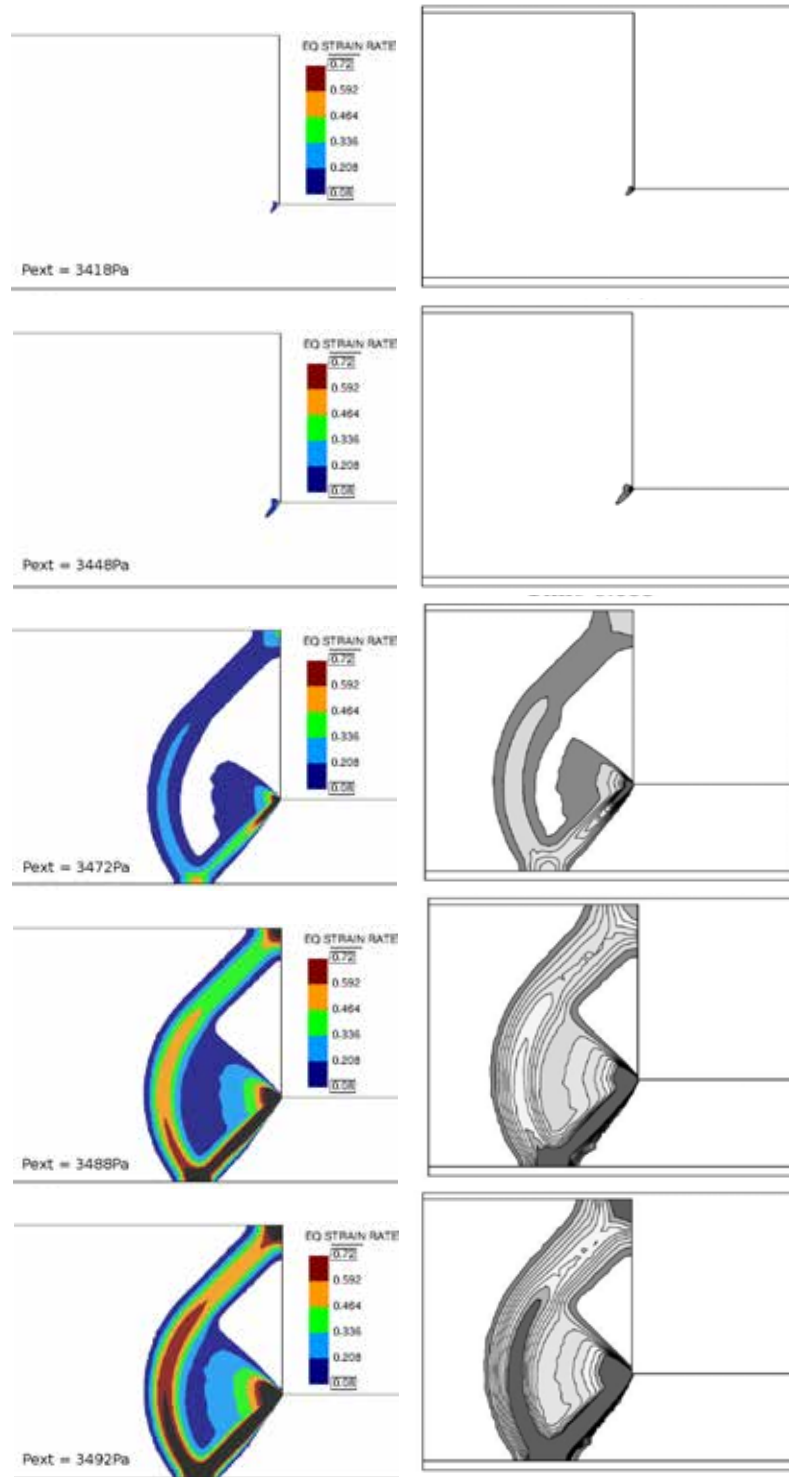Figure 3.20: Extrusion example. Evolution of the slip lines shown with a contour fill of the equivalent strain rate $\dot{\gamma}$. Comparison between the present model (left column) and the results presented in [105] (right column).
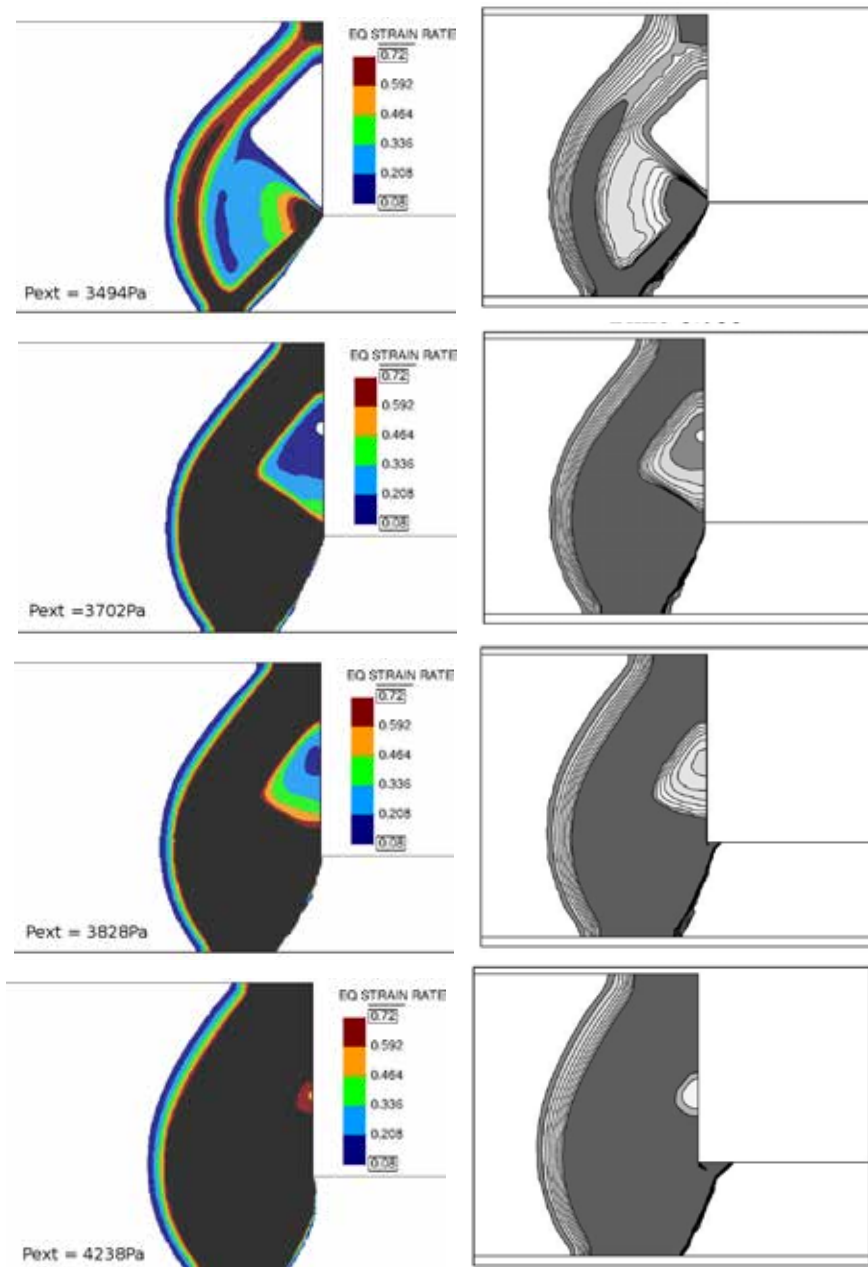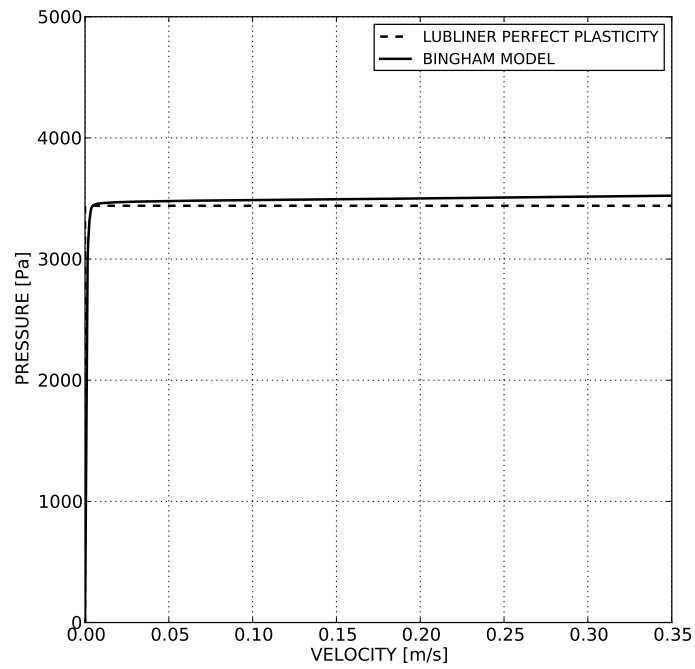
Figure 3.21: Extrusion example. Pressure-velocity relationship on point B.

(a) 2D

(b) 3D
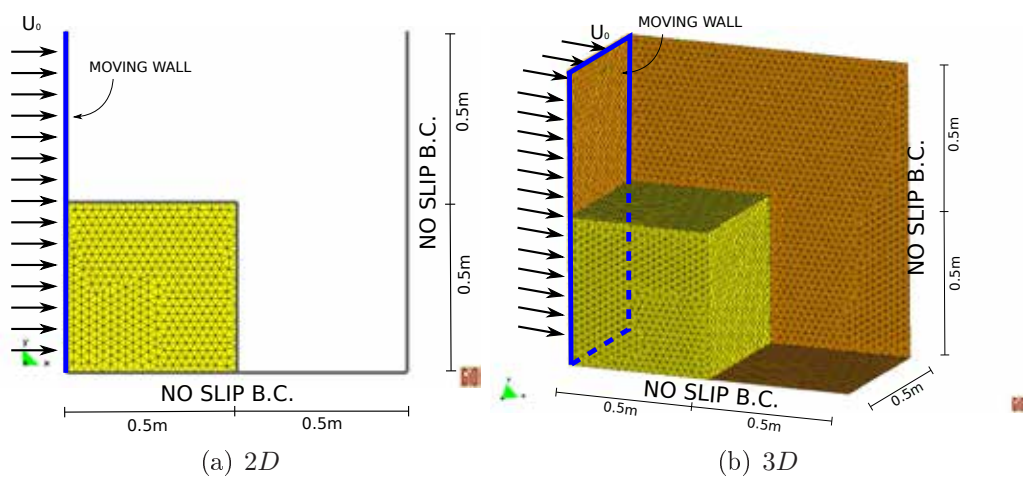
Figure 3.22: Pushed slope example. Geometry, mesh and boundary conditions of 2D and 3D models.

Dry density	ρ_s	$1000 kg/m^3$
Fluidified viscosity	μ	$10^{-6} Pa\,s$
Smoothing coefficient	m	$3000s$

Table 3.6: Pushed slope example. Material properties.

points is lower and it is exceeded also for lower pressure levels. Two different phases can be identified in the present example:

- *The settlement phase.* It is the initial part of the example. The granular material is left free to fall and to reach its stable configuration. It goes from the beginning of the example to the moment in which the material touches the right fixed wall.

- *The squeezing phase.* It begins when the material touches the right wall and starts to be squeezed between the two opposite walls that are getting closer.

In Figure 3.23 the $2D$ comparison between the Bingham model and the variable yield model during the settlement phase is shown. The contour fill of the equivalent strain rate is plotted in different time instances (the blue color indicates $\dot{\gamma} = 0$).

The Bingham model shows a sliding surface where the tangential stress reaches the yield stress ($1000Pa$), whereas all the rest of the model shows an almost rigid behavior. Conversely, in the variable yield model, if a node has a tangential stress which exceed its pressure times the friction angle tangent ($p_s tg\phi$), it shows a drop in the viscosity and it starts flowing. The main differences can be observed on the "free surface" where the yield stress tends to zero the closer the node is to the free surface (where the pressure is zero), i.e. no resistance is present. The variable yield material reaches a stable configuration that respects the internal friction angle of 30°. For more details the consultation of Section 3.8.5 is recommended.

In Figure 3.24 the behavior of the two models in the squeezing phase is compared. The sequence shows how the equivalent strain rate $\dot{\gamma}$ is almost zero up to the creation of the failure lines and the subsequent collapse of the material. In the granular material on the contrary, the "free surface" has zero pressure, which implies zero resistance and as soon as the material reaches the height of the walls it starts falling.

The same considerations can be done in $3D$, looking at the comparison between the two models in the settlement and the squeezing phase shown in Figures 3.25 and 3.26,

(a) Bingham model.   (b) Variable yield model.
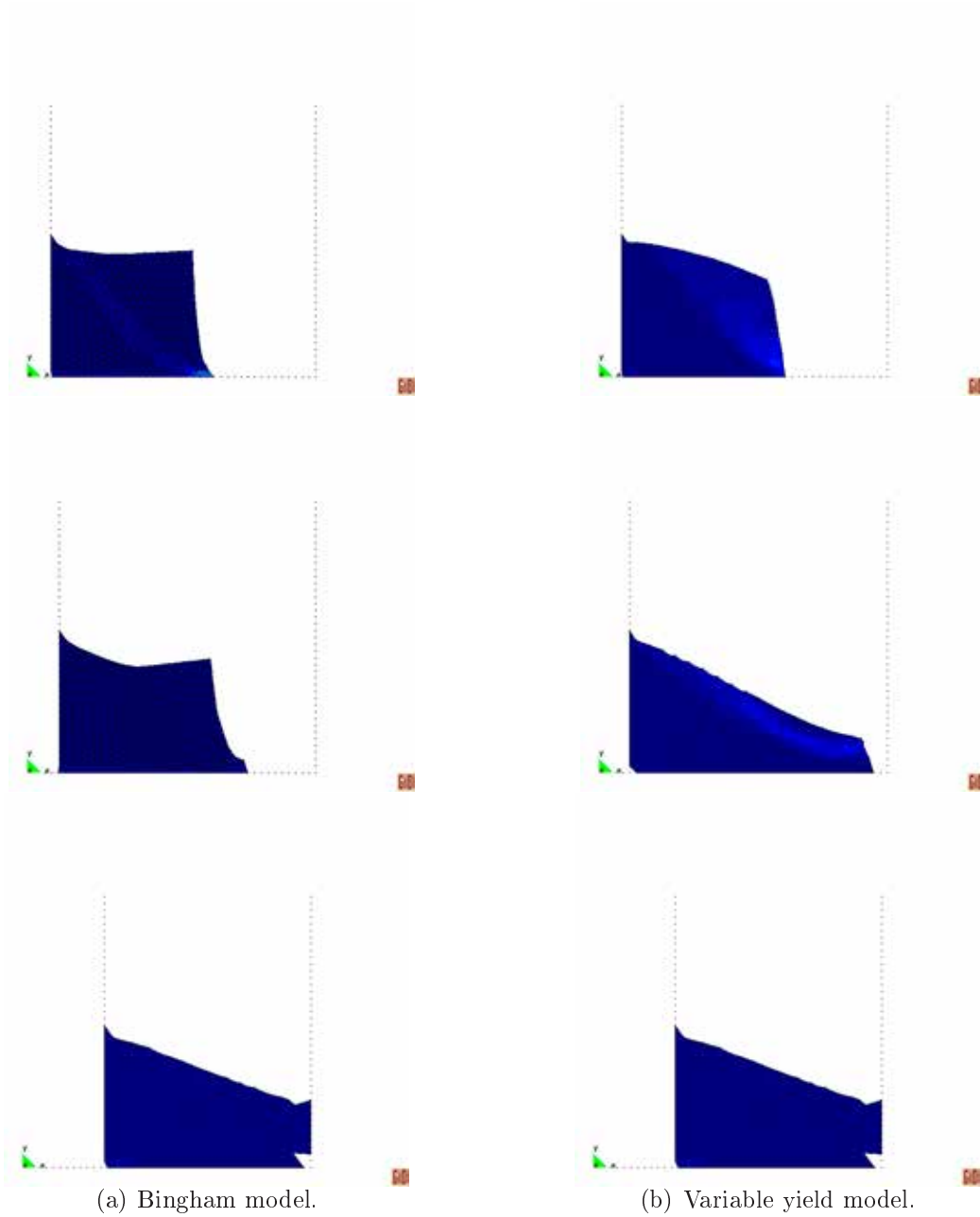
Figure 3.23: $2D$ pushed slope. $\dot{\gamma}$ in the initial pushing phase. Difference between the Bingham and the variable viscosity models.

respectively. The Bingham model in $3D$ shows less resistance in the squeezing phase due to the 3-dimensional effects. It is finally interesting to observe that the material which is falling down in the case of the Bingham model conserves the velocity imposed

(a) Bingham model.   (b) Variable yield model.
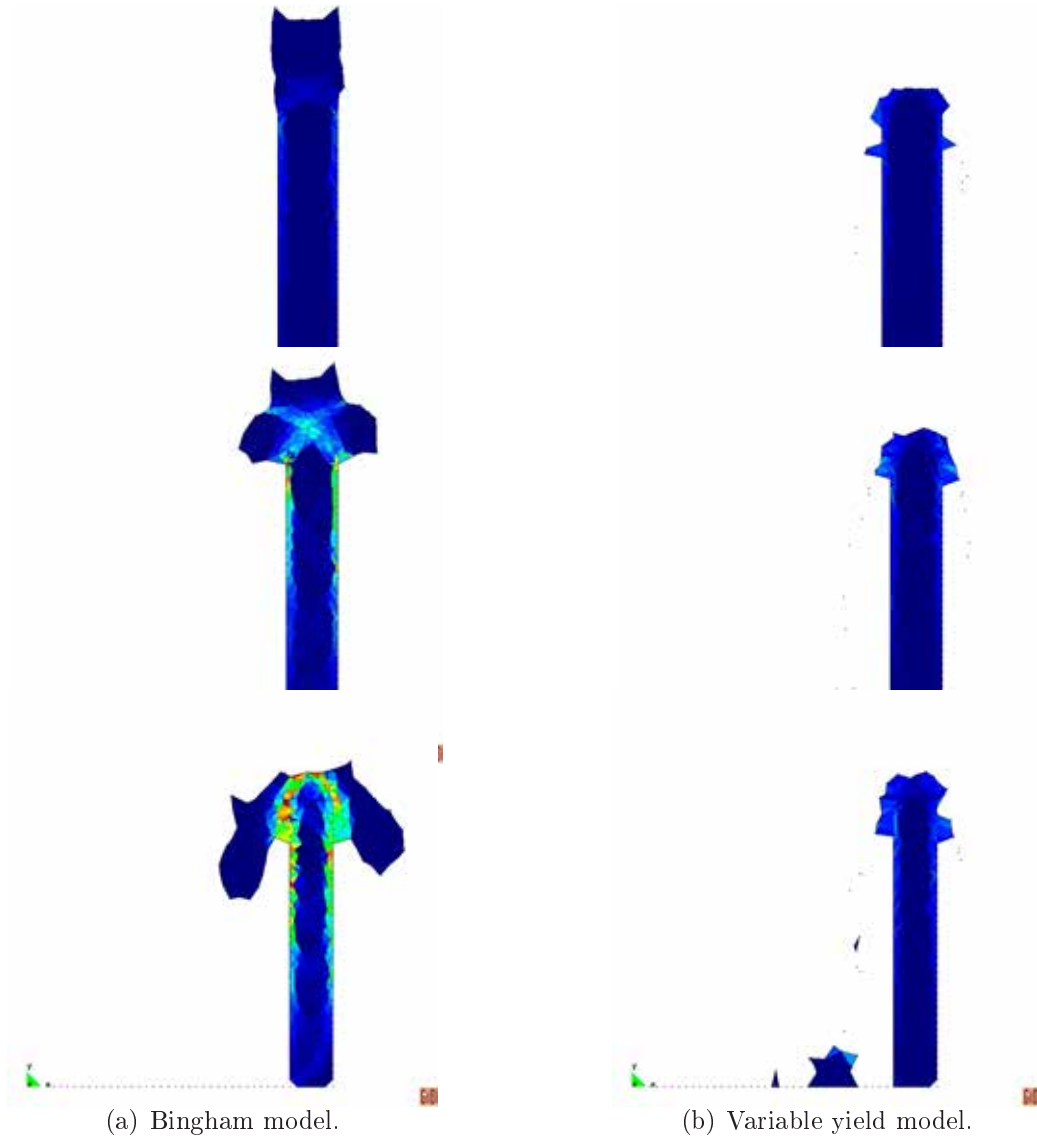
Figure 3.24: $2D$ pushed slope. $\dot{\gamma}$ in the squeezing phase. Difference between the Bingham and the variable viscosity models.

by the wall although this is very low, whereas this does not happen in the variable yield model.

(a) Bingham model. (b) Variable yield model.
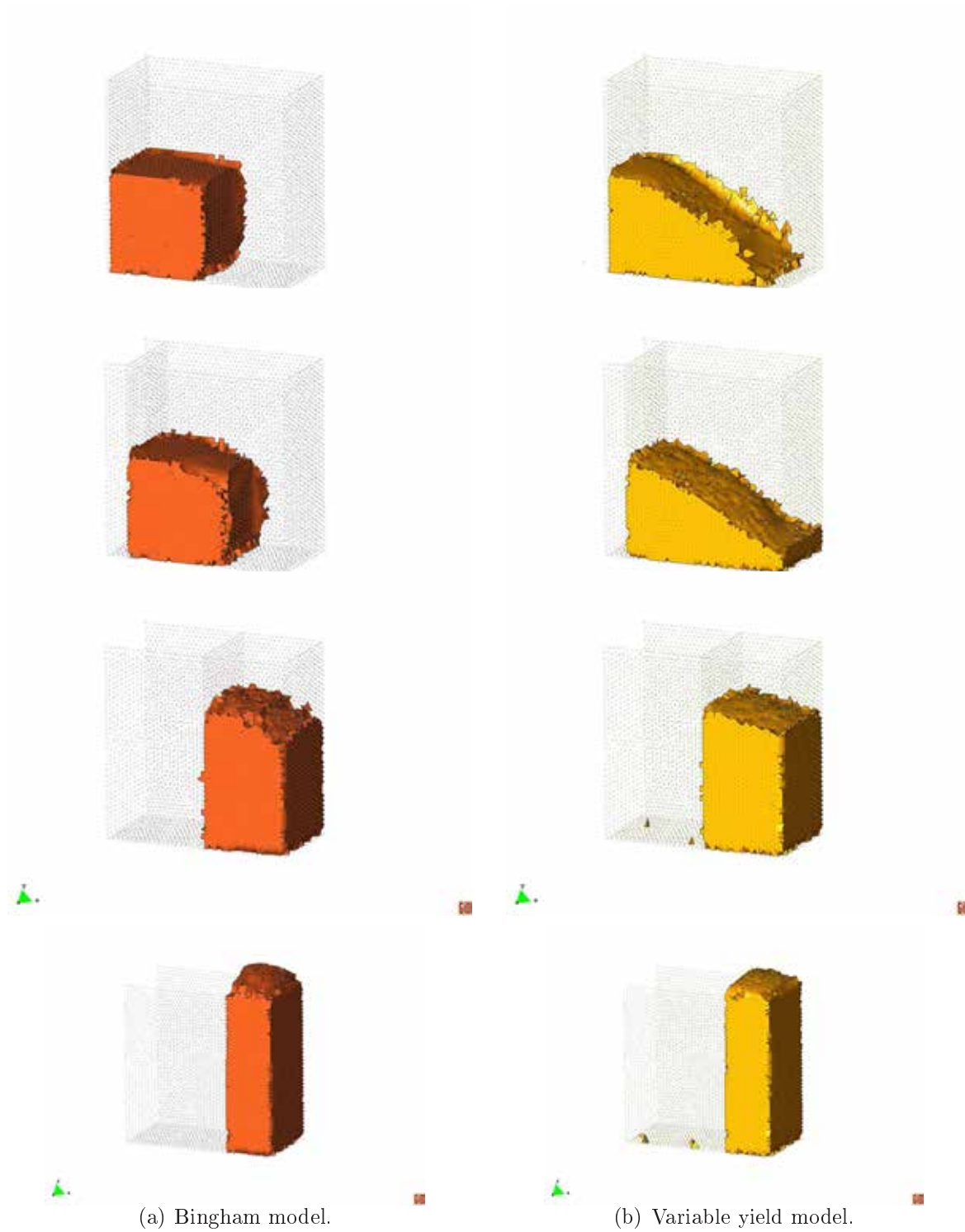
Figure 3.25: 3*D* pushed slope. Difference between the Bingham and the variable viscosity models in the initial pushing phase.

(a) Bingham model.   (b) Variable yield model.
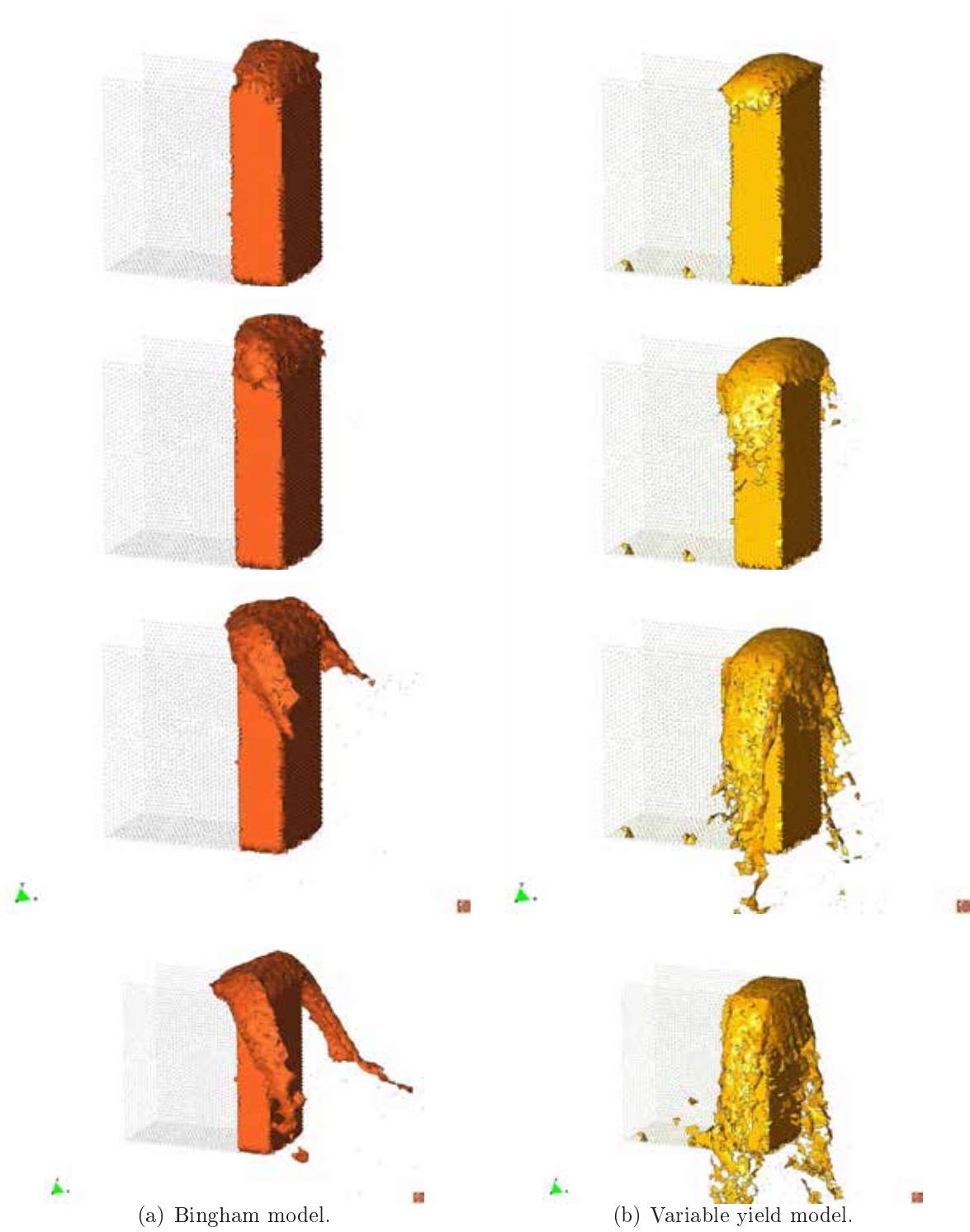
Figure 3.26: 3D pushed slope. Difference between the Bingham and the variable viscosity models in the squeezing phase.

3.8.5   Settlement of a vertical rockfill slope

The variable viscosity model is finally used to reproduce the settlement of a granular vertical slope with a given internal friction angle. The objective of this example is to verify the correct reproduction of the internal friction angle and the dependency of the stable configuration from the mesh size.

For this purpose a rectangular domain is constrained by a vertical wall in the left side and is left free on the right side as shown in Figure 3.27. The characteristics of the material are summarized in Table 3.7.
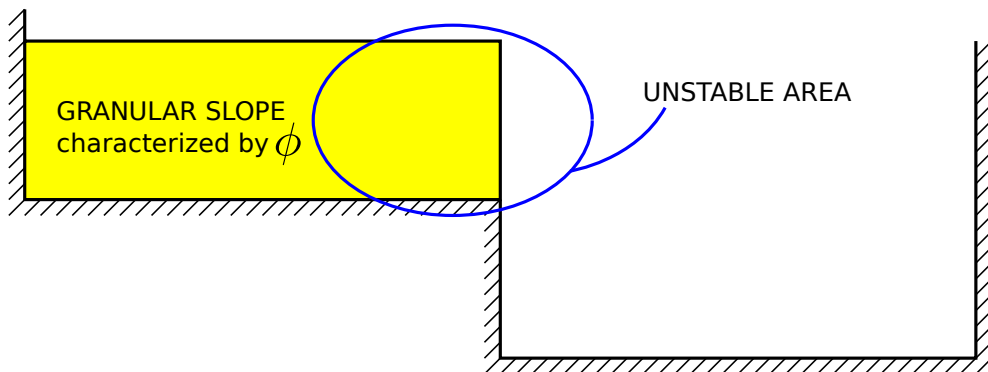
Figure 3.27: Settlement of a vertical slope. Geometry of the model.

Dry density	ρ_s	$1000 kg/m^3$
Fluidified viscosity	μ_s	$10^{-6} Pa\,s$
Smoothing coefficient	m	$3000s$

Table 3.7: Settlement example. Material properties.

Variable mesh size

Let us consider an internal friction angle $\phi = 30°$. Three different mesh sizes are taken into account for the simulation:

- Mesh A is $0.1cm$. The model has 444 nodes.

- Mesh B is $0.05cm$. The model has 1580 nodes.

• Mesh C is 0.01*cm*. The model has 35466 nodes.

They are shown in Figure 3.28.
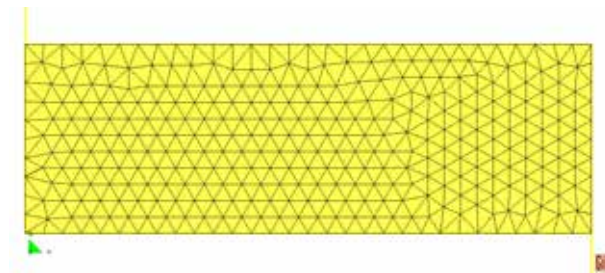
(a) Mesh A 0.1*m*.
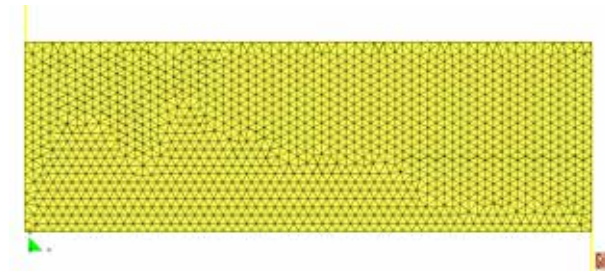
(b) Mesh B 0.05*m*.

(c) Mesh C 0.01*m*.

Figure 3.28: Different mesh sizes taken into account in the present example.

The evolution of the settlement is shown in Figure 3.29 for the above mentioned meshes. As expected the more accurate and realistic settlement process is obtained with the finer mesh but no relevant differences appear using the coarser ones. This is respected for any internal friction angle ϕ less than 45°. In fact in the latter case the correct behavior of the material is influenced by the mesh size. For coarse meshes the material behaves as rigid as shown in Figure 3.30 where two meshes are taken into account. However in the next section it will be pointed out that this value of ϕ is in the limit of validity of the model.

(a) Mesh A.   (b) Mesh B.   (c) Mesh C.
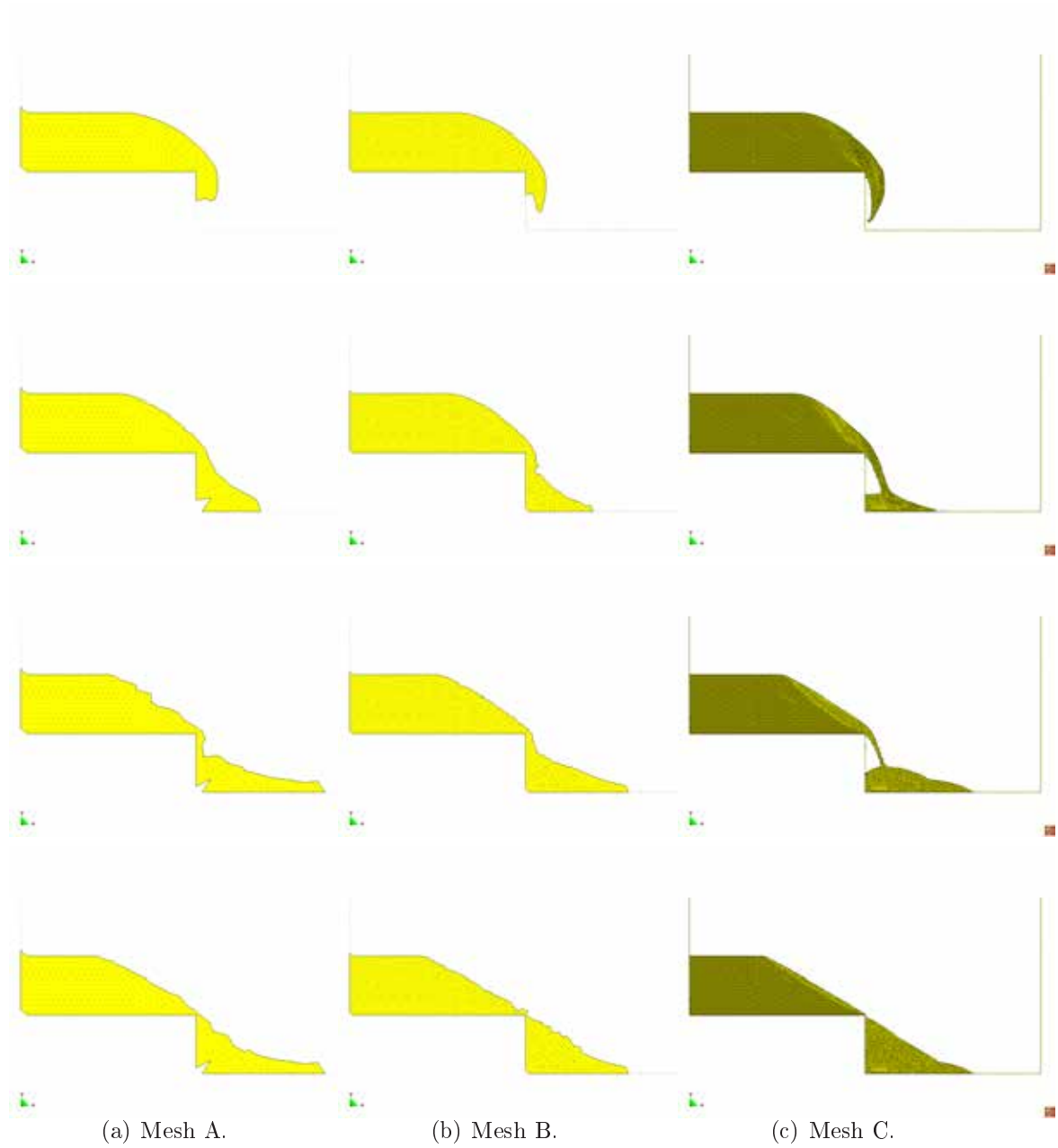
Figure 3.29: Settlements for a granular slope with internal friction angle $\phi = 30°$ for the three different mesh sizes indicated in Figure 3.28.

The same example is run in $3D$ using the meshes A and B of Figure 3.28 leading to analogous conclusions. The internal friction angle is well represented independently from the mesh chosen. A sequence of the $3D$ results for a slope with internal friction

(a) Mesh B 0.05*m*   (b) Coarse mesh 0.07*m*
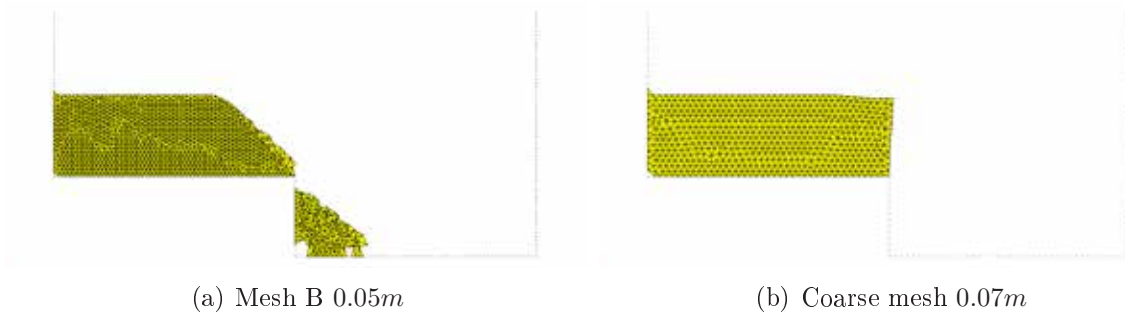
Figure 3.30: Different results of the model with *phi* = 45° in case of mesh B (0.05*m*) and a coarser mesh (0.07*m*). Both results are taken after 5*s* of simulation.

angle $\phi = 30°$ is shown in Figure 3.31.

Variable internal friction angles

Different values of the internal friction angle are taken into account in order to verify the correct behavior of the structural model. Mesh B is used for the discretization.

The different mechanical behavior controlled by the values of ϕ is correctly reproduced by the variable yield model presented in this work if the internal friction angle is lower than 45°, as can be observed in Figure 3.32 where the stable configuration of rockfill slope of 30°, 40°, 45°and 47° is simulated. The case with $\phi = 45°$ represents a practical limit of the model. Beyond that limit a dependency on the mesh appears as some level of locking can be observed. The conclusion is that the model is not able to correctly simulate materials that have internal friction angles higher than 45°. This is not so relevant considering that in rockfill slopes 45° can be considered an upper limit of the possible internal friction angles.

3.8.6   Friction angle test

The last example simulate a test for computing the internal friction angle ϕ. A cone filled with granular material with a bottom outlet is lifted up with a velocity of 0.025*m/s*. The geometry and the mesh used can be seen in Figure 3.33.

The mechanical characteristics of the material used are summarized in Table 3.8.

As expected, the final slope of the fallen material matches well with the 40° angle as shown in the last picture of Figure 3.34.

Finally in Figure 3.35 the same example has been repeated in the case of a Bingham

(a) Mesh A.   (b) Mesh B.
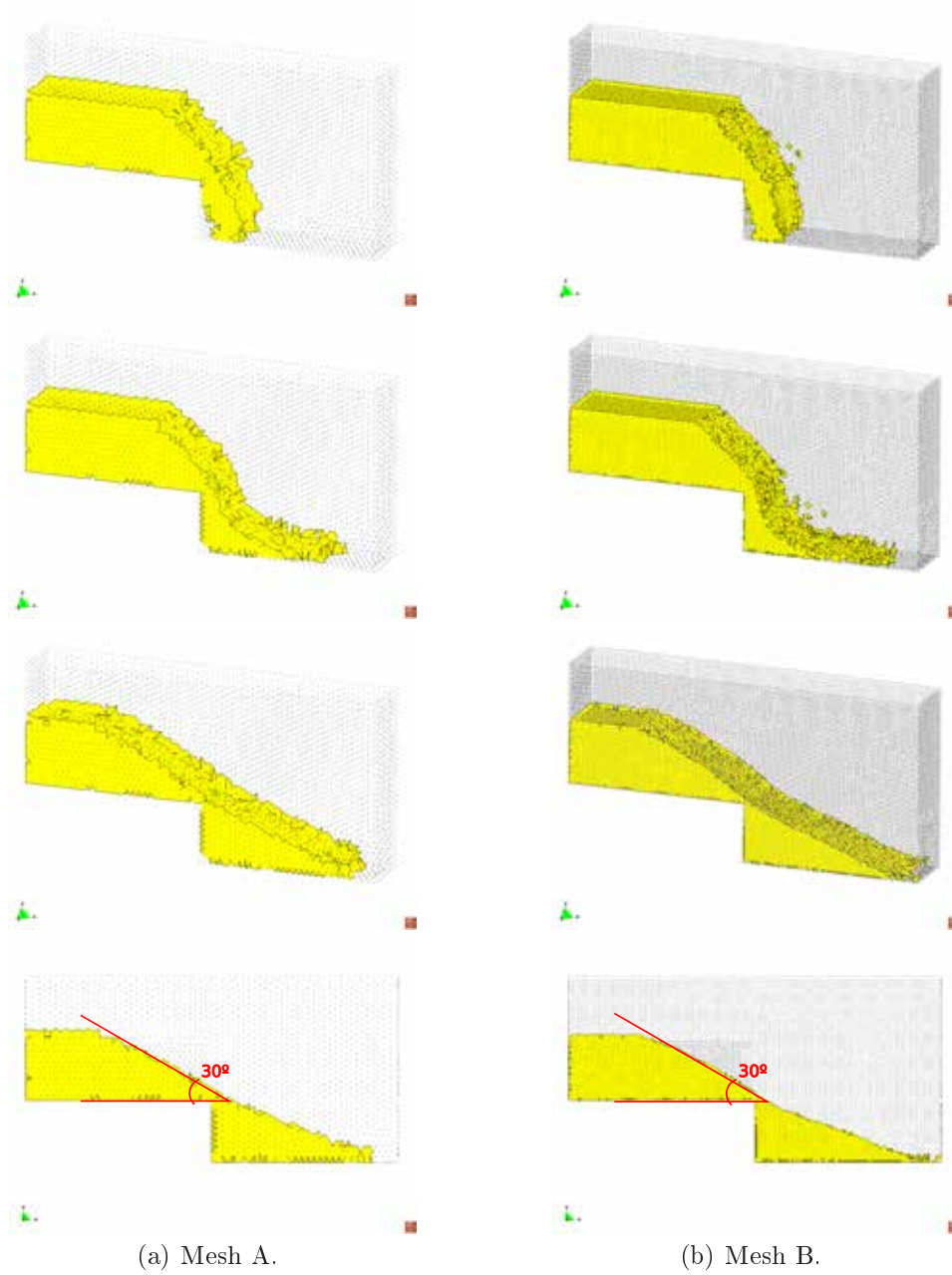
Figure 3.31: Settlements for a $3D$ granular slope with internal friction angle $\phi = 30°$ in the case of considering mesh A and B of Figure 3.28.

plastic with a yield threshold $\tau_0 = 500Pa$.

The different behaviour between the two models is evident: the material of the variable yield model "flows" down in a nearly continuous way and at the end of the simulation no

(a) $\phi = 30°$

(b) $\phi = 40°$

(c) $\phi = 45°$

(d) $\phi = 47°$
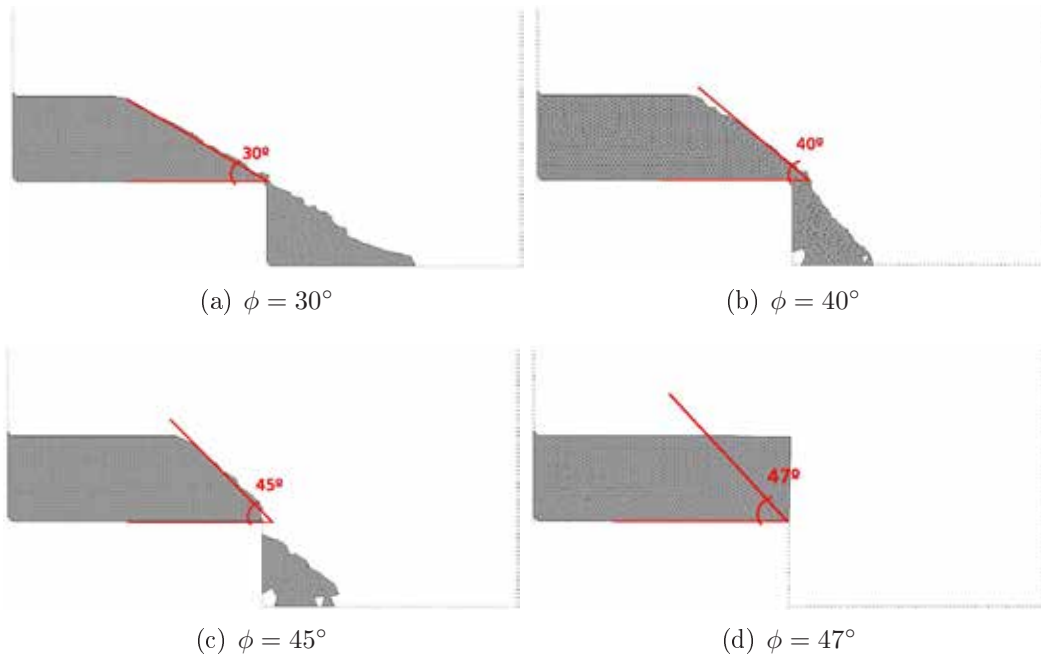
Figure 3.32: Stable results for different internal friction angles ϕ. The mesh used in the calculation is mesh B of Figure 3.28.

Dry density	ρ_s	$1490 kg/m^3$
Internal friction angle	φ	$40°$
Fluidified viscosity	μ	$10^{-6} Pa\,s$
Smoothing coefficient	m	$3000s$

Table 3.8: Friction angle test example. Material properties.

material is present in the cone (the cone is 41.6° steep). Whereas the Bingham material resembles a toothpaste and at the end of the simulation part of the material remains inside the cone. The tangential stresses, in fact, are lower than the yield threshold.
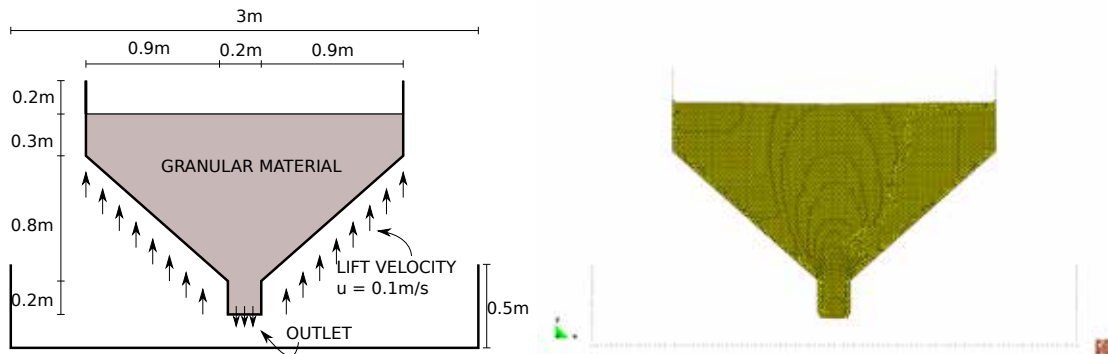
Figure 3.33: Friction angle test example. Geometry and mesh used for the calculation.
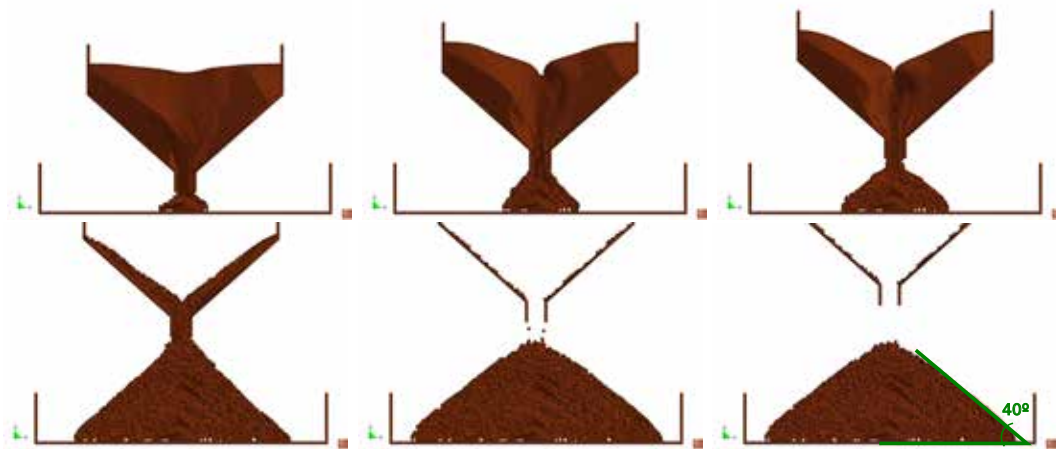
Figure 3.34: Friction angle test example. Variable yield model with $\varphi = 40°$.

3.9   Conclusions

In this chapter a model to describe the behavior of a rockfill slope is presented. A Non-Newtonian constitutive law is chosen and a regularized Bingham plastic model is developed as first approximation. This choice derives from the observation that the elastic behavior in rockfill slopes is negligible and when the yield stress is reached the material starts to flow more like a fluid than to deform like a structure. Moreover among
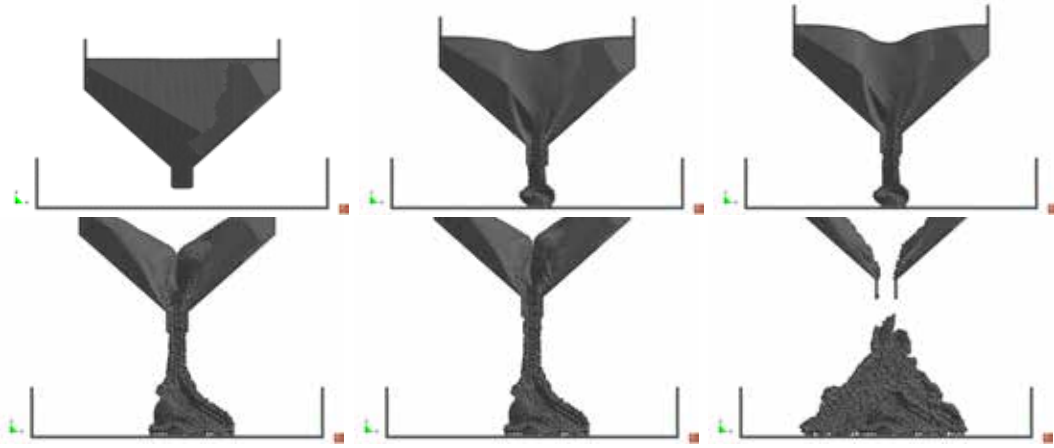
Figure 3.35: Friction angle test example. Bingham model with yield stress $\tau_0 = 500Pa$.

the non-Newtonian fluids, Bingham plastics have the capability of supporting a certain amount of shear stress before reaching large strains.

The good behavior of the Bingham model is verified through some benchmarks, but does not seem to be adequate for the simulation of the behavior of a granular slope. For this purpose a variable yield threshold is introduced in order to mimic a Mohr Coulomb failure criterion.

The differences between the regularized Bingham and the variable yield models are discussed in some examples.

The main advantage of the constitutive law proposed is its simplicity compared with any other plastic model. The treatment of the granular material as a fluid leads to balance equations similar to those presented in Chapter 2. Hence, most considerations already done for the fluid model can be used in this context as well, providing the necessary adaptation to non-Newtonian materials.

The variable yield model does not present serious limitations on the mesh sizes in general (although in Chapter 5 it will be pointed out that this is not always true in practical cases). Finally the variable yield model seems to be adequate to simulate materials with internal friction angles lower than 45°. Fortunately this value is higher than the maximum threshold of non cohesive rockfill slopes.

Chapter 4

The coupling

In this chapter the coupled model for fluid-structure interaction analysis is presented. First the fluid and the structural balance equations, already discussed in the previous parts of this work, are derived from the monolithic coupled system. A staggered solution strategy is adopted to couple the Eulerian fluid solver and the Lagrangian structural one. A simple example is presented to check the correct behaviour of the algorithm. Finally in order to fully describe the coupling algorithm, the projection tool created to map information between the fluid and the structural non-matching meshes is discussed. Additional examples of the application of the coupled analysis method are shown in Chapter 5.

4.1 Introduction

The structural stability of rockfill slopes is heavily influenced by its interaction with water. Traditionally the coupled problem of soils or rock and water is faced using a multiphase material whose behavior is governed by the coupling between the different phases: soil, water and air. The first mathematical models describing the coupling solid and fluid phase were developed by Biot [13, 14]. Nevertheless his work was suitable only for linear elastic materials and its extension to non-linear problems with large deformations was first carried on by Zienkiewicz and Shiomi only several years later [131]. Its should be mentioned that recently important steps ahead in this fieldhave been made by Lewis and Schrefler [78], Coussy [91] and Boer [49].

These classical and well established approaches in geomechanics were not considered as

an alternative in the present work for the following reasons:

- The possibility of accurately following the dynamic change of the flow throughout and over the rockfill is the key point of the model. The coupling of these two phenomena could be very challenging in the traditional models needing the transferring of interface conditions between the free surface problem and the seepage one in order to perform the coupling. On the contrary, in the present work this is automatically taken into account, as explained in Chapter 2.

- The consideration of the saturation level and of the interaction between air and water in the partially saturated pores, becomes an useless information. In fact according to experimental evidence, the problem of interest can always be considered fully drained, being the pores inter connected.

- Due to the time scale of the exceptional flooding that can be of the order of minutes or hours, the dam material can be considered as rigid (avoiding any elastic response in the unyielded region) and its compressibility can be neglected.

- The capability of tracking the material yield surface is not needed as commented in Chapter 3.

The need of developing an *ad hoc* fluid approach for the simulation of the *free surface-seepage* problem described in Chapter 2 leads, as a natural consequence, to the choice of a staggered strategy. Nevertheless for a consistent formulation both the fluid and structure balance equations should be derived from the imposition of the global equilibrium. For that purpose, in the following sections the monolithic global problem is used to obtain the balance equations for the structure. In this case, the equation discussed in Chapter 3 are completed with the coupling terms deriving from the global equilibrium.

Once the fluid and the structural problems are defined, the coupling strategy is presented. The need of working with an Eulerian and a Lagrangian model leads to implement a fully staggered explicit scheme. A key point of the coupled tool is the possibility of transferring information between the moving and the fixed mesh. For such purpose a mapping between non matching meshes has been developed. The performance of the tool is presented at the end of the chapter.

4.2   The coupled monolithic problem

Let us consider the balance equation of the global problem which can be written as follows

$$
\begin{aligned}
\rho_C \partial_t \mathbf{u}_C + \rho_C \mathbf{u}_C \cdot \nabla^s \mathbf{u}_C - \rho_C \nabla \cdot \boldsymbol{\sigma}_C - \rho_C \mathbf{b} &= \mathbf{0} \text{ in } \Omega,\ t \in (0, T), \\
\rho_C \nabla \cdot \mathbf{u}_C &= 0 \text{ in } \Omega,\ t \in (0, T),
\end{aligned}
\tag{4.1}
$$

where sub-index C indicates the characteristics of the coupled homogenized system. Under the assumption that both the fluid and the structure are incompressible materials, System 4.1 can be expressed in terms of the fluid and the structure contributions explicitly as

$$
\begin{aligned}
\rho_s \partial_t \mathbf{u}_s + \rho_s \mathbf{u}_s \cdot \nabla^s \mathbf{u}_s + \nabla p'_s - 2\nabla \cdot \tilde{\mu} \nabla^s \mathbf{u}_s - \rho_s \mathbf{b}_s + & \\
+ \rho \partial_t \mathbf{u} + \rho \overline{\mathbf{u}} \cdot \nabla \mathbf{u} + \nabla p - 2\nabla \cdot \mu \nabla^s \mathbf{u} - \rho n \mathbf{b}_f &= \mathbf{0} \text{ in } \Omega,\ t \in (0, T), \\
n\rho \nabla \cdot \mathbf{u} + \rho_s \nabla \cdot \mathbf{u}_s &= 0 \text{ in } \Omega,\ t \in (0, T),
\end{aligned}
\tag{4.2}
$$

Remark 18. Its should be pointed out that the assumption of fully drained problem is used. This consideration derives from the hypothesis that all the pores can be considered interconnected and that excess pore pressure will never develop.

Remark 19. The nodal global density ρ_C can be either a dry density (defined in equation 3.16) if the node is not immersed in water, or a nodal saturated density ρ_{sat}

$$
\rho_C = \rho_{sat} = n\rho + (1-n)\overline{\rho}_s + = n\rho + \rho_s.
\tag{4.3}
$$

4.3   The fluid and the structural balance equations

The balance equations of the fluid have been defined in Chapter 2 and are rewritten here for clarity. They are defined by

---

Fluid problem

$$\rho \partial_t \mathbf{u} + \rho \overline{\mathbf{u}} \cdot \nabla \mathbf{u} + n\nabla p - 2\nabla \cdot \mu \nabla^s \mathbf{u}$$
$$-\rho n\mathbf{b} + \mathbf{D} = \mathbf{0} \text{ in } \Omega, \ t \in (0,T); \quad (4.4)$$
$$\nabla \cdot \mathbf{u} = 0 \text{ in } \Omega, \ t \in (0,T);$$

$$\begin{aligned}
\mathbf{u}(\mathbf{x}, 0) &= \mathbf{u}_0(\mathbf{x}) &\text{in}& \quad \Omega; \\
\mathbf{u}(\mathbf{x}, t) &= \mathbf{g}(\mathbf{x}, t) &\text{on}& \quad \partial\Omega_D, \quad t \in (0,T); \\
\mathbf{n} \cdot \boldsymbol{\sigma}(\mathbf{x}, t) &= \mathbf{t}(\mathbf{x}, t) &\text{on}& \quad \partial\Omega_N, \quad t \in (0,T);
\end{aligned} \quad (4.5)$$

Therefore the equations governing the structural problem can be obtained subtracting 4.4 from 4.2. The structural system obtained is

$$\rho_s \partial_t \mathbf{u}_s + \rho_s \mathbf{u}_s \cdot \nabla^s \mathbf{u}_s + \nabla p'_s$$
$$-2\nabla \cdot \tilde{\mu}_s \nabla \mathbf{u}_s - \rho_s \mathbf{b} + (1-n)\nabla p_f - \mathbf{D} = \mathbf{0} \text{ in } \Omega_s, \ t \in (0,T), \quad (4.6)$$
$$\nabla \cdot \mathbf{u}_s = 0 \text{ in } \Omega_s, \ t \in (0,T).$$

Structural problem

$$\rho_s \partial_t \mathbf{u}_s + \rho_s \mathbf{u}_s \cdot \nabla^s \mathbf{u}_s + \nabla p'_s$$
$$-2\nabla \cdot \tilde{\mu}_s \nabla \mathbf{u}_s - \rho_s \mathbf{b} + (1-n)\nabla p - \mathbf{D} = \mathbf{0} \text{ in } \Omega_s, \ t \in (0,T), \quad (4.7)$$
$$\nabla \cdot \mathbf{u}_s = 0 \text{ in } \Omega_s, \ t \in (0,T),$$

$$\begin{aligned}
\mathbf{u}_s(\mathbf{x}, 0) &= \mathbf{u}_{s\,0}(\mathbf{x}) &\text{in}& \quad \Omega_s, \\
\mathbf{u}_s(\mathbf{x}, t) &= \mathbf{g}_s(\mathbf{x}, t) &\text{on}& \quad \partial\Omega_{s\,D}, \quad t \in (0,T), \\
\mathbf{n} \cdot \boldsymbol{\sigma}_s(\mathbf{x}, t) &= \mathbf{t}_s(\mathbf{x}, t) &\text{on}& \quad \partial\Omega_{s\,N}, \quad t \in (0,T),
\end{aligned} \quad (4.8)$$

This problem is equivalent to the one treated in Chapter 3 providing the following considerations:

- The DOFs of the problem stated by system 4.6 are the effective pressure (p'_s) and the solid velocity (u_s). This is essential in order to fully decouple the fluid and

the structural equations. This aspect was not explicitly discussed in Chapter 3 because the total pressure is equivalent to the effective one in absence of water.

- The external force term in equation 3.18 is composed only of the body forces whereas in system 4.6 the Darcy term ($\mathbf{D}$) and the fluid gradient of pressure ($(1-n)\nabla p_f$) are also present.

4.4   The coupling strategy
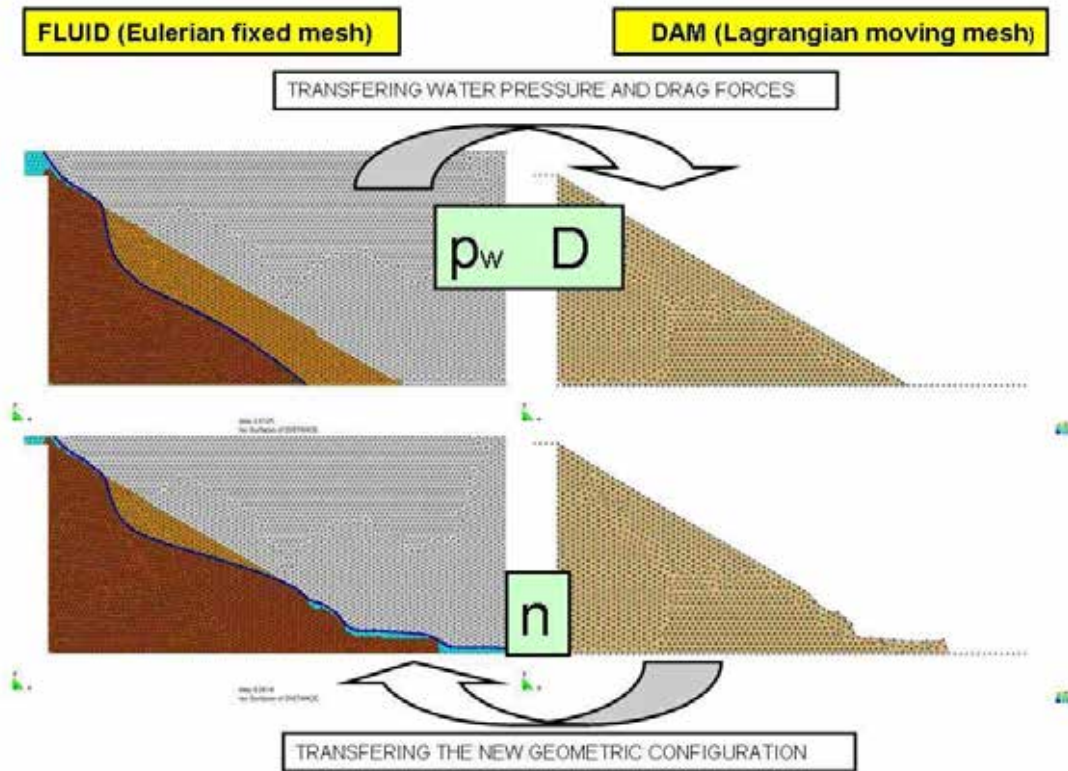
Figure 4.1: Graphical summary of the whole process.

A monolithic approach to the whole problem becomes impossible after the choice of two different kinematical frameworks for the structure and the fluid model. The use of a staggered scheme is therefore mandatory. Moreover in the context of partitioned schemes, the more accurate way of performing the coupling between the structural and the fluid model is by using an implicit coupling. In this case iterations are performed between the solution of the two models at each time step, till convergence is achieved.

This choice is very accurate although very expensive. The second possibility, which is the one used in the present work, is to perform an explicit coupling. This means that the solution at each time step is obtained by the solution of the fluid and the structural model calculated one after the other, without any iteration.

This is acceptable considering that :

- The adoption of a semi-explicit scheme for the fluid problem leads to the need of using time steps much smaller than for the fully implicit structural problem, to ensure stability. An implicit coupling would require adopting the smaller time step, i.e. that for the fluid solver, for both models, leading to an extremely expensive procedure;

- The coupling between the two models is weaker in one of the two directions. For the solution of the fluid problem, in fact, only the porosity distribution is needed to be transfered by the structural model. In other words, the shape of the rockfill slope or, more generally, of the granular material have to be transfered to the fixed fluid mesh. On the contrary the other way coupling, the fluid pressure and velocity are essential to correctly define the external forces acting on the rockfill material.

In summary the structural Lagrangian model is projected on the Eulerian fixed mesh domain where, at the beginning of the simulation, the only available information is the incoming discharge of water and the control domain. Th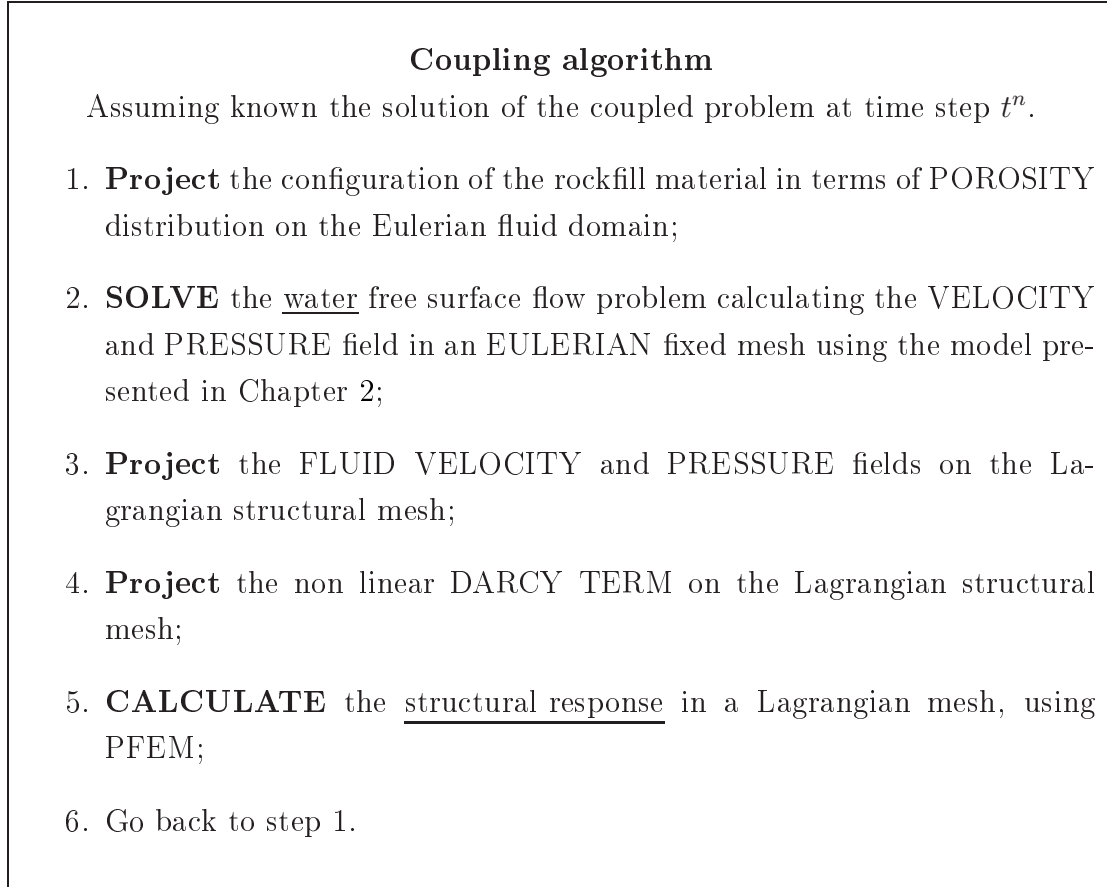e idea is that the fluid analysis step is evaluated once the distribution of porosity is projected from the structural domain. The solution of the fluid problem is then projected on the Lagrangian structural mesh. It is necessary to know the fluid pressure and the Darcy forces in order to evaluate correctly the external force term of the momentum equation in 4.6. Once this is done, the structural response can be calculated. Therefore, the granular domain deforms accordingly to the obtained velocity and pressure fields. This new deformed granular domain is finally projected onto the Eulerian mesh in order to solve for the subsequent time step.

Remark 20. The time step of the fluid model is typically one order of magnitude smaller than the one of the structural model. This is the consequence of the already discussed conditional stability of the semi-explicit scheme used for the fluid model. Therefore the fluid and the structural models have different time steps.

The main points of the entire simulation process are shown in Figure 4.1 and the flow chart of the algorithm are schematically summarized in the box below:

Coupling algorithm

Assuming known the solution of the coupled problem at time step t^n.

1. **Project** the configuration of the rockfill material in terms of POROSITY distribution on the Eulerian fluid domain;

2. **SOLVE** the <u>water</u> free surface flow problem calculating the VELOCITY and PRESSURE field in an EULERIAN fixed mesh using the model presented in Chapter 2;

3. **Project** the FLUID VELOCITY and PRESSURE fields on the Lagrangian structural mesh;

4. **Project** the non linear DARCY TERM on the Lagrangian structural mesh;

5. **CALCULATE** the <u>structural response</u> in a Lagrangian mesh, using PFEM;

6. Go back to step 1.

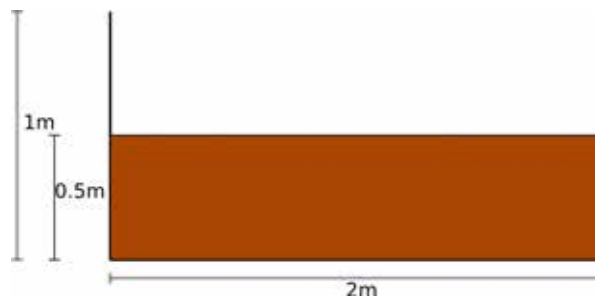
4.4.1 Numerical Example: Still water tank

Figure 4.2: Geometry of the tank and height of the contained porous medium.

The aim of this very simple example is to check the calculation of the effective pressure distribution when no velocity is present. A tank of porous material with three different

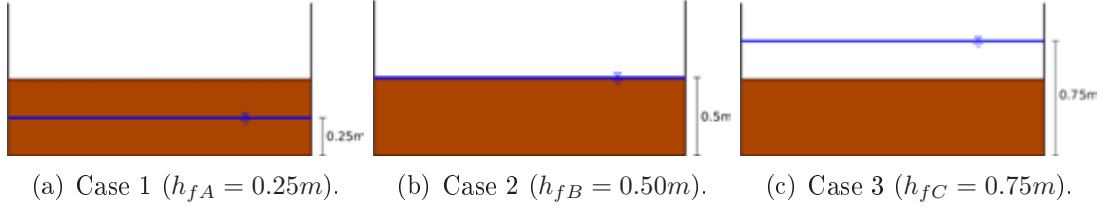(a) Case 1 ($h_{fA} = 0.25m$).   (b) Case 2 ($h_{fB} = 0.50m$).   (c) Case 3 ($h_{fC} = 0.75m$).

Figure 4.3: Depth of water in the three analyzed cases.

levels of water is analyzed. The geometry of the model can be seen in Figure 4.2 and the three analyzed cases are shown in Figure 4.3. The characteristics of the material are summed up in Table4.1. In the present example gravity is assumed to be $10m/s^2$.

ROCKFILL

Global density	ρ_C	$= 1895.2 \ kg/m^3$
Dry density	ρ_s	$= 1490 \ kg/m^3$
Porosity	n	$= 0.4052$
Average diameter	D_{50}	$= 35.04 \ mm$

WATER

Fluid density	ρ	$= 1000.0 \ kg/m^3$
Viscosity	μ	$= 0.001 \ Pa \, s$

Table 4.1: Characteristics of the materials considered in the model.

Let us define:

- h_s: the depth of the porous medium ($0.5m$ in the three cases);

- h_f: the water depth ($h_{fA} = 0.25m$, $h_{fB} = 0.50m$, $h_{fC} = 0.75m$);

- h_w: the wet part of h_s ($h_{wA} = 0.25m$, $h_{wB} = 0.50m$, $h_{wC} = 0.50m$);

- h_d: the dry part of h_s ($h_{dA} = 0.25m$, $h_{dB} = 0.0m$, $h_{dC} = 0.0m$);

- h_f^{fr}: the water column over the porous medium ($h_{frA} = 0.0m$, $h_{frB} = 0.0m$, $h_{frC} = 0.25m$);

The total bottom pressure (p_s) in each case can be calculated analytically like the sum of the pressure of the wet part, the pressure of the dry part and the pressure of the

| | Effective pressure [Pa] | |
	Analytical	Numerical
Case A	5963.0	5836.8
Case B	4476.0	4476.6
Case C	4476.0	4478.9

Table 4.2: Effective pressure at the bottom.

water column , i.e. in symbols

$$p_s = \rho_C \, g \, h_w + \rho_s \, g \, h_d + \rho \, g \, h_{fr} = [(1-n)\overline{\rho}_s + n\rho] \, g \, h_w + (1-n)\overline{\rho}_s \, g \, h_d + \rho \, g \, h_f^{fr}; \quad (4.9)$$

and the bottom water pressure is

$$U = \rho \, g \, h. \qquad (4.10)$$

Finally the effective pressure can be calculated as the difference between the total pressure and the water pressure

$$p_s' = p_s - U = (1-n)\overline{\rho}_s \, g \, h_s - (1-n)\rho \, g \, h_w. \qquad (4.11)$$

On the other hand equation 4.2 reduces to

$$\nabla p_s' + \nabla p - n\rho\mathbf{g} - (1-n)\overline{\rho}_s\mathbf{g} = 0; \qquad (4.12)$$

and the equilibrium of the fluid part is

$$n\nabla p - n\rho\mathbf{g} = 0. \qquad (4.13)$$

Rewriting the gradient of fluid pressure of equation 4.12 like $\nabla p = n\nabla p + (1-n)\nabla p$ and subtracting equation 4.13 from 4.12 the equilibrium of the solid matrix is obtained as

$$\nabla p_s' = (1-n)\overline{\rho}_s\mathbf{g} - (1-n)\nabla p; \qquad (4.14)$$

In Figures 4.4, 4.5 and 4.6 the numerical results in terms of effective pressure contour fills and effective pressure distributions are shown for the three cases and compared with analytical results. As expected the effective pressure distribution does not change in cases B and C. On the contrary in case A the effective pressure coincides with the total pressure distribution in the dry part of the solid matrix and decreases in the wet
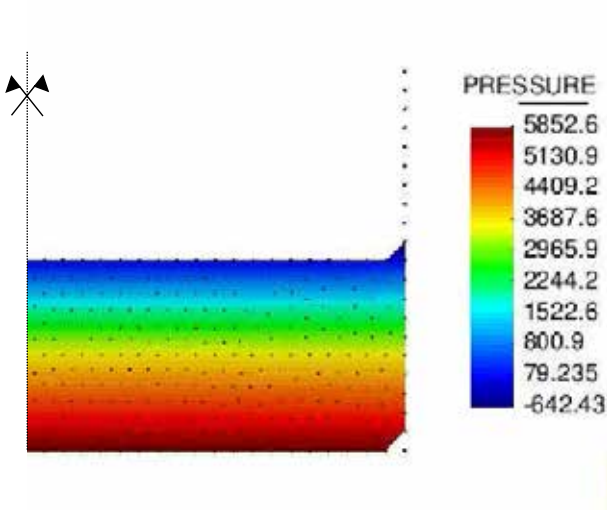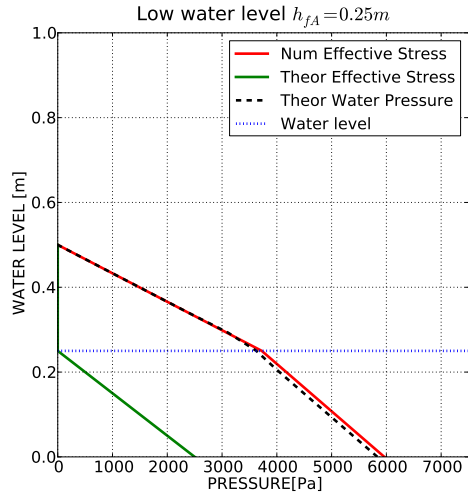
(a) Contour fill of pressure.   (b) Analytical and numerical results.

Figure 4.4: Case A. $h_{fA} = 0.25m$ Effective Pressure p'_s.

(a) Contour fill of pressure.   (b) Analytical and numerical results.

Figure 4.5: Case B. $h_{fB} = 0.50m$ Effective Pressure p'_s.
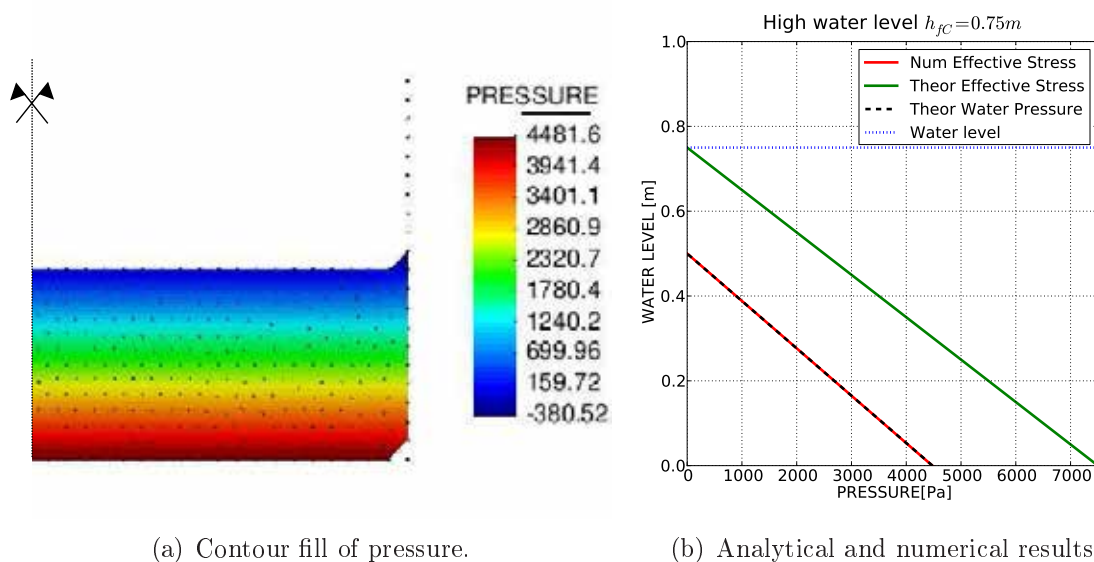
(a) Contour fill of pressure.

(b) Analytical and numerical results.

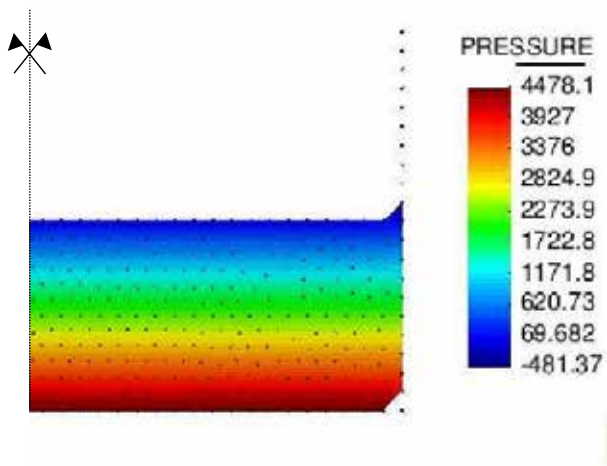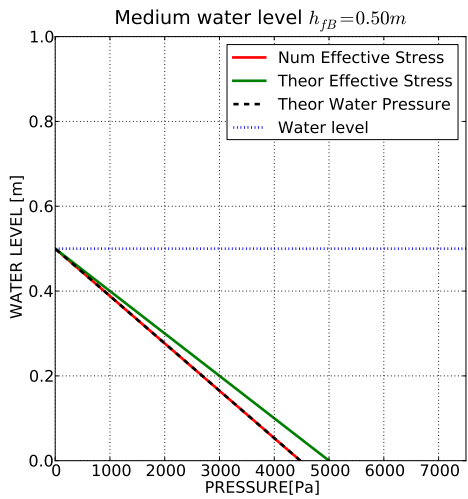Figure 4.6: Case C. $h_{fC} = 0.75m$ Effective Pressure p'_s.

part due to the action of the buoyancy forces.

4.5 Data mapping between non-matching meshes

The effectiveness and efficiency of the model is strictly dependent on the coupling procedure which up to now has only been explained conceptually. Managing a fluid and a structural models that are represented in two different kinematic frameworks requires a tool to transfer information between non-matching meshes.

In the problem of interest, the mapping is to be done on overlapping domains: the fluid control domain always includes the structural Lagrangian domain. In any case there is no need for one domain to be fully included in the other. The data transfer is performed from a $2D$ to a coplanar $2D$ domain or between $3D$ volumes. No mapping between surfaces or interfaces is needed for the current problem.

When dealing with mapping information between meshes the possible cases that can be considered are the following [52]:

1. Compatible identical meshes;

2. Nested meshes typical of multi-scale approaches;

3. Non-nested meshes with a large difference between their sizes, typical of aeronautic problems;

4. Dissimilar meshes in general.

In the present work the need of mapping from a moving to a fixed mesh and vice-versa leads to discard the first two groups. On the other hand, there is no particular reason why the order of magnitude of the two meshes should differ very much. Therefore the case of interest is the *4th* one. Also the fluid and the structural problems do not have any Gauss point variable to be mapped. This simplifies the problem that reduces to the transfer between nodal variables of non-matching meshes.

Let us define *origin mesh* (OM) the mesh from which the variable α is to be transfered to the *destination mesh* (DM). In this framework, according to [18] the transfer methods can be classified as follow:

1. The Element Transfer Method (ETM). For each node of the DM a search is performed in order to locate the element of the OM it is included in. The value of α is obtained by interpolating the nodal values of such element.

2. The Mortar Element Transfer Method (METM) in which conservation of the fields is imposed in a weak sense. The difference between the value of the field on the DM and its value on the OM is asked to be zero weakly performing an integration on the DM [52].

3. The Finite Volume Transfer Method (FVTM) where the conservation in a weak sense is obtained using the Finite Volume Method [102].

4. The Convection Transfer Method (CVM) which is a modification of the previous algorithm suitable for Arbitrary Lagrangian Eulerian methods in which neither the number of nodes, nor the connectivity change during the calculation [18].

The ETM is a dissipative procedure that might create a serious data loss if the dimension of the two meshes is very different. Nevertheless, due to its simplicity and considering the weak coupling of the physical simulated phenomenon , it is the method chosen in this work.

Let us refer to Figure 4.7 to explain the ETM algorithm. The data transfer can be performed via the following steps. For every element (ABC) of the OM:
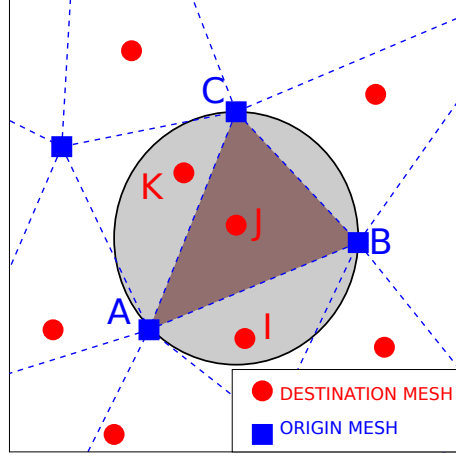
Figure 4.7: $2D$ example of the interpolation procedure. Node I, J and K are inside the circumscribed circle but only node J in inside the element and its value of alpha can be calculated.

1. Calculate the sphere that circumscribes the element, or circle in $2D$ (black circle in Figure 4.7);

2. Search all the nodes of the DM inside the sphere (nodes I, J and K in Figure 4.7);

3. Check which of them is inside the element (verifying that the value of the shape functions of the element nodes are all positive and smaller than one);

$$0 < N_A(\mathbf{x_J}) < 1; \tag{4.15}$$
$$0 < N_B(\mathbf{x_J}) < 1; \tag{4.16}$$
$$0 < N_C(\mathbf{x_J}) < 1; \tag{4.17}$$

4. For every destination node inside the element of the OM (node J of Figure 4.7), interpolate the value of α

$$\alpha_J = N_A(\mathbf{x_J})\alpha_A + N_B(\mathbf{x_J})\alpha_B + N_C(\mathbf{x_J})\alpha_C;$$

Remark 21. The variable α can be either a scalar or a vector. A third possibility is left to the user: he/she can choose to map the whole origin model on the destination one.

In order to perform step 2 the use of a spatial search data structure is needed. The

alternatives available in Kratos [47, 48] (Appendix A), which is the framework used to develop all the algorithms presented in this work, are briefly presented in next section.

4.5.1   The searching algorithm

The search algorithm is the key point of the efficiency of the method, in fact it turns out to be a time consuming part.

According to [113], the suitable containers for this kind of algorithms can be divided in three families:

1. Hash tables like bins and matrices. These structures are suitable for homogeneously distributed data. If this condition is met they are the fastest structure to be used for searching.

2. Trees (quadtrees, octrees, k-d trees for instance). These structures are ideal for a non-homogeneous data distribution. Nevertheless even if this is not the case, they are often preferred to hash tables due to their higher robustness.

3. The previous two families can be suitably combined in order to optimize the searching procedure.

A deep analysis of the topic is not the objective of the present work and the consultation of [113] is recommended for a complete overview on the topic. In what follows just a brief overview of the data structure available in Kratos is done.

The structures available in Kratos are:

1. **k-d tree** which denotes k-dimensional tree. It is a space-partitioning data structure for organizing points in a k-dimensional space. The k-d tree is based on a recursive subdivision of space into disjoint hyper-rectangular regions called cells. Each node of the tree is associated with such region, called cell, and is associated with a set of data points that lie within this cell. The root node of the tree is associated with a bounding box that contains all the data points.

   Considering an arbitrary node in the tree, as long as the number of data points associated with this node is greater than a small quantity, called the bucket size, the box is split into two boxes by an axis-orthogonal hyperplane that intersects this box. A representation of how the k-d tree works can be seen in Figures 4.8 and 4.9. There are a number of different splitting rules, which determine how
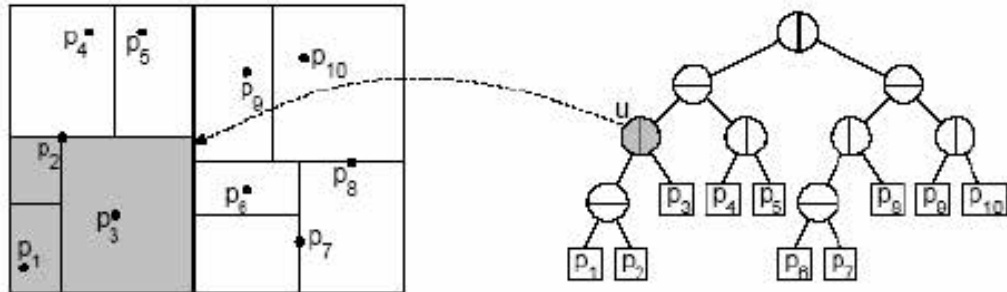
Figure 4.8: Schematic representation of a k-d tree data structure taken from [69].
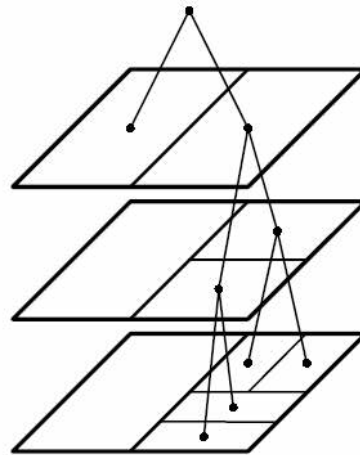
Figure 4.9: Representation of a k-d tree partitioning taken from [47].

this hyperplane is selected and characterize the k-d tree. In Kratos the available options are the following:

a) Mid splitting rule. The cell is always divided by half;

b) Balanced splitting rule. The cell is divided into two cells that contain the same number of nodes. This is an optimal rule but very time consuming;

c) Approximated balanced rule. It uses the average of the coordinates of the points as splitting dimension.

2. **Bins** It divides the domain into a regular $nx \times ny \times nz$ sub-domains as shown in Figure 4.10 and holds an array of buckets storing its elements (see Figure 4.11).

This structure provides an extremely fast spatial searching when entities are more or less uniformly distributed over the domain. The good performance for well distributed entities and their simplicity makes bins one of the most popular data structure for different finite element applications.
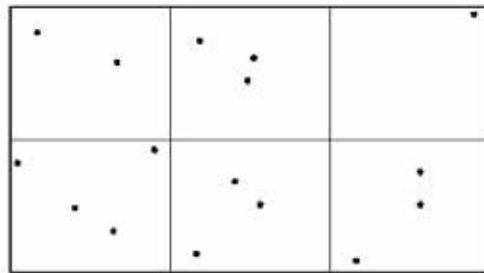
Figure 4.10: Representation of a bins partitioning taken from [47].
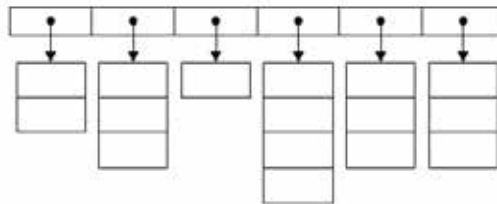
Figure 4.11: Bins structure taken from [47].

Two bins structures are implemented in Kartos:

a) Static bins. This is the most efficient bins structure organizing the data in sparse matrices but does not allow the insertion of additional data.

b) Dynamic bins. Slower than the previous one, it is basically a matrix of arrays of entries, allowing a more flexible modification of its content at any time.

3. **Octree**. It is a type of tree in which every node in $3D$ has children. Space is recursively subdivided into eight octants (only octants containing nodes are divided in turn). The creation of the tree is faster than in th k-d tree case but the resulting structure can often be less balanced. The searching procedure is faster than in k-d tree implying less jumps.

4. **K-d tree of bins** a combination of the previous described structures.

5. **Octree of bins** a combination of the previous described structures.

The advantages and drawbacks of every Kratos data structure can be found in [47, 48]. In the present work the k-d tree, bins and k-d tree of bins data structure have been used.

4.5.2 Numerical Examples

Mesh dimension influence in the mapping procedure

(a) Mesh A. Origin (PFEM) mesh.

(b) Mesh A. Destination (fixed) mesh.

(c) Mesh B. Origin (PFEM) mesh.

(d) Mesh B. Destination (fixed) mesh.

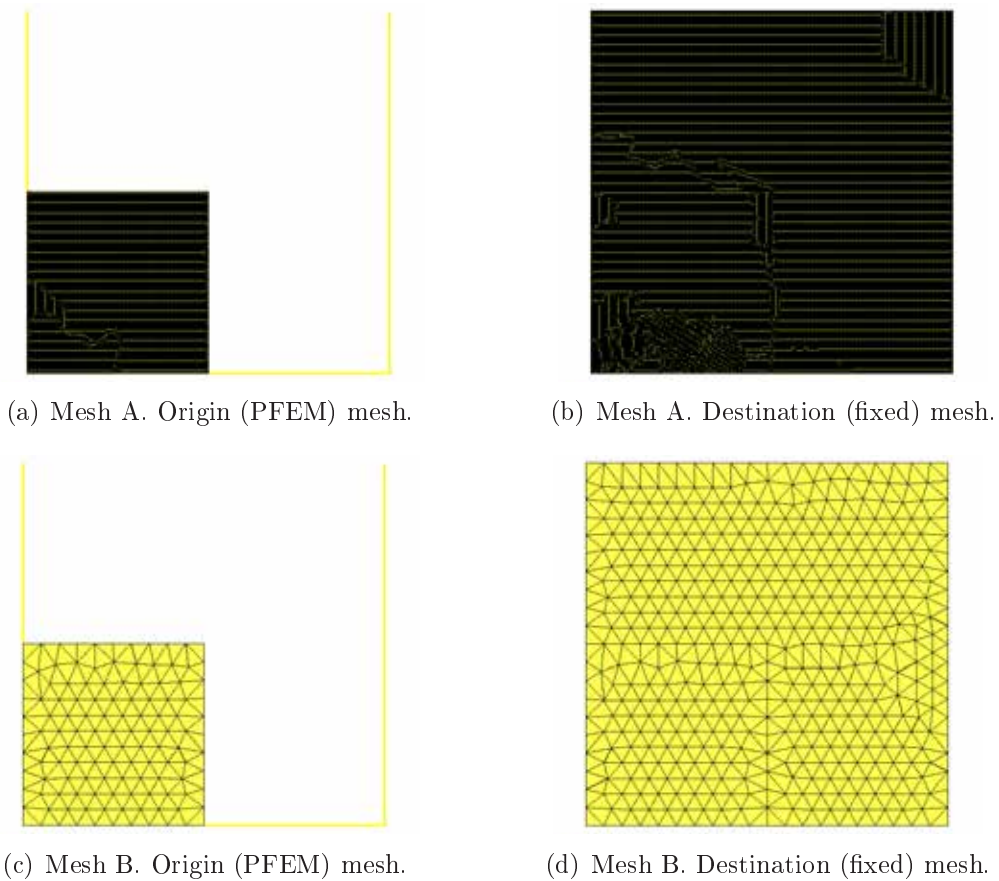Figure 4.12: Meshes used in the calculation whose element dimension is reported in Table4.3. Left: Lagrangian (PFEM) mesh and right: Eulerian fixed mesh.

The breaking of a $2D$ water column example is considered here to underline the limits and possibilities of the interpolation algorithm. The initial height and width of the water column is $0.5m$. The calculation is performed in a moving mesh (the origin mesh OM)

using PFEM, and at each time step the whole model part is projected to the fixed mesh (the destination mesh DM). A k-d tree data structure is used to perform the searching of the neighbors.

	Mesh A	Mesh B
Dimension [m]	0.005	0.05

Table 4.3: Size of the two meshes considered in the projection example.

Two different mesh sizes are considered for the interpolation procedure, a fine mesh (mesh A of Table4.3) with approximately 100 elements in the water column edge and a coarser one (Mesh B of Table 4.3) with 10. The Eulerian and Lagrangian initial domains for the two meshes considered are shown in Figure 4.12. In Figure 4.13 the interpolation is performed from mesh A to a fixed grid with the same mesh dimension. When interpolating data between coarser PFEM and fixed meshes (mesh B) the interpolation shows a lack of precision (figure 4.14). Nevertheless it should be observed that original data are already quite poor and no relevant data loss is present.

The worst performance is observed when interpolating form a PFEM model with mesh A to a coarse fixed mesh (mesh B). The loss of information is evident in Figure 4.15.

Therefore as a conclusion, the dimension of the origin and destination meshes has to be of the same order of magnitude to obtain an acceptable precision in the interpolation procedure.

Performing the projection algorithm

In the present example the time performance of the interpolation algorithm is calculated for a k-d tree, bins and k-d tree of bins data structures. The example considers the projection of a scalar variable (the porosity) from a PFEM model to a fixed grid model. The meshes are unstructured and homogeneous. The same dimension is considered in the Lagrangian and Eulerian models.

Four different meshes are considered for the comparison. The detail of each of them can be found in Table4.4. The results are summarized in Figure 4.16 where, as expected, in the case of an homogeneous mesh, the bins structure is much faster than the k-d tree one. The difference is clearer as much as the mesh is refined. Nevertheless the
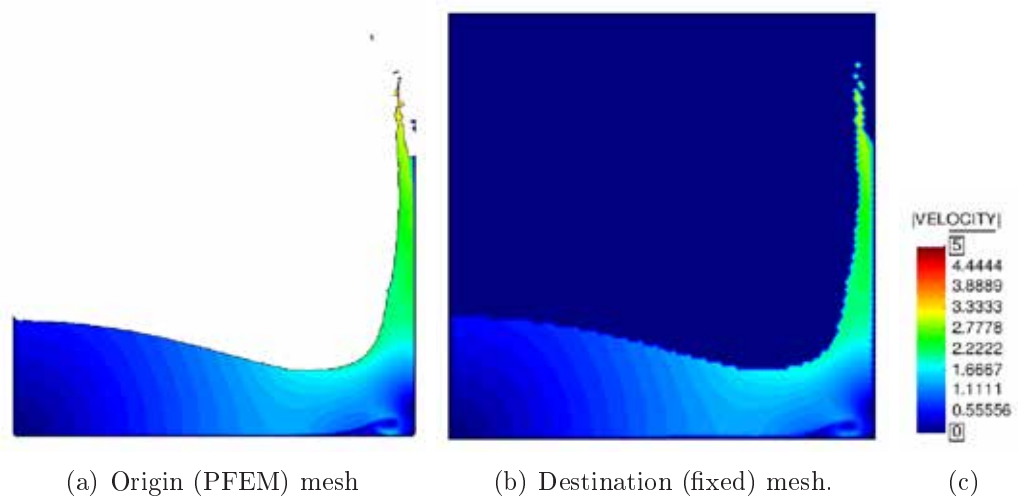
(a) Origin (PFEM) mesh   (b) Destination (fixed) mesh.   (c)

Figure 4.13: Mapping between models with Mesh A.

(a) Origin (PFEM) mesh   (b) Destination (fixed) mesh.   (c)
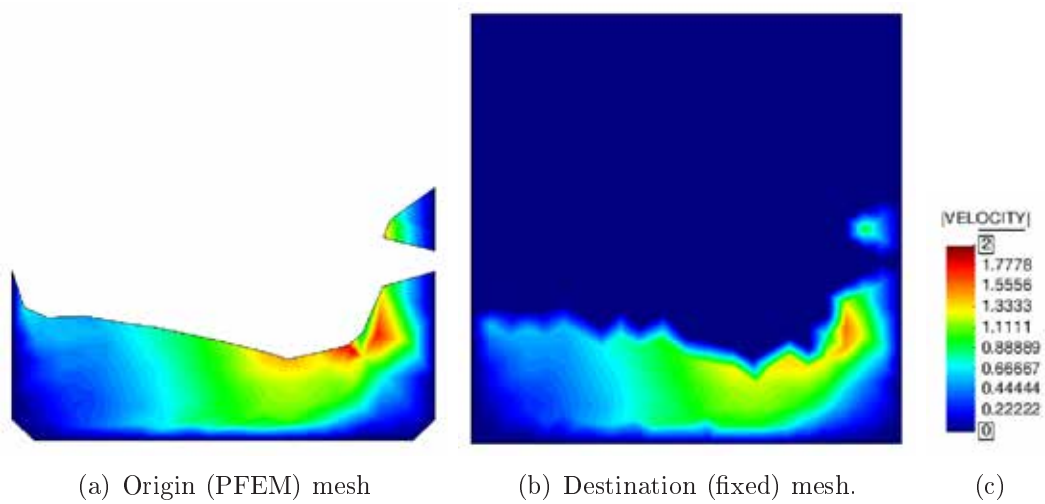
Figure 4.14: Mapping between models with Mesh B.

(a) Origin (PFEM) mesh   (b) Destination (fixed) mesh.   (c)
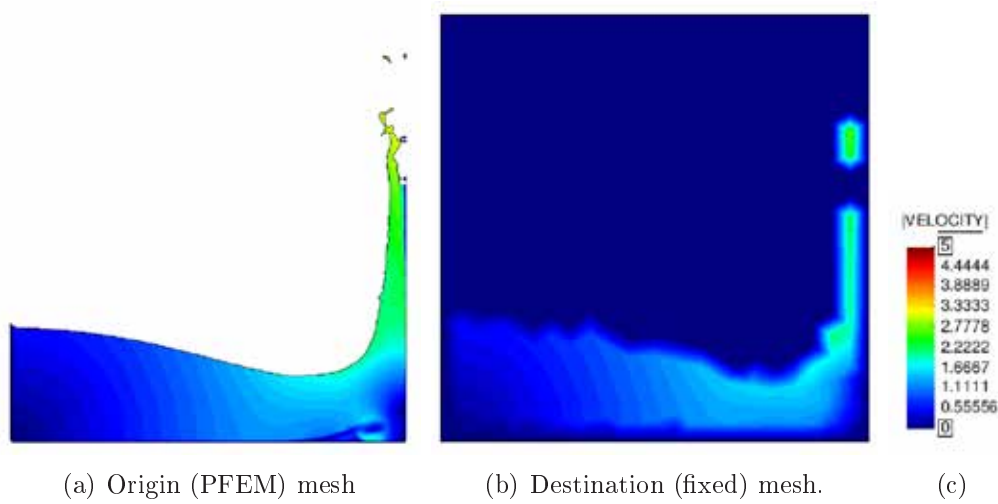
Figure 4.15: Mapping from a fine mesh (mesh A) to a coarse one (mesh B).

combination of these two structures resulting in a k-d tree of bins improve relevantly the efficiency of the simple k-d tree.

The efficiency of the bins can be compromised for a mesh with very high difference in the dimension. In that case, the splitting rule of the k-d tree is the faster searching procedure [113].

Concerning the problem of interest of the present work, the results confirm that there is no reason why the mesh should vary very much in the case of the coupled models of rockfill dams that will be presented in next chapter.

	Mesh A		Mesh B		Mesh C		Mesh D	
Dimension [m]	0.02		0.03		0.04		0.05	
	Eul	Lagr	Eul	Lagr	Eul	Lagr	Eul	Lagr
n. nodes	8 200	2 600	3 600	1 200	2 000	700	3 700	460
n. elem	15 900	7 400	7 000	3 300	4 000	1 800	7 000	1 200

Table 4.4: Mesh dimension of the four meshes considered in the projection example. The last two rows indicates the number of nodes and elements for the Eulerian destination mesh (Eul) and the Lagrangian origin one (Lagr).
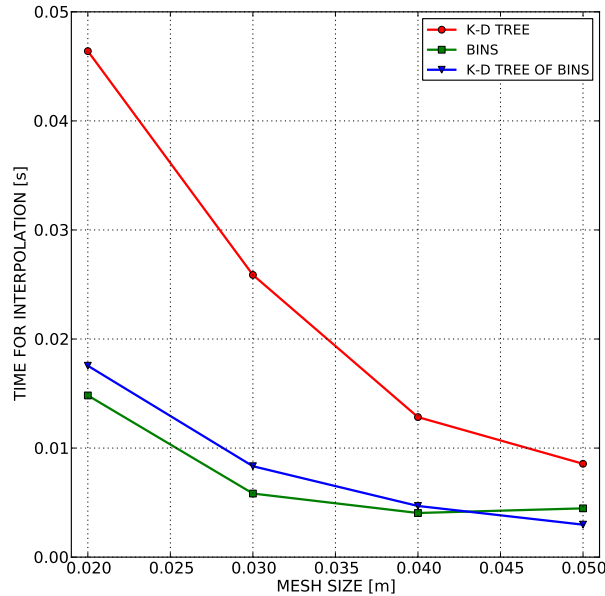
Figure 4.16: Comparison between the performance of k-d tree, bins, and k-d tree of bins data structures for the projection of a scalar variable for different mesh sizes.

4.6   Conclusions

In the present chapter the staggered balance equations of the coupled model have been derived from the global balance equations. The explicit coupling strategy is described and a simple example has been used to check the capability of the model of calculating the effective pressure distribution for a static case.

In the second part of the chapter a procedure to map variables from non-matching meshes is presented. After a brief overview of the possible data passing models the implemented Element Transfer Method is explained. In spite of the diffusivity of the method and its moderate accuracy, it is chosen because of its simplicity. In the future this tool could be easily substituted with a more efficient projection technique. The searching algorithms available in Kratos have been presented.

The examples analyzed lead to the following conclusions:

1. The origin and the destination mesh should be of the same order of magnitude to ensure an accurate data mapping.

2. The static bins structure is the best choice for an homogeneous distribution of the

nodes, Nevertheless the k-d tree data structure can be competitive for examples with an alternation of dense and sparse distribution of nodes.

In any case a deeper study on the performance of the mapping technique is to be done in order to optimize the code.

Chapter **5**

Failure analysis of scale models of rockfill dams under seepage conditions

In the present chapter the seepage and the coupled models are validated through a comparison with the experimental results on scale models of rockfill dams in different seepage conditions, carried out by UPM and CEDEX during the XPRES and E-DAMS projects [53, 127]. The effectiveness of the models are tested on $2D$ and $3D$ models of rockfill dams with different types of impermeabilization. The influence of some physical and mechanical parameters is studied to calibrate the codes.

5.1   Introduction

The extensive work of UPM and CEDEX during the XPRES and E-DAMS projects [53, 127] results in more than 100 experiments. Three experimental facilities of different dimensions have been used (they can be seen in Figure 1.6 of Chapter 1). The main objective of the experimentalists during the XPRES project was the analysis of the influence of a series of parameters and of their combination, on the failure mechanism of the dam.

The experimental campaign investigated the effect of

- the type of impermeabilization;

- the slope of the downstream part;

- the dimension of the material used;

- the randomness in the experiments;

- the incoming discharge[1];

- the scale effect;

Each experiment studies a scale model dam under a series of incremental "steps of discharge". After each increment, the incoming discharge is maintained constant till reaching the steady state. When a breach appears in the downstream slope, its stabilization is achieved before measuring its advance.

Pressure heads is registered and the length of failure is therefore measured at each "step".
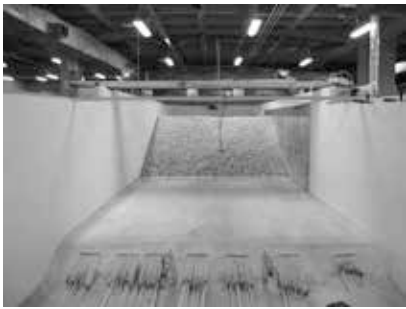
(a) Front view of UPM channel with the pressure sensors tubes.
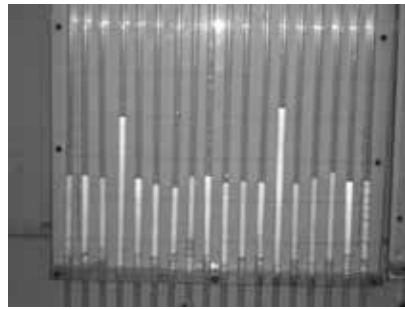
(b) One of the panels for reading pressure heights.

Figure 5.1: Pressure instrumentation.

Pressure at the bottom of the flumes is evaluated by a network of sensors Figure 5.1(a). Its value is read on millimetric panels like the one shown in Figure 5.1(b).

The deformation of the dam is analyzed through the evolution of the so called length of failure (B parameter in Figure 5.2(a)). It is, by definition, the horizontal projection of the distance between the initial undeformed downstream toe and the higher point of the failed area.

Usually colored horizontal strikes are painted on the initial slope. This helps the measurement of B (see Figure 5.2(b) for instance). In some of the experiments a more detailed measurement of the evolution of failure is performed using a *close-object-photogrammetry-technique*. It consists on taking a series of photos with a very short

---

[1]The incoming discharge is a boundary condition of the experiment. It is the discharge (in l/s) pumped upstream by the laboratory pumps.
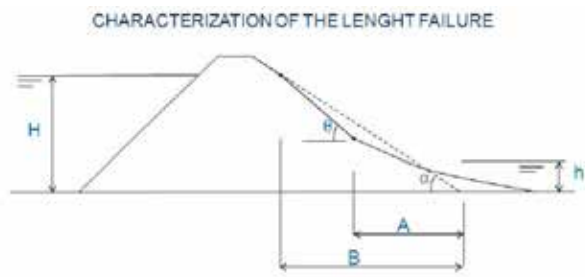
(a) Schematic view of the length of failure (B).
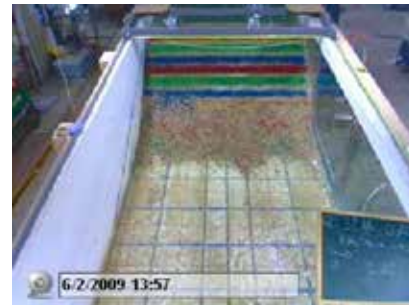
(b) Visual measurement of the advance of failure with the help of colored lines.

Figure 5.2: Length of failure. Characterization and operative measurement.

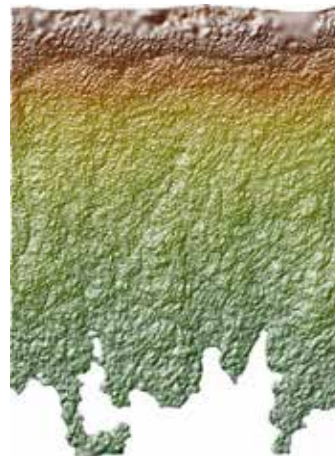Figure 5.3: Length of failure. Digital model of the deformed slope to evaluate the evolution of failure B.

time interval until the end of the simulation. Through the re-elaboration of this data, the creation of a digital model of the deformed dam is possible and the dynamic evolution of the breach is followed with high precision (see for instance Figure 5.3).

The experiment ends when failure reaches the crest of the dam.

The analysis of the experimental campaign is not the objective of the present work and for more details on the topic, the consultation of [21, 76] is recommended. Nevertheless some important conclusions of the experimental study are summarized here in order to motivate the choice of the case study presented in the following sections.

1. As explained in Chapter 1, there exists two main failure mechanisms in a rockfill slope when overtopping occurs: mass sliding and dragging of particles. They act in combined or alternative way principally depending on the geometrical characteristics of the downstream slope. For steep slopes ($1.5H : 1V$ for instance) mass sliding predominates over dragging of particles. The opposite occurs when the slope is very flat ($3H : 1V$ for instance). Taking into account this important aspect, UPM and CEDEX observed that data-scatter is higher in the experiments with "intermediate" slopes, where neither the mass sliding nor the erosion are predominant but their action is combined.

2. The length of failure of the first steps of discharge (that is for low water level), presents a rather high data scatter concerning the evolution of the breach. On the contrary the discharge for which failure reaches the crest is always in great accordance.

3. No clear relation can be found between the unit failure discharge[2] and the downstream slope.

4. Considering prototype dams of the same dimension, it has been observed that for a core dam, the unit failure discharge is between 10 and 20% lower than for other kind of dams.

5. The unit failure discharge increased for material with higher D_{50}.

6. Failure is observed to be more fragile in the case of steepest slopes for which the predominant failure mechanism is mass sliding.

---

[2]The unit failure discharge is the discharge for unit length of the flume, for which the failure reaches the crest of the prototype dam.

5.2   Overview of the case study

As a first step in the validation of the fluid and coupled code, a group of experiments has been reproduced numerically. A selection of the results is presented in this work.

The evolution of seepage and beginning of failure in three different types of dams is simulated: an homogeneous dam, without any sort of impermeabilization, a core dam and a dam with an impervious screen in order to identify the difficulties and limitations in all these cases.

All the dams considered have the same downstream slope: $1.5H : 1V$. This geometrical aspect does not have any influence in the modeling of seepage but strongly determines the deformation of the rockfill. In fact, according to experimental evidence (see point 6 of the previous section), mass sliding is predominant in this kind of slopes. The coupled code has been conceived for representing the predominance of this failure mode. For flat slopes (i.e. $H3 : V1$), the inclusion of an algorithm to simulate dragging of surface particles is required. This module has been already developed following [94, 98], nevertheless it still requires extensive testing and is not yet sufficiently mature to be presented in this context.

Only one material has been analyzed its characteristics are summarized in Table 5.1.

Porosity	n	0.4052
Average diameter	D_{50}	$35.04mm$
Dry density	ρ_s	$1490kg/m^3$
Saturated density	ρ_{sat}	$1910kg/m^3$
Apparent specific weight	W	$2500kg/m^3$
Pore index	P_i	0.68
Internal friction angle range	ϕ	$[37° − 42.5°]$

Table 5.1: Properties of rockfill material.

All the previous values are obtained by an external laboratory according to the Spanish norms. For instance the granulometric distribution, according to the UNE-EN 933-1, is the one shown in Figure 5.4. From this analysis, the diameter for which the 50% of the material passes the sieves (D_{50}) is $35.04mm$ as detailed in Table 5.1.

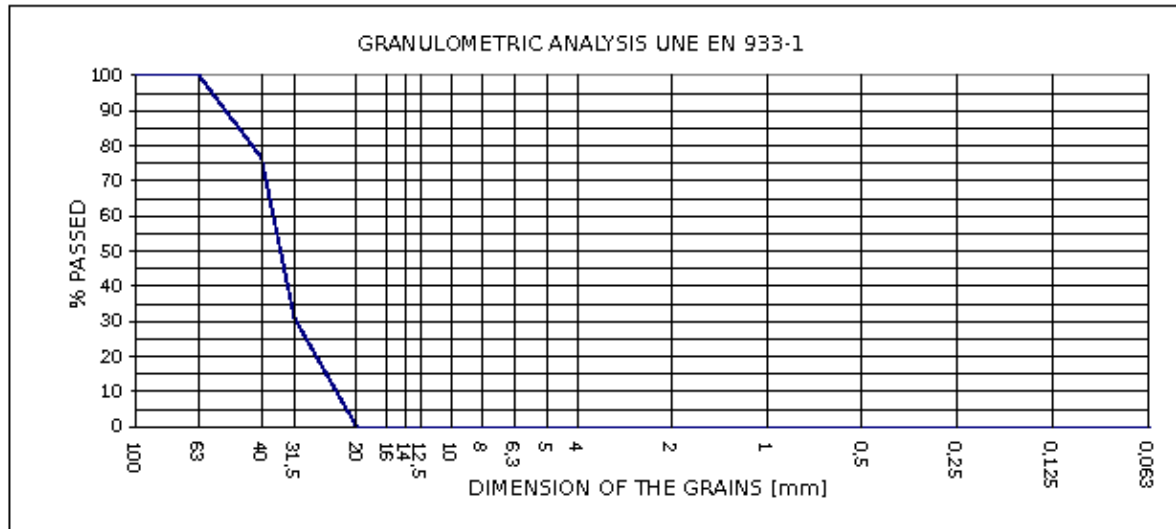| SIEVES UNE	63	40	31,5	20	16	14	12,5	10	8	6,3	5	4	2	1	0,50	0,25	0,125	0,063
% PASSED	100,0	76,6	31,0	0,1	0,1	0,1	0,1	0,1	0,1	0,1	0,1	0,1	0,1	0,1	0,1	0,1	0,1	0,1

Figure 5.4: Granulometric analysis of rockfill material according to the UNE-EN 933-1.

This is the largest material used in the experimental campaign. A direct relation between the dimension of the grains and the discharge of beginning of failure was observed. This implies the possibility of working with higher velocities. In fact this represents a positive aspect because the level set technique can present some problems with very low velocities (i.e. very low water depth). Just to make an example, at the beginning of the simulation the Froude number[3] can be of the order of 10^{-2}.

Finally for each experiment, different steps of discharge have been simulated. In all the cases with the lower discharge considered no movements in the downstream slope is observed. This implies that, in order to speed up the calculations, the fluid uncoupled code can be used for the simulation. The coupled model is used for the higher discharges.

Before presenting of the results, the nomenclature used to classify the cases is briefly resumed here.

Three different type of dams are simulated in the present chapter:

- **CASE A**: an homogeneous dam without impermeabilization.

---

[3]Froude number is an a-dimensional number indicating the ratio between gravity and inertia forces. It is used to classify the flow regime [58].

- **CASE B**: a dam with internal core. Only the downstream slope is simulated.

- **CASE C**: a dam with an upstream impervious face.

For each case i ($i = A, B$, and C), two sub-step analyses have been carried out:

- Case $i1$: Analysis of the non-linear seepage given an incoming/overtopping discharge. Experimentally no deformation is observed in the dam. This analysis is carried out with the fluid uncoupled code.

- Case $i2$: Analysis of the evolution of failure given an incoming/overtopping discharge. Several increasing values of discharges are considered for each case according to experiments. In this case the coupled code is employed.

Finally in Table 5.2 the discharge (Q in l/s) for every simulated case is detailed.

	CASE A Homogeneous dam	CASE B Core dam	CASE C Impervious face dam
WITHOUT FAILURE	A1 $Q = 25.46l/s$	B1a $Q = 5.93l/s$ B1b $Q = 4.0l/s$ B1c $Q = 16.7l/s$	C.1 $Q = 5.17l/s$
WITH FAILURE	A2.1 $Q = 51.75l/s$ A2.2 $Q = 69.07l/s$ A2.3 $Q = 90.68l/s$	B2a.1 $Q = 19.36l/s$ B2a.2 $Q = 30.45l/s$ B2a.3 $Q = 39.56l/s$	C2.1 $Q = 15.36l/s$ C2.2 $Q = 25.05l/s$ C2.3 $Q = 30.27l/s$

Table 5.2: Case study.

The detailed position of the pressure sensors and the experimental data for each case are not reported here but can be found in [74]. This benchmark was selected to be one of the three themes of the XI Benchmark workshop of ICOLD on Numerical Analysis of Dams that held in Valencia in October 2011. The proposed solution to this benchmark can be found in [73].

Figure 5.5: Experimental setting.

5.3   CASE A: Homogeneous dam

The first example reproduces an experiment carried out by UPM: a dam without any internal core or impervious screen is analyzed.

5.3.1   Case A. Experimental setting and geometry

The geometry of the prototype dam is presented in Figure 5.6, where also the distribution of the bottom pressure sensors is indicated.
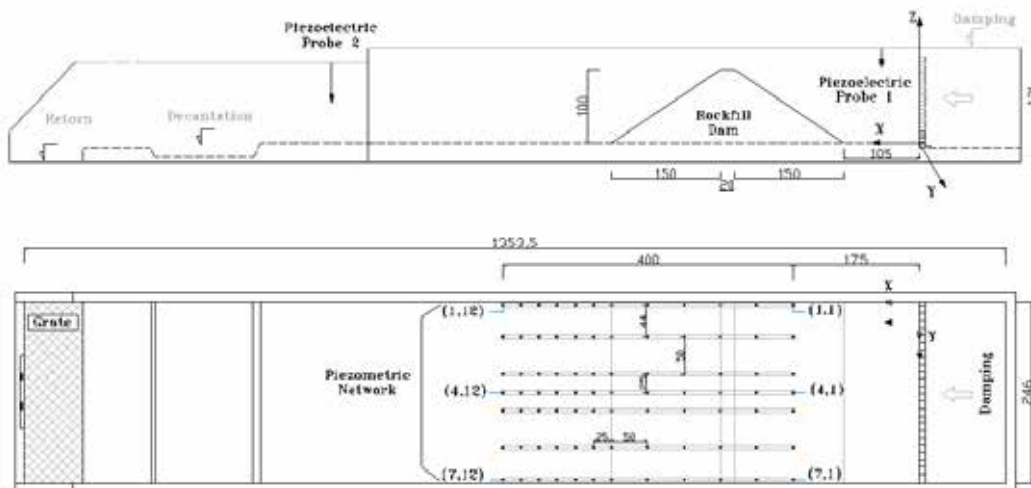

Figure 5.6: Case A. Geometry of the experimental setting and map of the sensors distribution.
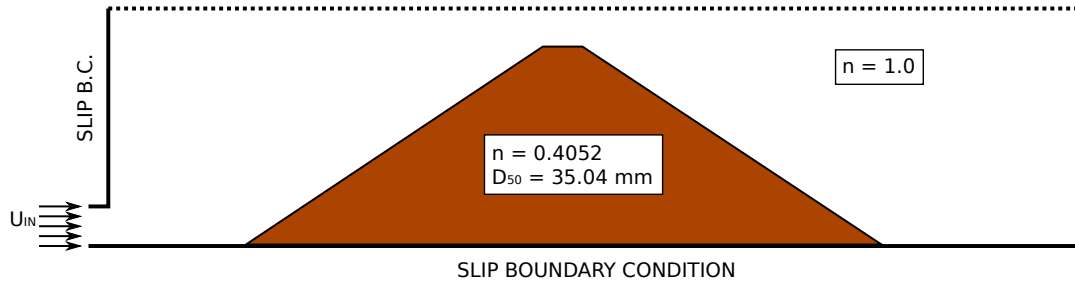
Figure 5.7: Case A1. Qualitative model geometry and boundary conditions

5.3.2 Case A1. $2D$ numerical model and results

The numerical model is built following the geometry of the experiment [74]. The control volume of the Eulerian fluid model has to be large enough in order not to influence the solution.

Concerning the boundary conditions, an inlet with fixed velocity is set in the left side of the control volume. A slip boundary condition is imposed on the walls as shown in Figure 5.7. The mesh used for the simulation has $16\,347$ linear triangular elements. As explained in the next sections, the mesh size does not affect relevantly the quality of the results.

The code can simulate the unsteady regime of the filling of the upstream reservoir even if experimental data only refers to the steady state. Figure 5.8 gives an example of the unsteady part of the simulation.

In Figure 5.9 the comparison between numerical and experimental head of pressure is shown.

The agreement is good even if the numerical code underestimates the experimental values. This is the consequence of the model chosen for the resistance law (see Section 2.1.3 for a discussion of the topic).

Considering that the geometry of the experiment and the inflow discharge are correct, the parameters that might influence the results of the model are:

1. The quality of the mesh;

2. The value of the porosity n;

3. The value of the average diameter D_{50}.

In order to understand how an error in the determination of each of these parameters can influence the solution, a deeper analysis is carried out in the following sections.
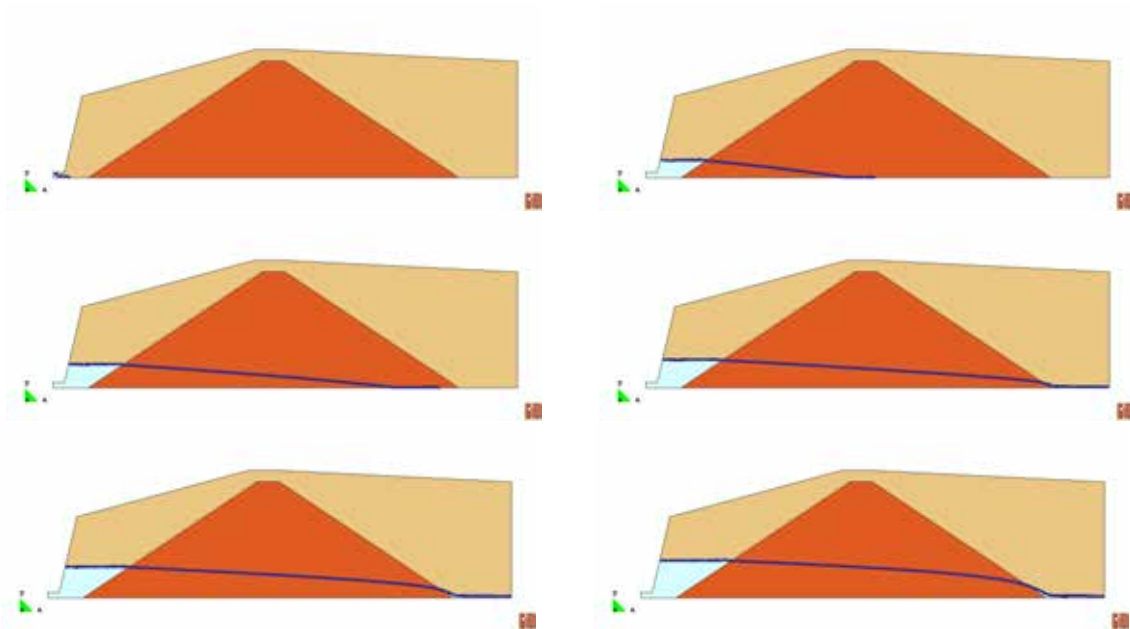
Figure 5.8: Case A1. Evolution of the seepage line in a dam with porosity $n = 0.4$ and $D_{50} = 35mm$. $Q = 25, 46l/s$.
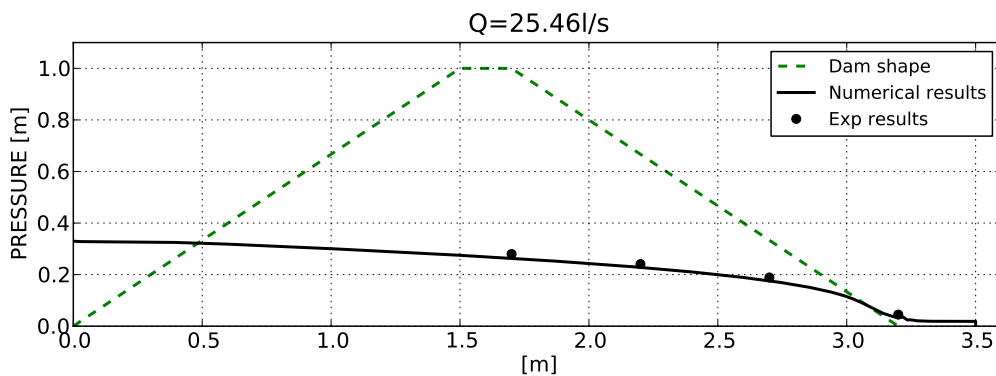

Figure 5.9: Case A1. Bottom pressure distribution at stationary regime for $Q = 25, 46l/s$. Porosity $n = 0.4$, $D_{50} = 35mm$. Numerical and experimental comparison.

5.3.3 Case A1. Mesh influence

In order to understand how the mesh influences the results, case A1 is run with different meshes. The inlet area has been left constantly refined ($h_{ref} = 0.01m^4$) in order to ensure a constant incoming discharge before entering the porous medium. The characteristics of the meshes are summarized in Table 5.3 and can be seen in Figures 5.10.

	Mesh A	Mesh B	Mesh C	Mesh D
Dimension [m]	0.01	0.1	0.15	0.20
n. elem	43 500	550	310	220
n. nodes	86 100	970	510	340

Table 5.3: Case A1. Mesh sizes used in the mesh sensitivity study.

Results shows that the mesh does not seem to have a strong influence on the quality of the results at least inside the dam when no impervious structures are present. The main difference can be observed at the downstream toe of the dam, where water comes out of the granular material. For coarser meshes an important loss of volume can be observed outside the rockfill. The presence of the porous medium with its dissipative effect is helpful in enforcing the volume conservation properties also for very coarse meshes like mesh D, for instance. This is no longer true outside the granular material.

This aspect should be taken into account when choosing the mesh for a simulation.

5.3.4 Case A1. Influence of porosity

The porosity of the material used in the experiments presented in this chapter is evaluated by an external laboratory according to the Spanish norm UNE-EN 1936:2007 and is 0.4052.

Keeping all the parameters of the models and the calculation mesh fixed, porosity is changed in the range $0.30 - 0.45$ in order to see the influence of this parameter in the analysis. A constant variation in the porosity value Δn induces a constant jump in the pressure head distribution as can be observed in Figure 5.12.

---

[4]h is the average mesh dimension. In this case the sub-index *ref* indicates that this h refers to the refined areas at the inlet.
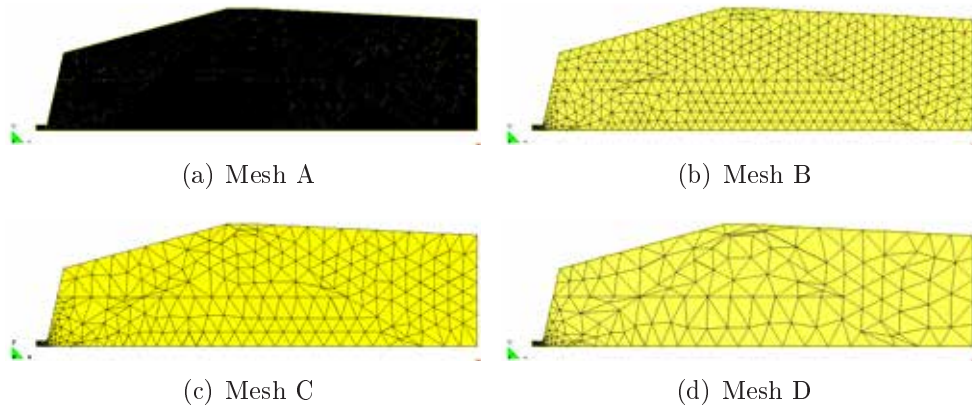
(a) Mesh A

(b) Mesh B

(c) Mesh C

(d) Mesh D

Figure 5.10: Case A1. Meshes used in the analysis of mesh sensitivity. Detailed characteristics of the meshes can be found in Table 5.3.
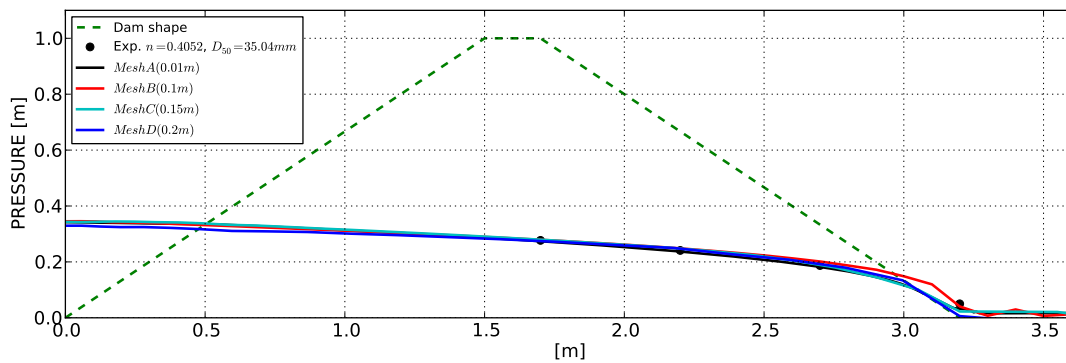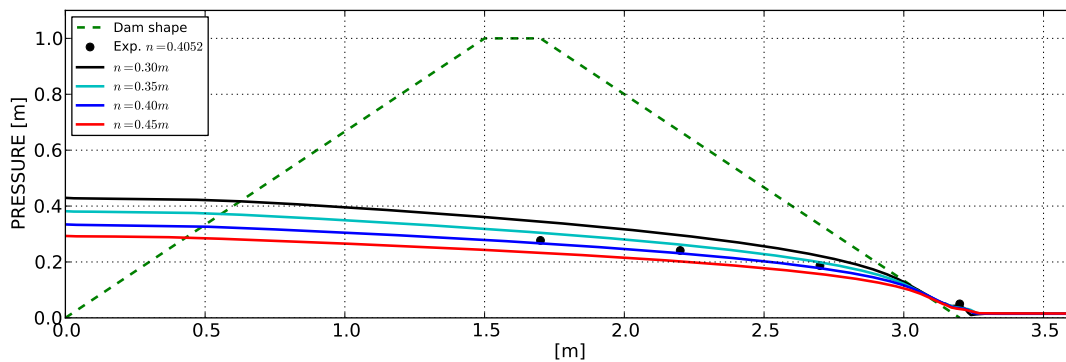

Figure 5.11: Case A1. Influence of the mesh.

Figure 5.12: Case A1. Pressure head distribution for porosity $n = 0.3, 0.35, 0.4$ and 0.45.

The numerical results obtained for $n = 0.4052$ yields a lower pressure head, while the case with $n = 0.35$ overestimates the experimental data. The same problem was subsequently analyzed in more detail considering smaller porosity increment. The results adopting $n = 0.37, 0.38$ and 0.39 are shown in Figure 5.13. The experimental data agree well with the case of $n = 0.38$.
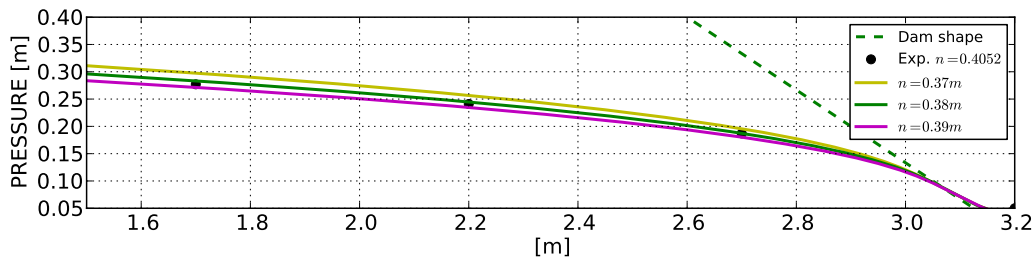

Figure 5.13: Case A1. Zoom of the pressure head distribution for porosity $n = 0.37, 0.38$ and 0.39.

5.3.5 Case A1. Influence of the diameter of the material

The last analysis concerns the influence of the D_{50} value. This value is changed with an increment of $1cm$ from 1 to $8cm$. It is interesting to observe Figure 5.14 where the decrement of pressure head is not linear with respect to D_{50}. Moreover if $D_{50} > 5cm$ its influence on the pressure distribution is negligible. On the contrary, the smaller the D_{50} is, the bigger its influence on the pressure distribution.
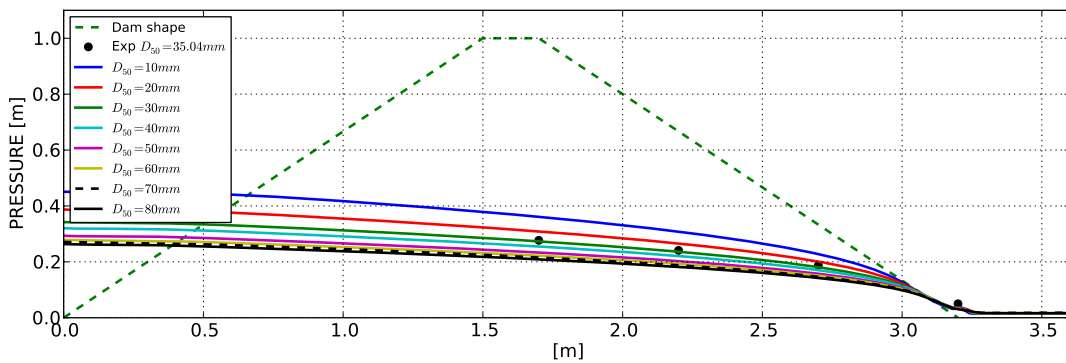

Figure 5.14: Case A1. Influence of the diameter of the material.

5.3.6 Case A1. $3D$ numerical model and results

The $3D$ model of case A has been considered following the geometry given in Figure 5.7. The control volume is meshed with a 1 264 015 4-noded linear tetrahedra linear elements as shown in Figure 5.15.

Figure 5.15: Case A1. 3D model and mesh.

Three lines of pressure sensors where activated during the experiments (respectively lines 1, 4 and 7 of the plane view of Figure 5.6). They are located along the central line and at $4cm$ from each side of the channel. By identifying Y with the coordinate in the transversal direction (as shown in figure 5.6), the exact position of the sensor lines for case A is detailed in Table 5.4.
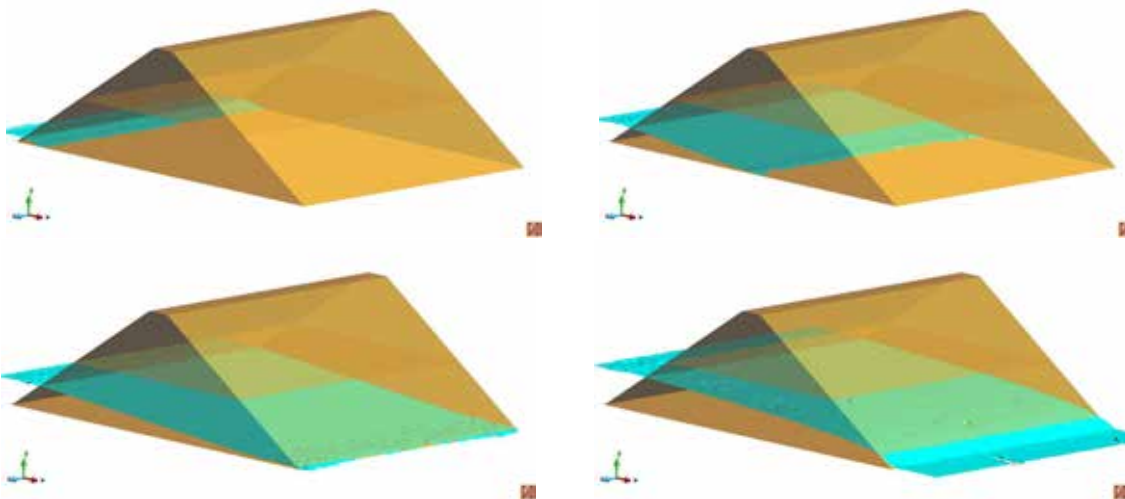

Figure 5.16: Case A1 3D. Evolution of the seepage line in a dam with porosity $n = 0.4$ and $D_{50} = 35mm$. $Q = 25, 46l/s$.

A sequence of the transitory phase of filling of the dam can be observed in Figure 5.16.

Line 1 at $Y = 0.04m$

Line 4 at $Y = 1.23m$

Line 7 at $Y = 2.42m$

Table 5.4: Activated sensors lines in case A.

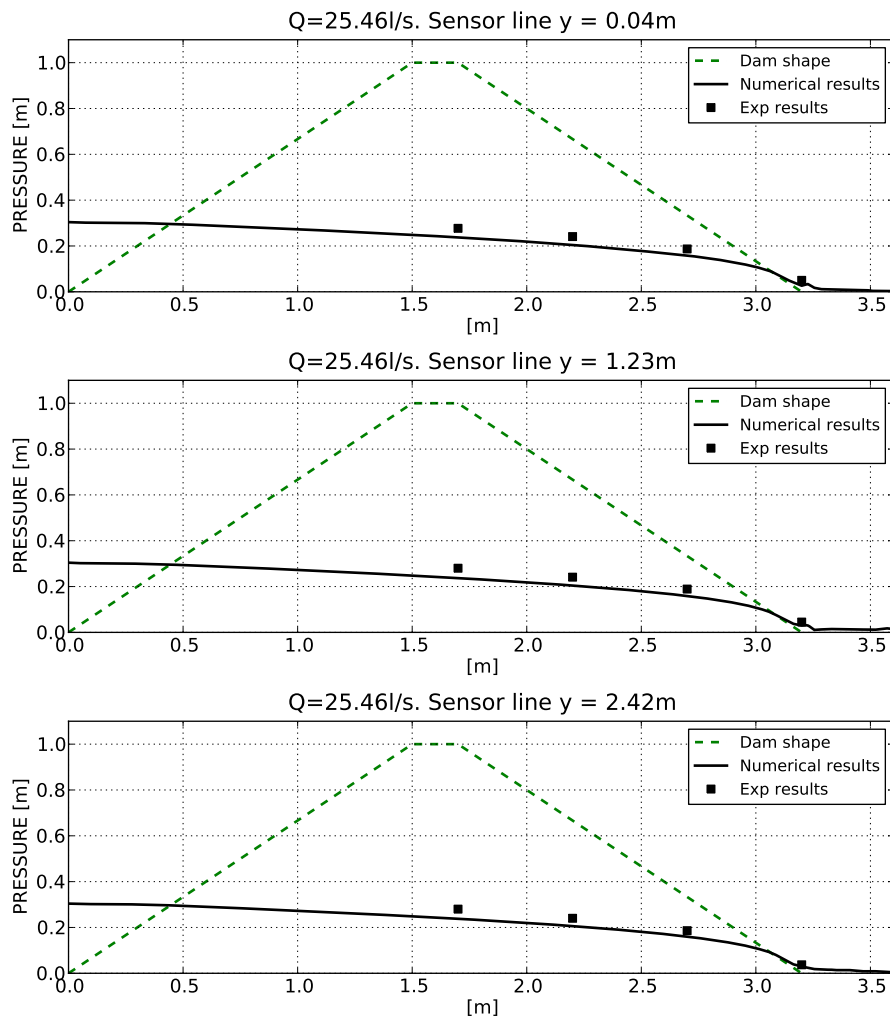Figure 5.17: Case A1 ($3D$). Bottom pressure distribution at stationary regime along the three sensors lines ($Y = 0.04m, 1.23m, 2.42m$ respectively) for $Q = 25, 46l/s$. Porosity $n = 0.4$, $D_{50} = 35mm$. Numerical and experimental comparison.
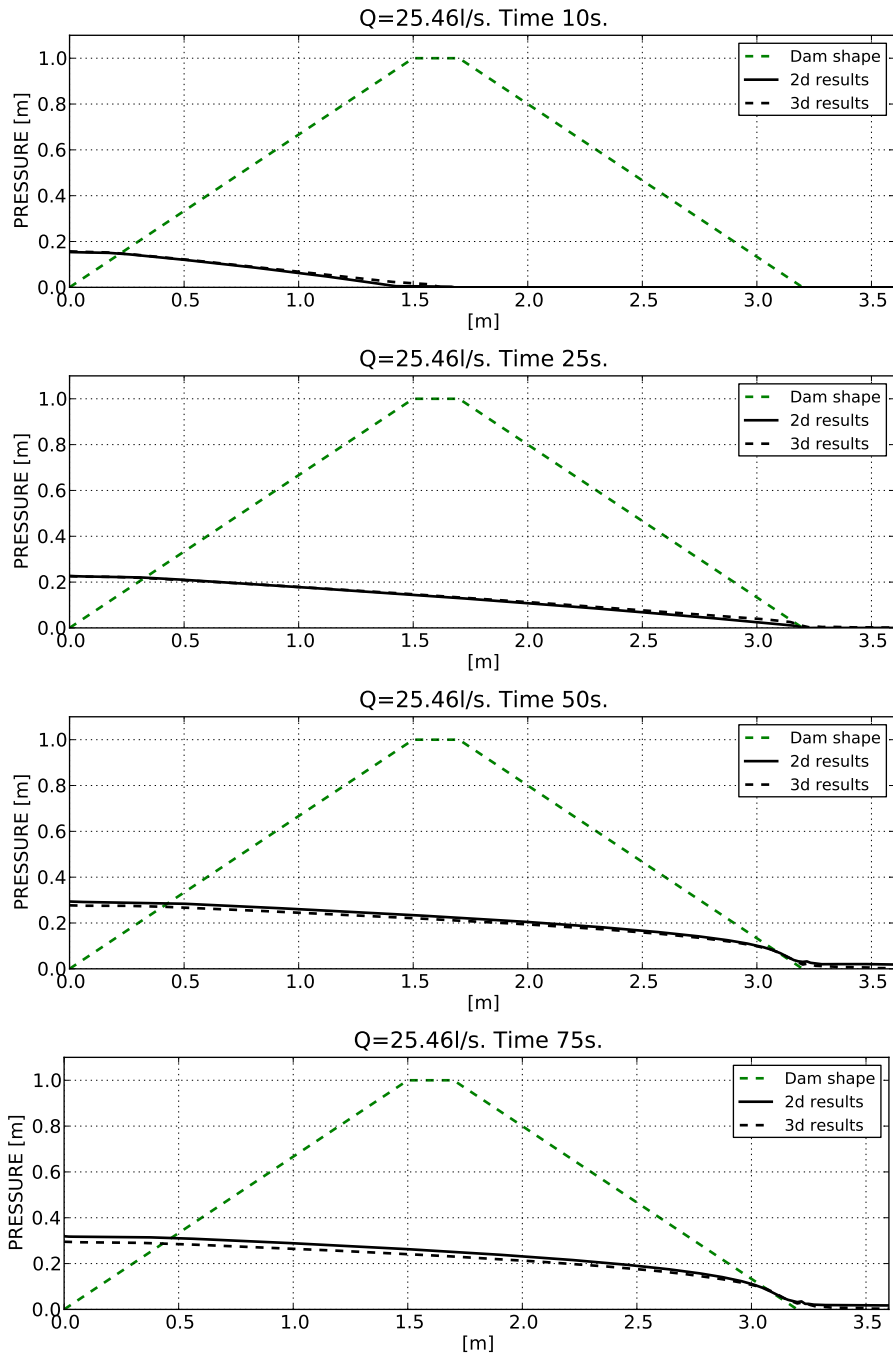
Figure 5.18: Case A1. Bottom pressure distribution in $2D$ and in $3D$ models at different instances of the transitory regime. $Q = 25.46l/s$. Porosity $n = 0.4$, $D_{50} = 35mm$.

Figure 5.17 shows the comparison between experimental values measured at different Y and the correspondent numerical results. The $3D$ results for case A1 confirm that the model underestimates the experimental results.

Finally a comparison between the $2D$ and $3D$ models is performed for the unsteady regime at different time instances and the bottom pressure distribution is plotted as shown in Figure 5.18.

5.3.7 Case A2. $2D$ coupled model and results
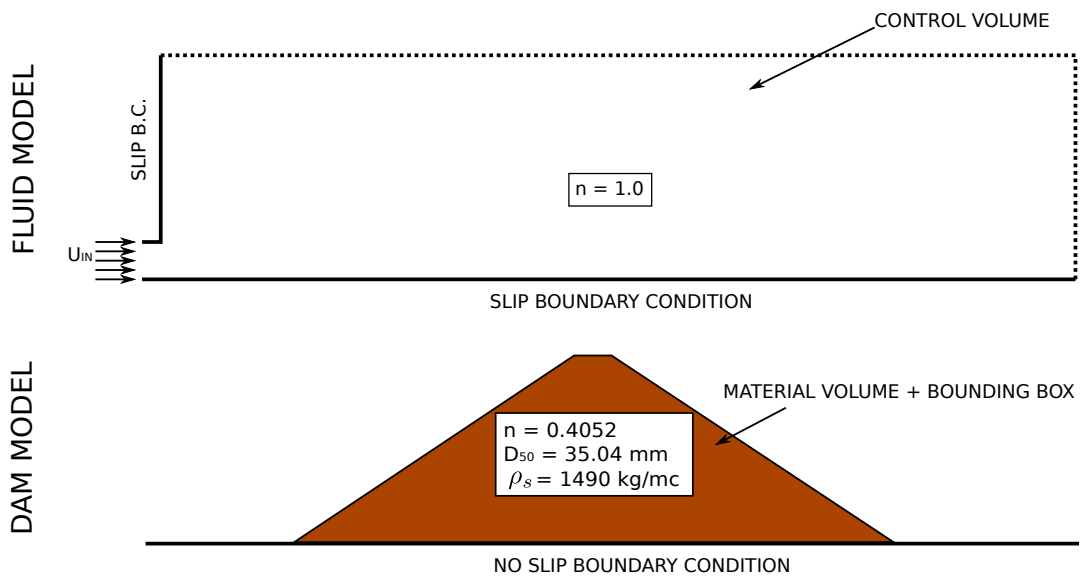
Figure 5.19: Case A2. Fluid and dam qualitative models and boundary conditions for the coupled analysis.

The coupled models aim to simulate the seepage line and the overtopping flow while following the evolution of the breach in the dam material. It is composed of two parts:

- The fluid Eulerian model. Its construction is analogous to the case A1 and the mesh properties are the same. The main difference derives from the absence of any porous material. This information is passed during the calculation, by the PFEM model.

- The PFEM structural model. The dam model is constructed in a Lagrangian framework. This implies modeling only the material domain (i.e. the dam initial shape and the walls if present). The definition of a bounding box is required. It

sets the maximum calculation domain. If a node exits the bounding box is no longer calculated and is deleted.

Remark 22. A preliminary remark on the interpretation of the experimental data should be made here. The experimental B length of failure is by definition the horizontal projection of the position of the higher particles that moves. This movement is not quantified. In the present work it was assumed that a particle is to be considered "moved" if its total displacement is higher than the average dimension of the granular material ($3.0cm$). This choice is arguable and, as it will be shown later on, it often makes our model too deformable. Nevertheless this empirical criterion was used in all the models analyzed in order to allow a comparative analysis.
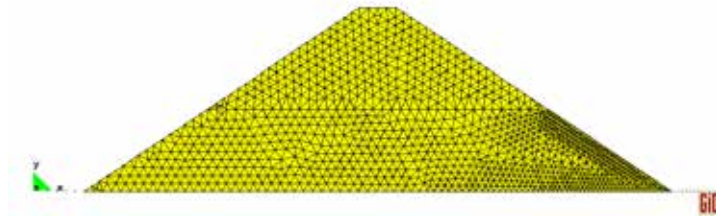

Figure 5.20: Case A2. $2D$ mesh of the dam model. 3.400 linear triangular elements.

In Figure 5.19 a schematic view of the fluid and structure boundary conditions is shown. The mesh used for the fluid model is the same used in case A1, whereas for the structural model, the mesh is composed of 3 400 linear triangular elements (Figure 5.20).

The photogrammetric analysis of the A cases was also available and helped the comparison between experimental and numerical results. Figures 5.21-5.23 show on the left the digital model derived by the photogrammetric analysis, and on the right the contour fill of the displacements. The colored area indicates the displacements larger than $3cm$. The reason for this choice is explained in Remark 22. A very good agreement is observed between experimental and numerical length of failure in the three cases.

Looking at the pressure head distribution (figures 5.24-5.24), the experimental bottom pressure head is underestimated by the numerical one. This aspect is more relevant than in case A1. It might be the signal of an internal variation of the material conditions (such as porosity or permeability) that is not taken into account in the model.

Figure 5.26 shows that in case A23, the pressure head presents a lower experimental value where the water exits the dam. The contraction of the flux can be induced by

(b) Numerical length of failure B= Bnum= 0.68m.

(a) Experimental length of failure B= Bexp = 0.71m.
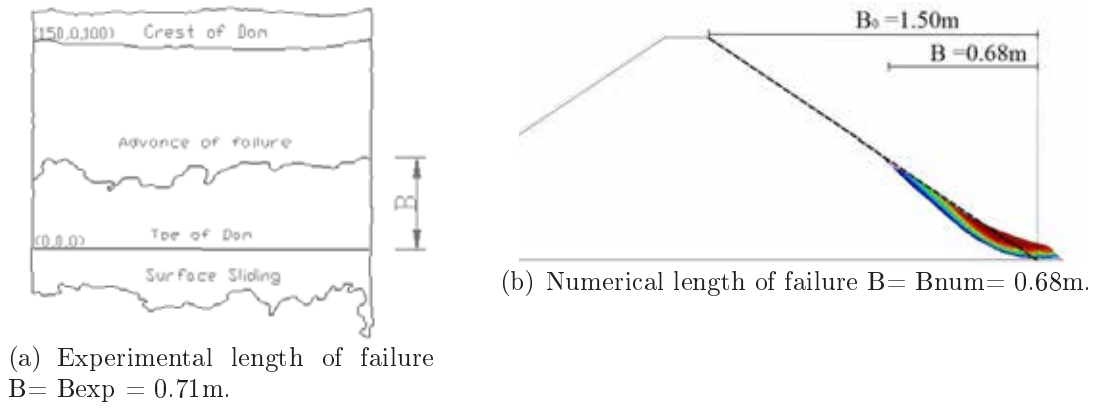
Figure 5.21: Case A21. 2*D* comparison between experimental and numerical length of failure.

(b) Numerical length of failure B= Bnum= 1.04m.

(a) Experimental length of failure B= Bexp = 1.08m.
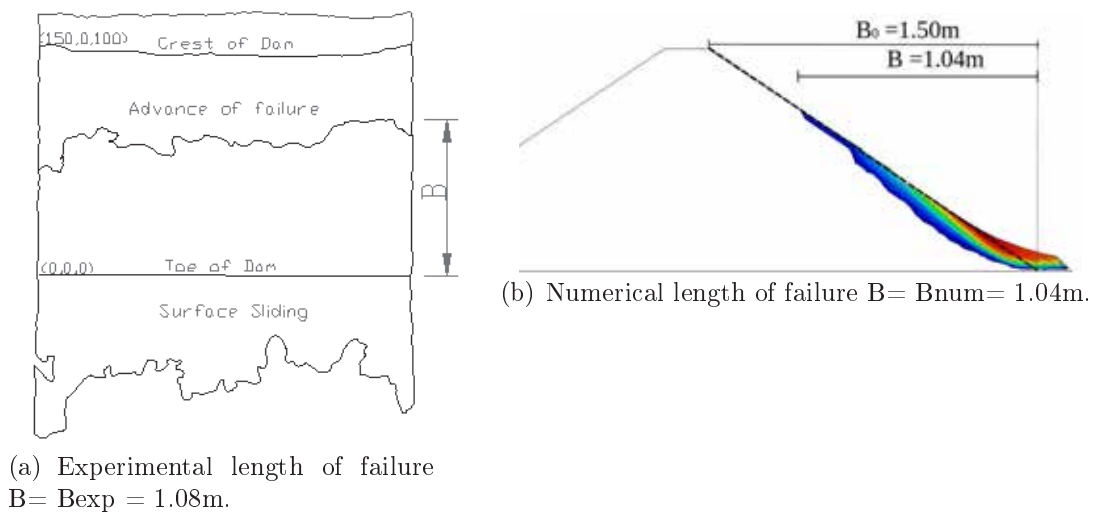
Figure 5.22: Case A22. 2*D* comparison between experimental and numerical length of failure.

(b) Numerical length of failure B= Bnum= 1.58m.

(a) Experimental length of failure
B= Bexp = 1.56m.
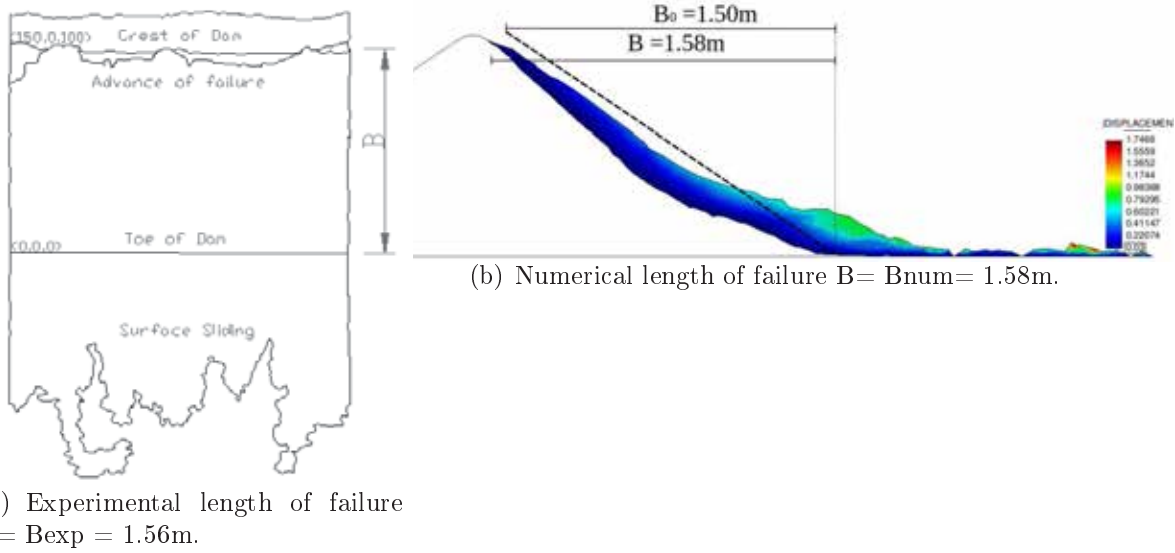
Figure 5.23: Case A23. $2D$ comparison between experimental and numerical length of failure.

Figure 5.24: Case A21. Bottom pressure distribution at stationary regime for $Q = 51.75l/s$. Porosity $n = 0.4$, $D_{50} = 35mm$. Numerical and experimental comparison.

	Q $[l/s]$	B_{exp}	B_{num}	Error
Case A21	51.75	0.71	0.68	4.2%
Case A22	69.07	1.08	1.04	3.7%
Case A23	90.68	1.56	1.58	1.3%

Table 5.5: Case A2. Comparison between experimental (B_{exp}) and numerical (B_{num}) length of failure.

Figure 5.25: Case A22. Bottom pressure distribution at stationary regime for $Q = 69.07l/s$. Porosity $n = 0.4$, $D_{50} = 35mm$. Numerical and experimental comparison.

the absence of the rockfill that flowed away during the failure process. This leads to the conclusion that the failed material in the numerical model is more rigid than in the real case. Its accumulation over the original toe of the dam induces a higher value of pressure than in the experiment.
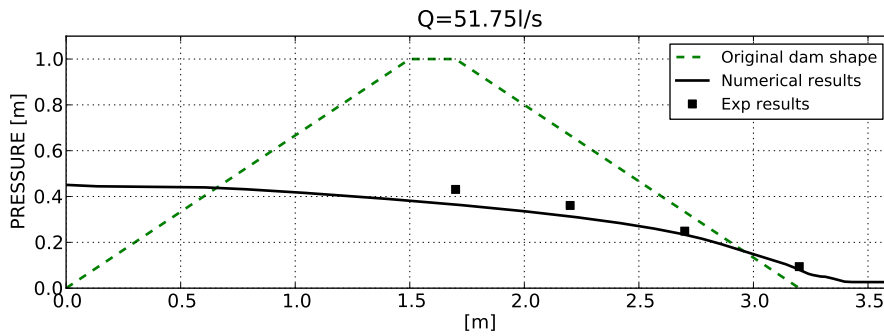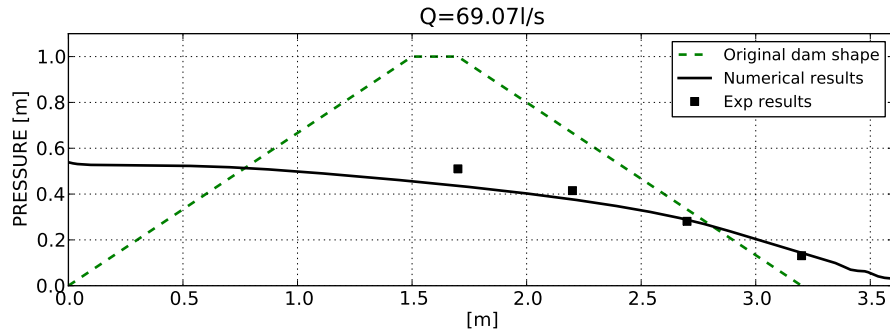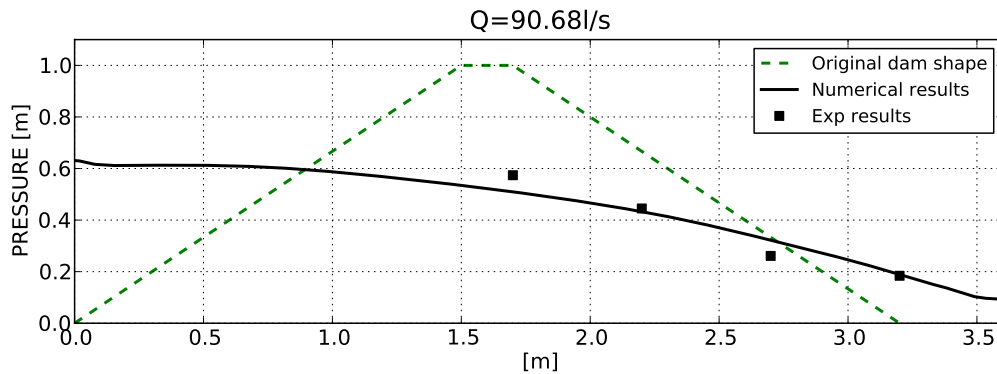

Figure 5.26: Case A23. Bottom pressure distribution at stationary regime for $Q = 90.68l/s$. Porosity $n = 0.4$, $D_{50} = 35mm$. Numerical and experimental comparison.

5.3.8   Case A2. $2D$ sequence of incremental discharges

The code was conceived to analyze the consequence of transitory incoming discharges, allowing inserting flooding curves as an input. Unfortunately this capability has not been exploited in the examples presented because the experimental results where given for the stationary regime and no comparison can be made in the transitory regime. Fortunately in the last months, the UPM partners in the E-DAMS project have been

performing some experiments considering variable incoming discharges according to a hydrogram.
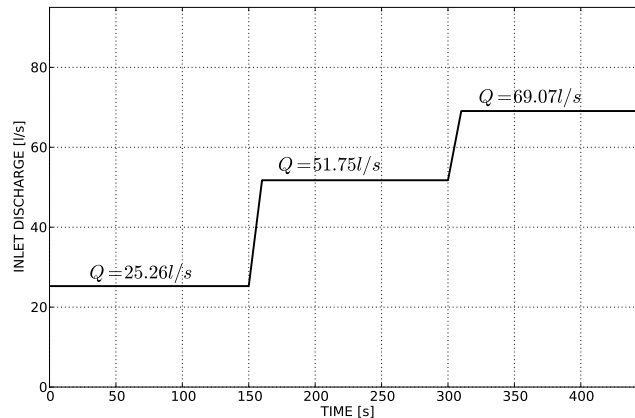
Figure 5.27: Imposed incoming discharge in function of time.

 As a preliminary test, cases A1-A21-A22 were run in sequence leaving the sufficient time for the intermediate stationary regime to be achieved. The imposed curve representing the inlet discharge in function of time, is reported in Figure 5.27. The pressure head in correspondence of two pressure sensors location is registered as can be seen in Figure 5.28. The two points are located at $2.2m$ and $2.7m$ from the upstream toe of the dam. The dotted line in the graph is the stationary value of pressure read from the piezometers in the cases A1, A21 and A22 respectively. Also in this case the numerical results underestimate the experimental ones and the error is analogous to the one presented in the previous section.

5.3.9   Case A2. $3D$ coupled model and results

Some preliminary results have been obtained also in $3D$. The fluid and structural models have been developed according to what explained in Section 5.3.7 for the $2D$ validation. On the other hand, the deformation of the dam is not so clear as in the $2D$ case. This happens because the deformation is partially skewed by the remeshing at each time step. As explained in Section 3.7, remeshing is a key point of PFEM. In fact this method was originally conceived to treat Newtonian free surface problems where the regeneration of the mesh is always required. This is not the case of the present non-Newtonian algorithm where in most of the steps all the nodes are in the unyielded region and do not move.
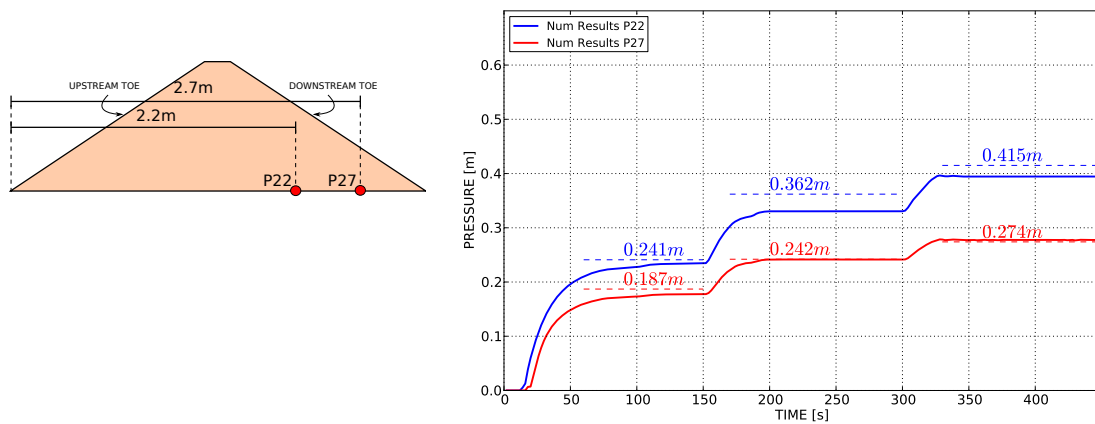
Figure 5.28: Bottom pressure distribution considering the hydrogram presented in Figure 5.27. Porosity $n = 0.4$, $D_{50} = 35mm$. Numerical and experimental comparison.
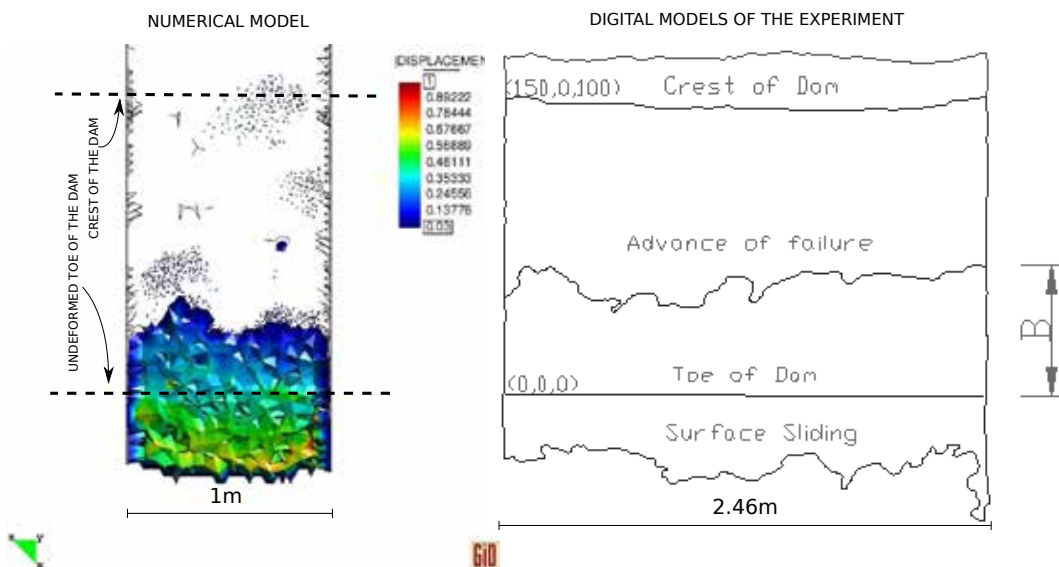
Figure 5.29: Case A22 $3D$. Numerical and experimental length of failure.

For this reason the possibility of inserting a conditional remeshing in the problem is to be added in the code in order to have a viable $3D$ coupled analysis code.

A preliminary tool that allows a conditional remeshing has already been inserted in the code and yields good results like the one shown in 5.29.

The plots of the pressure drop (figure 5.30) shows a good agreement between the results of the $2D$ and $3D$ models (dotted and continuous line respectively). This confirms the results obtained in Section 5.3.6 for the A1 case in $3D$, where only the fluid code was used.
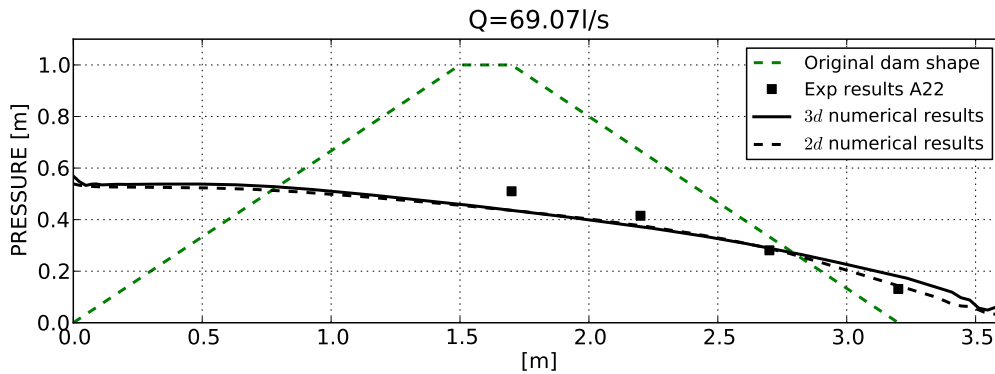
Figure 5.30: Case A22 $3D$. Bottom pressure distribution at stationary regime for $Q = 69.07l/s$. Porosity $n = 0.4$, $D_{50} = 35mm$. $2D$ and $3D$ numerical results compared with experimental data points.

5.4   CASE B. Core dam
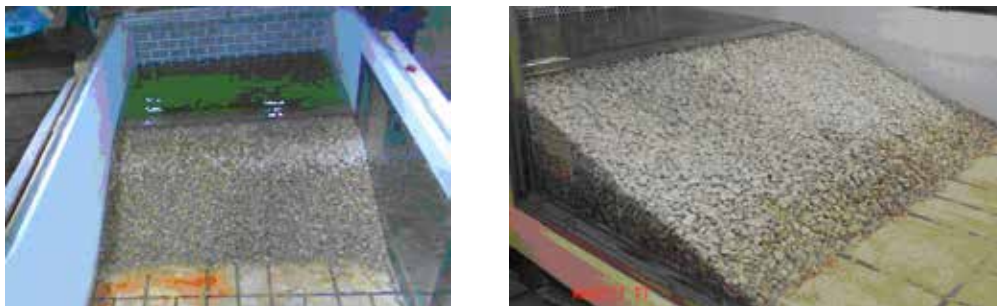
Figure 5.31: Core dam. Experimental setting.

The second experiment simulated in this work is the seepage inside a core dam. The core is considered fixed and undeformable. The experiment is carried out building exclusively

the downstream slope as can be seen in Figure 5.31. The water entrance is set in the upper left part, omitting the simulation of the filling of the reservoir that is useless in the present analysis.

5.4.1 Case B. Core dam. Experimental setting and geometry

The geometry of the dam is presented in Figure 5.32 where the distribution of the pressure sensors on the bottom of the channel can be seen.

The model is built in order to reproduce the real geometry of the experimental setting. Since the case of interest is the simulation of the overtopped flow, the geometry of the model does not include the reservoir. The entrance of water is set in the upper left part as shown in Figure 5.33.
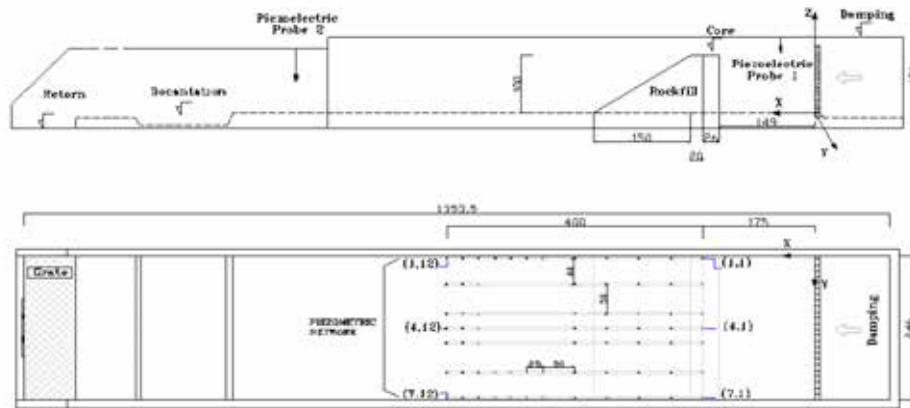
Figure 5.32: Case B. Geometry of the experimental setting and map of the sensors distribution.
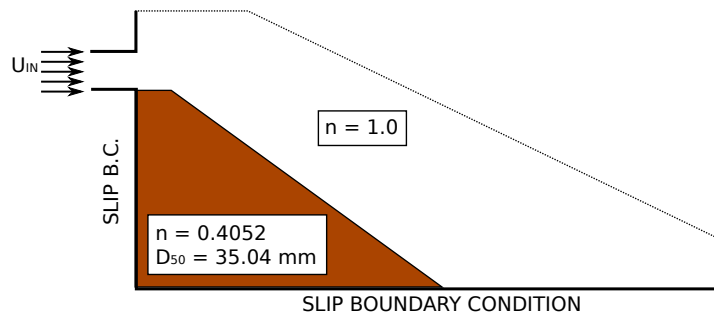
Figure 5.33: Case B1. Qualitative model geometry and boundary conditions.

A slip boundary condition is imposed on the bottom of the channel and on the core side.

5.4.2 Case B1a. Core dam. $2D$ numerical model and results
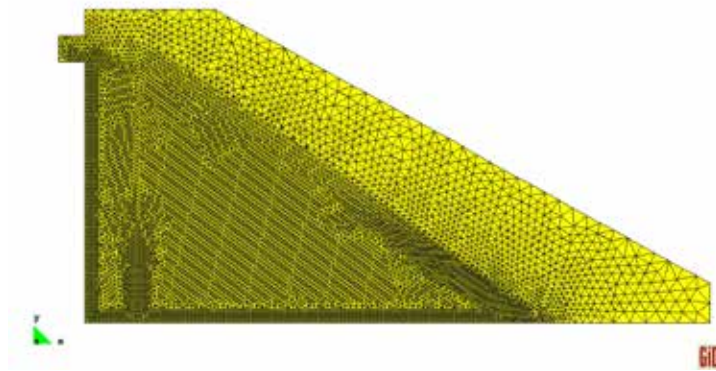
Figure 5.34: Case B1a. Mesh used in the calculation.

The mesh used for the calculation can be seen in Figure 5.34. It has $14\,859$ linear triangular elements. The comparison between experimental and numerical pressure heads can be observed in Figure 5.35.

A refinement of the mesh is performed in the critical zones of the falling of the water and near the bottom of the channel. The reason for that choice will be explained in Section 5.5.2 when describing case C1.
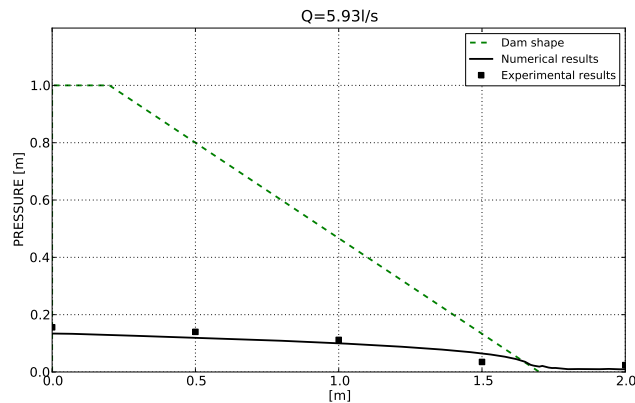
Figure 5.35: Case B1a. Bottom pressure distribution at stationary regime for $Q = 5.93l/s$. Porosity $n = 0.4$, $D_{50} = 35mm$. Numerical and experimental comparison.

Case B presents an additional difficulty in the fluid dynamic problem. It is particularly challenging to simulate correctly the falling jet of water (especially if the incoming water velocity is very slow), without suffering serious mass loss. The good agreement between experimental and numerical pressure heads confirms that this problem can be accurately modeled with the method developed in this work. This is confirmed in the $3D$ simulation of case B1a in Section 5.4.4.

5.4.3 Cases B1b and B1c. Core dam. Comparison with theoretical Ergun model

It has been observed that the numerical pressure head gives lower values than the experimental ones. To verify if the problem can be attributed to the choice of the resistance law, a comparison with the theoretical results is performed according to the work of Lopez Verdejo [125]. In order to do that a slightly different geometry is taken into account. The dam studied is made of the same material as the one presented in the previous sections but the height of the dam is $0.5m$ and the length of the downstream slope is $1.5m$. The slope ratio is $H3 : V1$.

The mesh used is shown in Figure 5.36. It has $2\,865$ nodes and $5\,728$ linear triangular elements.
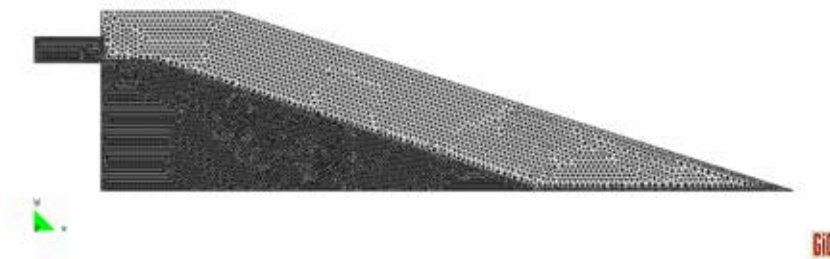
Figure 5.36: Case B1(b-c).Mesh used in the calculation.

The theoretical solution for an incoming discharge of $4.0l/s$ and $16.7l/s$ is plotted in red dotted line in Figures 5.37 and 5.38 respectively. The numerical approximation is very close to the Ergun theoretical one as expected. Both these curves underestimate the experimental values. This confirms that Ergun model might not be the best choice for the resistance law of this kind of problem. In order to overcome this issue the next step will be to modify the code in order to let the user insert a custom quadratic resistance

law.

 As a consequence of this observation CEDEX will build a permeameter for rockfill in order to study deeply this aspect and eventually derive an experimental resistance law for the materials used in the project.

Figure 5.37: Case B1b. Bottom pressure distribution at stationary regime for $Q = 4.0 l/s$. Porosity $n = 0.4$, $D_{50} = 35mm$. Numerical, experimental and theoretical comparison.
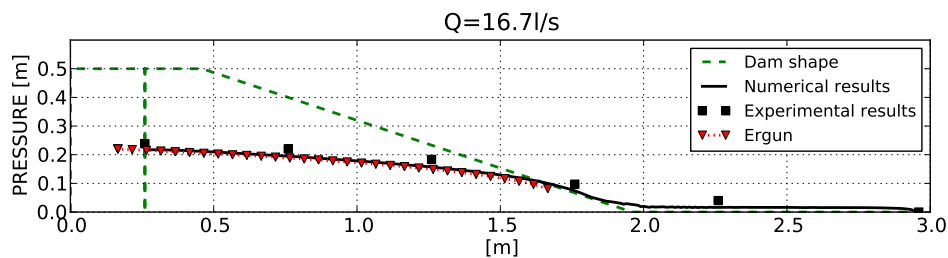
Figure 5.38: Case B1b. Bottom pressure distribution at stationary regime for $Q = 16.7 l/s$. Porosity $n = 0.4$, $D_{50} = 35mm$. Numerical, experimental and theoretical comparison.

5.4.4   Case B1a. Core dam. $3D$ numerical model and results

Case B1a has been simulated in $3D$ as well. Figure 5.39 shows a sequence of the transitory regime of the filling of the core dam. Three different meshes are taken into consideration in order to understand which is the minimum element length to correctly reproduce the experiments, without relevant volume losses.
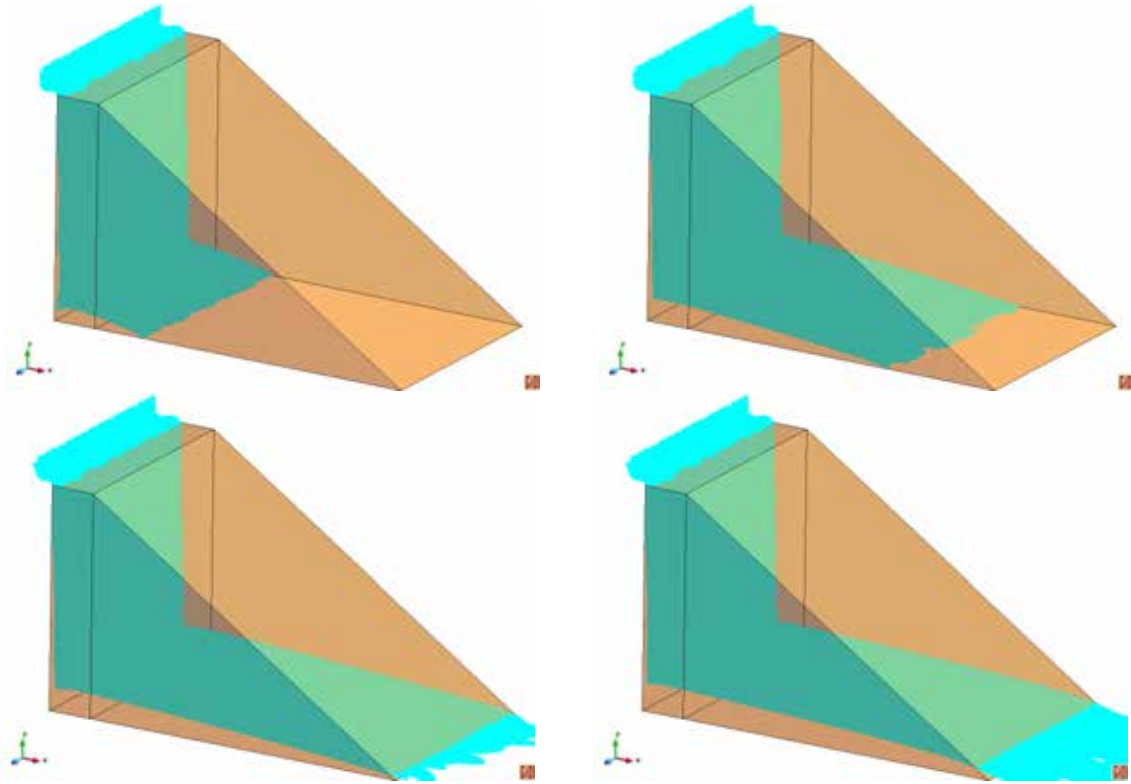
Figure 5.39: Case B1a $3D$. Evolution of the seepage line in a dam with porosity $n = 0.4$ and $D_{50} = 35mm$. $Q = 5.93l/s$.

	Mesh A	Mesh B	Mesh C	Mesh D
Dimension [m]	0.02	0.03	0.04	0.05
n. elem	1 460 000	517 000	281 000	183 000
n. nodes	250 000	89 600	49 000	34 000

Table 5.6: Case B1a. Meshes used for the analysis.

The characteristics of the four meshes analyzed are summarized in Table 5.6. The refinement is performed only in the dam volume, whereas the dimension of the elements is kept fixed in the rest of the domain as it can be observed in Figure 5.40.

(a) Mesh A

(b) Mesh B

(c) Mesh C

(d) Mesh D
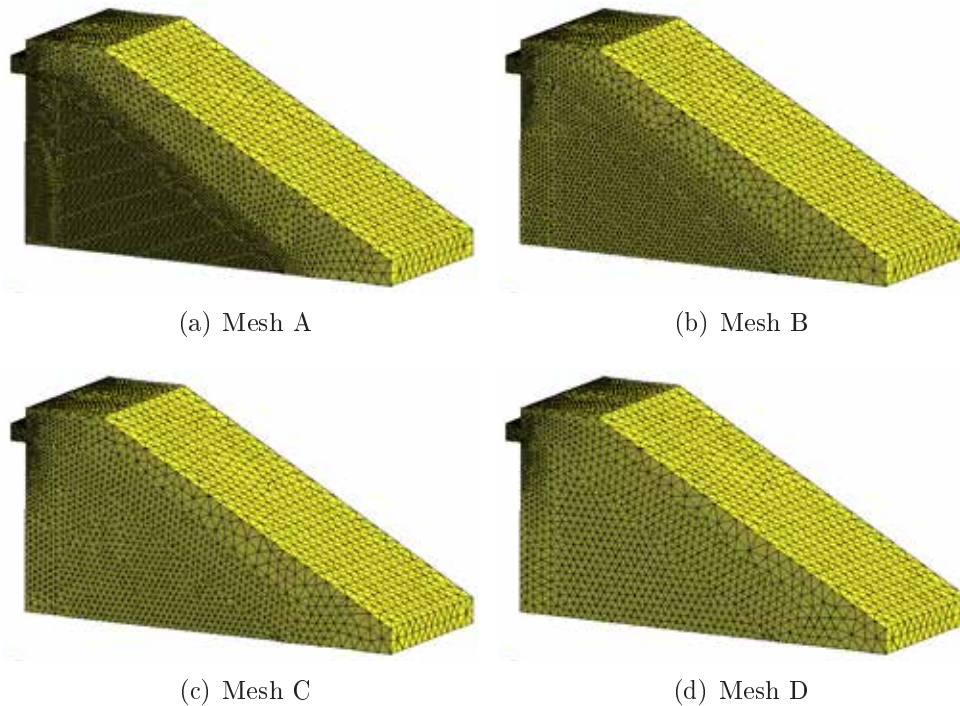
Figure 5.40: Case A1. Meshes used in the analysis of mesh sensitivity. The characteristics of the meshes can be found in Table 5.6.

Figure 5.41 shows the pressure heads for the different mesh sizes. The convergence is achieved when the mesh is finer than $0.03m$. For larger meshes the volume conservation is seriously compromised. This loss takes place when the flux falls down vertically. Therefore particular care should be taken in the refinement for the analysis of a core dam.

5.4.5 Case B2. Core dam. Coupled model and results

The construction of the models for the coupled case is analogous to what already explained in Section 5.3.7 for the A2 case. A schematic representation of the boundary conditions can be found in Figure 5.42.

Figure 5.43 shows the Lagrangian mesh used in the calculation. It has 8 000 linear triangular elements.
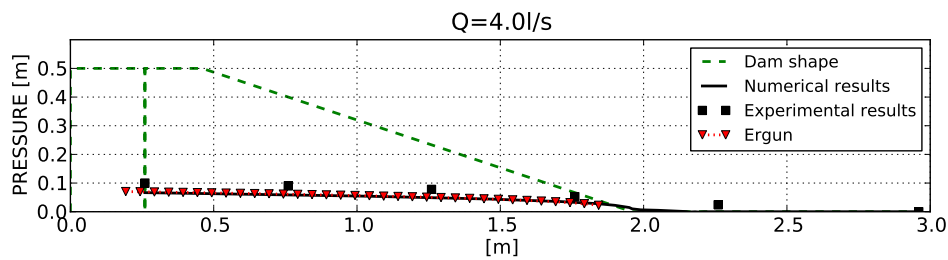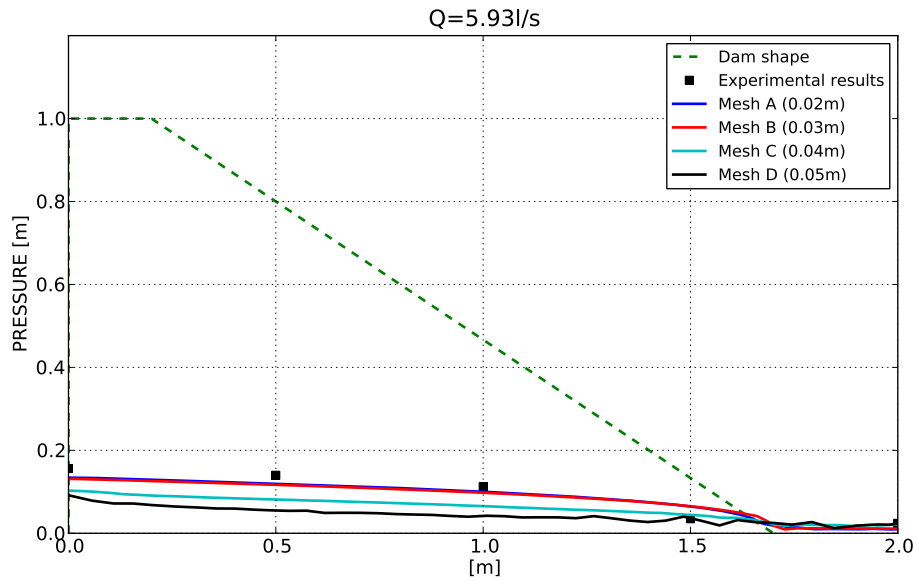
Figure 5.41: Case B1a (3D). Bottom pressure distribution at stationary regime for $Q = 5.93l/s$. Porosity $n = 0.4$, $D_{50} = 35mm$. Numerical, experimental and theoretical comparison.
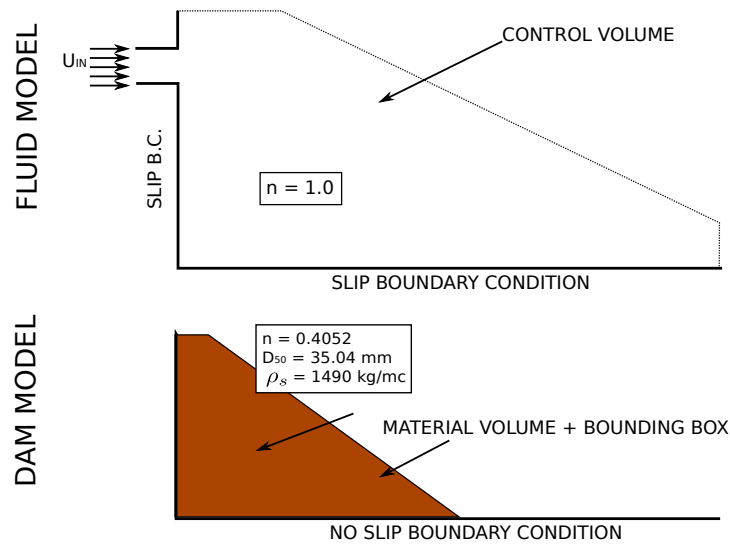

Figure 5.42: Case B2. Fluid and dam qualitative models and boundary conditions for the coupled analysis.
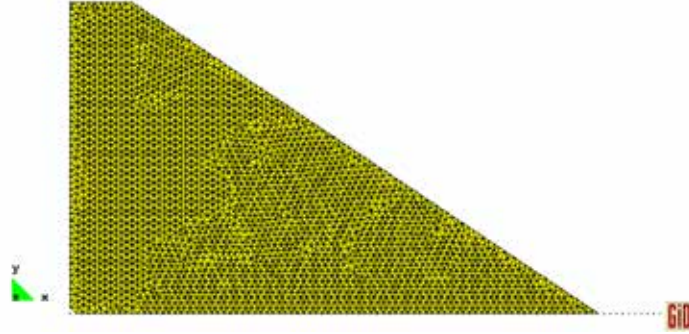
Figure 5.43: Case B2. $2D$ mesh of the dam model. $8\,000$ linear triangular elements.

5.4.6 Case B21. Core dam. Sensitivity analysis: internal friction angle

The numerical length of failure obtained for material with friction angle of 40° and 41° exceeds significantly the experimental measurements. Additional tests were carried out increasing ϕ. The dam remains completely rigid if $\phi = 42°$. Therefore, the intermediate angles were considered as shown in Table 5.7 where the length of failure B obtained for different values of ϕ is summarized.

$\phi\,[^0]$	$B\,[m]$
40	0.92
41	0.76
41.5	0.75
41.54	0.75
41.548	0.74
41.55	0.0
42	0.0

Table 5.7: Case B21. Length of failure B for different ϕ.

The model is able to catch the motion if $\phi < 41.55^0$. Moreover in the range $\phi \in [41 - 41.55]$ no relevant differences are found in the evaluation of B. This indicates that the model is not able to catch correctly the first deformation of the slope. As expected

no relevant changes are observed in the pressure head of the considered cases (figure 5.44).

Figure 5.44: Case B21. Bottom pressure distribution at stationary regime for $Q = 19.36l/s$. Porosity $n = 0.4$, $D_{50} = 35mm$. Numerical and experimental comparison for different internal friction angles ϕ.

The accuracy improves for cases B22 and B23 as explained in the next sections. This fact coincides with what was observed experimentally: the length of failure induced by the lower step of discharge presents a high data scatter whereas the failure achieves the crest always at the same discharge level.

5.4.7   Case B2 with $\phi = 41°$

Since the difference in the length of failure is not so relevant if $\phi \in [41 - 41.55]$, the internal friction angle adopted for case B2 is $\phi = 41°$.

Figures 5.45-5.47 show the comparison between experimental and numerical dam deformation at each step of discharge for $\phi = 41°$. The error in the evaluation of B is progressively reduced when increasing the discharge as detailed in Table 5.8.

An additional consideration can be made looking at the pressure head distribution of the three cases shown in Figures 5.48-5.50. As for the A2 case, the amount of moved rockfill is lower in the simulation than in the experiments. In fact the higher value of numerical pressure at the toe of the dam indicates that granular material is present over the sensor position (i.e. the resistance given by the grains increases the water level and the pressure head as well). This seems to indicate that the material settles faster than in the experiment. It may be the consequence of the visco-rigid constitutive model adopted.
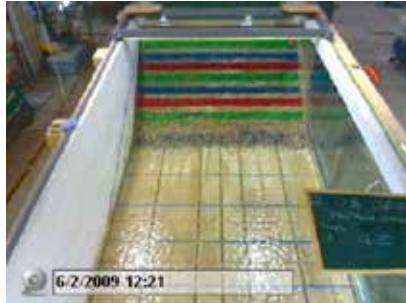
(a) Experimental length of failure Bexp = 0.32m.
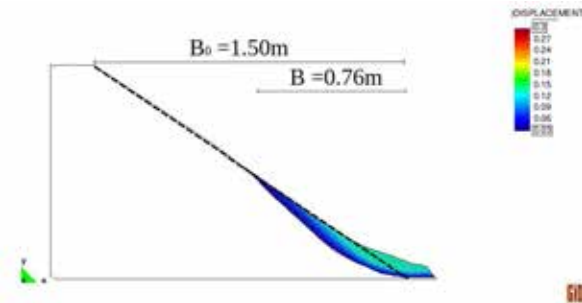
(b) Numerical length of failure B= Bnum= 0.76m.

Figure 5.45: Case B21. 2*D* comparison between experimental and numerical length of failure.
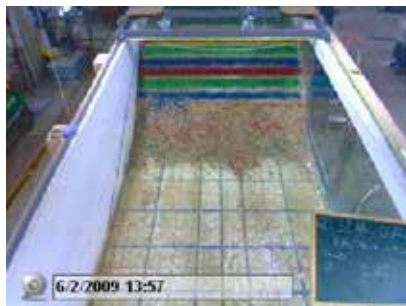
(a) Experimental length of failure Bexp = 0.68m.
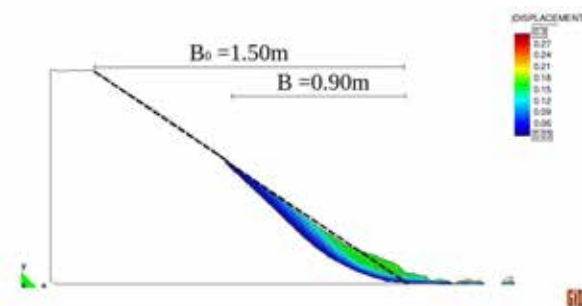
(b) Numerical length of failure B= Bnum= 0.90m.

Figure 5.46: Case B22. 2*D* comparison between experimental and numerical length of failure.

(a) Experimental length of failure Bexp = 1.00m.
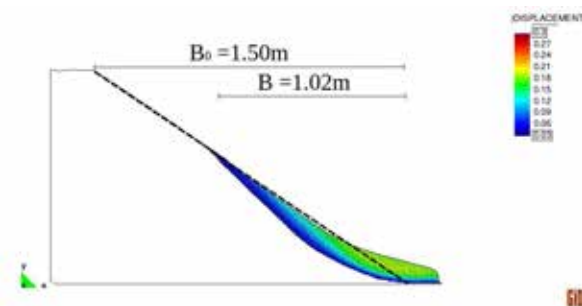
(b) Numerical length of failure B= Bnum= 1.02m.

Figure 5.47: Case B23. 2*D* comparison between experimental and numerical length of failure.

	Q [l/s]	B_{exp}	B_{num}	Error
Case B21	19.36	0.32	0.76	137%
Case B22	30.45	0.68	0.90	32%
Case B23	39.56	1.00	1.02	2%

Table 5.8: Case B2. Comparison between experimental (B_{exp}) and numerical (B_{num}) length of failure for $\phi = 41°$.

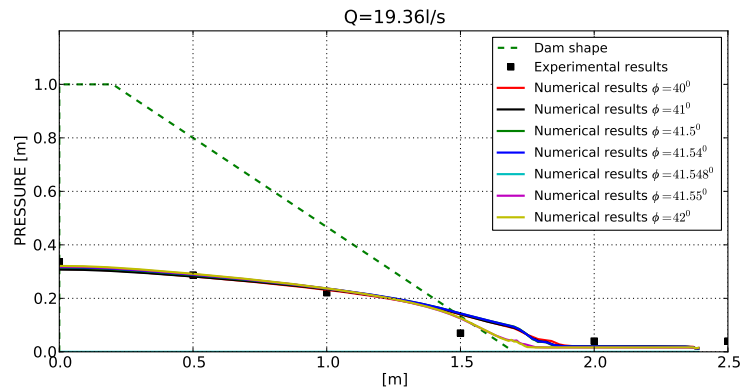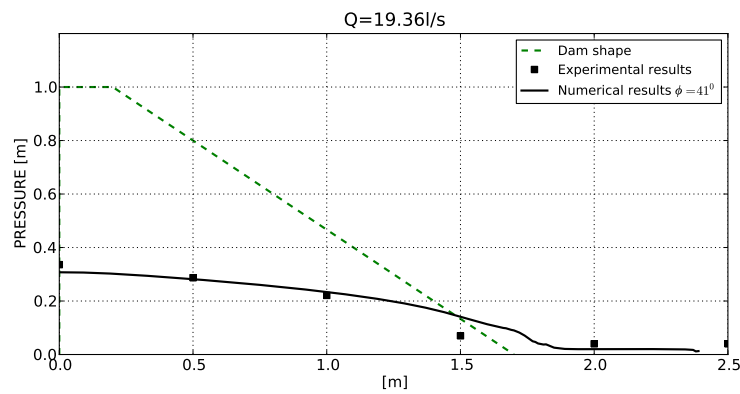
Figure 5.48: Case B21. Bottom pressure distribution at stationary regime for $Q = 19.36l/s$. Porosity $n = 0.4$, $D_{50} = 35mm$. Numerical and experimental comparison.
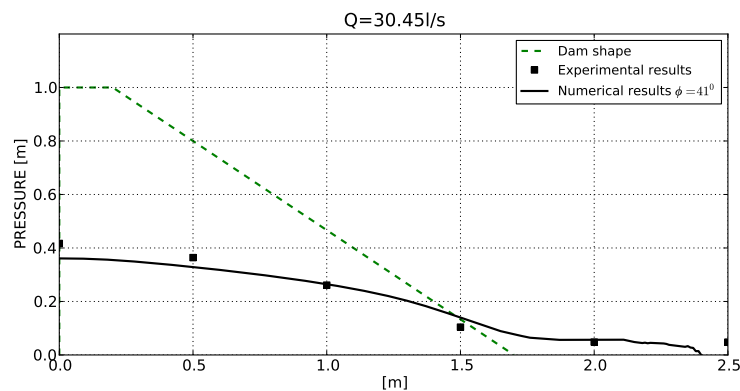
Figure 5.49: Case B22. Bottom pressure distribution at stationary regime for $Q = 30.45l/s$. Porosity $n = 0.4$, $D_{50} = 35mm$. Numerical and experimental comparison.
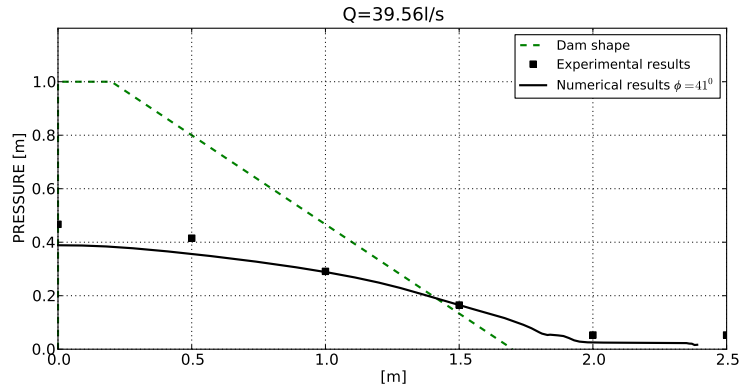
Figure 5.50: Case B23. Bottom pressure distribution at stationary regime for $Q = 39.56l/s$. Porosity $n = 0.4$, $D_{50} = 35mm$. Numerical and experimental comparison.

5.5   CASE C. Impervious face dam

The simulation of a dam with an impervious screen is the most challenging case from a fluid dynamic point of view. The inlet of water is set in the upper left part, according to what already done in case B. It implies that a falling jet should also be simulated.

The impemeabilization of the experimental dam is obtained making use of a plastic deformable material used to cover the upstream slope. Special care is observed on the perimeter, where the plastic is connected with the side walls and the bottom of the channel. In fact, there is a high possibility of leakage that could invalidate the experiment. Figure 5.51 shows a view of the experimental setting, unfortunately no photos are available of the upstream slope with the plastic coverage.

Figure 5.51: Case C1. Experimental setting.

5.5.1 Case C. Impervious face dam. Experimental setting and geometry

The details of the geometry of the experimental setting can be seen in Figure 5.52, where the pressure sensors distribution is also shown. The red rectangles indicate the three lines of sensors activated. They are respectively at $Y = 0.3m$ $Y = 0.5m$ and $Y = 0.7m$.
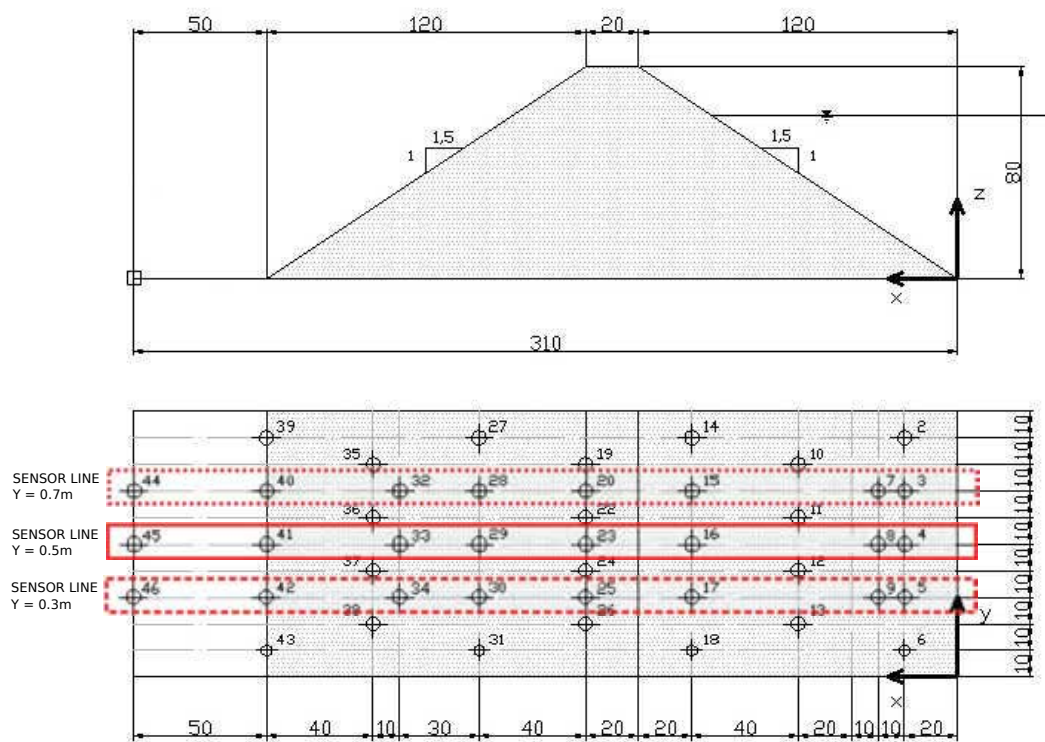
Figure 5.52: Case C1. Impervious face dam. Geometry of the experimental setting and map of the sensors distribution.

5.5.2   Case C1. Impervious face dam. Uncoupled model and results

In order to optimize the computational domain, the upstream reservoir is not simulated and the entrance of water is directly set in the upper left part, at the crest level, as shown in Figure 5.53. The upstream screen is therefore considered perfectly impermeable and it is simulated as a rigid wall with a slip condition.
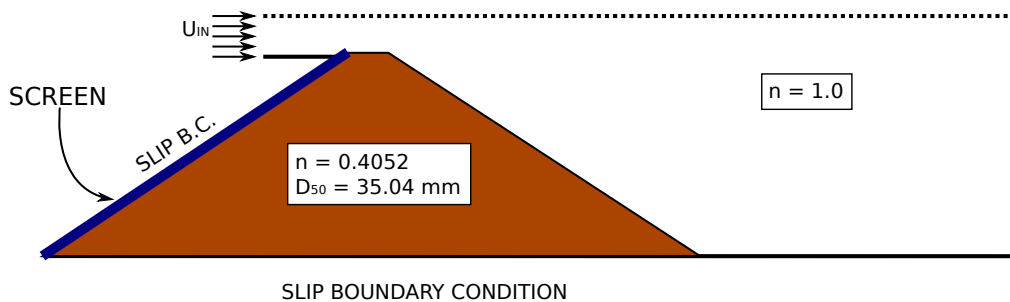
Figure 5.53: Impervious face dam. Qualitative model geometry and boundary conditions.

The rest of the boundary conditions are similar to those of the previous models and they are schematically presented in Figure 5.53. A qualitative geometry is also shown in the image.

It has been experimentally observed that no deformation of the downstream slope occurs up to a discharge of $5.71 l/s$.

	Mesh A	Mesh B	Mesh C	Mesh D
Dimension [m]	0.03	0.02	0.015	0.01
n. elem	4 700	8 500	13 000	20 000
n. nodes	2 900	4 200	6 800	10 000

Table 5.9: Case C1. Meshes used in the analysis.

Different mesh are used in order to identify the minimum element size that yields a correct conservation of the fluid volume. Their characteristics are summarized in Table 5.9 and they are shown in Figure 5.54. The first mesh taken into consideration is mesh A shown in Figure 5.54 where the average dimension of the elements is set to $0.03m$.

This condition is not sufficient for the flow to be simulated correctly and the mass loss compromises the results. The final level of water obtained is in fact much lower than in the other cases, as shown in Figure 5.55.

(a) Mesh A

(b) Mesh B

(c) Mesh C

(d) Mesh D
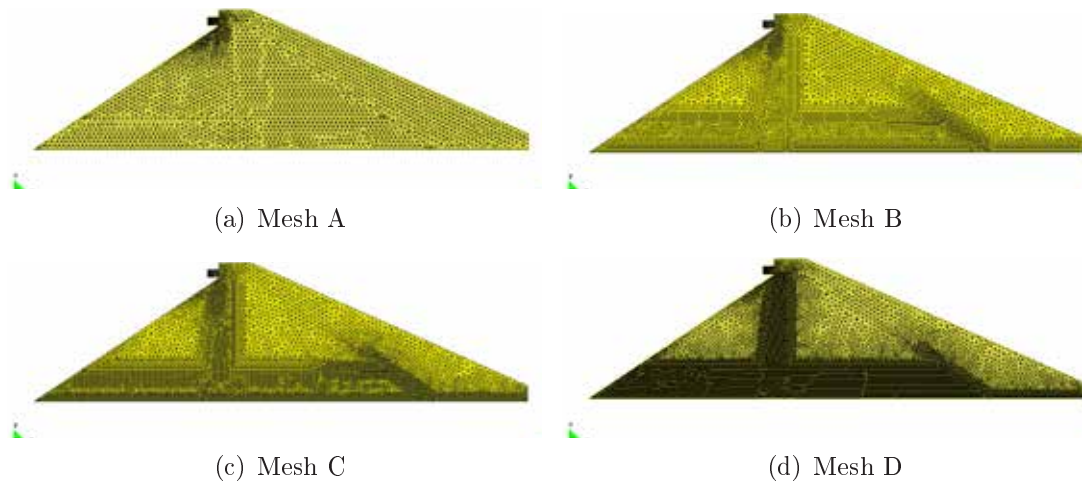
Figure 5.54: Case C1. Meshes used in the analysis of mesh sensitivity. Detailed characteristics of the meshes can be found in Table 5.9.

This problem is solved just refining the area where the jet falls and the bottom of the channel as for mesh B, C and D. It is interesting to observe how the mesh size requirements are stricter than in case B1a.

The comparison between bottom pressure distribution of the analyzed cases shows that for a mesh finer than $0.015m$ the results converge to the same solution. In the same graph the wrong behavior of the model with the coarsest mesh is clearly reflected in term of pressure head.

(a) Mesh A

(b) Mesh D
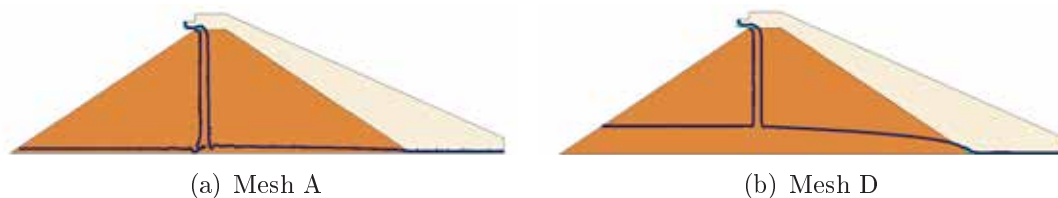
Figure 5.55: Case C1. Steady state configuration in C1 case with mesh A anc D respectively. The blue line represents the free surface.
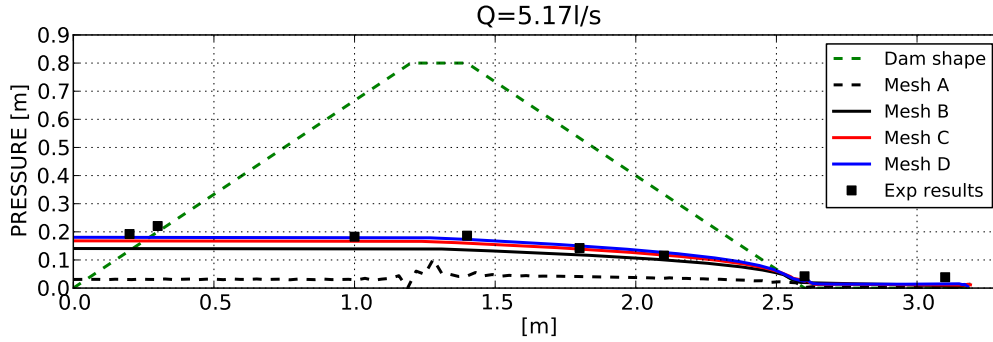
Figure 5.56: Case C. Bottom pressure distribution at stationary regime for $Q = 5.17l/s$. Porosity $n = 0.4$, $D_{50} = 35mm$. Numerical and experimental comparison for the different meshes analyzed.

5.5.3 Case C2. Impervious face dam. Coupled model and results

The construction of the models for the coupled analysis is done as explained for cases $A2$ and $B2$ and is shown in Figure 5.57. The mesh used in the fluid model is mesh D used for the $C1$ case (Figure 5.54) whereas the mesh of the dam is shown in Figure 5.58.
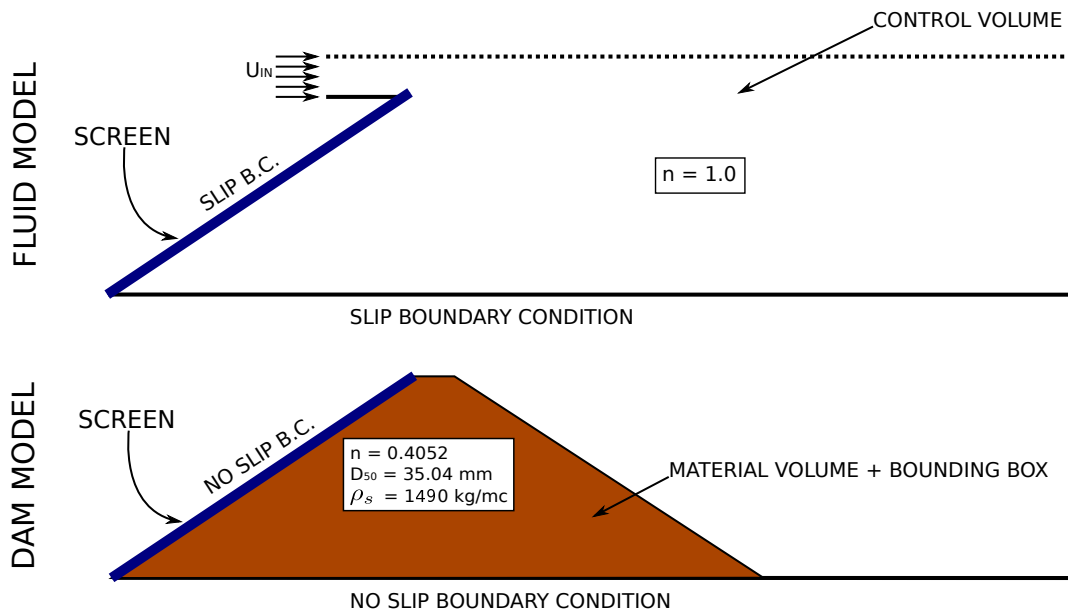
Figure 5.57: Case C2. Fluid and dam qualitative models and boundary conditions for the coupled analysis.

Looking at Figure 5.59 it can be observed that the coupled model overestimates the length of failure in case $C21$. The results improve for higher discharges, as explained in the following sections. The overestimation of the length of failure when $B_{exp} << B_0$ has already been discussed in Section 5.4.7.
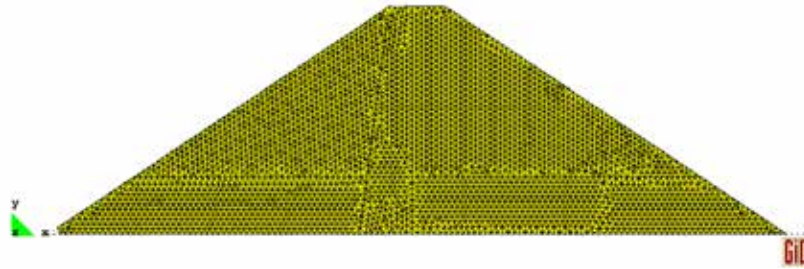
Figure 5.58: Case C2. $2D$ mesh of the dam model. 9.400 linear triangular elements.

The pressure head distribution (see Figure 5.62) according to what has been explained in the previous cases is underestimated by the model. On the other hand, the variation in the pressure head at the deformed toe of the dam can be, also in this case, the consequence of a too fast settlement of the fluidified material. This issue is expected to be corrected by including of the possibility of dragging the superficial particles.
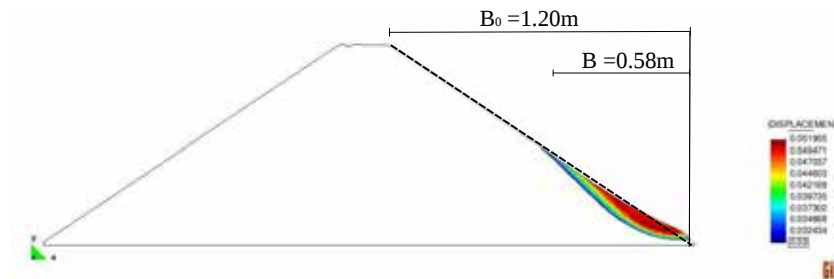
Figure 5.59: Case C21. $2D$ comparison between experimental and numerical length of failure.

In case C22 the numerical length of failure is $B_{num} = 0.61m$, as shown in Figure 5.60, which is close to the experimental value of $B_{exp} = 0.59m$. Nevertheless, the numerical pressure heads are lower than the experimental ones (Figure 5.63).

In the last example failure achieves the crest of the dam both in the numerical ($B_{num} = 1.40m$) and in the experimental ($B_{exp} = 1.44m$) models (Figure 5.61) as expected. Finally a good accordance can be found in the pressure head distribution, as shown in Figure 5.64.
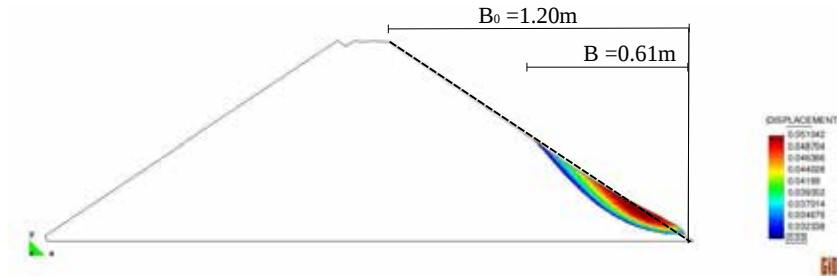
Figure 5.60: Case C22. $2D$ comparison between experimental and numerical length of failure.
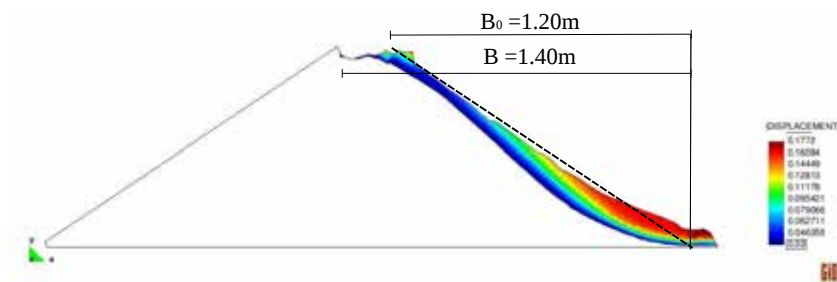
Figure 5.61: Case C23. $2D$ comparison between experimental and numerical length of failure.

	Q $[l/s]$	B_{exp}	B_{num}	Error
Case C21	15.36	0.24	0.58	142%
Case C22	25.05	0.59	0.61	3.2%
Case C23	30.27	1.44	1.40	2.7%

Table 5.10: Case C2. Comparison between experimental (B_{exp}) and numerical (B_{num}) length of failure.
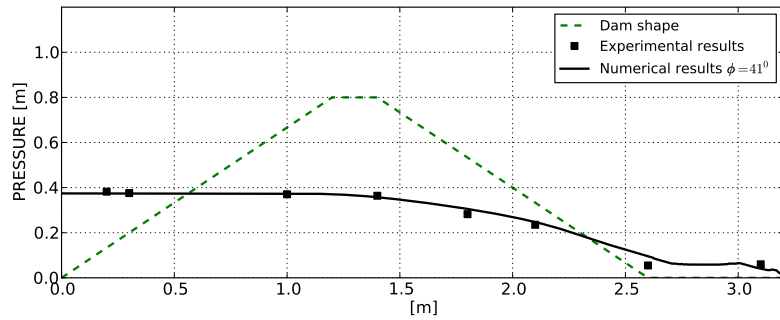
Figure 5.62: Case C21. Bottom pressure distribution at stationary regime for $Q = 39.56l/s$. Porosity $n = 0.4$, $D_{50} = 35mm$. Numerical and experimental comparison.
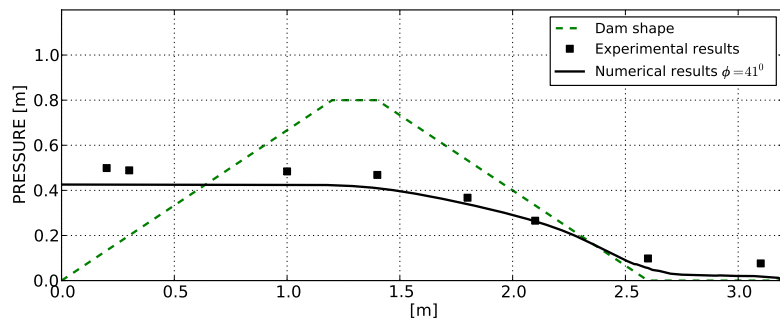
Figure 5.63: Case C22. Bottom pressure distribution at stationary regime for $Q = 39.56l/s$. Porosity $n = 0.4$, $D_{50} = 35mm$. Numerical and experimental comparison.
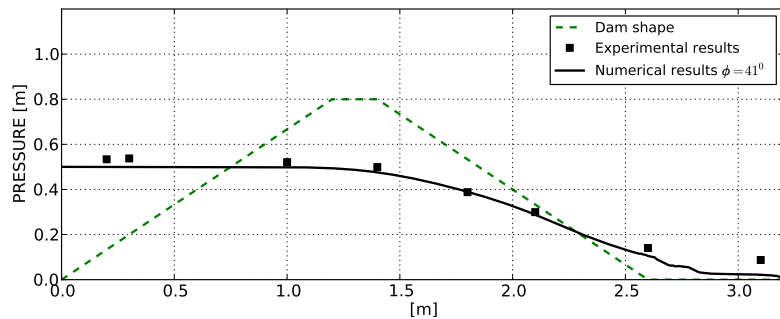
Figure 5.64: Case C23. Bottom pressure distribution at stationary regime for $Q = 39.56l/s$. Porosity $n = 0.4$, $D_{50} = 35mm$. Numerical and experimental comparison.

5.6   Conclusions and future work

In this work a novel approach for the simulation of the onset of failure of downstream slopes in rockfill dams is presented. The dynamic evolution of seepage and the free surface flow both upstream and downstream the dam are simultaneously analyzed. This is done using the edge-based code presented in Chapter 2. The structural response is evaluated with a visco-rigid constitutive model. As a failure criterion, Mohr Coulomb has been adopted. The rockfill is treated as a highly viscous non-Newtonian fluid (the reason for this choice is explained in Chapter 4). The viscosity drastically decreases when, due to the hydrodynamic forces, the yield stress is exceeded. When this happens failure occurs and the material starts to flow. The fluid-structure coupling is performed using a fully staggered scheme and a projection tool between non-matching meshes. In what follows the conclusions and the future work concerning the validation presented in this chapter are detailed

- The fluid module.

  1. There is a good agreement between experimental and numerical pressure heads for the undeformed cases (A1, B1, C1) both in $2D$ and $3D$. Nevertheless the numerical results always slightly underestimate the experimental values. Additional numerical experiments carried out in the framework of XPRES and EDAMS projects can confirm that the pressure line is always lower than the experimental one, especially when increasing the porosity values. This aspect, together with the comparison with theoretical Ergun curves shown in Section 5.4.3, lead to the conclusion that the Ergun coefficients underestimate the pressure drop in the seepage problem. In the near future, we plan to generalize the quadratic law of the Darcy non linear term ($\alpha u + \beta u^2$) and let to the user the choice of the suitable α and β coefficients.

  2. The overestimation of the pressure head at the toe of the deformed dam (cases A2, B2, C2), might be the consequence of a smaller deformation of the failed material. Whereas the length of failure is correctly reproduced, the failed material settles faster than in the real case and accumulates close to the original toe. In the experiments the path run by the failed rockfill material is much larger (see the conclusion about the coupled model for additional comments on this issue).

3. The code has a good performance also in the challenging cases of a falling jet of water. The only requirement is a refinement of the mesh in the falling part of the domain.

4. Another challenging aspect of cases A1, B1, C1 is that the discharges are very low. This might represent a problem at the beginning of the simulation when a very thin layer of water starts filling the dam. This issue can be easily corrected by refining the mesh close to the bottom.

5. It might be interesting to test the model with different materials and eventually with several different porosities in the same dam. In this context some preliminary results (not shown in the work) have been obtained using the fluid code. This aspect is interesting because it will allow a more realistic representation of the rockfill slope. The construction process in fact is usually done layer by layer and a mechanical compaction is performed with a roller before passing to the next level. This compaction causes a crumbling of the superficial material. A thin layer is obtained on the surface. It is formed by particles with average diameter much smaller than the rest of the rockfill leading to a different porosity.

6. The scale effect is another aspect that must be taken into account in the future. CEDEX is now building a channel that will allow setting up dams of up to 2 meters high (the maximum height of prototype dams built up to now was $1m$).

- The coupled module.

   1. The code represents the incremental failure of the dam when increasing the overspilling discharge. It is also able to represent correctly the cases for which failure achieves the crest of the dam. On the contrary for lower discharges B is overestimated. This aspect is also reflected at experimental level. In fact when repeating the same experiment, the beginning of formation of the breaching suffers of a certain data scatter. Conversely, the discharge for which the failure reaches the crest is always the same.

   2. As already observed in the conclusions regarding the fluid module, the failed material settles faster than in the real case. This can be a consequence of the visco-rigid constitutive model chosen. In fact when the shear stress decreases under the yield stress threshold, the viscosity dramatically increases causing

a sudden stop of the element. The insertion of an erosion tool might solve the problem dragging away the deposed material.

3. In the experiments presented the high downstream slope ($1.5H : 1V$) can lead to the conclusion that the principal failure mechanism is mass sliding. Nevertheless in the most general case erosion, i.e. superficial dragging of particles, plays a relevant role, acting in combined or alternate way. The possibility of including a procedure to evaluate erosion is essential in order to fully describe the phenomenon.

4. The $3D$ coupled model has given encouraging results. Nevertheless the possibility of inserting a conditional remeshing should be taken into account in order to control the deformation avoiding excessive viscous effects that lead to an excessive fluency of the downstream slope.

5. The coupled code was conceived to analyze the consequence of transitory incoming discharges, allowing inserting flood hydrograms as an input. This capability is not exploited in the presented examples. Just a preliminary example is shown in Section 5.3.8. Experiments are currently carried out at UPM considering hydrograms and not incremental steps of discharge. In a near future it may be possible a validation of this important aspect.

6. In the present chapter it was pointed out the low reliability of the B parameter used to quantify the length of failure. In the future, the possibility of comparison between the $3D$ digital model and $3D$ numerical results should be investigated in more detail.

Chapter 6

Conclusions

In this chapter the conclusions of the work are presented and an overview of the future lines of research is made.

6.1 Summary and achievements

The aim of this work was to development a numerical tool for the simulation of the overtopping in rockfill dams. For that purpose three are the main points developed in the present work (reflected in Chapters 2, 3 and 4 respectively):

1. The development of a fluid code able to simulate the free surface flow over and throughout the rockfill. The classical Navier-Stokes equations have been modified to automatically account for a change in porosity values. The non linear seepage is evaluated using a quadratic form of the resistance law. Ergun's coefficients have been chosen. The possibility of including variable incoming discharges is an essential requirement for the objectives of the work. A fixed mesh approach has been used and a level set technique has been implemented for tracking the evolution of the free surface both outside and inside the rockfill. Of the two approaches presented in Chapter 2, the edge-based one has been chosen for its better performances in terms of computer time.

2. The implementation of a code to simulate the behaviour of a granular non-cohesive material. A non- Newtonian modified Bingham law is proposed. This approach gives the possibility of considering a pressure sensitive resistance criteria. This is

obtained by inserting a Mohr Coulomb failure criteria in the Bingham relation. Since the rockfill is expected to undergo severe deformation during the failure process, a Lagrangian approach is preferred to a fixed mesh one. PFEM was the adopted technique.

3. The implementation of a strategy to couple the models mentioned in Points 1 and 2. This tool needs to include an algorithm for the data mapping between non matching meshes being the structural and the fluid models in two different kinematic frameworks (the Lagrangian and the Eulerian one).

Finally in chapter 5 an extensive validation of the code is done, simulating the experiments performed by UPM and CEDEX in the XPRES and E-DAMS projects. Several different experimental settings have been taken into account. For each of them a sensitivity analysis of the main parameters has been carried out in order to understand the capabilities and limitations of the code.

The results are encouraging considering that this work represents a first step for the solution of a complex problem.

6.2 Future lines of research

To conclude some ideas of possible applications and future lines of research deriving from this work are provided in this section.

The fluid-seepage code has been used in this work for a very specific application. Nevertheless once the possibility of defining a custom resistance law is inserted in the code, it becomes a general tool to treat a wide range of problems. For instance all the problems dominated by Darcy incompressible flows can be simulated setting to zero the non-linear term. Several problems in harbor engineering need to evaluate the dissipation suffered by incoming waves when smashing over tetrapods, or general protections of dikes and levees, that behaves like rockfill. Another application can be, for instance, turbine simulation. In fact the pressure drop induced by this type of machines is often simulated with an equivalent porous medium in order to study the effects in the surrounding fluid environment.

The fluid code itself has been already applied to a number of free surface flow problems without the presence of any porous material. Some of them have been shown in Chapter 2 (the flip bucket example or the water column collapse). This code has been successfully

used for the calculation of the discharge on a spillway as detailed in [112], or for the simulation of mould filling processes as shown in [108].

The modified Bingham model coupled with the fluid code can also be used for the simulation of the effect of a landslide into a reservoir. In fact the code naturally simulates the interaction between the solid falling into the water and the resulting wave.

Concerning the problem of overtopping in rockfill dams, it should be remarked that the whole work was conceived to easily change the structural model maintaining the coupling strategy and the fluid-seepage module. As a complement of the FEM-PFEM continuous approach presented in this work, the possibility of a FEM-DEM model is currently being explored by other researchers of the same working team.

Appendix A

Kratos Multiphysics

A.1 Kratos

All the algorithms presented in this thesis are developed inside *Kratos Multiphysic* [3, 48]. Kratos is a framework for building multi-disciplinary finite element codes as well as a common platform for natural interaction of these modules in different ways. It is written in $C++$ language.

It provides several tools for easy implementation of finite element codes and a common platform for their natural interaction in different ways.

It is addressed to a variety of people ranging from developers (finite element experts or application programmers) to engineers or designers who stop at the user level without getting involved in the programming features.

A.1.1 Object-oriented approach

The main goal of an object-oriented structure is to split the whole problem into several objects and to define their interfaces. With regard to the simulation of multi-disciplinary problems using FEM, the objects defined in Kratos are based on a general finite element methodology. Figure A.1 illustrates the main classes.

`Vector`, `Matrix` and `Quadrature` come from basic concepts of numerical analysis. `Node`, `Element`, `Condition`, `Mesh` and `Dof` are taken directly from finite element concepts. `Model`, `Properties`, `ModelPart` and `SpatialContainer` are conceived for a better organization of all necessary data. `IO`, `LinearSolver`, `Process` and `Strategy` are basilar
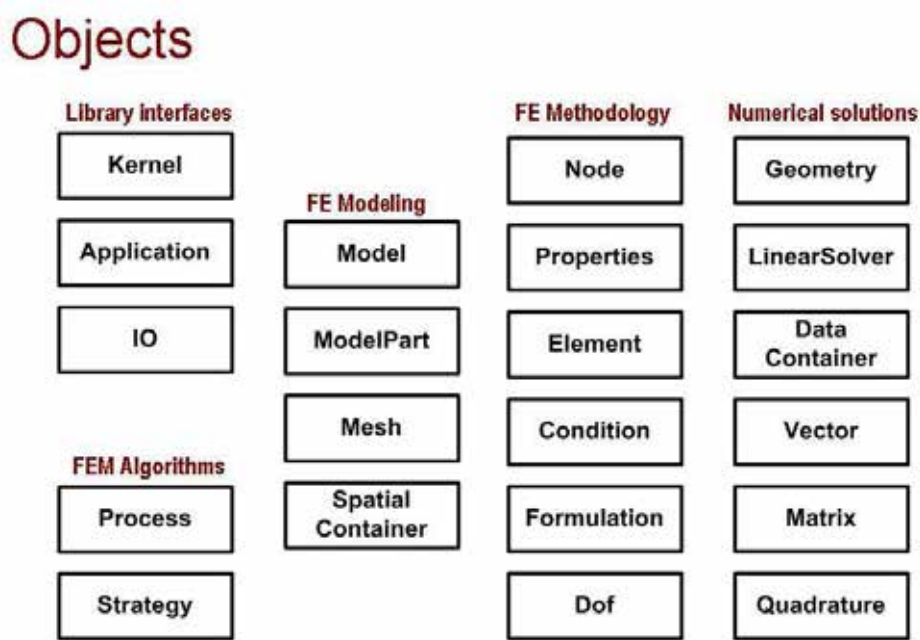
Figure A.1: List of the principal object in Kratos. Image taken from [47].

different tools of finite element programs. Finally, `Kernel` and `Application` handle the library management and define Kratos interface.

A.1.2   Multi- layer design

Kratos uses a multi-layer approach in its design. This imply that each object only interfaces with objects in the same layer or in lower ones. Layering reduces the dependency inside the program. It helps in the maintenance of the code and also helps developers to understand the code and clarifies their tasks.

The layers structure has been designed to be addressed to different category of users. It was conceived to lead the user to work with the minimum number of layers as possible. This was done in order to reduce conflicts between users and especially to reduce as much as possible the part of the code touched by each developer.

Following the design mentioned above, Kratos is organized as follow:

Basic Tools Layer. It holds all the basic tools used in Kratos. This layer using advance C++ techniques is essential in order to maximize the performance. It is designed to be implemented by an expert programmer not necessarily FEM expert.
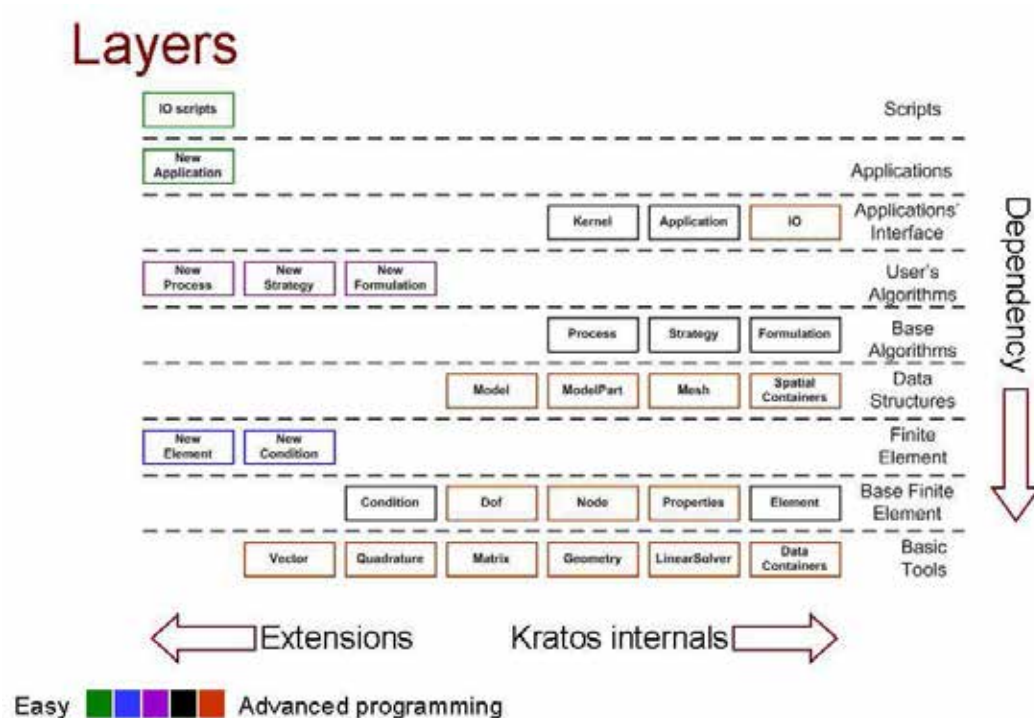
Figure A.2: Graphical summary of the multi.layer design. Image taken from [47].

This layer may also provides interfaces with other libraries.

Base Finite Element Layer. It holds the objects that are necessary to implement a finite element formulation. It also defines the structure to be extended for new formulations. This layer hides to the finite element developers the difficult implementations of nodal and data structure and other common features .

Finite Element Layer. The layer for finite element developers. It only uses basic and average features of C++ and uses the previous described layers in order to optimize the performance without entering into optimization details.

Data Structures Layer. It contains all objects organizing the data structure. This layer has no implementation restrictions. Advanced language features are used to maximize the flexibility of the data structure.

Base Algorithms Layer. Generic algorithms are implemented here to be available for users in different fields.

User's Algorithms Layer. This layer is to be used by high level finite element

programmers. It contains all classes implementing the different algorithms in Kratos.

Applications' Interface Layer. It holds all the objects that manage Kratos and their relation with other applications. The components of this layer are implemented using high level programming techniques in order to provide the required flexibility.

Applications Layer. It contains the interface of certain applications with Kratos.

Scripts Layer. Holds a set of IO scripts which can be used to implement different algorithms from outside Kratos. Package users can use modules in this layer or create their own extension without having knowledge of C++ programming or of the internal structure of Kratos. Via this layer they can activate and deactivate certain functionalities or implement a new global algorithm without entering into Kratos structure details.

A graphical representation of the structure can be seen in fig. A.2

A.1.3 Python interface

Kratos uses the facilities of Python language for IO data transmission [4]. This flexible interpreter with its object-oriented high level language can be used to implement and execute new algorithms using Kratos. Python allows an high level of flexibility, without the need of recompiling the code when debugging or testing new algorithms.

A.2 GiD problem types and interfaces

The pre and post- processing is done using the in-house commercial sofware GiD [2]. Different problem types have been developed in TCL to customize GiD insert the data and print the results of the different applications presented in this work. They are all available in the kratos website [3].

Bibliography

[1] *Banqiao Dam.* http://worldphotocollections.blogspot.com/2010/01/worlds-worst-ten-deadliest-natural.html.

[2] *GiD the Personal Pre and Post Processor.* http://www.gidhome.com/.

[3] *Kratos, Multiphysics opensource fem code.* http://www.cimne.com/kratos.

[4] *Python programming language.* http://www.python.org/.

[5] *TetGen, A quality tethraedral mesh generator and three dimensional Delaunay.* http://tetgen.berlios.de.

[6] D.D. Adam and W.L. Wood. Comparison of hilber-hughes-taylor and bossak α methods for the numerical integration of vibration equations. *International Journal for Numerical Methods in Engineering*, 19:765–771, 1983.

[7] I. Akkerman, Y. Bazilevs, C. Kees, and M. Farthing. Isogeometric analysis of free-surface flow. *Journal of Computational Physics*, 230:4137–4152, 2011.

[8] A. Amiri and K. Vafai. Transient analysis of incompressible flow through a packed bed. *International Journal of Heat and Mass Transfer*, 41:4259–4279, 1998.

[9] I. Babuška. Finite element method with lagrangian multipliers. *Numerische Mathematik*, 20:179–192, 1973.

[10] J. Baiges. *The Fixed-Mesh ALE method applied to multiphysics problems using stabilized formulations.* PhD thesis: Universidad Polititécnica de Cataluña, 2010.

[11] E. Barozzi and E. Gonzalez. *Calculus Vol. I.* Libreria Progetto Padova, 1996.

[12] J. Bear. *Dynamics of fluids in Pouros Media.* Courier Dover Pubblications, 1988.

[13] M.A. Biot. General theory of three dimensional consolidation. *Journal of Applied Physics*, 12:155–164, 1941.

[14] M.A. Biot. Theory of eleasticity and consolidation for a porous anisotropic solid. *Journal of Applied Physics*, 26:182–185, 1955.

[15] R.B. Bird. *Dynamics of polymeric liquids.* John Wiley and Sons, 1987.

[16] F. Brezzi. On the existence, uniqueness and approximation of saddle point problems araising from lagrange multipliers. *Revue Française d'Automatique Informatique et Recherche Opérationalle*, 8:129–151, 1974.

[17] A.N. Brooks and T.J.R. Huges. Streamline upwind/petrov-galerkin formulations for convection dominated flows with particular emphasis on the incompressible navier-stokes equations. *Computer Methods in Applied Machanics and Engineering*, 32:199–259, 1982.

[18] P. Bussetta, R. Boman, and J.P. Ponthot. Comparison of data transfer methods between meshes in the frame of the abitrary lagrangian eulerian formalism. *Proceeding of the V Internationa conference on Advances Computational Methods in Engineering (ACOMEN 2011)*, -, 2011.

[19] K. Butler, E. Oñate, S.R. Idelsohn, and R. Rossi. Modeling polymer melt flow using the particle finite element method (pfem). *Proceeding of the Interflam Conference 2007*, 2:929–940, 2007.

[20] N. Calvo. *Generación de mallas tridimensionales por métodos duales.* PhD thesis: Univesidad Nacional del Litoral, Argentina, 2005.

[21] H. Campos, R. Morán, and M.A. Toledo. Estudio de la rotura de presas de material granular grueso uniforme no cohesivo sin elemento impermeable. fase de inicio. *Dam maintenance and rehabilitation II, CRCpress Balkema*, pages 599–608, 2010.

[22] J.M. Carbonell. *Modeling of ground exavation with the particle element method.* PhD thesis: Universidad Polititécnica de Cataluña, 2009.

[23] J.M. Carbonell, E. Oñate, and B.Suárez. Modeling of ground exavation with the particle finite element method (pfem). *ASCE: Journal of Engineering Mechanics*, 136:455–463, 2008.

[24] P.J. Carreau, D. Dekee, and R.P. Chhabra. *Rheology of polymeric systems*. Hansen, 1997.

[25] M. Cervera, M. Chiumenti, and R. Codina. Mixed stabilized finite element methods in nonlinear solid mechanics. part i: Formulation. *Computer Methods in Applied Mechanics and Engineering*, 199:2559–2570, 2010.

[26] M. Cervera, M. Chiumenti, and R. Codina. Mixed stabilized finite element methods in nonlinear solid mechanics. part ii: Strain localization. *Computer Methods in Applied Mechanics and Engineering*, 199:2571–2589, 2010.

[27] M. Cervera, M. Chiumenti, and C. Agelet de Saracibar. Softening, localization and stabilization: capture of discontinuous solutions in j2 plasticity. *International Journal for Numerical and Analithical Methods in Geomechanics*, 28:373–393, 2004.

[28] M. Cervera, M. Chiumenti, and C. Angelet de Saracibar. Shear band localization via local j2 continuum damage mechanics. *Computer Methods in Applied Mechanics and Engineering*, 193:849–880, 2004.

[29] M. Cervera, M. Chiumenti, and Q. Valverde C. Agelet de Saracibar. Mixed linear/-linear simplicial elements for incompressible elasticity and plasticity. *Computer Methods in Applied Machanics and Engineering*, 192:5249–5263, 2003.

[30] H. Chanson. *Embankments overflow protection system and earth dam spillways.*, chapter Chapter 4 of Dams: Impacts, stability and design, pages 101–132. Nova Science Publishers, Inc., 2009.

[31] R.P. Chhabra. *Non-Newtonian Fluids: An Introduction, Rheology of Complex Fluids (Chapter 1)*. Springer, 2010.

[32] M. Chiumenti, Q. Valverde, C. Agelet de Saracibar, and M. Cervera. A stabilized formulation for incompressible plasticity using linear triangles and tetrahedra. *International Journal of Plasticity*, 20:1487–1504, 2004.

[33] A.J. Chorin. A numerical method for solving incompressible viscous problems. *Journal of Computational Physics*, 2:12, 1967.

[34] R. Codina. A nodal-based implementation of a stabilized finite element method for incompressible flow problems. *International Journal for Numerical Methods in Fluids*, 33:737.766, 2000.

[35] R. Codina. On stabilized finite element methods for linear system of convection-diffusion-reaction equations. *Computer Methods in Applied Machanics and Engineering*, 188:61–82, 2000.

[36] R. Codina. Pressure stability in fractional step finite element methods for incompressible flows. *Journal of Computational Physics*, 170:112–140, 2000.

[37] R. Codina. Stabilization of incompressibility and convection through orthogonal sub-scales in finite element method. *Computer Methods in Applied Machanics and Engineering*, 190:1579–1599, 2000.

[38] R. Codina. Stabilized finite element approximation of transient incompressible flows using orthogonal subscales. *Computer Methods in Applied Mechanics and Engineering*, 191:4295–4321, 2002.

[39] R. Codina and A. Folch. A stabilised finite element predictor-corrector scheme for the incompressible navier-stokes equations using a nodal-based implementation. *International Journal for Numerical Methods in Fluids*, 44:483–503, 2004.

[40] R. Codina, G. Houzeaux, H. Coppola-Owen, and J. Baiges. The fixed-mesh ale approach for the numerical approximation of flows in moving domains. *Journal of Computational Physics*, 228:1591–1611, 2009.

[41] R. Codina and O. Soto. Approximation of the incompressible navier-stokes equations using orthogonal subscale stabilization and pressure segregation on anisotropic finite element meshes. *Computer Methods in Applied Machanics and Engineering*, 193:1403–1419, 2004.

[42] H. Coppola. *A finite element model for free surface and two fluid flows on fixed meshes*. PhD thesis: Universidad Polititécnica de Cataluña, 2009.

[43] A.H. Coppola-Owen and R. Codina. Improving eulerian two-phase flow finite element approximation with discontinuous gradient pressure shape functions. *Int. J. Numer. Meth. Fluids*, 49:1287.1304, 2005.

[44] P. Coussot. *Rheometry of pastes, suspensions and granular materials.* Wiley and sons., 2005.

[45] M. Cremonesi, L. Ferrara, A. Frangi, and U. Perego. Simulation of the flow of fresh cement suspensions by a lagrangian finite element approach. *Journal of Non-Newtonian Fluid Mechanics*, 165:1555–1563, 2010.

[46] M. Cremonesi, A. Frangi, and U. Perego. A lagrangian finite element approach for the simulation of water-waves induced by landslides. *Computers and Structures*, 89:1086–1093, 2011.

[47] P. Dadvand. *A framework for developing finite element codes for multi-disciplinary applications.* PhD thesis: Universidad Politécnica de Cataluña, 2007.

[48] P. Dadvand, R. Rossi, and E. Oñate. An object-oriented environment for developing finite element codes for multi-disciplinary applications. *Archives of Computational Methods in Engineering*, 17:253–297, 2010.

[49] R de Boer. *Theory of porous media.* Springer-Verlag, Berlin, 2000.

[50] L. Da Deppo, C. Datei, and P. Salandin. *Sistemazione dei corsi d'acqua.* Libreria Internazionale Cortina (Padova), 2002.

[51] J. Donea and A. Huerta. *Finite Elements Methods for Flow Problems.* Wiley, 2003.

[52] D. Dureisseix and H. Bavastrello. Information transfer between incompatible finite element meshes: application to coupled thermo-viscoelasticity. *Computer Methods in Applied Machanics and Engineering*, 195:6523–6541, 2006.

[53] E-DAMS. Numerical and experimental techniques for safety assessment and protection of embankment dams in overtopping scenarios. *project of the National Plan R+D of the Spanish Ministry of Science and Innovation I+D BIA2010-21350-C03-00*, 2010-2013.

[54] R. Elias and A. Coutinho. Stabilized edge-based finite element simulation of free-surface flows. *Int. J. Numer. Meth. Fluids*, 54:965–993, 2007.

[55] R. Elias, M. Martins, and A. Coutinho. Parallel edge-based solution of viscoplastic flows with the supg/pspg formulation. *Computational Mechanics*, 38:365–381, 2006. 10.1007/s00466-005-0012-y.

[56] R.N. Elias, M.A.D. Martins, and L.G.A. Coutinho. Simple finite element-based computation of distance functions in unstructured grids. *International Journal for Numerical Methods Engineering*, 72:1095–1110, 2007.

[57] S. Ergun. Fluid flow through packed columns. *Chemical Engineering Progress*, 48:89–94, 1952.

[58] A. Ghetti. *Idraulica*. Ed. Cortina, 1984.

[59] A.M. Grillet, B. Yang, and B. Khomamiand E.S.G. Shaqfeh. Modeling of viscoelastic lid driven cavity flow using finite element simulations. *Journal of Non-Newtoninan Fluid Mechanics*, 88:99–131, 1999.

[60] H.M. Hilber, T.J. Hughes, and R.L. Taylor. Improved numerical dissipation for time integration algorithms in structural dynamics. *Earthquake Engineering and Structural Dynamics*, 5:283–292, 1977.

[61] T.J.R. Hughes. *The finite element method. Linear static and dynamic finite element analysis*. Englewood Cliffs, 1987.

[62] T.J.R. Hughes. Multiscale phenomena: Green's function, the dirichlet to neumann formulation, subgrid scale models, bubbles and the origins of stabilized formulations. *Computer Methods in Applied Machanics and Engineering*, 127:387–401, 1995.

[63] T.J.R. Hughes, L.P. Franca, and G.M. Hulbert. A new finite element formulation for computational fluid dynamics: Viii. the galerkin/least-squares method for advective-diffusive equations. *Computer Methods in Applied Machanics and Engineering*, 73:173–189, 1989.

[64] ICOLD. *Bulletin 99, Dam Failures Statistical Analysis*. ICOLD, 1995.

[65] S. Idelsohn, M. Mier, and E. Oñate. Multi-fluid flows with the particle finite element method. *Computer Methods in Applied Mechanics and Engineering*, 198:2750–2767, 2009.

[66] S. R. Idelsohn and E. Oñate. The challenge of mass conservation in the solution of free-surface flows with the fractional-step method: Problems and solutions. *International Journal for Numerical Methods in Biomedical Engineering,*, 26:1313–1330, 2010.

[67] S.R. Idelsohn, E. Oñate, and F. Del Pin. The particle finite element method: a powerful tool to solve incompressible flows with free-surfaces and breaking waves. *International Journal for Numerical Methods in Engineering.*, 61:964–984, 2004.

[68] S.R. Idelsohn, E. Oñate, F. Del Pin, and N. Calvo. Fluid-structure interaction using the particle finite element method. *Computer Methods in Applied Mechanics and Engineering*, 195:2100–2123, 2006.

[69] U. Israel. *Implementation of an algorithm for data transfer on the fluid structure interface between non matching meshes in kratos and an algorithm for the generation of an interface between GiD and Kratos.* Master thesis: Technische Universität München, 2006.

[70] R. Juon and W.H. Hager. Flip bucket with and without deflectors. *Journal of Hydraulic Engineering*, 126:837–845, 2000.

[71] C. Kees, I. Akkerman, M. Farthing, and Y. Bazilevs. A conservative level set method suitable for variable-order approximations and unstructured meshes. *Journal of Computational Physics*, 230:4536–4558, 2011.

[72] K.M.T. Kleesfman, G. Fekken, A.E.P. Veldman, B. Iwanowski, and B. Buchner. A volume -of-fluid based simulation method for wave impact problems. *Journal of Computational Physics*, 206:363–393, 2005.

[73] A. Larese, R. Rossi, and E. Oñate. Coupling eulerian and lagrangian models to simulate seepage and evolution of failure in prototype rockfill dams. *Proceeding of the XI ICOLD Benchmark Workshop on Numerical Analysis of Dams*, ISBN: 978-84-695-1816-8, 2011.

[74] A. Larese, R. Rossi, and E. Oñate. Theme b: simulation of the behavior of proto-types of rockfill dams during overtopping scenarios: seepage evolution and beginning of failure. *Proceeding of the XI ICOLD Benchmark Workshop on Numerical Analysis of Dams*, ISBN: 978-84-695-1816-8, 2011.

[75] A. Larese, R. Rossi, E. Oñate, and S.R. Idelsohn. Validation of the particle finite element method (pfem) for simulation of free surface flows. *Engineering Computations*, 25:385–425, 2008.

[76] C. Lechuga, A. Lara, M. Berga, M. Viña, M.A. Toledo, R. Morán, H. Campos, J. García, and A. Larese. Estudios sobre el comportamiento de presas de escollera ante vertidos por coronación. *Proeeding for the IX Jornadas Españolas de presas. Valladolid*, 2010.

[77] S. Leliavsky. *Design of dams for percolation and erosion*. Hall UK, 1965.

[78] R.L. Lewis and B.A. Schrefler. *The finite element method for the static and dynamic deformation and consolidation of porous media*. John Wiley and Sons, 1998.

[79] B. Li. *Flowthrough and overtopped rockfill dams*. PhD Thesis: University of Ottawa, 1995.

[80] G. Lipscomb and M. Denn. Flow of a bingham fluid in complex geometries. *Journal of Non-Newtonian Fluid Mechanics*, 14:337–346, 1984.

[81] R. Löhner. *Applied computational fluid dynamics techniques*. Wiley, 2001.

[82] J. Lubliner. *Plasticity Theory*. Macmillan Publishing Company, New York, NY., 1990.

[83] M. May. *Implementation of a general algorithm for incompressible and compressible flows within the multi-physics code KRATOS and preparation of fluid-structure coupling*. Diploma thesis: Technische Universität München, 2008.

[84] M. Mier, S. Idelsohn, and E. Oñate. Advances in the simulation of multi-fluid flows with the particle finite element method. *International Journal for Numerical Methods in Fluids*, 2010.

[85] E. Mitsoulis and Th. Zisis. Flow of bingham plastics in a lid-driven square cavity. *Journal of Non-Newtonian Fluid Mechanics*, 101:173–180, 2001.

[86] F. Mossaiby, R. Rossi, P. Dadvand, and S. Idelsohn. Opencl-based implementation of an unstructured edge-based finite element convection-diffusion solver on graphics hardware. *International Journal for Numerical Methods in Engineering*, 2011.

[87] D.A. Nield and A. Bejan. *Convection in porous media.* Springer, 1992.

[88] P. Nithiarasu, K.N. Seetharamu, and T. Sundararajan. Natural convective heat transfer in a fluid saturated variable porosity medium. *International Journal of Heat and Mass Transfer*, 40:3955–3967, 1997.

[89] P. Nithiarasu, K. S. Sujatha, K. Ravindran, T. Sundararajan, and K. N. Seetharamu. Non-darcy natural convection in a hydrodynamically and thermally anisotropic porous medium. *Computer Methods in Applied Mechanics and Engineering*, 188:413–430, 2000.

[90] P. Nithiarasu, T. Sundararajan, and K. N. Seetharamu. Double-diffusive natural convection in a fluid saturated porous cavity with a freely convecting wall. *International Communications in Heat and Mass Transfer*, 24:1121–1130, 1997.

[91] O.Coussy. *Mechanics of porous media.* John Wiley and Sons, 1995.

[92] E. Oñate. Derivation of stabilized equations for numerical solution of advective-diffusive transport and fluid flow problems. *Computer Methods in Applied Mechanics and Engineering*, 151:233–265, 1998.

[93] E. Oñate. A stabilized finite element method for incompressible viscous flows using a finite increment calculus formulation. *Computer Methods in Applied Mechanics and Engineering*, 182:355–370, 2000.

[94] E. Oñate, M.A. Celigueta, and S.R. Idelsohn. Modeling bed erosion in free surface flows by the particle finite element. *Acta Geotechnica*, 1:237–252, 2006.

[95] E. Oñate, M.A. Celigueta, S.R. Idelsohn, F. Salazar, and B. Suarez. Possibilities of the particle finite element method for fluid-soil-structure interaction problems. *Journal of Computational Mechanics*, 48:307–318, 2011.

[96] E. Oñate and J. García. A finite element method for fluid structure interaction with surface waves using a finite calculus formulation. *Computer Methods in Applied Mechanics and Engineering*, 191:635–660, 2001.

[97] E. Oñate, J. García, S.R. Idelsohn, and F. Del Pin. Fic formulations for finite element analysis of incompressible flows. eulerian, ale and lagrangian approaches. *Computer Methods in Applied Mechanics and Engineering*, 195:3001–3037, 2006.

[98] E. Oñate, S.R. Idelsohn, M.A. Celigueta, and R. Rossi. Advances in the particle finite element method for the analysis of fluid multibody interaction and bed erosion in free surface flows. *Computer Methods in Applied Mechanics and Engineering*, 197:1777–1800, 2008.

[99] E. Oñate, S.R. Idelsohn, M.A. Celigueta, R. Rossi, J. Marti, J.M. Carbonell, P. Ryzakov, and B. Suárez. *Advances in the particle finite element method (PFEM) for solving coupled problems in engineering Book chapter: Particle-Based Methods, Computational Methods in Applied Sciences.*, volume 25. E Oñate and R. Owen, 2011.

[100] E. Oñate, S.R. Idelsohn, F. Del Pin, and R. Aubry. The particle finite element method. an overview. *International Journal of Computational Methods*, 1:267–307, 2004.

[101] E. Oñate, A. Valls, and J. García. Modeling incompressible flows at low and high reynolds numbers via finite calculus-finite element approach. *Journal of Computational Physics*, 224:332–351, 2007.

[102] A. Orlando and D. Peric. Analysis of transfer procedures in elastoplasticity based on the error in the constitutive equations: theory and numerical illustration. *International Journal for Numerical Methods in Engineering*, 60:1595–1631, 2004.

[103] S. Osher and R.P.Fedkiw. *Level Set Methods and dynamic implicit surfaces.* Springer, 2003.

[104] T. C. Papanastasiou. Flows of materials with yield. *Journal of Rheology*, 31:385–404, 1987.

[105] D. Perić and S. Slijepcević. Computational modelling of viscoplastic fluids based on a stabilised finite element method. *Engineering Computations*, 18:577–591, 2001.

[106] J. Principe. *Subgrid scale stabilized finite elements for low speed flows*. PhD thesis: Universidad Polititécnica de Cataluña, 2008.

[107] M. Quecedo, M. Pastor, M.I. Herreros, and J.A. Fernandez Merodo. Numerical modelling of the propagation of fast landslides using the finite element method. *International Journal for Numerical Methods in Engineering*, 59:755–794, 2004.

[108] R. Rossi, A. Larese, P. Dadvand, and E: Oñate. An efficient edge-based level set finite element method for free surface flow problems. *International Journal for Numerical Methods in Fluids (DOI: 10.1002/fld.3680)*, 2012.

[109] P. Ryzhakov. *Lagrangian FE methods for coupled problems in fluid mechanics*. PhD thesis: Universitat Politécnica de Cataluña, 2010.

[110] P. Ryzhakov, R. Rossi, S.R. Idelsohn, and E. Oñate. A monolithic lagrangian approach for fluid-structure interaction problems. *International Journal of Computational Mechanics*, 46-6:883–899, 2010.

[111] P. Ryzhakov, R. Rossi, and E. Oñate. An algorithm for the simulation of thermally coupled low speed flow problems. *Int. Journal for Num. Methods in Fluids*, 2011.

[112] F. Salazar, R. Moran, R. Rossi, and A. Larese. Numerical modeling of the hydraulic performance of oliana dam spillway using kratos. *Proceeding of the XI ICOLD Benchmark Workshop on Numerical Analysis of Dams, Valencia*, ISBN: 978-84-695-1816-8, 2011.

[113] Hanan Samet. *Foundations of Multidimensional and Metric Data Structures*. Morgan Kaufmann, 2006.

[114] J.A. Sethian. A fast marching level set method for monotonically advancing fronts. *Proceedings of the National Academy of Sciences*, 93(4):1591–1595, 1995.

[115] O. Soto, R. Lohner, J. Cebral, and F. Camelli. A stabilized edge-based implicit incompressible flow formulation. *Computer Methods in Applied Mechanics and Engineering*, 193:2139–2154, 2004.

[116] B. Moran T. Belytschko, W. K. Liu. *Nonlinear Finite Elements for Continua and Structures*. John Wiley and Sons, 2000.

[117] D.W. Taylor. *Fundamentals of soil mechanics*. John Wiley and Sons, New York, 1948.

[118] W. Taylor. Aplicaciones de algoritmos que conservan la energía-momentum en dinámica no-lineal. Technical report, Publicación CIMNE n.259, 2004.

[119] R. Temam. Sur l'approximation de la solution des équations de navier-stokes par la méthode des pas fractionaires (i). *Arch. Ration. Mech. Anal*, 32:135, 1969.

[120] T.E. Tezduyar. Stabilized finite element formulations for incompressible flow computations. *Advances in Applied Mechanics*, 28:1–44, 1992.

[121] T.E. Tezduyar, S. Shih, and S. Mittal. Time-accurate incompressible flow computations with quadrilateral velocity-pressure elements. *University of Minnesota. Supercomputer Institute Research Report USMI*, 90:143, 1990.

[122] M.A. Toledo. *Presas De Escollera Sometidas a Sobrevertido. Estudio del Movimientos dal Agua a Través de la Escollera e de la Estabilidad Frente al Deslizamiento en Masa*. PhD thesis: Universidad Politécnica de Madrid, 1997.

[123] M.A. Toledo. Safety of rockfill dams subject to overtopping. *Proceding of the International Symposium on new Trend an guidelines on Dam Safety*, 1998.

[124] P. Vasseur, C.H. Wang, and M. Sen. Natural convection in an inclined rectangular porous slot: the brinkman-extended darcy model. *ASME Journal of Heat Transfer*, 112:507–511, 1990.

[125] J.C. López Verdejo. *Caracterización del Proceso de Saturación de una Presa de Escollera Meidiante Métodos Unidimensionales*. Diploma de Estudios Avanzados :Universidad Politécnica de Madrid, 2005.

[126] W.L. Wood, M. Bossak, and O.C. Zienkiewicz. An alpha modification of newmark's method. *Int. J. for Num. Meth in Eng.*, 15:1562–1566, 1980.

[127] XPRES. Desarrollo de un método para el estudio del proceso de rotura de presas de escollera por sobrevertido combinando técnicas de elementos finitos y partículas. *project of the National Plan R+D of the Spanish Ministry of Science and Innovation I+D BIA2007-68120-C03-01*, 2007-2010.

[128] M. Zagonjolli. *Dam Break Modelling, Risk Assessment and Uncertainty Analysis for Flood Mitigation.* PhD thsis: Delft University of Technology, 2007.

[129] J. Zhang. An augmented lagrangian approach to bingham fluid flows in a lid-driven square cavity with piecewise linear equal-order finite elements. *Computer Methods in Applied Mechanics and Engineering*, 199:3051 – 3057, 2010.

[130] O.C. Zienkiewicz, A.H.C. Chan, M. Pastor, B.A. Schrefler, and T. Shiomi. *Computational Geomechanics with special reference to earthquake engineering.* Wiley, 1999.

[131] O.C. Zienkiewicz and T. Shiomi. Dynamic behaviour of saturated porous media: the generalised biot formulation and its numerical solution. *International Journal Num. Anal. Meth. Geomech.*, 8:71–96, 1984.

[132] O.C. Zienkiewicz, R.L. Taylor, and P. Nitharasu. *Vol. 3. The finite element method. Fluid dynamics.* Elsevier, 2005.